NAVAL POSTGRADUATE SCHOOL

MONTEREY, CALIFORNIA

DISSERTATION

CAPTURING CHARACTERISTICS OF ATMOSPHERIC REFRACTIVITY USING OBSERVATIONS AND MODELING APPROACHES

by

Robin C. Cherrett

June 2015

| Dissertation Supervisor | Qing Wang |

Approved for public release; distribution is unlimited

THIS PAGE INTENTIONALLY LEFT BLANK

REPORT DOCUMENTATION PAGE		*Form Approved OMB No. 0704–0188*
Public reporting burden for this collection of information is estimated to average 1 hour per response, including the time for reviewing instruction, searching existing data sources, gathering and maintaining the data needed, and completing and reviewing the collection of information. Send comments regarding this burden estimate or any other aspect of this collection of information, including suggestions for reducing this burden, to Washington headquarters Services, Directorate for Information Operations and Reports, 1215 Jefferson Davis Highway, Suite 1204, Arlington, VA 22202-4302, and to the Office of Management and Budget, Paperwork Reduction Project (0704-0188) Washington, DC 20503.		

1. AGENCY USE ONLY *(Leave blank)*	2. REPORT DATE June 2015	3. REPORT TYPE AND DATES COVERED Dissertation
4. TITLE AND SUBTITLE CAPTURING CHARACTERISTICS OF ATMOSPHERIC REFRACTIVITY USING OBSERVATION AND MODELING APPROACHES		**5. FUNDING NUMBERS**
6. AUTHOR(S) Robin C. Cherrett		

7. PERFORMING ORGANIZATION NAME(S) AND ADDRESS(ES)
    Naval Postgraduate School
    Monterey, CA 93943-5000
		8. PERFORMING ORGANIZATION REPORT NUMBER

9. SPONSORING /MONITORING AGENCY NAME(S) AND ADDRESS(ES) N/A		**10. SPONSORING/MONITORING AGENCY REPORT NUMBER**
11. SUPPLEMENTARY NOTES The views expressed in this dissertation are those of the author and do not reflect the official policy or position of the Department of Defense or the U.S. Government. IRB Protocol number ____N/A____.		
12a. DISTRIBUTION / AVAILABILITY STATEMENT Approved for public release; distribution is unlimited		**12b. DISTRIBUTION CODE**

13. ABSTRACT (maximum 200 words)

Electromagnetic wave propagation is sensitive to gradients of refractivity derived from atmospheric temperature, humidity, and pressure. It is thus critical to understand the atmospheric conditions leading to the formation of the gradient layers and explore methods to better represent the gradients in forecast models. This study first examines the sensitivity of the surface evaporative ducts to key physical parameters of the atmospheric surface layers. This analytical study is followed by analyses of relationships between the ducting/propagation variables and air-sea interaction parameters using input from buoy-based measurements in diverse meteorological conditions. We further explore numerical simulations using a single column model (SCM) forced by the 3-dimensional Coupled Ocean-Atmosphere Mesoscale Prediction System (COAMPS). This hybrid modeling approach leverages the mesoscale model's strength to provide large-scale forcing while using high vertical resolution simulations to capture the strong gradient layers. The SCM approach works effectively for the stratocumulus-topped boundary layers. Its performance for the cloud-free cases from Trident Warrior 2013 was limited due to the complexity of external forcing in coastal regions. A new blending technique is developed based on SCM to effectively patch the surface evaporative duct to forecasts from COAMPS with consistent model physics throughout the entire atmospheric column.

14. SUBJECT TERMS Propagation, surface layer, boundary layer, air-sea interaction, flux parameterization, COAMPS, single column model	**15. NUMBER OF PAGES** 207
	16. PRICE CODE

17. SECURITY CLASSIFICATION OF REPORT Unclassified	**18. SECURITY CLASSIFICATION OF THIS PAGE** Unclassified	**19. SECURITY CLASSIFICATION OF ABSTRACT** Unclassified	**20. LIMITATION OF ABSTRACT** UU

NSN 7540–01-280-5500

THIS PAGE INTENTIONALLY LEFT BLANK

**CAPTURING CHARACTERISTICS OF ATMOSPHERIC REFRACTIVITY
USING OBSERVATION AND MODELING APPROACHES**

Robin C. Cherrett
Lieutenant Commander, United States Navy
B.S., University of Washington, 1999
M.S., Naval Postgraduate School, 2006

Submitted in partial fulfillment of the
requirements for the degree of

DOCTOR OF PHILOSOPHY IN METEOROLOGY

from the

**NAVAL POSTGRADUATE SCHOOL
June 2015**

Author: Robin C. Cherrett

Approved by: Qing Wang   Wendell Nuss
                    Professor of Meteorology   Professor of Meteorology
                    Dissertation Supervisor

                    Peter Guest   Rebecca Stone
                    Professor of Meteorology   Professor of Oceanography

                    Shouping Wang
                    Naval Research Laboratory

Approved by: Wendell Nuss, Chair, Department of Meteorology

Approved by: Douglas Moses, Vice Provost for Academic Affairs

iii

THIS PAGE INTENTIONALLY LEFT BLANK

ABSTRACT

Electromagnetic wave propagation is sensitive to gradients of refractivity derived from atmospheric temperature, humidity, and pressure. It is thus critical to understand the atmospheric conditions leading to the formation of the gradient layers and explore methods to better represent the gradients in forecast models. This study first examines the sensitivity of the surface evaporative ducts to key physical parameters of the atmospheric surface layers. This analytical study is followed by analyses of relationships between the ducting/propagation variables and air-sea interaction parameters using input from buoy-based measurements in diverse meteorological conditions. We further explore numerical simulations using a single column model (SCM) forced by the 3-dimensional Coupled Ocean-Atmosphere Mesoscale Prediction System (COAMPS). This hybrid modeling approach leverages the mesoscale model's strength to provide large-scale forcing while using high vertical resolution simulations to capture the strong gradient layers. The SCM approach works effectively for the stratocumulus-topped boundary layers. Its performance for the cloud-free cases from Trident Warrior 2013 was limited due to the complexity of external forcing in coastal regions. A new blending technique is developed based on SCM to effectively patch the surface evaporative duct to forecasts from COAMPS with consistent model physics throughout the entire atmospheric column.

THIS PAGE INTENTIONALLY LEFT BLANK

TABLE OF CONTENTS

LIST OF FIGURES

LIST OF TABLES

THIS PAGE INTENTIONALLY LEFT BLANK

LIST OF ACRONYMS AND ABBREVIATIONS

ABL	Atmospheric Boundary Layer
AREPS	Advanced Refractive Effects Prediction System
CFSR	Climate Forecast System Reanalysis (CFSR)
COAMPS	Coupled Ocean/Atmosphere Mesoscale Prediction System
DOD	Department of Defense
ED	evaporation duct
EDH	evaporation duct height
EDS	evaporative duct strength
EKE	eddy kinetic energy
EM	electro-magnetic
ESM	Electronic Surveillance Measure
FAM	Forecast Analysis Module
GCM	global circulation model
GPS	Global Positioning System
HIRLAM	High Resolution Limited Area Model
HPC	high performance computer
IGRA	Integrated Global Radiosonde Archive
IOP	intensive observation period
JPDF	joint probability distribution function
LAM	limited area model
LES	large eddy simulation
MABL	marine atmospheric boundary layer
MASFLUX	Mini Air Sea Flux
MO	Monin-Obukhov
MOST	Monin-Obukhov Similarity Theory
NAVSLAM	Navy Atmospheric Vertical Surface Layer Model
NCOM	Navy Coastal Ocean Model
NPS	Naval Postgraduate School
NRL	Naval Research Laboratory
NWP	numerical weather prediction

PDF	probability distribution function
PF	propagation factor
PL	propagation loss
POD	probability of detection
RCM	regional Circulation Model
RHIB	ridged hull inflatable boat
SCM	single column model
SSC PAC	SPAWAR Systems Center Pacific
SST	sea surface temperature
TOGA COARE	Tropical Ocean-Global Atmosphere Coupled Ocean-Atmosphere Response Experiment
TW13	Trident Warrior 2013
UADC	Upper-Air Ducting Climatology
UAV	unmanned aerial vehicle
USV	unmanned surface vehicle
UUV	unmanned underwater vehicle
VACAPES	Virginia Capes
WMO	World Meteorological Organization
WWIII	Wavewatch III

ACKNOWLEDGMENTS

I would like to thank the following individuals and groups:

- Professor Qing Wang, my advisor, for all the mentoring and dedication that you so willingly gave. There's not enough room here to express all of my thanks.

- Ms. Hway-Jen Chen for all the effort and time you gave to essentially teach me all the aspects of understanding, running, and modifying COAMPS and the SCM model and for all the contributions in model development and modifications.

- Committee members Dr. Shouping Wang, Prof. Peter Guest, Prof. Wendell Nuss, and CAPT (ret) Rebecca Stone for your support, assistance, expertise, and insights along the way, and all your valuable review and feedback.

- Mr. John Kalogiros for providing surface layer model and data analysis tools.

- Mr. Ted Rogers and Ms. Amalia Barrios for the enthusiastic willingness to generate ideas, assist me with fundamental EM propagation concepts, numerous discussions concerning results, and always answering the phone for my many questions.

- Dr. James Doyle, Mr. John Cook, and Ms. Tracy Haack for discussions and assistance with the model, and running and providing the COAMPS datasets.

- Dr. Dan Eleuterio, CDR (ret) Matt Moore, LCDR (ret) Chuck Bragg for introducing and involving me in Trident Warrior 2013 and all the assistance while underway for data collection.

- Mr. Paul Frederickson for discussions and comparison data processing.

- Mr. Dick Lind for all your assistance in building and providing instrumentation for Trident Warrior 2013. Mr. Robert Creasy for all your assistance and discussions in the computing lab. Crew of R/V Knorr for a fantastic underway. Ms. Kate Horgan for datasets and processing. Naval Postgraduate School Meteorology Department.

- Family and friends.

And most of all, I would like to thank my lovely wife, Emily, for everything.

THIS PAGE INTENTIONALLY LEFT BLANK

I.   INTRODUCTION

A.   IMPROVED ELECTRO–MAGNETIC PROPAGATION AND THE NAVY

Improved capability to model and forecast the propagation of the electro-magnetic (EM) spectrum in the battle space has broad applications throughout nearly all Navy and Department of Defense (DOD) functional areas due to the utilization of the EM energy in either active or passive manners for all sensing and communications systems as well as state-of-art weapon systems. Refraction is the property of the atmosphere that bends EM energy (e.g., radar, communications) from a straight line path and is caused by spatial variations in temperature, humidity, and pressure. The modified index of refractivity (M) is calculated using the following formula:

$$M = N + 0.157z = 77.6\frac{P}{T} - 5.6\frac{e}{T} + 3.75x10^5\frac{e}{T^2} + 0.157z$$

where N is index of refractivity, P is pressure (mb), T refers to temperature (K), e is vapor pressure (mb), and z is height (m).

The vertical gradient of M is used to determine how EM rays are bent relative to the Earth's curvature. Since M is dependent on humidity and temperature, significant vertical gradients of M are often found in the surface layer and at the top of the atmospheric boundary layer (ABL) where there are typically significant gradients in temperature and humidity. When the gradient is strong enough, an effect known as "trapping" is observed where EM energy refracts back towards the surface and is effectively trapped within the layer. This trapping effect creates "ducts," or wave guides, through which anomalously high EM energy can be observed to propagate far beyond line-of-sight which can dramatically change effective communication and radar detection ranges within, above, or below the duct. This process yields a tactical change in EM system performance. Since the ABL is also the layer of the atmosphere in which nearly all Navy and DOD communication and remote sensing transmissions originate, occur, and/or terminate, this effect has a very broad impact. Therefore, accurate representation

of the ABL for use in EM propagation models becomes critical in successful prediction of EM behavior for Navy and DOD application.

B.   THE EVAPORATION DUCT

The Evaporative Duct (ED) is the ducting feature near the maritime surface that results from surface evaporation that generates a significant moisture gradient, and thus an M gradient, near the surface. Whereas ducts that occur at the inversion level are common depending on the weather pattern, the evaporation duct is nearly always present in the maritime environment (Babin 1997). The prevalent existence of ducting layer near the surface and its impacts on propagation make the evaporative duct a critical feature for many Navy applications and warrants a thorough understanding of its major characteristics (Reilly and Dockery 1990; Paulus 1990).

To understand the characteristics of ED, we must first understand the sensitivities of M to the environmental variables. It is widely accepted that the moisture gradient has the most impact upon the M gradient, but a comprehensive sensitivity and scale analysis could not be located in published literature. To fill this void, this study intends to perform a systematic scale analysis on dependence of the gradient of modified refractivity on surface layer meteorological conditions in order to quantify the relative contributions of the environmental variable gradients to the total M gradient.

Although it is the gradient of M in the ED that impacts the propagation of EM energy, the ED is often described in terms of the properties of evaporation duct height (EDH) and M-deficit, or evaporation duct strength (EDS) as it is referred in this study. These two properties attempt to describe the shape of the near surface M profile where the EDH is the height at which the M gradient is zero and the EDS is the difference in M-units between the surface and the EDH. Yet it is desirable to relate the ED properties to variable space that directly describes the surface layer thermodynamic and wind conditions. Most commonly used quantities as independent variables include air-sea temperature difference (ASTD) for thermal stability, and relative humidity (RH) for water vapor amount, and wind speed.   In previous studies, these variables are allowed to vary within their reasonable ranges. The EDH and EDS are hence examined as a joint function of ASTD and RH at a given wind speed. Two issues exist in this

approach. One is the adequacy of the ASTD, RH, and wind speed used to describe the EDH and EDS dependence. Some of the currently used variables (e.g., RH) may not be the most appropriate quantity to relate to ED properties. The use of ASTD is also questionable since it does not directly relate to the dynamic stability of the surface layer turbulence. Another issue is whether the choices of the surface layer conditions are realistic representations of the atmosphere. Some of the extreme values of the diagnosed ED properties may be a result of unphysical combination of the input quantities to the ED models.

The ultimate goal in this analysis is to relate the sensitivities of the effects on EM propagation to the ED properties. It is generally understood that EDs with larger EDH values have greater impacts on the EM propagation. However, it is also generally understood that the EDH value alone does not adequately describe the shape of the M profile. Until now, analysis has usually been bound by individual case studies where surface layer profiles are individually run through a propagation model and the results investigated. Conclusions generated from this method lacks representation from a large number of samples. Recent improvements in the Navy's Advanced Refractive Effects Prediction System (AREPS), which uses the Advanced Propagation Model (APM) to calculate the propagation path and loss, have enabled a capability to produce results from multiple cases (M profiles) automatically. This improvement has made it possible to produce results from a very large volume of cases for meaningful statistical analyses. With a large number of surface layer cases, the ED will be calculated using the COARE surface flux algorithm modified to produce mean wind and scalar profiles in the surface layer following Monin-Obukhov similarity theory. The EDH and EDS are then diagnosed based on the derived M profile. To avoid using unrealistic surface layer conditions generated from given ranges of the parameters involved, observations from buoys around the U.S. coast are used to include a wide range of surface conditions. Measurements from eight buoys yielded more than 45,000 surface layer M-profiles. These M-profiles were used as input to AREPS to generate a database of propagation loss for certain target heights and propagation distances and relate these quantities to the distribution of EDH and EDS. By using this approach we attempt to describe the impacts of ED properties on propagation.

3

The results suggest that bulk Richardson number, specific humidity depression, and wind speed are the most appropriate surface layer variables to describe the variability of EDH and EDS and that propagation loss is most sensitive to EDH and to a lesser extent to EDS.

C.   MESOSCALE MODEL FOR EM PROPAGATION APPLICATION

In the past two decades, mesoscale models, such as the Navy's limited area model (LAM), the Coupled Ocean/Atmosphere Mesoscale Prediction System (COAMPS), have shown significant improvements for forecasting winds, precipitation, clouds, and other weather-related variables. Success in mesoscale forecast for weather phenomena is largely attributed to increase amount of observational data and the ever improving technique of data assimilation. The same mesoscale models are also used to generate environmental conditions as input to EM prediction models for propagation loss prediction. Although improvements in weather system prediction should lead to better characterization of the general refractive environment, mesoscale models are not designed for the purpose of EM propagation prediction. The apparent shortcoming in these models for providing atmospheric profiles to propagation models is the coarse vertical resolution, which leads to its inadequacy in representing the gradient layers in the atmosphere, particularly in the atmospheric surface layer. This is elaborated in the following.

The lowest vertical level in a mesoscale model is typically 10 m with a vertical resolution on the order of 10 to 20 m in the lowest few layers. Given that a typical surface layer is about 100 m and sometimes much lower, mesoscale models do not resolve surface layer gradients well. This is not an issue for a mesoscale model aimed at weather forecasting when the role of the surface layer with regard to weather forecast is to provide the correct surface fluxes of momentum, sensible heat, and latent heat. COAMPS uses the Louis scheme (Louis 1979) to calculate vertical eddy fluxes within the surface layer using polynomial functions of the bulk Richardson number based on the temperature, wind, and moisture values at the lowest grid level, which is typically a height of 10 m. While this is effective for determining the surface layer fluxes in the

model, the poor vertical resolution in the surface layer is incapable of producing the correct vertical moisture and temperature structure in the surface layer, which is critical to determining evaporation duct properties.

A current engineering remedy for the missing surface layer in a mesoscale model is to pad the vertical profiles generated from the mesoscale model with a surface layer profile generated by a diagnostics surface layer model with high vertical resolution. These surface layer models are all based on Monin-Obukhov (MO) similarity theory. When a surface layer model is used specifically for obtaining evaporative duct height and strength, it is referred to as the evaporative duct model, such as the Navy Atmospheric Vertical Surface Layer Model, or NAVSLaM (Fredrickson 2015). Since the surface layer model is only valid for the surface layer, the resulting profile must be appended to the bottom of a balloon sounding or a COAMPS model profile in some fashion in order to provide a complete profile for use in propagation models. This appending concept is inherently challenging due to two considerations. First, there is uncertainty in identifying the vertical extent of the surface layer in any particular case. Additionally, the surface layer profile is derived nearly independent from the upper level profile in that it uses only one data point and the surface temperature as input. To address practical issues, Frederickson (2015) developed a blending algorithm to append the surface layer profile with the upper air profile. One mode of the blending algorithm is automatic which makes assumptions as to how the profiles should be blended together. The manual mode requires a scientific knowledge and experience that is likely beyond that of the typical end user and, therefore, raises concern over its use. This is the current state of the Navy's EM propagation modeling toolkit and has resulted in significant improvement in the Navy's ability to effectively represent and predict propagation effects. However, due to challenges described, the resulting combined profile occasionally has a "kink" feature. Additionally, the combined profile is the result of an engineering solution of merging two distinct models that are not physically connected and therefore this approach is not physically based. This is the practical problem of having an ED model that is only valid in the lowest part of the atmosphere.

Above the surface layer, the vertical resolution of COAMPS increases from 20 meters near the surface to 100 meters at 1 km. The vertical gradient in moisture at the inversion is often observed to only span a scale of meters to tens of meters which makes the typical vertical resolution of COAMPS inadequate to represent the sharp gradients found within and at the top of the ABL. A logical solution to address the vertical resolution issue is to employ a higher vertical resolution 3D model. However, the computational expense of increasing vertical resolution quickly grows to a level that cannot be used operationally as an increase in resolution also requires a significant reduction in time step. Limited computing resources, operational demand to run many limited area models (LAMs) in various regions around the globe in support of Navy operations, and the need for relatively short run cycles to make the model output available to forecasters quickly enough to have operational value severely limit such an approach.

An alternative approach to address the requirements and shortcomings of the approaches discussed thus far is to employ a single column model (SCM). The SCM is a 1D mode of a full 3D model which has historically been used to isolate physical processes in atmospheric modeling to fine tune parameterization schemes and has also been used in climate modeling. One of the benefits of the SCM is the significant computational savings that are realized due to the vast reduction in number of calculations that are normally required in full 3D models. That computational trade space can be leveraged to implement a very high vertical resolution grid as well as more complex physics packages that are often significantly parameterized due to their high computational cost.

The intent of this study is to examine the SCM's ability to represent the refractivity profile in the boundary layer based on various conditions to address the issues described above that are common with operational LAM solutions used by EM propagation models. An atmospheric and oceanographic measurement and modeling field campaign in 2013 located in the waters just off the Virginia coastline, known as Trident Warrior 2013 (TW13), is leveraged as the requisite data sets for this study. The Naval Research Laboratory in Monterey (NRL-MRY) ran the COAMPS model at high

resolution for evaluation during this field campaign. Since the SCM, as with all models, requires initial and forcing conditions, the NRL COAMPS simulations will be used for SCM set up as well as for comparison with the SCM results. Additionally, the measurements taken during the intensive observation period (IOP) in July 2013 will provide a baseline for validation.

D.   OBJECTIVES OF RESEARCH

This work first focuses on an in-depth understanding of the evaporation duct and its impacts on EM propagation in the atmosphere. We first explore the sensitivity of the gradient of the modified refractivity by performing a comprehensive sensitivity and scale analysis of the modified refractivity equation. We continue by using a COARE algorithm modified to produce surface layer profiles of temperature, moisture, and wind to produce a very large sample of profiles based on observations from buoys in the coastal U.S. water. These profiles are analyzed for their evaporation duct properties and the relationship between these properties and the physical independent variables are examined. The very large number of evaporation duct profiles is then run through AREPS to calculate the propagation loss of EM energy along the path of varying geometric and transmitter setups in order to examine the relationship and sensitivity of signal loss to evaporation duct properties.

This work also develops and explores the use of an SCM as an alternative approach to address the vertical resolution issues common with operational LAM solutions used by EM propagation models and the issue of blending two physically disaggregated models to produce a single representative refractivity profile. The COAMPS is run in SCM mode with the initial and forcing conditions from full COAMPS 3D output. In this sense, the system is a hybrid model leveraging the benefits of the 3D model synoptic and mesoscale solutions while adding value for the purposes stated above by running at high vertical resolution for short-term forecasts. The SCM is tested repeatedly under different idealized and non-idealized conditions to assess its sensitivity, behavior, and performance. Additionally, a modification of the surface layer scheme within COAMPS is explored in order to fit the objective of resolving surface

layer non-linear processes and the resulting variable profiles since that is not the objective of the full 3D model. Ultimately, the hybrid SCM approach is also tested with a nudging scheme that controls the upper level grid values while allowing the surface layer processes to evolve the profile and thereby fully leveraging the benefits of both the 3D model and the SCM. When the nudging level is low enough to reach the surface layer, the SCM essentially blends the SCM generated surface layer with the COAMPS output, which results in blending of the COAMPS and a surface layer. The new blending scheme utilizes the same COAMPS model with consistent model physics.

E.   SUMMARY OF DISSERTATION

Chapter II provides background on EM propagation and effects, surface layer and air-sea interface processes and their modeling and parameterization in numerical weather prediction, and previous and current uses of the single column model. Chapter III describes the models and data sources used in this study including the Navy's EM propagation model system known as the Advanced Refractive Effects Prediction System (AREPS), the Trident Warrior 2013 (TW13) field campaign including the COAMPS model and data that was run and collected during the intensive observation period (IOP), and the development of the single column model and it's supporting modules. In Chapter IV, a comprehensive scale and sensitivity analysis of the modified refractivity gradient equation is performed. Additionally, the variability of evaporation duct parameters based on surface layer model results from buoy observations is analyzed and the effect of variable evaporation duct properties on EM energy propagation loss is also analyzed. The results of the hybrid modeling approach are presented in Chapter V, including idealized cases and various test cases demonstrating sensitivity of the system to different forcing and schemes. Also in Chapter V, a new approach for modeling and representing the evaporation duct is introduced and preliminary results presented. Chapter VI provides a summary of this study, conclusions, and recommendations for future work.

II. BACKGROUND

A. EM PROPAGATION

1. EM Propagation Basics and Abnormal Propagation Conditions

EM propagation path depends on the structure of the index of refraction of the medium through which the wave is propagating. The index of refraction is the ratio of the speed of light in a vacuum to that in the medium.

$$n = \frac{c_{vacuum}}{c_{medium}},$$

where c is the phase velocity of light and n is the unitless index of refraction. Since the index of refraction in the atmosphere is normally very close to one, refractivity (N) is used, which is simply

$$N = (n - 1) \text{ x } 10^6$$

N values in the troposphere typically range between 200 and 400 N-units and therefore, are much simpler to use than values of order 10^{-4}.

Refractivity can also be calculated by the properties of the atmosphere. An in-depth derivation to calculate refractivity is available in Bean and Dutton (1968) but is summarized in the following four relevant points. First, the index of refraction for EM frequencies less than 80 GHz is frequency independent. This frequency range includes the common radio and microwave spectrum which is the range this work is focused on. Second, the index of refraction is directly proportional to the density of the medium with the exception of the influence of water vapor. Third, dipole charged molecules, such as water vapor, have a significantly greater impact on the index of refraction than normal symmetrically charged molecules. Finally, a considerably simplified formula for calculating the index of refraction in the troposphere for EM frequencies between 100 MHz and 80 GHz is:

$$N = 77.6\frac{P}{T} - 5.6\frac{e}{T} + 3.75\text{x}10^5\frac{e}{T^2} \qquad (2.1)$$

where p is atmospheric pressure in mb, e is vapor pressure in mb, and T is temperature in K. The directly proportional relationship with density is apparent in that pressure is in the numerator and temperature is in the denominator. Specifically, higher pressure increases

density which yields an increase in refractivity. Conversely, higher temperature decreases density which yields a decrease in refractivity. The significance of the water vapor as a dipole molecule is also apparent in that it is the only other variable considered in this simplified equation and that an increase in water vapor pressure yields an increase in refractivity.

A gradient in refractivity causes an EM wave front to change orientation which effectively changes the direction in which the wave is propagating. This process is called refraction. The effect is to bend EM energy toward higher values of *N* and the amount of refraction is directly proportional to the gradient of *N*. A notional gradient of -40 *N*-units km^{-1} exists for a Standard Atmosphere with average humidity gradients. The negative gradient means that normal EM propagation in the atmosphere is bent slightly downward from a straight line path, allowing the energy to wrap around the surface of the Earth slightly before leaving the atmosphere as shown in Figure 1. This is considered "normal" refraction and is so defined when *dN/dz* is between 0 and -79 N/km. When the environment is such that the value of *dN/dz* > 0 N/km, it is referred to as "sub-refraction" and EM energy will bend up before ever reaching the geometric horizon. When *dN/dz* < -79 N/km, it is known as "super-refraction" and if *dN/dz* < -157 N/km, bending is significant enough to actually bend the EM energy back downward relative to the curving Earth. This is called "trapping." After EM energy has bent back toward the Earth, it eventually propagates below the trapping layer, where it bends back up again (or reflects off the surface) and begins its ascension path again. Assuming the EM energy encounters the same vertical profile of *M*, it will again enter the trapping layer and the process will repeat for as long as the environment allows. This path is known as a "duct." The refraction paths just discussed are illustrated in Figure 2.

The modified refractivity index, denoted as *M*, is used to determine how radar rays are bent relative to Earth's curvature. To a close approximation, the curvature (1/R, where R is the radius of curvature) of a near horizontally propagating EM wave is given by *–dn/dz* (director of Naval Oceanography and Meteorology 1984; Turton 1988). Thus, the *dN/dz* required to bend EM energy downward relative to the surface is the inverse of the Earth's radius of 6371 km multiplied by 10^{6}, or 0.157 m^{-1}. Therefore,

$$M = N + 0.157z = 77.6\frac{P}{T} - 5.6\frac{e}{T} + 3.75x10^5\frac{e}{T^2} + 0.157z \qquad (2.2)$$

M is often used because when it is plotted as a vertical profile it offers immediate visual recognition of trapping layers in the atmosphere. That is to say that when *dm/dz* <0, EM energy will be trapped.

Another refractivity index sometimes used is called potential refractivity. It is calculated using Equation 2.2 except potential temperature, potential water vapor pressure, and 1000 hPa atmospheric pressure are used in lieu of ordinary air temperature, water vapor pressure, and actual surface pressure (Jeske 1973). The advantage of this index was the assumption that potential refractivity was a conserved quantity (Babin 1997).
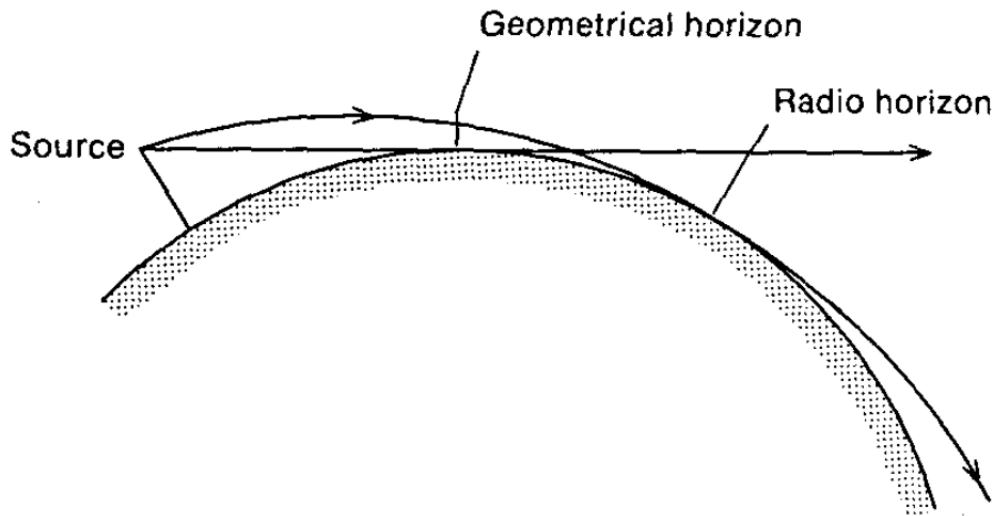
Figure 1.   Illustration showing the difference between the horizon of a linear
geometric path and a refracted radio wave
(from Turton 1988)
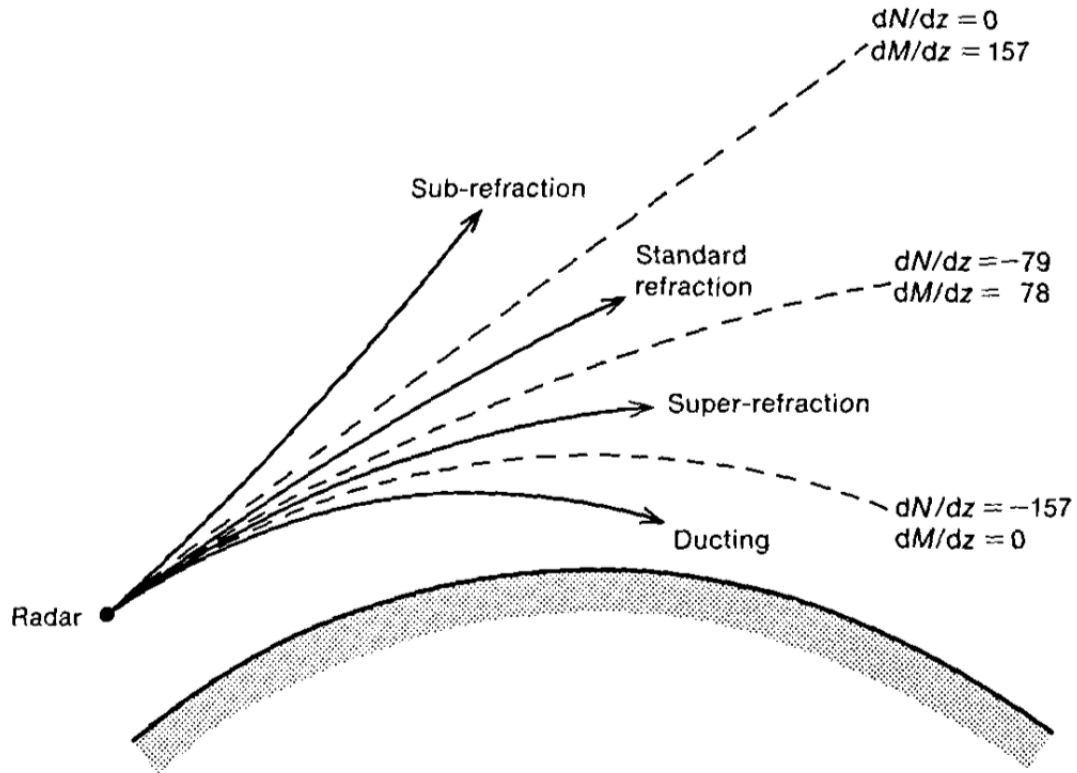
Figure 2.   Illustration of refractivity propagation categories and the ray-paths
             of horizontally transmitted rays. Categories are based on the slopes
             of *N* (*dN/dz*) and *M* (*dM/dz*) for sub-refraction, standard refraction,
                      super-refraction, and trapping
                            (from Turton 1988)

Three different categories of ducts are illustrated by vertical profiles of *M* in Figure 3. The first is an elevated duct (left) which occurs when there is a trapping layer aloft and the local minimum of *M* at the top of the trapping layer is greater than the value of *M* at the surface. In this case, the waveguide (duct) is entirely above the surface. The second is a surface-based duct (center) which occurs when there is a trapping layer aloft but this time the magnitude of the local minimum of *M* at the top of the trapping layer is less than that at the surface. In this case, the waveguide uses the surface as the bottom boundary which results in some portion of the EM energy that is refracted down from the trapping layer to reflect off the surface. The third category of ducts is the surface duct (right) which occurs when the trapping layer extends all the way to the surface.

General diagnostic terminology when discussing ducts is also indicated in Figure 3. The trapping layer top is indicated in red and is the height of the local *M* minimum. The bottom of the trapping layer (blue) is the base height (Rogers 1997). The duct itself (cyan) spans the layer between the trapping layer top and the height below which has the same *M* value as the trapping layer top. If the local minimum is also the absolute minimum, then the duct bottom is the surface. The difference between minimum and maximum values of the trapping layer is the M-deficit. Finally, the difference between the local trapping layer minimum and next minimum *M* value below is the M-excess.
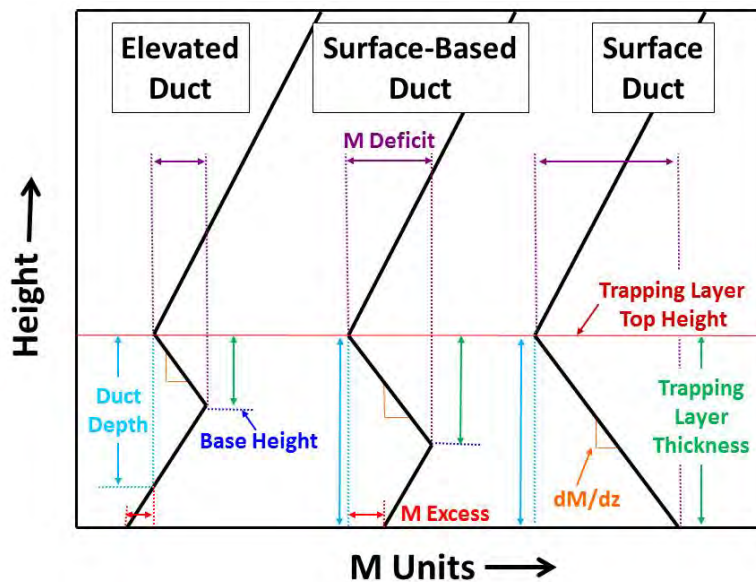
Figure 3.   M-profile and common diagnostic parameters for three general classifications of ducts. The black line is the M profile, the x-axis is M-units increasing to the right and the y-axis is height.

Typical propagation paths of EM energy in the presence of ducts are illustrated in Figure 4. The ducting feature and corresponding *M*-profile is illustrated on the left and the resulting propagation ray trace is illustrated on the right. A "ray" is a line that is perpendicular to the EM wave front at all locations and indicates the path of propagation.

In surface ducts (Figure 4a), near horizontally emitted energy is trapped in the duct, greatly extending the effective range of the sensor over the geometric horizon.

Another key feature illustrated is the "radio hole" that exists above the trapping layer which is caused by the absence of EM energy due to trapping energy near the surface. The reality is that ducts are not rigid and some energy does "leak" into the radar hole (Turton 1988), but the available energy is significantly reduced from normal and may not be useful. The surface-based duct (Figure 4b) shows relatively the same pattern of extended ranges and a radio hole. However, important additional features to note are the "skip zones" which are holes in the coverage near the surface. Usually only one or two skip zones are formed, however under the right conditions and geometry there may be several skip zones. Figure 4c shows the rays when a transmitter is in an elevated duct. The over-the-horizon extended ranges are contained only within the duct and energy below the duct is relatively non-existent (except at close range).

Ducts are formed by a variety of mechanisms that create vertical profiles of warmer and/or dryer air over cooler and/or moister air (Turton 1988). The most common mechanism is the subsidence associated with anticyclones in which subsiding air creates a stable layer that separates the cooler and moister marine boundary layer from the free atmosphere. Any mechanism involving subsidence (i.e., sea breeze) has potential to form or strengthen a duct at the inversion and these mechanisms typically produce elevated and surface based ducts. Another mechanism in creating ducts is a frontal zone because of the warm-overriding-cold structure. However, these ducts, if they exist, are typically weaker due to the lack of hydro lapse between the cooler and warmer air masses. Night-time radiative cooling is another mechanism that can lead to duct formation. These ducts may evolve to any form of the classification of ducts depending on where and how strong the temperature and moisture lapse rates are. A fourth significant mechanism of duct formation is advection when warm and/or dry continental air is advected over cooler seas that are then cooled and moistened at the lower levels.
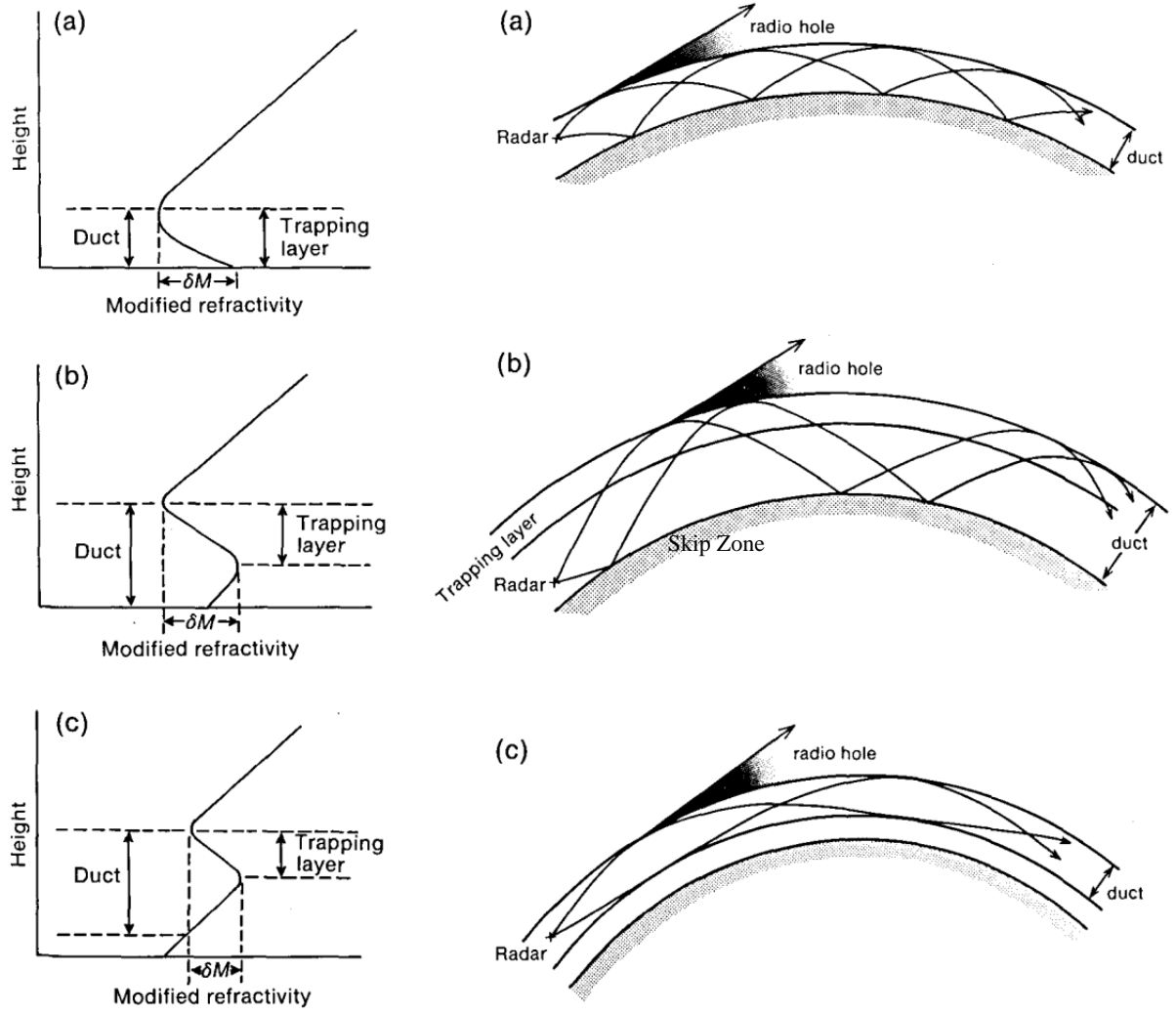
Figure 4. Examples of ducting conditions based on *M* gradient (left) and the
typical resulting EM propagation paths (right) for a) surface duct, b)
surface based duct, and c) elevated duct
(after Turton 1988)

The evaporation duct (ED) is a special form of a surface duct. Specifically, the *M* gradient that forms the trapping layer is the result of the significant moisture gradient over the water surface due to evaporation.   This strong moisture gradient over water exists in stable, neutral, and unstable surface layers, and therefore an ED over water almost always exists. Just as described for surface ducts, the height at which *dM/dz* is zero (i.e., the local minimum) is the top of the trapping layer. This is called the evaporation duct height (EDH) and is a key diagnostic parameter when describing an ED.

15

The EDH has typical values of 1 to 40 meters as opposed to the surface duct which is as deep as the boundary layer on the order of 10^2 to 10^3 meters. The M deficit will be referred to as evaporative duct strength (EDS) in this work. Correctly representing the temperature and humidity structure of the marine atmospheric surface layer is critical to properly diagnosing the evaporation duct.

It is also important to note that combinations of these ducts may also exist. It is not uncommon for a complex M profile to have multiple elevated ducts in combination with a surface-based duct and an evaporation duct.

2.   Quantifying Propagation Loss

Propagation loss and propagation factor are common measures by which EM propagation is assessed and will be the basis for illustrating propagation for the remainder of this paper. Propagation loss (PL) is the ratio of effective transmitted power to the power received at the specified location (i.e., less propagation loss means more EM energy is received) and is quantified in units of decibels (dB). Causes of propagation loss include free-space path loss, refraction effects, diffraction, absorption, scattering, and multimodal interference. Free-space path loss is due to the natural 3-D expansion of an EM wave front through free space that is effectively expanding in the shape of a sphere while conserving the total EM energy. Refraction can affect received power by focusing or dispersing the wave front through lensing effects. Diffraction loss is when part of an EM wave front is blocked by an obstacle. Absorption and scattering is simply when EM energy is absorbed or reflected by the medium respectively. Multimodal interference is the canceling and superimposing effect when slightly different waves from the same path or similar waves from different paths arrive at the same place at the same time. Propagation factor (PF) is the ratio of received power to the power that would have been received had only free-space path loss been applied along the path and it is also commonly given in units of decibels (dB). Propagation loss diagrams in this paper are generated by the Advanced Refractive Effects Prediction System (AREPS) that is discussed in greater detail in Chapter III.

The pattern of propagation loss from surface based emitters deviates significantly from standard when ducts exist due to the propagation paths as illustrated previously in Figure 4. When EM energy is ducted, it can greatly reduce the propagation loss because it effectively has removed a dimension of spherical spreading loss. Figure 5 demonstrates a comparison of propagation loss of a C-band (5.5 GHz) radar in (a) a standard atmosphere environment and (b) surface based duct environment. The surface based duct yields a propagation loss pattern with energy trapped in the surface based duct, skip zones, and a radar hole above the duct top. It's also noticeable that there is energy leaking out of the duct above the second skip zone. Additionally, note that the lobe pattern is a result of the multi-modal interference.

a)
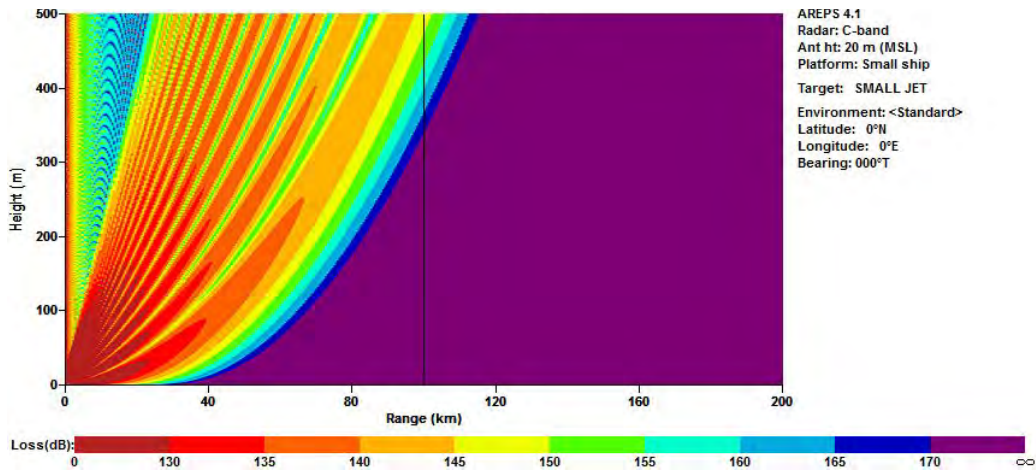
b)
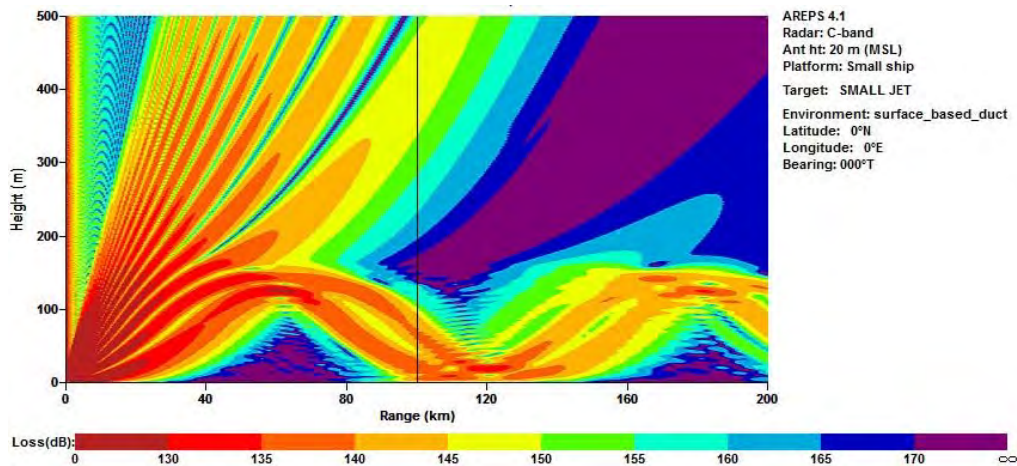
Figure 5.   Propagation loss diagram for a C-band radar at 20 meters in a) a standard atmosphere and b) surface based duct at a height of 164 m.

17

Propagation loss is also very sensitive to height of the transmitter relative to the duct height. Figure 6 shows a comparison of propagation loss of an X-band (10Ghz) radar in a 12 meter evaporation duct height environment where the transmitter is at a height of a) 20 m (i.e., above the duct) and b) 10 m (i.e., in the duct). Both diagrams show substantial energy trapped within the duct near the surface providing extended ranges however Figure 6b indicates significantly more energy has been trapped. Also, there is a significantly different propagation loss solution aloft as well.

Propagation loss is also sensitive to the frequency of the EM energy. To be clear, the sensitivity of refractivity (or modified refractivity or index of refraction) to frequency is negligible for EM waves less than 80 Ghz, but the propagation effects are significant. Figure 6c shows the C-band radar in the same environment and at the same transmitting height (10 m) as the X-band radar in Figure 6b. The propagation effect is dramatically different because the wavelength of the C-band radar is too long to effectively be trapped by the shallow evaporation duct. A simplified formula for establishing duct intensity, which is given in terms of the maximum wavelength that is trapped by a duct, is given as

$$\lambda_{max} = \frac{2}{3} CD\Delta M^{\frac{1}{2}} \qquad (2.3)$$

where λ_{max} is the maximum trapped wavelength (m), D is the duct depth (m), ΔM is the M-deficit, and C=3.77x10^{-3} for a surface-based duct, and C=5.66x10^{-3} for an elevated duct (Kerr 1951; Turton et al. 1988). It's important to note that the wavelength cutoff is not sharp and longer wavelengths will be ducted to some extent. Also, shorter wavelengths will not be perfectly ducted and energy will leak out of the duct (Brooks 1999). The significance is that longer wavelengths (lower frequencies) will be trapped more effectively with larger duct depths and larger M-deficits. Comparison between Figure 5a (standard atmosphere) and Figure 6c (evaporation duct), which have the same C-band radar at the same transmitting height, shows a significant change in the propagation loss pattern due to the evaporative duct despite the lack of a near surface bright band indicating completely trapped energy such as what is seen with the X-band radar plots in Figures 6a and 6b.

a)

AREPS 4.1
Radar: X-band
Ant ht: 20 m (MSL)
Platform: Small ship

Target: SMALL JET

Environment: sample_e...ion_duct
Latitude: 0°N
Longitude: 0°E
Bearing: 000°T

Loss(dB): 0   130   135   140   145   150   155   160   165   170   ∞

b)

AREPS 4.1
Radar: X-band
Ant ht: 10 m (MSL)
Platform: Small ship

Target: SMALL JET

Environment: sample_e...ion_duct
Latitude: 0°N
Longitude: 0°E
Bearing: 000°T

Loss(dB): 0   130   135   140   145   150   155   160   165   170   ∞

c)

AREPS 4.1
Radar: C-band
Ant ht: 10 m (MSL)
Platform: Small ship

Target: SMALL JET

Environment: sample_e...ion_duct
Latitude: 0°N
Longitude: 0°E
Bearing: 000°T

Loss(dB): 0   130   135   140   145   150   155   160   165   170   ∞

Figure 6.   Propagation loss diagram for an X-band (10 GHz) radar in a 12
meter evaporation duct height environment where the radar is at
height of a) 20 m and b) 10 m. Figure (c) is the same environment
with a C-band (5.5 GHz) radar at 10 m.

19

B. MARINE ATMOSPHERIC SURFACE LAYER PROCESSES AND MONIN-OBUKHOV SIMILARITY THEORY

1. Physical Processes in the Marine Surface Layer

The air-sea interface is the lower boundary to the atmosphere where significant transfers of mass, momentum, and energy occur. Mass is transferred in the form of moisture, aerosol, and gas exchange, momentum by wind stress and energy is transferred in the form of sensible heat, latent heat, and radiation. The rate of exchange of mass, momentum and energy greatly affects the structure of both the marine atmospheric surface layer (MASL) and the ocean surface layer, which can have either stabilizing or positive feedback relationships to the rate of exchange. Representation of the air-sea processes and their interactive nature and effects in environmental models remains one of the most difficult areas of modeling. The flux of mass, momentum and energy (except radiation) is carried out primarily through turbulence which, in the surface layer, have eddies whose sizes are determined by their proximity to the surface. The surface layer is generally considered to be the lowest 10% of the boundary layer and is characterized by turbulence and flux values that do not deviate by more than 10% (Stull 1988). As such, to a first order approximation, the fluxes at one level can be used to represent the respective fluxes in the entire surface layer. Most processes to be described are sub-grid scale and are therefore parameterized in forecast models. Figure 7 illustrates many of the processes that occur that affect the ocean and atmospheric surface layers.

With regard to EM propagation, moisture flux processes are the most significant type of mass exchange at the sea surface. The primary mechanism for moisture flux is evaporation which adds water in the form of vapor to the atmosphere. Factors that affect evaporation rate include the sea surface temperature, atmospheric temperature, wind speed, humidity, and sea state (or wave action). Higher air and water temperature and lower humidity increase evaporation rate. Higher wind speed can also increase evaporation rate by turbulent motion that will evacuate saturated air away from the surface and thus effectively lowering the humidity at the surface. Wave motion can add surface area which increases evaporation as well as induce a modest wind flow just above the surface in what is called the wave boundary layer. The wave affected boundary layer

can be especially significant in low wind states. Finally, wind and waves can combine to create sea spray which greatly increases the surface area due to droplets (Fairall et al. 1994). Significant processes that transfer water from the atmosphere to the ocean include precipitation and condensation. Major non-water mass exchanges include gas exchange and aerosols. Gas exchanges are very significant on climatic timescales, but not as much on boundary layer process timescales except that bubbles caused by wave action can affect albedo and the radiative transfer properties. Similarly aerosols can precipitate to the water surface and effect evaporation and radiative properties or be born from the surface through wave action to provide a source of cloud condensation nuclei.
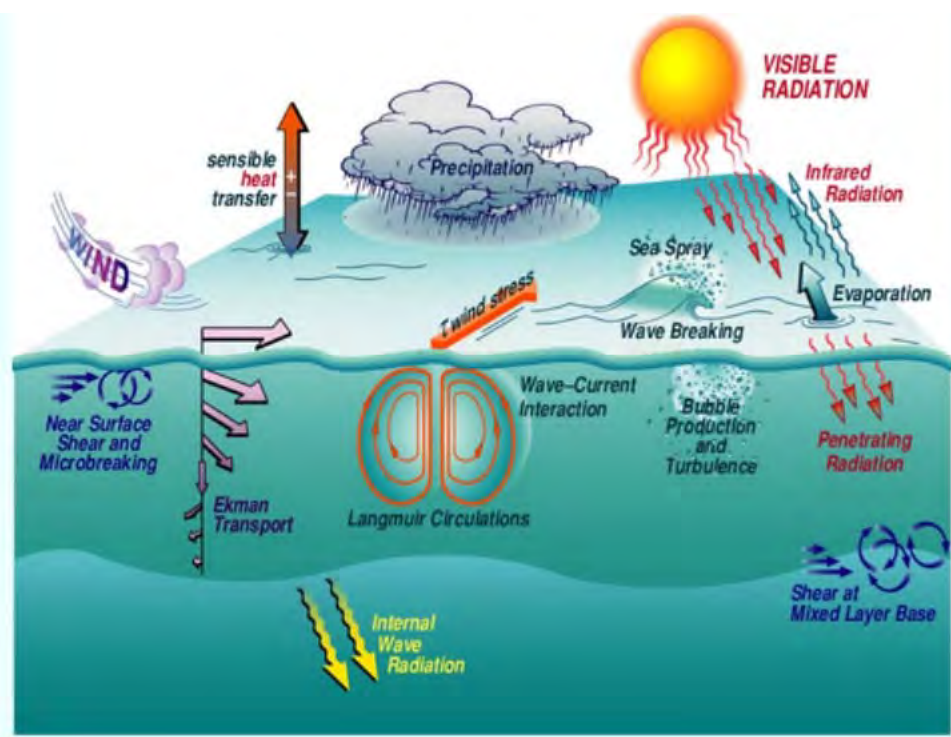
Figure 7.   Diagram illustrating the many physical processes that occur at the air sea interface that affect the structure and evolution of the MASL and ocean surface layer (from Edson et al. 2005).

Latent heat transfer is often discussed in lieu of moisture or water vapor flux. The latent heat is the energy that is required to change the state of the water molecules from liquid to vapor. Effectively, when evaporation from the ocean surface occurs, it is transferring heat from the ocean and storing it in the atmosphere, which will be released

when it condenses. This will cause a cooling effect of the ocean surface, which is a stabilizing factor for the atmospheric surface layer and destabilizing for the upper ocean.

Sensible heat transfer is due to the physical conduction of heat due to the air-sea temperature difference at the interface. As such, heat transfer is increased by greater air-sea temperature difference or an increase in wind speed for the same reasons as discussed above for evaporation. Another consideration, although not an actual method of sensible heat transfer, is the mixing of precipitation into the upper ocean surface. Precipitation can vary considerably which can help to produce significant variability in sea surface temperature and salinity which has a feedback into the other mechanisms discussed.

Radiative energy transfer has a key role in the total energy budget at the surface and can significantly affect the thermal stability in both the MASL and the upper ocean. Incoming shortwave radiation will either scatter at the surface or penetrate the water. Scattering at the surface can be affected by the incident angle and surface albedo which is affected by surface roughness and presence and concentration of sea foam and impurities such as aerosols or biologics. After shortwave radiation has entered the water, it will be back scattered or absorbed. Scattering can be affected by bubbles caused by wave action and by other impurities such as suspended particles and biologics. The remaining radiation energy is absorbed in a logarithmic decreasing manner with depth. This logarithmic distribution of heating warms the near surface water more than the water below which has a stabilizing effect on the ocean surface layer and a destabilizing effect on the atmospheric surface layer (Fairall et al. 1996). As opposed to shortwave radiation where seawater is relatively transparent, seawater is essentially opaque to outgoing long wave radiation. That is to say that all of the outgoing long wave radiation from the sea surface originates within just the top skin (i.e., on the order of 1 mm) of the water. This contributes to the energy balance at the surface (considering sensible and latent heat) which often has a net effect to form a very thin cool skin which is destabilizing in the ocean surface layer but stabilizing in the atmospheric surface layer. Other factors that affect the radiation balance include diurnal cycle, season and latitude, presence of clouds and at what altitudes, atmospheric water vapor and other greenhouse gas concentrations and aerosols.

The transfer of momentum at the air-sea interface is the last major contributor to the MASL and ocean surface layer processes. Wind blowing across the water creates capillary waves due to frictional drag between the two mediums. The capillary waves increase the roughness which increases the frictional drag and ultimately create waves whose average wave height is proportional to the wind speed that created them. Due to the frictional effects, a mean wind shear is established in the atmospheric surface layer which is a source of turbulence. Additionally, the momentum exchange induces a surface current in the ocean which also establishes shear in the ocean surface layer to generate turbulence. The wind stress on the surface drives secondary organized circulations called Langmuir circulation. Gradients in wind driven surface stress over a temporal and spatial mesoscale also produces an effect called Ekman pumping. This can induce upwelling or down-welling which can generate internal waves in the ocean pycnocline. All these processes may contribute to upper ocean turbulence and mixing which can entrain waters from below and mix down the cool skin water at the surface.

Turbulent transfer of sensible and latent heat and momentum are expressed in terms of turbulent (or eddy) flux defined as the transfer of heat or momentum across a surface of unit area per unit time. The momentum flux is also referred to as stress. In a kinematic form, the kinematic flux of a property, ζ, can be mathematically expressed as the product of the perturbation flow velocity perpendicular to the surface and the perturbation of the property to be transported. When considering the flux transport across the horizontal plane, we get

$$\text{Kinematic vertical eddy flux} = \overline{w'\zeta'}$$

where w' is the perturbation of vertical wind, ζ' is the perturbation of ζ, and the overbar denotes an ensemble average. In the context of the surface layer processes, we are mostly interested in the vertical flux transport relative to the horizontal plane. In the atmospheric surface layer, a velocity scale which is called the friction velocity, u_*, is defined based on kinematic vertical momentum flux as

$$u_*^2 = \sqrt{|u'w'|^2 + |v'w'|^2} \tag{2.4}$$

where the u' are the velocity fluctuations along the mean wind direction and v' along the cross wind direction. This surface layer velocity scale leads to the definition of the surface layer temperature and humidity scales:

$$\theta_* = \frac{-\overline{w'\theta'}}{u_*} \tag{2.5}$$

$$q_* = \frac{-\overline{w'q'}}{u_*} \tag{2.6}$$

These surface layer scaling parameters are frequently used to represent turbulent momentum flux and sensible and latent heat flux effects.

2.   Monin-Obukhov Similarity Theory

The Monin-Obukhov Similarity Theory (MOST) relates the non-dimensional gradient of velocity, temperature, and humidity in the atmospheric surface layer to universal functions of atmospheric stability (Monin and Obukhov 1954). It is based on the assumption that flows with similar ratios of convective to mechanical generation of turbulence at a given height should have similar turbulent structure (Edson 2004). It was derived using the fundamentals of basic π theory that states that if a process has a physical relationship involving *m* variables with *n* fundamental dimensions, then there exist *m-n* non-dimensional quantities that can describe the process using the *m* variables. Based on this analysis, a non-dimensional group, z/L, is defined where *L* is the Monin-Obukhov length (Obukhov 1946) defined as

$$L = -\frac{u_*^3 \bar{\theta}_v}{\kappa g \left(\overline{w'\theta'}_v \right)} = \frac{u_*^2 \bar{\theta}_v}{\kappa g \theta_*} \tag{2.7}$$

where $\bar{\theta}_v$ is the mean virtual potential temperature and $\kappa = 0.4$ is the von Karman constant. This non-dimensional group (z/L) is referred as the stability parameter. The resulting relationship from the complete π theory analyses yields the commonly known flux-profile relationship and has the form of

$$\frac{\partial X}{\partial z} = \frac{X_*}{\kappa z} \varphi_X \left(\frac{z}{L}\right) \tag{2.8}$$

where X denotes velocity, potential temperature, or specific humidity, X_* is the scaling parameter for $u, \theta,$ or q. φ_X is the universal function that has been empirically derived through experimentation that followed. It is often considered that the universal functions or non-dimensional gradient for heat and moisture are equivalent and are denoted with a subscript of h whereas momentum is denoted with a subscript of m.

The universal functions were originally derived over land and have been updated for the MASL. Businger et al. (1971) provided a set of these functions based on the Kansas experiment from 1968 that was conducted over a grass field in Kansas:

$$\emptyset_m \left(\frac{z}{L}\right) = \begin{cases} 1 + 4.7 \left(\frac{z}{L}\right), & \frac{z}{L} > 0 \quad (stable) \\ 1, & \frac{z}{L} = 0 \quad (neutral) \\ \left(1 - 15\frac{z}{L}\right)^{-1/4} & \frac{z}{L} < 0 \quad (unstable) \end{cases} \tag{2.9}$$

$$\emptyset_h \left(\frac{z}{L}\right) = \begin{cases} 0.74 + 4.7 \left(\frac{z}{L}\right), & \frac{z}{L} > 0 \quad (stable) \\ 0.74, & \frac{z}{L} = 0 \quad (neutral) \\ \left(1 - 9\frac{z}{L}\right)^{-1/2} & \frac{z}{L} < 0 \quad (unstable) \end{cases} \tag{2.10}$$

For any sets of known fluxes of momentum, sensible heat, and latent heat, the x gradient at level z can be estimated using Equations (2.8), (2.9), and (2.10). Furthermore, Equation (2.8) can be integrated which then takes the form

$$\bar{U} = \left(\frac{u_*}{\kappa}\right) \left[ln \left(\frac{z}{z_0}\right) + \psi_m \left(\frac{z}{L}\right) \right] \tag{2.11}$$

$$\bar{\theta}_z - SST = \left(\frac{\theta_*}{\kappa}\right) \left[ln \left(\frac{0.74z}{z_{0t}}\right) + \psi_h \left(\frac{z}{L}\right) \right] \tag{2.12}$$

$$\bar{q}_z - q_{s(SST)} = \left(\frac{q_*}{\kappa}\right) \left[ln \left(\frac{0.74z}{z_{0q}}\right) + \psi_h \left(\frac{z}{L}\right) \right] \tag{2.13}$$

where z_0 is the aerodynamic roughness length and ψ_m and ψ_h are the universal functions in integrated form from the roughness length to z. This form describes the corresponding variables as a function of height when the scaling parameters, surface roughness, and surface temperature are given. The aerodynamic roughness length is defined as the height at which the wind speed becomes zero. One early method of determining the roughness length over water was using the Charnock relationship (Charnock 1955) which is

$$z_0 = 0.014 \frac{u_*^2}{g} \tag{2.14}$$

Simply, higher wind stress makes higher waves resulting in greater roughness length.

The bulk aerodynamic formulation for surface fluxes is based on MOST for the surface layer while simplifying the appearance of the equation by including factors such as thermal stability and surface roughness into the drag and exchange coefficients, C_D and C_H respectively, in equation (2.15). Equation (2.15) becomes the well-known bulk flux parameterization.

$$\begin{aligned}
\overline{u'w'} &= -C_D \overline{U_{10}^2} \\
\overline{w'\theta'} &= -C_H \overline{U}(\bar{\theta}_{10} - \bar{\theta}_0) \\
\overline{w'q'} &= -C_H \overline{U}(\bar{q}_{10} - \bar{q}_0)
\end{aligned} \tag{2.15}$$

Liu et al. (1979) had later updated the Businger et al. relationship using data collected over water, their relationship became known as the "LKB" scheme. Wieringa (1980) criticized the original Kansas experiment design as using an unrealistic von Karmon constant due to flow distortion problems of the tower, over speeding of the cup anemometers, and unstable performance of the sonic anemometers. In response, Hogstrom (1988) reformulated the universal functions of Businger et al. (1971) and a new value of the von Karman constant has been widely accepted. Fairall et al. (1996) presented an extended effort in obtaining surface fluxes based on the MOST theory. They used ship-based measurements from Tropical Ocean-Global Atmosphere Coupled Ocean-Atmosphere Response Experiment (TOGA COARE) which included consideration of various overwater related issues such as wind-wave interaction, SST modification by cool skin and warm layer effects, and effects of precipitation and gustiness on surface fluxes. Results from Fairall et al. (1996) are still considered the near state-of-the-art surface flux parameterizations and have been widely used in forecast and climate models.

3.   K-Theory Turbulence Closure

Turbulent mixing is one of the key processes determining the evolution and structure of the atmospheric boundary layer. Turbulent eddies of many sizes contribute to this process of which the smaller eddies cannot be explicitly represented by models of finite grid resolution. As a result, turbulent mixing is parameterized on scales resolvable

to the model referred to as the mean. K-theory is one of the methods to represent the effects of turbulent mixing. K-theory assumes that the turbulent flux of variable ζ in kinematic form, $\overline{w'\zeta'}$, is related to the mean vertical gradient of the variable:

$$\overline{w'\zeta'} = -K\frac{\partial \bar{\zeta}}{\partial z} \tag{2.16}$$

K is referred to as the eddy diffusivity in general. When ζ represents the horizontal wind components, then K is referred to as eddy viscosity and is denoted as K_m. Similarly, eddy diffusivity for specific humidity or potential temperature is written as K_h. The K-theory is also referred to as the first-order turbulence closure or simply the down-gradient turbulent transport due to the explicit involvement of the vertical gradient of the mean quantity.

Because of the direct involvement of the vertical gradient of the mean quantity, the K-closure represents well the turbulent transport by small scale eddies. Early observational studies revealed that positive heat flux may exist in spite of a positive potential temperature gradient (Bunker 1956). This indicates turbulent transport may counter to the local gradient, which happens when the turbulent large eddies dominate the flux transport (Deardorff 1966).

In the atmospheric surface layer, K_m and K_h can be expressed using the MOST flux-profile relationship:

$$K_m = \frac{u_* \kappa z}{\varphi_m\left(\frac{z}{L}\right)} \tag{2.17}$$

and

$$K_h = \frac{u_* \kappa z}{\varphi_h\left(\frac{z}{L}\right)} \tag{2.18}$$

where u_* is the frictional velocity, κ the von-Karman constant, φ_m and φ_h are the non-dimensional gradients for momentum and heat, respectively. It is seen that K_m and K_h generally increase with height and with increasing instability.

Although with significant differences in details, nearly all forecast models of climate-scale, synoptic-scale, and mesoscale models use the eddy-diffusivity approach to parameterize turbulent transport in the atmospheric boundary layer. The physical

27

parameterizations of these models are essentially one-dimensional (1D) in the vertical. One-dimensional modeling of the boundary layer has been an essential tool for the development and validation of turbulence parameterizations for a variety of boundary layer conditions (e.g., Troen and Mahrt 1986; Ayotte et al. 1996; Bretherton et al. 2003) and for the improvement of weather prediction and climate models. The most commonly used turbulence closure in the boundary layer above the surface layer is a hierarchy of closure models developed by a series of publications by Mellor and coauthors (e.g., Mellor and Yamada 1974). Among the various types of closure outlined in Mellor and Yamada, the level $2\frac{1}{2}$ closure has been widely used in various mesoscale models including COAMPS. In particular, the eddy viscosity K_m and the eddy diffusivity K_h are expressed as:

$$(K_m, K_h) = lq(S_m, S_h) \tag{2.19}$$

where l and $q^2/2$ are the turbulence macro-scale and the turbulent kinetic energy (TKE), respectively. The stability functions S_m and S_h can be solved from a system of two algebraic equations involving empirical constants and two dimensionless quantities, G_m and G_h, related to mean shear and buoyancy:

$$(G_m, G_h) = \frac{l^2}{q^2}\left(\left|\frac{\partial u}{\partial z}\right|^2, -\frac{\partial b}{\partial z}\right) \tag{2.20}$$

where u and b are the horizontal wind and the buoyancy. Refer to Mellor and Yamada (1974) for the algebraic equations for S_m and S_h. The K_m and K_h obtained this way generally continue to increase above the surface layer and reach a maximum in the mid-boundary layer and then decrease with further increase of height (Therry and Lacarrere 1983).

The eddy diffusivity is particularly sensitive to the turbulence macro-scale, or "mixing length," and the formulation of the mixing length used is therefore a difficult and a distinguishing trait of models (Therry and Lacarrere 1983). The mixing length, l_K, is generally considered to be equal to the dissipation length scale, l_ε, and thus many discussions refer to the formulation of the dissipation length scale in lieu of the mixing length. Henceforth, for simplicity, we will simply denote the mixing length scale as l. The form of the mixing length is often taken of the form after Blackadar 1962 as:

$$\frac{1}{l} = \frac{1}{kz} + \frac{1}{l_\infty} \qquad (2.21)$$

where the length scale is interpolated between the two limits such that $l \sim kz$ as $z \to 0$ and $l \sim l_\infty$ as $z \to \infty$ (Mellor and Yamada 1974).

The first term on the right of Equation (2.21) accounts for the physical limitation of the mixing length in the surface layer. Specifically, the size of the turbulent eddies is limited by the presence of the Earth's surface (Stull 1988). Blackadar (1962) had considered this term only in a neutral surface layer at which the term took the form as shown in Equation (2.21). A modified form of this term accounts for stability and introduces the Monin-Obukhov universal functions as defined above in Equations (2.9) and (2.10) (Djolov 1973: Yu 1976) resulting in the form:

$$\frac{\varphi_{m,h}(z/L)}{kz} \qquad (2.22)$$

In the case of a neutral surface layer, the numerator would be unity. Many large scale models, including COAMPS, only calculate stability parameter and apply the universal function at lowest resolved vertical grid level for two reasons. The first reason is because the primary interest of the parameterized surface layer in these models is to account for total surface flux. The second reason is that the vertical grid resolution is sufficiently sparse so that only the lowest level is assumed to consistently be in the surface layer under all conditions.

The second term in Equation (2.21) accounts for the length scale outside of the limiting surface layer and the formulation of l_∞ is varied. Early propositions of this value stipulated proportionality to the geostrophic wind velocity (Blackadar 1962). Mellor and Yamada (1974) proposed the length scale account for the vertical extent of the turbulence field and defined the term to be the ratio of the first to the zeroth moment of the turbulence intensity profile giving the form:

$$l_\infty = \alpha \frac{\int_0^\infty zq\,dz}{\int_0^\infty q\,dz} \qquad (2.23)$$

29

where α is an empirical constant. Burk and Thompson (1982) set α to 0.2 for COAMPS.

The K-closure theory has some advantages which include its ability to be simple and fast compared to higher order closure models. Also, as shown above, the feedback of turbulence as a forecasted parameter can be implemented which makes this a KE-closure model where KE accounts for the eddy kinetic energy (EKE) feedback. A disadvantage of the K-closure model as discussed thus far is that there is no account for counter-gradient flux. The earlier work of Deardorff (1966, 1972) introduced a non-local transport term into the K-closure framework to account for flux transport by large eddies that mix heat in a manner that was counter to the local gradient. Many follow-on works were done through theoretical analyses and/or large eddy simulations to explore the true physical representation of such counter gradient terms (e.g., Wyngaard 1984; Wyngaard 1985). Troen and Mahrt (1986) presented a simple boundary layer formulation on the nonlocal turbulence parameterization and made it possible to include such effects to be incorporated into weather and climate prediction models.

4.   Evaporation Duct Models

The evaporation duct exists primarily due to a significant negative vertical gradient in humidity near the water surface. Evaporation duct models provide the refractivity characteristics in the surface layer to account for the temperature and specific humidity gradients near the air-sea interface. Standard operational measurement of the near surface layer using radiosondes, rocketsondes, dropsondes, shipboard sensors, etc., is not possible due to insufficient vertical resolution, inability to sample to the surface, or ship contamination of the near-surface flow field (Frederickson, Davidson, et al., no date). Typically, the only operationally available observation includes a bulk measurement of temperature, humidity, pressure and wind at a single elevation within the surface layer and the SST.

Since the evaporation duct is usually limited to the surface layer, MO similarity theory is typically used to generate the surface layer mean vertical structure. The evaporation duct models use this approach to calculate the vertical refractivity gradient

30

(Babin, 1997). This profile of refractivity gradient can then be processed to determine evaporation duct characteristics such as duct height and strength. Two types of evaporation duct models that have been developed include the potential refractivity model and the LKB-based models. These two types of ED models are described below.

The Paulus-Jeske (PJ) evaporation duct model (Jeske 1973; Paulus 1984, 1985, 1989) was once the most widely used model (Babin, 1997) and uses the potential refractivity quantity discussed previously. It was incorporated into Integrated Refractive Effects Prediction System (IREPS) and then AREPS, and was used operationally by the U.S. Navy from 1978 until 2012. This model assigns inputs of air temperature, relative humidity, and wind speed to a height of 6 m, regardless of the actual observation height. SST is also used and surface pressure is assigned a constant value of 1000 hpa. Cook and Burk (1992) showed that potential refractivity in stable conditions did not obey MOST because when properly non-dimensionalized, the vertical gradient of potential refractivity was not a single universal function of z/L. This suggested that the premise assumption for this model in using potential refractivity was likely an error for at least stable conditions. Another aspect unique to the PJ model is that it uses a critical potential refractivity gradient of -0.125 to determine ducting vice the typical -0.157 gradient of refractivity. The Obukhov length is estimated from an empirical relationship between Richardson number and Obukhov length to decrease computation time. For stable or neutral conditions, if the calculated duct height is either negative or greater than the estimate Obukhov length, the PJ model assumes the Obukhov length estimate is an error and substitutes the duct height variable for L and recalculates. This effectively limits the EDH to the Obukhov length which is a limit that had no physical basis (Babin 1997). Conversely, the PJ model also sets a limit to the EDH of 40 m. PJ model assumes a constant aerodynamic roughness length, which, over water, can vary by as much as 2 orders of magnitude. Finally, as a slight change in water vapor pressure gradient can significantly alter the surface layer refractivity profile, the most up-to-date algorithm for calculating saturation vapor pressure over water should be used to limit the correctable error wherever possible. The PJ model uses the Kiefer (1941) equation and doesn't correct for salinity as suggested by Sverdrup et al. (1942).

The LKB-based evaporation duct models are so categorized because they use similarity theory with near surface properties parameterized by Liu, Katsaros, and Businger (1979). Liu et al. (1979) developed the surface layer model of air-sea exchanges of heat, moisture, and momentum which led to bulk atmospheric parameterizations for determining flux profile relationships within MOST. Fairall et al. (1996) modified the parameterizations based on data from the Tropical Ocean and Global Atmosphere Coupled Ocean-Atmosphere Response Experiment (TOGA COARE) project. Although TOGA COARE took place over the tropical waters where conditions were nearly always unstable with light to moderate winds, the resulting modifications to the LKB parameterizations are preferred in over water conditions since the original LKB Kansas Experiment (1979) surface layer model was derived from a land borne experiment. Four LKB-based evaporation duct models of note are listed here: Babin, Young, and Carton (1997) referred to as BYC; Frederickson, Davidson, Goroch (2000) referred to as NPS (for Naval Postgraduate School); Cook and Burk (1992) referred to as NRL (for Naval Research Lab); and Kurt Cral of the Naval Warfare Assessment Station based upon the LKB code described in Liu and Blanc (1984) and referred to as NWA. Some subtle differences exist between these LKB models. Several have different methods of calculating pressure (e.g., linear pressure gradient, integrated hypsometric equation assuming hydrostatic linear virtual temperature profile, etc.). Another difference is that only NPS and BYC models incorporate the gustiness correction of Godfrey and Beljaars (1991), which is used to extend MOST to low wind speeds. However, the most significant difference between the models is they use different forms for $\psi(z/L)$ in Equations 2.11 to 2.13. More details on similarity theory are available in section B.2. Of note, the NPS model has since been developed and integrated into AREPS in 2012 and is now known as NAVSLaM (Navy Atmospheric Vertical Surface Layer Model). AREPS also incorporates the NPS vertical refractivity profile blending algorithm that blends the surface layer model output with upper air M profile derived either from measurement or mesoscale model.

C. SINGLE COLUMN MODEL

The Single Column Model (SCM) is a 1-dimensional employment of a full 3-dimensional model or a single-grid column of a global circulation model or mesoscale model. This allows isolation of column physics to be explored such as convection, clouds, radiation, and surface fluxes. One of the focuses of this study is to assess the feasibility of using a SCM to provide a short-term forecast, or "nowcast," which may adequately represent the structure of the marine atmospheric surface layer thermodynamic properties.

There are two advantages of the SCM approach. The SCM is extremely computationally efficient in comparison to full 3-dimensional models such as non-hydrostatic limited area models (LAM), large eddy simulations (LES), or direct numerical simulations. The SCM does not incorporate imbedded horizontal structure or large scale dynamics. The compounded computation time of physics at every grid point in a full 3-dimensional model is also avoided. As a result, SCM can handle more complex physics over possibly a significantly much higher vertical resolution, smaller time step, or both. Another advantage is the ability to more simply specify or control the forcing for idealized simulations than that in full 3D models. Since an SCM only represents a 1-D problem, horizontal advection must be represented via prescribed horizontal tendency forcing. Similarly, since divergence is not calculated in the SCM setting, large scale vertical motion must also be prescribed. These external forcings may be provided from either observation, 3-dimensional model output, or idealized and prescribed values designed to represent specific conditions of interest. When observations are used, assuming the observations are correct, any resulting parameter deviations when compared to future observations cannot be attributed to problems with the model that have nothing to do with the column physics being tested (Randall, session paper). This makes it so the SCM can be effectively used for sensitivity and evaluation studies of physical parameterizations.

To illustrate the prediction and forcing terms in the SCM model, the following set of 3D primitive equations for temperature and humidity are provided:

$$\frac{\partial \theta}{\partial t} = -v \cdot \nabla \theta - \omega \frac{\partial \theta}{\partial p} + Q \qquad (2.24)$$

$$\frac{\partial q}{\partial t} = -v \cdot \nabla q - \omega \frac{\partial q}{\partial p} + S \qquad (2.25)$$

where ω is vertical velocity in pressure coordinates, and Q and S represent the diabatic temperature and moisture terms, respectively, that are calculated in physics parameterizations with the SCM (Bergman and Sardeshmukh 2003).

The first term on the right of both Equations (2.24) and (2.25) is the horizontal advection term and the second term on the right is the vertical advection term. Since the horizontal gradient $(\nabla \xi)$ is not represented in a single column model, this term must be provided as an external forcing to the SCM. In a similar manner, since the vertical velocity (ω), which is a result of column divergence through continuity, must also be provided to the SCM.

There are also disadvantages using an SCM. The SCM alone cannot generate large-scale forcing such as divergence and/or horizontal advection, and lacks the feedback to the full 3D system. Even though tendency terms can be idealized when prescribed which can be an advantage, this also becomes a complex problem when trying to account for mesoscale variability that can change this forcing rapidly and in complex manners, especially in the vicinity of complex terrain or coastlines. The evolution of the SCM solutions is very sensitive to advection forcing. Similar issues are present in the term involving large scale vertical motion. Additionally, more complex feedbacks into the large-scale circulation are undetectable in the single column mode. Finally, as with all models, other characteristics of the SCM that require care include the provision of a solar constant, surface characteristics (elevation, albedo, roughness, vegetation type, etc.,) and planetary time and position (Randall session paper).

Previous studies using SCM mostly focused on developing or verifying specific physical processes in weather and climate models. By prescribing interactions with circulation dynamics, the SCM allows extended runs useful to climate researchers to test long term balance scenarios (e.g., Manabe and Wetherald 1967; Lee et al. 1997).

Additionally, the SCM has been extensively applied to study various sub-grid physical processes that are parameterized in full 3-dimensional models such as cumulus entrainment (Gregory 2001), diurnal cycle of convection (Betts and Jakob 2002; Guichard et al. 2004), cloud cover (Tompkins, Gierens 2007), PBL, stratocumulus, shallow cumulus parameterization (Neggers et al. 2009), surface parameterization (Trigo and Viterbo 2003), and radiation parameterization (Randall, Hu et al. 1994/1995; Somerville and Iacobellis 1999).

A significant conclusion regarding the use of an SCM is the rapid divergence of SCM solutions from that of a parent 3D model or observation even within 6 hours (Bergman and Sardeshmukh 2003). This short-range error growth limits the SCM's ability to be used as a long term prognostic model without additional adjustment as the SCM solution drifts toward highly unrealistic thermodynamic structures. Bergman and Sardeshmukh (2003) investigated using a dynamic parameterization scheme to maintain a coupled relationship between diabatic and adiabatic tendencies that did reduce the solution errors at six hours. Another common approach to reduce drift is to add relaxation terms to "nudge" the SCM's thermodynamic variables toward observed values (e.g., Ghan et al. 1999; Lohmann et al. 1999; Randall and Cripe 1999).

SCM has been implemented in several cases for short-term forecasting. Terradellas and Cano (2007) have employed an SCM using external forcing provided by the HIRLAM (High Resolution Limited Area Model) to improve skill in fog formation forecasting. Another investigation of a 1D model system employed to improve skill in very short-term forecasts of fog, cloud, and visibility in France by Bergot et al. (2005) concluded that improvement is a consequence of the ability of the forecast system to more accurately characterize the boundary layer processes. They also demonstrate that the use of a 1D model to forecast fog and low clouds could only be beneficial if it is associated with local measurements and a local assimilation scheme.

As discussed earlier, although some uses of deterministic short-term forecasting have resulted in skill improvement, other studies have found significant sensitivity of the SCM result to initial conditions and external forcing which decreases skill. Hack and Pedretti (2000) found that an ensemble approach to running the SCM resulted in such

strong sensitivity and that solution members bifurcate and cluster to form multiple solution states. This multiple attractor behavior is characteristic of highly nonlinear systems and illustrates the need for statistical characterization of single-column model solutions. This need for an ensemble approach may also be justified by the observational premise that small scale variations in the state variables are prevalent in a turbulent boundary layer in addition to variations in the underlying sea surface temperature, roughness length variables, and cloud impacted radiation forcing. Due to time and scope restraints, this work did not include an ensemble approach.

Many previous studies have examined the potential of using an SCM to model the marine boundary layer (MBL) structure. Burk and Thompson (1982) used an incompressible Boussinesq model with 55 levels in the lowest 3.75 km of the atmosphere. They investigated using either radiosondes from Navy platforms or interpolated low vertical resolution global circulation model (GCM) data to initialize the column and used 12 hour tendency, calculated from GCM output, to provide external forcing. The resulting RMS scores performed better than persistence, however no follow up study was found. In this study, a similar approach is evaluated for various boundary layer conditions for much shorter forecasts.

III.   MODELS AND DATA SOURCES

A.   ADVANCED REFRACTIVE EFFECTS PREDICTION SYSTEM

1.   Overview

The Navy's primary tool to model atmospheric propagation of radio frequency EM energy is the Advanced Refractive Effects Prediction System (AREPS). This system was developed and is maintained by SPAWAR Systems Center Pacific (SSC PAC) and it is a component of the Windows based Navy Integrated Tactical Environmental System (NITES), a program of record. The AREPS program computes and displays a number of EM system performance assessment tactical decision aids (SOF 2006) to include:

- Radar Probability of Detection (POD)

- Electronic Surveillance Measure (ESM) vulnerability

- High frequency (HF) to extremely high frequency (EHF) communications

- Simultaneous radar detection and ESM vulnerability

- Surface search detection ranges

Additionally, AREPS is a 2D model and is therefore able to capture horizontal differences over the propagation path. It is effective in coastal and overland areas of interest due to its capability to account for surface features to include terrain, finite conductivity, and dielectric ground constants. Our study, however, will focus on over water propagation effects.

The propagation model used by AREPS is the Advanced Propagation Model (APM) (Barrios 1992; Barrios 2002). This is a hybrid model that uses both ray optics and parabolic equation methods to model the propagation for frequencies between 2MHz and 57GHz.

The EM system database is user defined and maintained. Parameters of radar systems, transmitters, receivers, target descriptions, antennae patterns, frequency, system altitude, and all relevant parameters are stored in a changeable database that is preloaded

with a few sample systems. Classified databases are available and provide parameters for known U.S. and foreign systems.

Input of environmental conditions to AREPS can be obtained from numerical models or observations. AREPS can read or derive atmospheric refractivity profiles from an assortment of sources and can operate using either a horizontally homogenous environment or a spatially range dependent environment. Atmospheric refractivity data can be derived from mesoscale models in either GRIB2 or NETCDF format. COAMPS is operationally available to the Navy's end user in GRIB2 format with all the AREPS requisite variables. Additionally, profile data may be derived from a coded World Meteorological Organization (WMO) upper air observation message or entered via free-form column format. Also, the Naval Postgraduate School (NPS) continues to expand an existing climatological database for WMO upper air station locations for profile and ducting climatology as well as an evaporation duct climatology derived from model reanalysis data. Finally, for ocean reporting stations or profiles derived from numerical weather prediction over water, AREPS can calculate a surface layer profile using NAVSLaM and append it using a "blending" algorithm to the bottom of the upper air profile either automatically or with user input. Both the NAVSLaM and the blending algorithm were developed at NPS.

2.   Operationally Available Environmental Data

Propagation modeling is only useful if relevant data is available operationally which specifically needs to include either the atmospheric refractivity profiles or the variables required to calculate the refractivity profile. Currently, datasets available operationally are from upper air station soundings, numerical weather prediction, and climatology. Their limitations in EM propagation prediction are discussed in this section.

a.   *Upper Air Soundings*

Upper air soundings are vertical profiles of temperature, humidity, and pressure and, if Global Positioning System (GPS) equipped, position which can be used to derive wind speed and direction. The instrument package without position information is called a "radiosonde" whereas the instrument package with position information is called a

"rawinsonde" ("radar wind-sonde"). The instrument package is suspended from a buoyant balloon which is released from the surface and often reaches heights of around 30,000 m (about 100,000 ft) before bursting (Mass 2012). Weather agencies worldwide coordinate coincident land-based releases of these weather balloons at 00Z and 12Z for the primary purpose of data assimilation into environmental models. These soundings are also made available via the Internet. Upper air soundings may also be conducted as individual cases for research purposes or operationally such as for the DOD in support of EM propagation forecasting.

One of the greatest backward steps in data availability to the Navy for EM propagation assessments happened when the Navy ceased its at-sea upper air observation program in 2011. The Navy's balloon program has long served many purposes, two of which are still relevant to this study and include the direct impact of providing a high vertical resolution dataset of temperature and humidity used for atmospheric refraction models, and the indirect impact of providing atmospheric profiles for data assimilation into global and mesoscale atmospheric models. The program was canceled partly due to the cost to benefit ratio having declined in recent history due to availability of satellite derived soundings that could be assimilated into the atmospheric models over historically observation sparse regions of the oceans. Although the sheer number of these satellite derived profiles compensates for its reduced accuracy and vertical resolution for the purpose of data assimilation into atmospheric models, the poor quality of individual sounding retrievals are essentially useless for atmospheric propagation modeling purposes due to their coarse resolution, error range, and inability to resolve low level moisture gradients. However, this loss of direct data source capability was decided as acceptable due to advances in the atmospheric models themselves and their ability to provide the refractivity conditions to the end users. This point will be discussed later in the section about NWP limitations.

Additional limitations of upper air sounding data as a source for EM propagation forecasting include near surface measurement ship effect contamination as well as the question as to how well single temporal and spatial point sampling represents an often turbulent and variable atmosphere. Additionally, balloons tend to be sucked into updrafts.

Rogers (1996) concluded that range dependent sampling could improve EM propagation forecasts, but only if the samplings used to represent the spatial variability were measured within 2 hours of each other. Otherwise, the additional measurements no longer improved propagation estimates over using a single sample to describe a "plywood" environment (i.e., no spatial variability). Regarding measurement contamination, prior to launch the instrument is typically guarded to some degree from clean, undisturbed, and unmodified ambient air (Lin and Johnson 1996). This is especially true for ship based launches where preparation and launch typically occur near the stern of the vessel with the vessel turned into the wind. The instrument package can reach altitudes of tens to several hundreds of meters before uncontaminated air wash over the instruments to make the measurement accurately reflect the ambient atmosphere.   This contaminated portion of the sounding is one of the most critical parts when using the profile for EM propagation modeling making low level surface ducts questionable and evaporation ducts impossible to measure. As for the remainder of the lower atmospheric profile, natural horizontal variability in inversion height and strength leaves uncertainty as to how well the single point profile measurement represents the local atmosphere. Also, the single time measurement does not establish a trend. Without supplementary atmospheric model support, the single measurement loses even more relevance and representativeness in forecast space operational planning.

b.   Numerical Weather Prediction

The benefits of using Numerical Weather Prediction (NWP) as a data source for EM propagation forecasting is the combination of the versatility of the model to be setup in selected regions of interest, the continuous coverage over a domain, and its ability to provide the critical environmental parameters for refractivity in forecast space. In addition to semi-permanent hot spot regions of the world with nearly continuous Department of Defense presence, Operational COAMPS domains are set up on demand to be run in requested regions. These requests may be related to specific exercises or operations and the collective priority of which regions to run must be established so as not to exceed the maximum operational computing capacity. Once established however, the nested mesoscale model provides another quality source of guidance for general

weather forecasting as well as data for EM propagation forecasting for many range dependent profiles out to as many forecast hours as the model is assessed to perform well. This may be limited by nest size, boundary conditions, and the rate of advection from the boundaries to the points of interest.

There are limitations to using NWP for EM propagation forecasting. EM propagation conditions are categorized using the gradient of refractivity with respect to altitude (Almond and Clarke 1983). As such, EM propagation forecasts rely on accurate characterization of the environmental parameters temperature and humidity which have the most impact on refractivity. Specifically, it requires accurate quantification of the vertical gradient of the atmospheric thermodynamic variables near the surface and near the top of the atmospheric boundary layer. Accurate and adequate representation of these strong gradients requires a model with very high vertical resolution in the atmospheric boundary layer. This vertical resolution requirement for EM propagation forecasting purposes imparts a significant and prohibitive additional computational expense on existing 3-D limited area models whose primary purpose is mesoscale forecasting. In other words, although significant improvements have been made in high-resolution COAMPS simulations, the vertical resolution does not meet the requirements to adequately represent the refractive index gradients necessary for EM propagation modeling, and simply increasing the 3-D modeling resolution is unrealistic due to computation expense. Another design approach appears to be necessary.

A multitude of recent modeling studies have been focused on assessing whether global or mesoscale models possess sufficient fidelity to adequately provide range dependent profile data to EM propagation models (Burk and Thompson 1997; Haack and Burk 2001; Atkinson et al. 2001; Burk and Haack 2003; Atkinson and Zhu 2006). The 3D models in these studies parameterized the surface layer fluxes and did not resolve the lower boundary layer gradient. Haack et al. (2010) assessed the status of using mesoscale models for the purpose of characterizing the refractivity conditions. Their findings revealed the most critical aspects necessary for this purpose. They include in order of importance:

- Accurate large-scale forcing in initial fields and at lateral boundaries.

- Horizontal grid resolution of at most 5 km.

- Vertical grid resolution of at most 60 meters in the lowest 1 km of the atmosphere.

- Mesoscale structure retained in analysis or allowed to spin up on finer grids.

- Accurate and evolving SST fields of equivalent resolution to the model grid.

- 3DVAR and 4DVAR data assimilation techniques for proper moisture analysis.

The top three on the list include resolution that is not always available for operational models and model accuracy that suffers significantly when not in a region with ample data availability. Additionally, the vertical grid resolution findings resulted from a study focused on the Wallops Island 2000 experiment which did not include cloud topped boundary layer conditions and was based upon a limited study using 4 models of which COAMPS was evaluated at ~60m vertical grid spacing. The higher vertical resolution model, the MM5 which had ~45 m vertical grid spacing, had shown results in this limited study that had greater bias and root-mean-square error, and therefore performed worse overall than COAMPS. Those results may have been due to many circumstances or model intricacies; higher vertical resolution is likely to offer many other benefits.

c.   *EM Ducting Climatology*

EM ducting climatology is continuing to be developed by NPS and SSC Pacific and added to the existing AREPS database (Frederickson 2014; Amalia Barrios personal communication; AREPS User's Manual 2014). The Upper-Air Ducting Climatology (UADC) and Median Upper Air Profile databases are computed from the Integrated Global Radiosonde Archive (IGRA) to compile statistics from 996 observing stations from 1971 to present. Additionally, model reanalysis data from the Climate Forecast System Reanalysis (CFSR) dataset from 1979–2009 combined with the Navy Atmospheric Vertical Surface Layer Model (NAVSLaM) is being used to derive evaporation duct statistics for ocean regions around the globe. This provides key

historical statistics and profiles that represent the range of conditions previously measured or analyzed from model data. This is a significant improvement in overall long term planning capability for the Navy. However, it does not provide a forecast data point.

B. TRIDENT WARRIOR 2013 FIELD CAMPAIGN

Trident Warrior is an annual U.S. Navy exercise intended for experimentation and trials to test systems and doctrines. Trident Warrior 2013 (TW13) occurred in the Virginia Capes (VACAPES) Operations Area and included a specific segment focused on the utility of unmanned aerial vehicles (UAVs) launched and recovered at sea to collect data for the purpose of data assimilation into COAMPS to aid model performance for EM propagation modeling. A large coordinated supporting atmospheric and oceanographic data collection was conducted along with EM propagation loss measurements during an intensive observation period (IOP) run from the Research Vessel Knorr from July 13–18, 2013. This data set continues to be analyzed and provides measurements that can be used to validate model simulations.

Measurements directly relevant to this research include vertical profiles from rawinsonde measurements, tethersonde profiles, surface drifting flux buoy measurements, EM propagation loss measurements, and shipboard sampling of radiation, sea surface temperature, flux, and other mean variables. Other measurements that have potential to be of direct relevance include the UAV flux and mean variable data set and unmanned surface vehicle (USV) platforms, however these data sets are still in quality control and not available yet. Other supporting measurements included a small fleet of unmanned underwater vehicle (UUV) ocean observations that provided significant observation data to the ocean models and thus assisted analysis of SST for COAMPS. Figure 8 marks the approximate region of the IOP and also shows significant SST variability due to the southward coastal countercurrent, Chesapeake outflow, the Gulf Stream, and eddies that have broken off from the main currents.
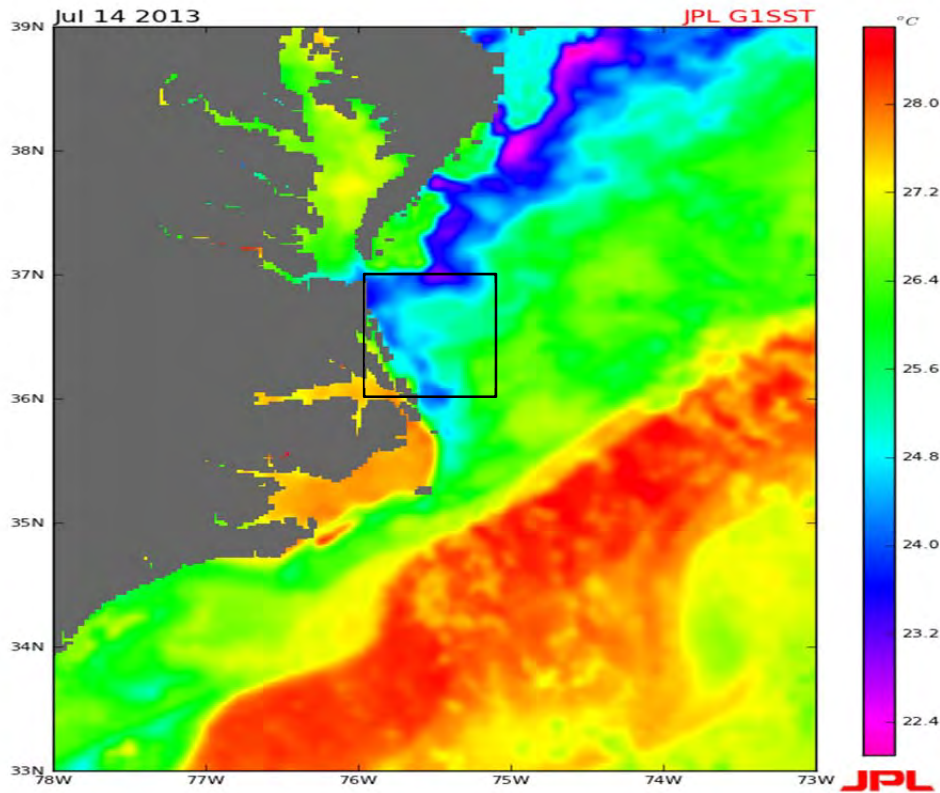
Figure 8.   Spatial variability of SST on July 14, 2013 on the U.S. East Coast
(after Jet Propulsion Laboratory year). The black box denotes the
region of TW13 measurements.

Fifty balloon soundings were launched from R/V Knorr during TW13. Synoptic soundings were launched from the R/V Knorr every 6 hours during the IOP and were generally the responsibility of the Naval Postgraduate School. In addition, up/down soundings were launched with greater frequency during UAV flight operations by the Naval Surface Warfare Center Dahlgren Division. Up/down soundings are launched the same as normal rawinsondes except a controlled leak device is inserted in the balloon opening to allow a steady release of helium. With practice, target altitudes of 1000 m were reached at the flight path apogee before descent. The benefit of the up/down method is that the downward sample is away from the launch platform which eliminates contamination so data is reliable much closer to the surface than the up sounding data. A clear and consistent deviation between the up and down portions of the sounding representing specific humidity in the surface layer as shown in Figure 9 illustrating the

44

common and significant shortcoming of an up sonde's ability to accurately measure the surface layer humidity gradient. Tethersondes were also deployed six times during TW13 where a rawinsonde was suspended from a kite or a tethered balloon, depending on the wind speed, launched from a ridged hull inflatable boat (RHIB) and the height was controlled by how much line was paid out and RHIB speed relative to the wind. The benefit of this tethered sounding method is that repeated soundings can be made from the same instrument away from the large profile research vessel that contaminates the lower level measurements. The measured profiles ranged in altitude from nearly half a meter up to about 150 meters. Figure 10 shows the locations of all the soundings and the drifting flux buoy. Figure 11 shows the timeline of the measurements conducted that were relevant to this study.
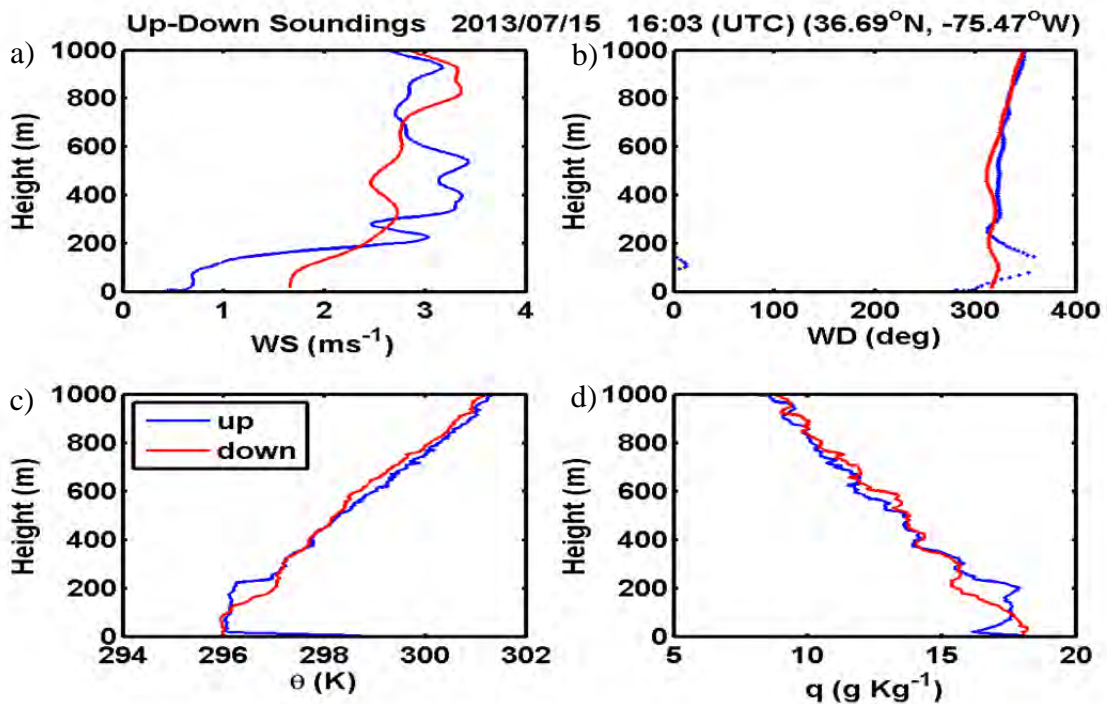
Figure 9.   Example sounding profiles from TW13 experiment. (a) wind speed;
(b) wind direction; (c) potential temperature; and (d) water vapor
specific humidity.
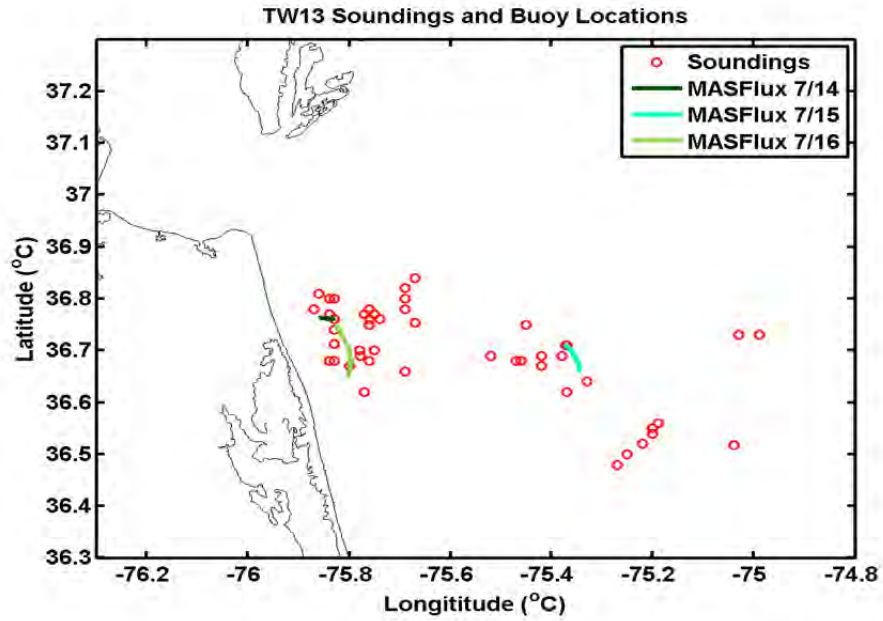
Figure 10.   Rawinsonde sounding locations from TW13 field experiment.
Drifting trajectories of the MASFlux buoy deployed on three
different days are also shown as solid lines.
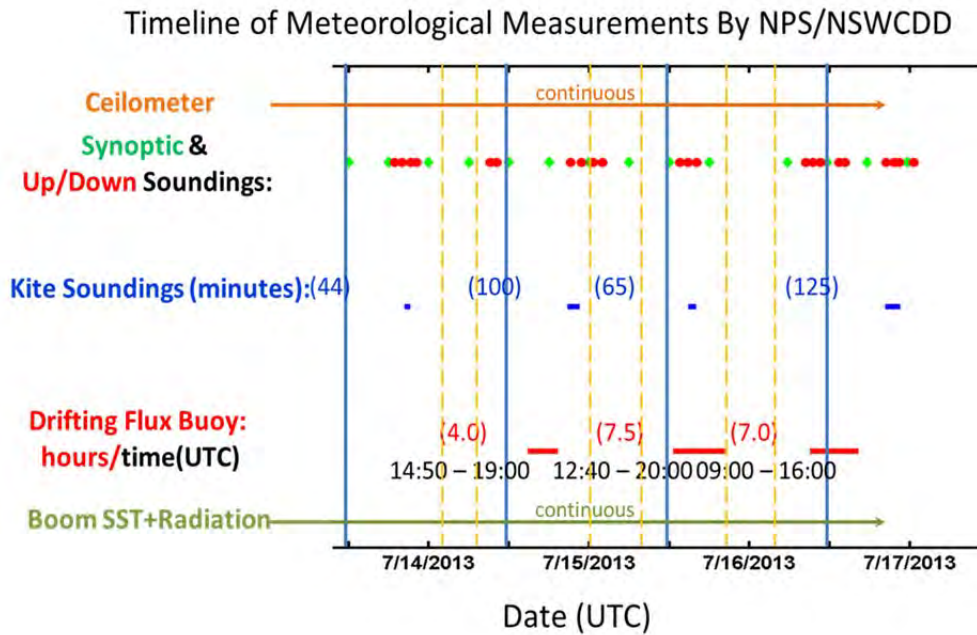
Figure 11.   Timeline of all meteorological and ocean surface measurements
from TW13 that are relevant to this thesis study.

46

The surface drifting Mini Air Sea Flux (MASFLUX) buoy had three successful deployments during the IOP. This spar buoy was developed at NPS and is instrumented to provide the following measurement capability: Eddy correlation flux measurements at 3.5 m, four levels of mean temperature and relative humidity and three levels of wind all within the first 3.1 m of the ocean surface; three levels of water temperature within the first half meter of the surface; and directional surface waves. This low profile and lightweight measurement system provided multiple level measurements within the surface layer while avoiding significant flow distortion or other contamination (Zuniga 2013). Figure 12 shows a time series of the deployment on July 15 clearly showing a warming and destabilizing trend in the surface layer. This trend may be a result of either temporal or spatial variation as the buoy is a drifter and therefore its location changing. Figure 13 shows a different view of the same data which is profiles of hourly means for both air and water temperatures. In this view it is apparent that the surface layer is unstable, there appears to be a near surface cooling effect in the ocean and early in the period the mean profile was slightly stable between 1.5 m and 3.1 m.
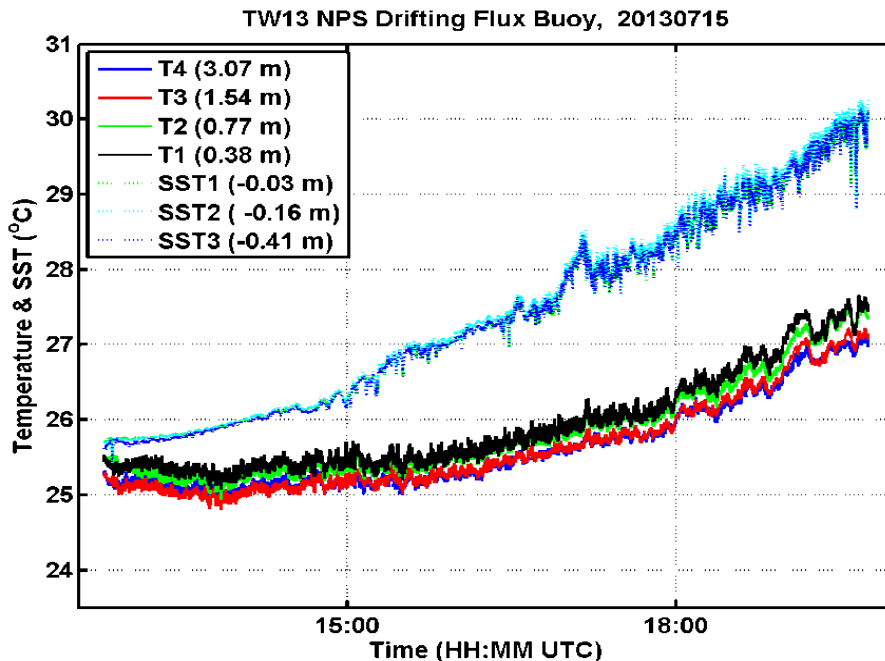
Figure 12.   Evolution of air and water temperature at various height/depth measured by the NPS MASFlux buoy on July 15, 2013, during Trident Warrior field measurements.

47
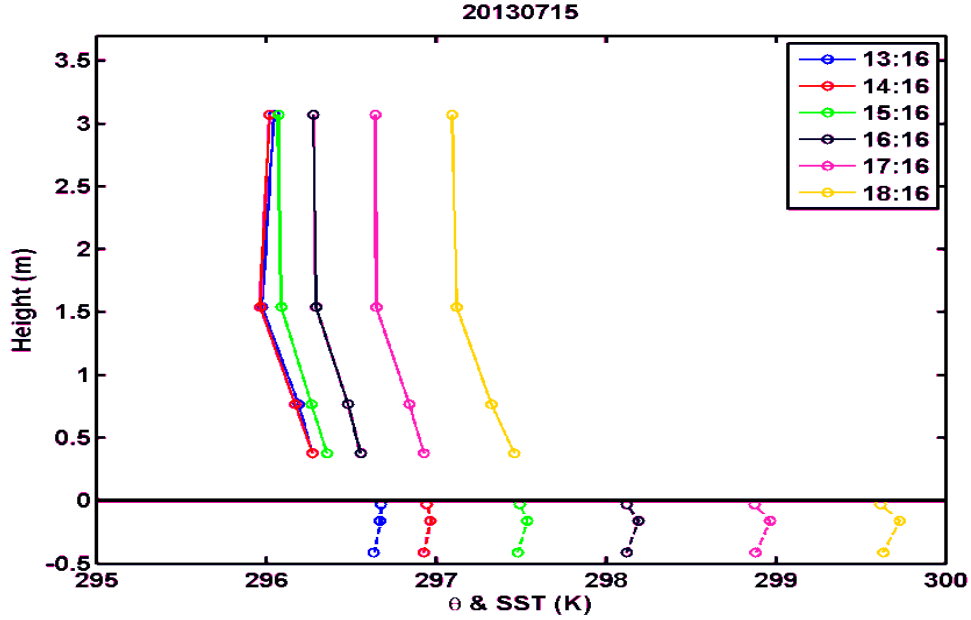
Figure 13.   Evolution of near surface air and water temperature sampled from the NPS MASFlux buoy during TW13. Shown here are examples from July 15, 2013.

C.   COAMPS – LOCAL AREA MODEL

The U.S. Navy's Coupled Ocean Atmosphere Mesoscale Prediction System (COAMPS) version 5, developed at the Naval Research Laboratory (NRL), was the regional circulation model (RCM) used during the TW13 field campaign.

COAMPS is a non-hydrostatic finite differencing model that uses an Arakawa-Lamb (1977) scheme C staggered grid and is also vertically staggered using terrain following sigma levels. COAMPS turbulent mixing uses a 1 ½ order turbulence K – closure model that uses a level 2.5 scheme (Mellor and Yamada 1974). Details of the K-closure scheme used in COAMPS are given in Chapter II.B.3. Surface layer parameterization follows the Louis (1979) scheme which uses polynomial functions of the bulk Richardson number to directly compute surface sensible and latent heat flux and surface drag. The bulk Richardson number is based on variables at the lowest COAMPS level. The roughness length is calculated using Fairall et al. (1996)

$$z_0 = c_0 \frac{u_*^2}{g} + c_v \frac{v}{u_*} \qquad (3.1)$$

48

where c_0 is the Charnock constant, u_* is the friction velocity, g is the acceleration due to gravity, c_v is a constant, v is the molecular viscosity. The first term accounts for wind-wave generated surface roughness and the second term is for smooth flow conditions generally in low wind conditions.

During the TW13 field campaign, NRL ran COAMPS with 4 nested grids with horizontal grid spacing of 36km, 12km, 4km, and 1.33km (Figure 14) and 60 vertical levels (Doyle et al. 2013). The boundary conditions were provided by the Navy Global Environmental Model (NAVGEM) GCM. COAMPS used the NRL Atmospheric Variational Data Assimilation System (NAVDAS) to assimilate roughly 45,000 atmospheric observations and 6000 ocean observations per cycle. All four COAMPS nests were run 4 times per day (6 hour cycle) for a 48-hour forecast. It was run in 3-way coupled mode with the Navy Coastal Ocean Model (NCOM) at 3 km resolution and Wavewatch III at 0.05 deg forecasts. For the majority of this study, we worked with the nest 2 and nest 3 data (12km and 4km resolution respectively) since this is the current expectation for operational LAM modeling support. A general description of COAMPS is given in Hodur et al. 1997.
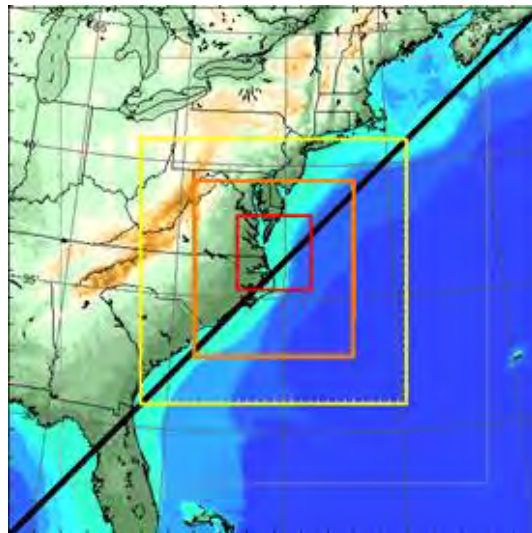
Figure 14.   The coverage areas of the four nested COAMPS grids during TW13. The nests have horizontal resolutions of 36 km, 12 km, 4 km, and 1.33 km. (from Doyle et al. 2013)

D.   FORECAST ANALYSIS MODULE

We developed a Forecast Analysis Module (hereafter FAM) that reads the COAMPS 3D model output and calculates the required SCM inputs. The calculations are controlled by settings defined by the user at run time. Two required inputs for running an SCM are the initialization profile of the state variables and the external forcing that simulates interaction with neighboring grid points in a full 3D model (i.e., the advection tendency terms). The FAM is written in FORTRAN and runs in the Linux environment on the Hamming HPC at the Naval Postgraduate School.

The initial conditions created by FAM include profiles of pressure, potential temperature, specific humidity, horizontal wind and SST. The SCM forcing created by the FAM includes pressure gradient force in x and y direction, SST, large scale vertical motion, and horizontal advection of temperature, humidity, and momentum.

The user defined settings for FAM currently allow for horizontal and vertical averaging centered at the corresponding grid point of interest for both the state variables and the advection terms. Mesoscale variability resolved by the mesoscale model might initialize the SCM with an extreme thermodynamic state that may produce undesirable evolution not representative of the local regime. Also, this same range of values due to mesoscale variability when used as external forcing may attempt to force the SCM with unsustainable change producing unreasonable evolution and model instabilities. User settings for horizontal and vertical averaging of initial conditions, advection and pressure gradient terms, and large scale vertical velocity forcing can be assigned independently. Horizontal advection is calculated using a center differenced 2nd order advection scheme.

Since many combinations of averaging schemes for the initial conditions, forcing conditions, and vertical motion were used, the following convention is used to define the averaging used in any particular case. The word "FAM" will be followed by 3 two-digit numbers. The first two-digit number will describe the number of grid points that the horizontal averaging was performed over. For example, if the number is 11, then the average was performed over 11 grid points in both the i and j direction centered at the point of interest (i.e., i-5 to i+5 and j-5 to j+5). This would be the equivalent to 11 x

50

4000m = 44km averaging. The second two-digit defines the grid point averaging for forcing terms and the third two-digit number defines averaging for vertical motion.

E.   COAMPS IN SINGLE COLUMN MODEL MODE

1.   Configuration

The Single Column Model (SCM) used in this study was the COAMPS version 5 that was run during TW13 field campaign as described in the previous section as its foundation modified to run in a single column mode. As a default, the SCM is set up as a 7x7 grid with double periodic lateral boundary conditions on a Cartesian map over water (i.e., no terrain). A 7x7 grid is necessary to allow for calculations involving neighboring grid points and specifically 4th order diffusion requires the minimum of 7 grid points (Dr. Jim Doyle, personal communication). In this study, the SCM was run as a short term forecast to focus on the evolution and structure of the boundary layer. In order to test the sensitivity of vertical resolution on the resultant boundary layer vertical structure, four different vertical level configurations were run. Specifically, those configurations included 60, 96, 180, and 200 vertical levels with more layers designated near surface region or in the boundary layer below 1 km in order to decrease the vertical grid spacing. The SCM simulations were made in the Linux environment on the NPS HPC Hamming.

2.   Initial and Forcing Conditions

Initial and forcing conditions are calculated by FAM from the hourly 3D COAMPS output using the nearest COAMPS grid points surrounding the SCM location. Depending on the setup, the SCM is initialized using a vertical profile at the SCM start time that may or may not have been horizontally averaged within FAM. The initialization input includes profiles of temperature, humidity, pressure, and horizontal winds. The forcing input includes large scale vertical motion, horizontal pressure gradient force, sea surface temperature, and horizontal advection of temperature, moisture, and momentum. Additionally, sea surface temperature and horizontally averaged profiles of temperature, moisture, and momentum are updated hourly to be used for nudging purposes.

Horizontal and vertical advections are handled differently as external forcing to the SCM. Horizontal advection is calculated from the 3D COAMPS forecast fields using 2nd order center differencing for each grid point. This calculation is a three-step process. First, the variable field (wind and the advected variables) are averaged over a user defined area for every gridpoint. Second, the advection is calculated at every grid point using 2nd order center differencing. Third, another optional averaging over a user defined area of the calculated advection at every grid point. This procedure of averaging is used to minimize the influence of local variability. Updating of the horizontal advection effects can be done in several different methods. The first was to provide constant forcing based on the tendencies at the time of initialization. However, this approach was found prone to create instabilities as the 1-D model does not have the feedback mechanism as in a full 3-D model, which led to extreme gradients and instabilities in the SCM results. The second method was to update the forcings when updates were available in forecast space. The frequency of the updates was controllable, however since only hourly COAMPS data was available for updates, the ability to avoid transient and/or extreme values for both forcing and initialization was severely limited. Consequently, the SCM tended to drift away from the COAMPS forecast rather rapidly for certain cases. The third method was to update the forcing every time step using a linearly interpolated value between the available (hourly) updates to allow for smooth temporal variation in between available COAMPS updates.

Several methods of calculating the vertical advection of momentum and scalar quantities were tested. The advection may be calculated entirely from the COAMPS forecast fields where specifically the COAMPS forecasted vertical velocity advects the COAMPS forecasted vertical gradient of the advected variable. We refer to this forcing as "external" vertical advection. The other option is to input the vertical velocity calculated from COAMPS into the SCM which acts on the SCM profile of the parameter at every time step. This allows the large scale vertical motion to act on updated SCM profiles with much finer vertical resolution. The vertical velocity is linearly interpolated between the COAMPS hourly updates and horizontally averaged per specification at run time. We refer to this forcing as "internal" vertical advection.

3.   SCM Weighted Nudging and Advection

The nudging method was used in some SCM simulations to avoid SCM model results deviating too much from the forcing model, COAMPS, due to discrepancies in the derived forcing terms from those used in the 3-D model. Since the objective of the nudging approach is only to constrain the free atmosphere or levels above some portion of the atmospheric boundary layer, a height dependent nudging weighting function was applied to help control the SCM forecast from drifting too far from the forcing COAMPS. The nudging function was designed after Ghan (1999) and Randall and Cripe (1999) and is intended to nudge the SCM toward the "observation" as it would be known in data assimilation. The observation, in our case, is the 3D COAMPS forecast field as linearly interpolated between updates. For an SCM forecast variable f, the added nudging term is expressed as:

$$n(z) = -\frac{(f_{scm} - f_{3D})}{\tau}, \tag{3.2}$$

where $\tau = \frac{\Delta x}{|u|}$ is the relaxation timescale, in which Δx is the grid spacing and $|u|$ is the magnitude of the advecting wind as calculated from COAMPS. In this form, the portion of the difference between the SCM and the observation that is nudged is proportional to wind speed. As a result, the nudging timescale is adjusted to the advection time scale. Lastly, even though the COAMPS profile is only updated hourly, the linearly interpolated value between updates allows a smooth transition in "observations" to nudge to. Combining the nudging with advection, denoted as $A(\psi)$, and applying a weighting function α, we arrive at:

$$n(z) = -\alpha \left[A(\psi) - \frac{(f_{scm} - f_{3D})}{\tau} \right], \tag{3.3}$$

The height dependent weighting function was designed after Burk and Thompson (1982):

$$\alpha = \begin{cases} 0, & \text{for } z \leq h_1 \\ \left(\frac{z - h_1}{h_2 - h_1} \right), & \text{for } h_1 < z < h_2 \\ 1, & \text{for } z \geq h_2 \end{cases} \tag{3.4}$$

where h_1 and h_2 are the upper and lower limits that defines the range of partial nudging to avoid abrupt transition between the no nudging ($\alpha = 0$) and full nudging ($\alpha = 1$) zones. These nudging height limits can be connected with the PBL height as determined

by COAMPS which can be read in from the COAMPS output files and then linearly interpolated between updates. The COAMPS calculated PBL height is determined by analysis of the vertical potential temperature gradient, turbulence, and Richardson Number.

This entire weighted combined nudging and advection term is intended to assign the large advection and a small nudging relaxation timescale at higher altitudes (i.e., free atmosphere) while assigning no advection and large nudging relaxation timescale (i.e., infinite) to the lower nudging limit. The purpose is to strictly control the model drift in the free atmosphere above the boundary layer so that the overall synoptic dynamic forcing resolved by the 3D model is dominant in the evolution of the atmospheric conditions aloft while the boundary layer itself has little or no nudging and advection and the structural evolution is dominated by the local physical processes. With the advection and nudging process influencing the top of the MBL, the effectively adjusted conserved variables are mixed downward though turbulence but the direct nudging does not disturb the models solution of the surface layer structure. This gives the desired effect since this study is focused on the surface layer structure based on larger scale forcing.

4. Modified Eddy Diffusivity

Since turbulent mixing is the dominant process in the surface layer and significantly impacts the energy transfer and balance of energy through the boundary layer, a deeper look at the calculation of the eddy diffusivity as calculated by COAMPS was necessary. The existing COAMPS eddy diffusivity calculation is somewhat simplified compared to the methods discussed above in Chapter II. Specifically, the numerator in Equation 2.22 is calculated only at the lowest level grid level for the reasons discussed. This also means that the value of φ is not a function of height. This is not a problem for normal COAMPS or other 3D models where the vertical resolution in the surface layer is poor and the goal of the surface layer scheme is to transport total flux. However, for the SCM with a configuration focusing on high resolution in the surface layer, the height dependence of stability and its effect on mixing length is essential to predict the surface layer using MOST.

For the SCM in this study, we have modified the mixing length calculation in order to account for the stability and height dependence in the surface layer. Specifically, we modified the calculation of φ in Equation 2.22 to be dependent on z/L as described in Equations 2.9 and 2.10.

For simplicity in writing and labeling, this modified eddy diffusivity is often referred to as "New K" throughout the remainder of this paper. Likewise, the original COAMPS calculated eddy diffusivity is often referred to as "Old K."

THIS PAGE INTENTIONALLY LEFT BLANK

IV. MARINE SURFACE LAYER AND EVAPORATIVE DUCT VARIABILITY AND THEIR EFFECTS ON EM PROPAGATION

The marine surface layer normally provides for a strong vertical gradient in atmospheric moisture content which, as introduced in Chapter II, can lead to anomalous propagation conditions for EM energy. This chapter will outline a detailed analysis on the sensitivity of the evaporative duct properties to various surface layer thermodynamic variables to better understand the environmental factors leading to ducting conditions due to surface evaporation. This chapter will begin with the equation for the modified refractive index (M) and explore its sensitivities to temperature and moisture gradients in the marine surface layer. This theoretical exploration will lead us to identify and quantify the contributions of different terms to the M-unit gradient. We will then use the Monin Obukhov Similarity Theory to derive a relationship that connects the evaporation duct height and strength with surface layer forcing parameters such as flux of momentum, heat, and moisture, and stability parameter, the bulk Richardson number (R_b).

The results of the above theoretical analyses will be used to examine the variability of the EDH and M-deficit that occur in nature using measured air-sea interfacial quantities. In situ buoy measurements collected by NOAA National Data Buoy Center (NDBC) from various coastal locations are used for this purpose where profiles of wind speed, temperature, and moisture were derived from the buoy measurements based on MOST. We run statistical analysis on the resulting M profiles and analyze the relationship between the mean quantities from the buoys (referred to as bulk parameters) and their impact on EDH and M-deficit. Finally, we run AREPS using the profiles we generated to assess the impact and sensitivity of propagation loss to the bulk parameters.

A. METEOROLOGICAL FACTORS AFFECTING M-GRADIENTS, THEORETICAL ANALYSES

1. Derivation

The equation for the modified index of refractivity (M) was introduced in Chapter II as Equation 2.2 and is written again here for convenience. The independent variables in this empirical formula are pressure, temperature, vapor pressure, and height.

$$M = 77.6\frac{p}{T} - 5.6\frac{e}{T} + 3.75\text{x}10^5\frac{e}{T^2} + 0.157z$$

In order to work with variables that are conserved in adiabatic near surface processes, we seek to substitute specific humidity, q, for vapor pressure and potential temperature, θ, for temperature. To convert from vapor pressure to specific humidity, we use the relationship

$$q \cong r = \frac{\varepsilon e}{p - e} \tag{4.1}$$

where r is mixing ratio and ε is the ratio of mass of water vapor to dry air which is approximately 0.622. Rearranging then gives

$$e \cong \frac{pq}{\varepsilon} \tag{4.2}$$

The definition for potential temperature is:

$$\theta = T\left(\frac{P_0}{P}\right)^{R/c_p} \tag{4.3}$$

where R and c_p are the gas constant and isobaric specific heat of dry air, respectively.

Hence,

$$T = \theta\left(\frac{P_0}{P}\right)^{-R/c_p} = \theta\left(\frac{1000}{P}\right)^{-\gamma} \tag{4.4}$$

where $\gamma = {}^{R}\!/_{c_p} = 0.286$.

Substituting (4.2) and (4.4) into (2.2) we get:

$$M = 77.6 \frac{p}{\theta \left(\frac{1000}{P}\right)^{-\gamma}} - 5.6 \frac{\frac{pq}{\varepsilon}}{\theta \left(\frac{1000}{P}\right)^{-\gamma}} +$$

$$3.75 \times 10^5 \frac{\frac{pq}{\varepsilon}}{\left(\theta \left(\frac{1000}{P}\right)^{-\gamma}\right)^2} + 0.157z \qquad (4.5)$$

which can be simplified to yield

$$M = 560 \frac{p^{.714}}{\theta} - 64.9 \frac{p^{.714}q}{\theta} + 3.14 \times 10^7 \frac{p^{.428}q}{\theta^2} + 0.157z \qquad (4.6)$$

Equation (4.6) thus represents the M-unit as a function of height, pressure, and conserved thermodynamic variables in a dry adiabatic process (potential temperature and specific humidity).

To obtain the M vertical gradient, we differentiate both sides of Equation (4.6) with respect to z, group coefficients of common gradient terms, and simplify and thus obtain

$$\frac{dM}{dz} = \left[\underset{(a)}{\frac{400}{\theta p^{.286}}} - \underset{(b)}{\frac{46.3q}{\theta p^{.286}}} + \underset{(c)}{\frac{1.34 \times 10^7 q}{\theta^2 p^{.572}}} \right] \frac{dp}{dz}$$

$$+ \left[-\underset{(d)}{\frac{560 p^{.714}}{\theta^2}} + \underset{(e)}{\frac{64.9 p^{.714}q}{\theta^2}} - \underset{(f)}{\frac{6.28 \times 10^7 p^{.428}q}{\theta^3}} \right] \frac{d\theta}{dz}$$

$$+ \left[-\underset{(g)}{\frac{64.9 p^{.714}}{\theta}} + \underset{(h)}{\frac{3.14 \times 10^7 p^{.428}}{\theta^2}} \right] \frac{dq}{dz} + \underset{(i)}{0.157} \qquad (4.7)$$

Equation (4.7) depicts how the M gradient is dependent on gradients of pressure, potential temperature, and specific humidity. The terms in each bracket in front of the respective variable gradient indicate that the dependence on thermodynamic variables can be highly variable depending on the magnitude of the variables themselves. However, each individual term within the bracket may contribute differently. To evaluate the

relative importance of the terms in each bracket, we perform scale analysis using typical values of the variables: p=1013.25 mb, θ=288 K, and q=0.010 kg kg^{-1}. The resulting magnitude of each term is given in Equation (4.8) below.

$$\frac{dM}{dz} = [\ 0.192 \quad + \quad 2.22\text{x}10^{-4} \quad + \quad 0.0308\ ]\frac{dp}{dz}$$

$$\text{(a)} \qquad\qquad \text{(b)} \qquad\qquad\quad \text{(c)}$$

$$+[-0.945 \quad + \quad 1.10\text{x}10^{-3} \quad - \quad 0.508\ ]\frac{d\theta}{dz}$$

$$\text{(d)} \qquad\qquad \text{(e)} \qquad\qquad\quad \text{(f)}$$

$$+[-31.5 \quad + \quad 7320\ ]\frac{dq}{dz} + 0.157 \tag{4.8}$$

$$\text{(g)} \qquad\quad \text{(h)} \qquad\quad \text{(i)}$$

We see immediately that terms (b), (e), and (g) contribute at least two orders of magnitude less than any other term in the same coefficient and therefore can be neglected. These terms all originated from the same term in Equation (2.2) and therefore we can also conclude that the second term in Equation (2.2) can be neglected. This is consistent with similar analyses by Marshall (2011).

Ignoring the apparently small terms in Equation (4.7), we obtain:

$$\frac{dM}{dz} = A\frac{dp}{dz} + B\frac{d\theta}{dz} + C\frac{dq}{dz} + 0.157 \tag{4.9}$$

$$\text{(I)} \quad\quad \text{(II)} \quad\quad \text{(III)} \quad \text{(IV)}$$

where,

$$A = \left[\frac{400}{\theta p^{.286}} + \frac{1.34\text{x}10^7 q}{\theta^2 p^{.572}}\right]$$

$$B = \left[-\frac{560 p^{.714}}{\theta^2} - \frac{6.28\text{x}10^7 p^{.428} q}{\theta^3}\right]$$

$$C = \left[\frac{3.14\text{x}10^7 p^{.428}}{\theta^2}\right]$$

and p is in millibars, θ is in Kelvin, and specific humidity is in kg kg^{-1}. A, B, and C will be referred to as gradient coefficients.

Inspection of Equation 4.9 reveals the sign of the contributing terms to the total dM/dz. Specifically, coefficient A will be positive and dp/dz will always be negative. Therefore, the contribution from term (I), or the pressure gradient term, will always be negative. Coefficient (B) will always be negative. However, the sign of $d\theta/dz$ varies depending on the thermal stability of the layer. In unstable conditions the contribution is positive and in stable conditions the contribution is negative. Therefore, the contribution from term (II), or the thermal gradient term, can be positive or negative. Coefficient C will always be positive and, although not always the case, usually dq/dz is negative in the marine surface layer. Therefore, the contribution from term (III), or the moisture gradient term, is usually negative. Finally, the last term is a positive constant. This result is summarized in Table 1.

Sign of Coefficients and Gradients in Equation (4.9)					
Term (I)		Term (II)		Term (III)	
A	dp/dz	B	dθ/dz	C	dq/dz
+	-	-	+ or -	+	usually -
-		+ or -		usually -	

Table 1.   Sign of contributions from the terms in Equation 4.9.

2.   M-Gradient Dependence on Thermodynamic Variables

In this section, we will examine each term in Equation (4.9) closely by quantifying the range of variability of coefficients A, B, and C and their dependence on pressure, potential temperature, and specific humidity. Each coefficient will be evaluated using a reasonable range of the dependent variables in order to find a total range of values and order of magnitude for each term. This will help us understand the sensitivity of the gradient of M to the contributing parameter gradients.

a.   Term I

This term in Equation 4.9 depicts the M-gradient dependence on vertical pressure gradient, dp/dz. Coefficient A is originally composed of terms (a) and (c) from Equation 4.7.

Term (a) is a function of pressure and potential temperature only and is plotted in Figure 15a. In the figure, we see that between temperatures of 270 K to 300 K and pressures between 1000 mb and 1022 mb, the range of values for term (a) are from +0.184 to +0.205. Also, the slope of the contour lines clearly indicates that this term is mostly sensitive to temperature and almost constant with variations in pressure.

Term (c) is a function of pressure, potential temperature, and specific humidity and is plotted in Figure 15b. The axes are temperature and humidity and the data absent region is where the air would be supersaturated and thus unlikely in the atmosphere. The contours are nearly horizontal showing that there is significant sensitivity of this term to specific humidity, but nearly no sensitivity to temperature. Also note that there appear to be double lines plotted. These are the same contours plotted using 1000 mb and 1020 mb for pressure. Since the results from the two surface pressure values nearly overlap, this figure demonstrates that term (c) is not sensitive to variations in pressure. The overall range of term (c) using the same temperatures and pressures as described above and specific humidity from 1 to 20 g kg^{-1} is +0.0029 to 0.0570. This result is somewhat expected from the formulation of term (c) in Equation (4.7), where it is proportional to q and inversely proportional to the square of θ and nearly the square root of p.

Coefficient (A), which is the combination of terms (a) and (c), is plotted in Figure 16 as a function of θ and q. Again, the region with no data represents supersaturated conditions and is thus ignored. The range of coefficient (A) is +0.1866 to +.2439.

Pressure gradient, dp/dz, varies only slightly in the surface layer of the depth of ~100 m or less. Using the ideal gas law and a reasonable range of temperature, moisture, and pressure values for the surface layer, we get:

$$\frac{dp}{dz} = \frac{-pg}{R_d T_v} \qquad (4.10)$$

where p={1000 mb to 1022 mb}, T={270 K to 300 K}, and q={0.001 kg kg^{-1} to 0.020 kg kg^{-1}), The resulting values of dp/dz is between -0.112 to -0.129 mb m^{-1}.

Hence, **Total contribution** to dM/dz from Term (I) is -0.0315 to -0.0209.
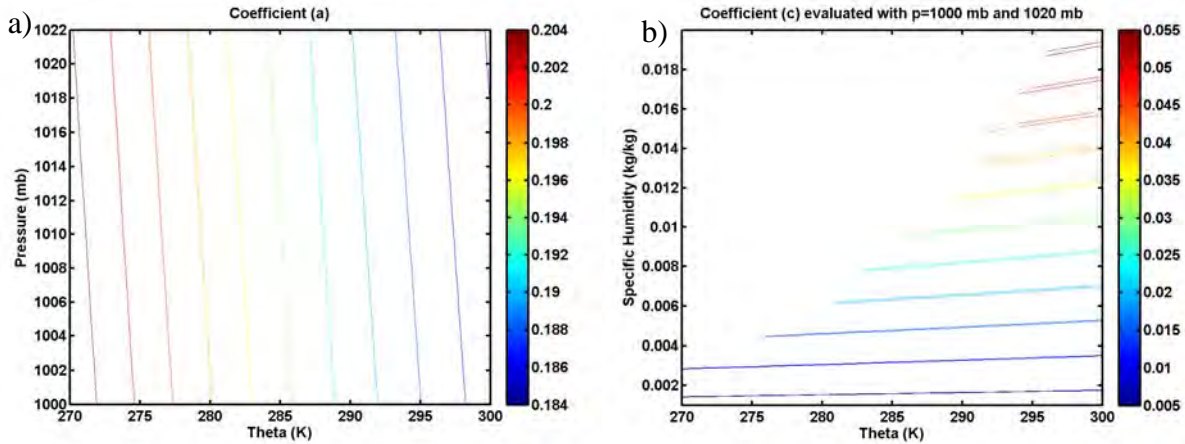
Figure 15.   Notional values for terms (a) and (c) in Equation (4.7). a)
magnitude of term (a) as a function of temperature and pressure; b)
magnitude of term (c) as a function of potential temperature and
specific humidity.
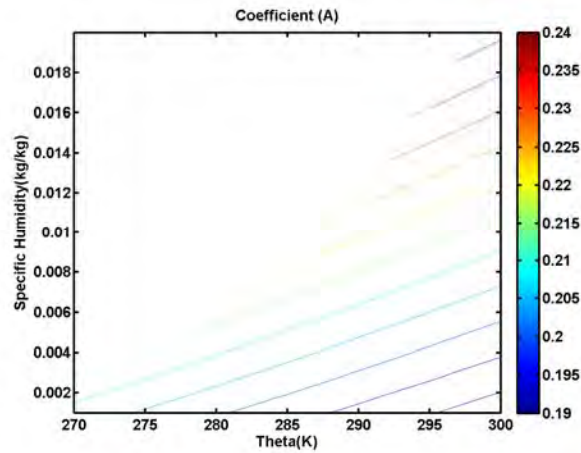
Figure 16.   Contours of coefficient (A) values with respect to temperature and
humidity.

b.   *Term II*

This term in Equation 4.9 is composed of coefficient (B) and $d\theta/dz$. Coefficient
(B) is originally composed of terms (d) and (f) from Equation 4.7.

Term (d) is a function of pressure and potential temperature only and is plotted in
Figure 17a. In this figure, we see that within the same range of pressure and potential
temperature as evaluated for the term (I) analysis above, the range of values for term (d)

are from -1.082 to -0.863. Also, the slope of the contour lines clearly indicates that this term is mostly sensitive to temperature and almost constant with variations in pressure.

Term (f) is a function of pressure, potential temperature, and specific humidity and is plotted in Figure 17b. As with term (c) in Figure 15b, the data absent region is where conditions would be supersaturated and therefore have been removed. Again, the slope of the contour lines indicates that this term is also mostly sensitive to specific humidity and much less to temperature. Also, as in Figure 15b, the nearly overlapping contour lines are the values of term (f) evaluated at 1000 mb and 1020 mb. Similar to term (c), term (f) is a rather weak function of pressure. The overall range of term (f) using the range of pressure, temperature, and specific humidity as described previously is from -0.930 to -0.045.

Coefficient (B), which is the combination of terms (d) and (f), is plotted in Figure 18 as a function of temperature and humidity at a constant pressure of 1000 mb. The range of coefficient (B) is -1.800 to -0.916.

To determine the magnitude of terms (II) and (III) in Equation (4.9), potential temperature and specific humidity gradients ($d\theta/dz$ and dq/dz) are needed. The two scalar gradients can vary significantly both in sign (for $d\theta/dz$ mainly) and in magnitude in the surface layer. In normal stable and unstable surface layers, based on MOST, $d\theta/dz$ is the largest at the surface and decreases logarithmically with height. To help limit the scope of reasonable values for this specific analysis, we'll omit the significant near-surface gradient by calculating the temperature gradients at a height of 4 meters based on MOST and typical values of surface layer wind speed ($0 - 20$ m s^{-1}), sensible heat flux (-10 to 30 W m^{-2}), and latent heat flux ($10 - 100$ W m^{-2}). At the given wind speed range for U_{10}, we can estimate the typical value range of u_* from the bulk surface flux parameterization (Equation 2.15) using a typical drag coefficient of 10^{-3}. This yields a u_* ranging between 0.029 to 0.57 m s^{-1}. Given that the air density is of ~1.2 kg m^{-3}, the specific heat under constant pressure, $c_p = 1005$ J K^{-1} kg^{-1}, and the latent heat of the atmosphere being $L_v = 2.5 \times 10^6$ J kg^{-1}, we obtain that temperature and water vapor scales, θ_* and q_*, where θ_* ranges from -0.84 to 0.28 K and q_* from 1.1×10^{-3} to 5.7×10^{-6}

kg kg^{-1} based on Equations (2.5) and (2.6). Finally, $d\theta/dz$ and dq/dz at 4 m are estimated to be from -0.39 to +0.13 K m^{-1} and from -5.1x10^{-4} to -2.6x10^{-6} kg kg^{-1} m^{-1} respectively using the expressions of nondimensional gradient in Equations (2.10).

The total contribution to dM/dz from term (II) is between -0.23 to 0.70.
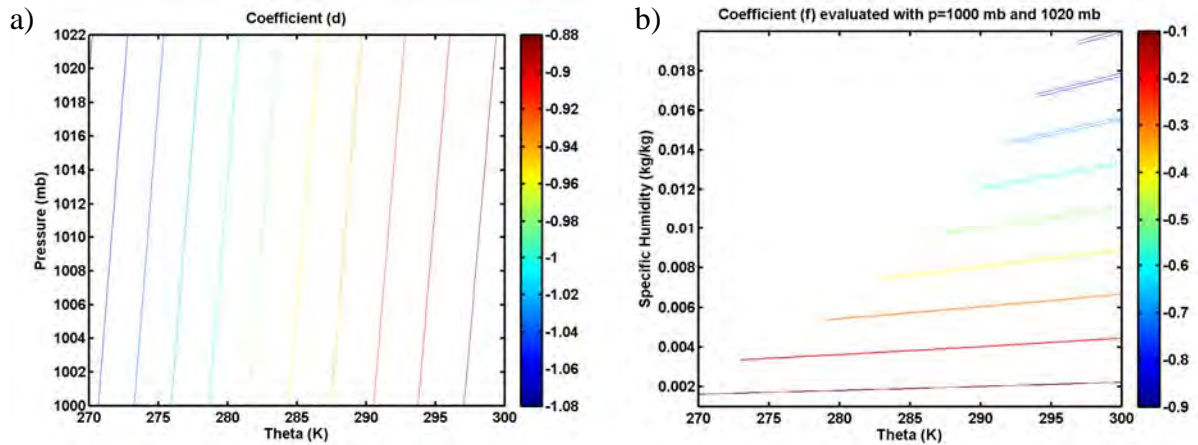
Figure 17.   Same as in Figure 15 except for coefficient terms (d) and (f).
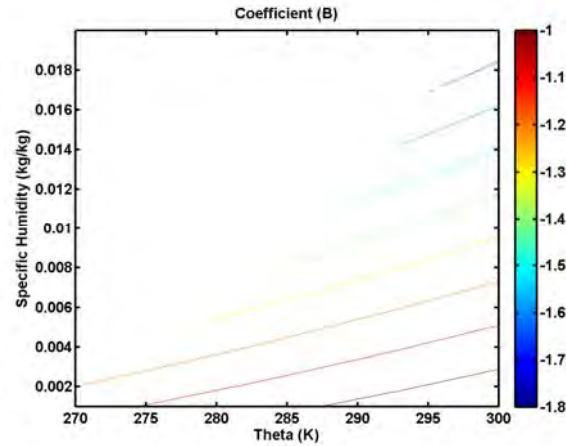
Figure 18.   Contours of coefficient (B) values with respect to temperature and humidity.

c.   Term III

This term in Equation 4.9 is a product of coefficient (C) and dq/dz. Coefficient (C) is originally composed solely of term (h) from Equation 4.7.

Coefficient (C), same as term (h), is a function of pressure and potential temperature and is plotted in Figure 19. In this figure, we see that within the same range of pressure and potential temperature as those used for evaluating term (I), the range of values for term (C) are from 6710 to 8360. The slope of the contour lines clearly indicates that this term is mostly sensitive to temperature and almost constant with variations in pressure. Using the range of dq/dz estimated in Section b above, we obtain the total contribution from Term III is between -4.3 and -0.017.
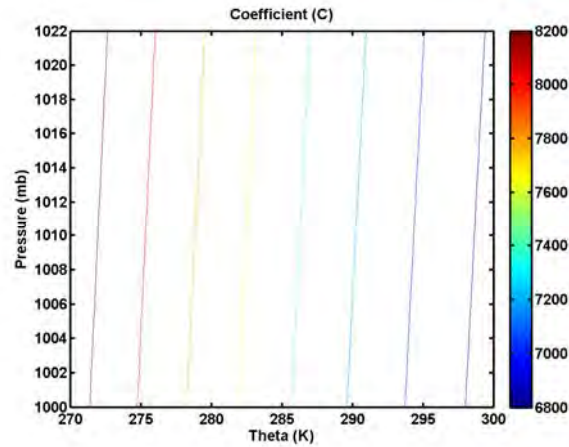
Figure 19.   Contours of coefficient (C) values with respect to temperature and pressure.

3.   Summary of Scale Analysis of Equation 4.9

Table 2 summarizes the ranges of each term in Equation 4.9 from discussions in the previous section denoting the range of contribution to the surface layer M gradient at the specified range of typical conditions within the marine atmospheric surface layer. Comparison of the bottom row shows that term (III) most likely dominates this equation and contributes to negative M gradient for a trapping layer. This term represents the effect of strong negative water vapor gradient associated with surface evaporation over water, which is the case for an evaporative duct. It is also clear that term (I) associated with the pressure gradient always promotes a trapping layer (negative M gradient), although its effects may be masked by other factors due to its small magnitude. However, the overlap in ranges for all four terms indicates that any one of the four terms can play a

66

dominant role depending on the relative magnitude of the gradient of potential temperature and specific humidity. Also note that the sign of term (II) may change according to thermal stratification. Moisture contribution should mostly be negative although positive gradient of specific humidity may exists in stable and saturated or near-saturated conditions such as in radiation or advection fog where dq/dz would be positive. In order for temperature to contribute to trapping conditions, a very stable surface layer is needed.

It should be noted that the magnitude of the gradient of temperature and moisture increases significantly near the surface. This is a direct result of the inverse dependence of height in the non-dimensional gradient relationship shown in Equations (2.9) and (2.10). Near the surface, the formulation of $\emptyset_m$ and $\emptyset_h$ is close to the neutral stratification values of 1 or 0.74 as small height (z) result in very small $^z/_L$. Hence, the near surface gradients of moisture and temperature can be significantly higher than what was estimated above. An increase in either positive potential temperature gradient or negative moisture gradient would increase the contributions of terms (II) or (III) respectively toward a negative dM/dz.

Term (II) with the temperature gradient can be positive or negative depending on thermal stability. However, because of the potential of term (III) to have greater value especially nearer the surface, and to a less extent that Term (I) makes consistent negative contribution, the value of dM/dz will almost always have a negative gradient near the surface that increases with height. In other words, the existence of an evaporation duct is almost always present.

Term	I		II		III		IV
	A	dp/dz	B	$d\theta/dz$	C	dq/dz	0.157
Range	+0.1866 to +0.2439	-0.112 to -0.129	-1.800 to -0.916	-0.39 to +0.13	+6710 to +8360	-5.1×10^{-4} to -2.6×10^{-6}	0.157
Total	-0.0315 to -0.0209		-0.23 to +0.70		-4.3 to -0.017		0.157

Table 2.   Magnitude of contributions from the terms in Equation 4.9.

4. Determining the Evaporation Duct Height

The evaporation duct, as described above, is the negative vertical gradient of M in the marine surface layer that is predominantly the result of the negative moisture gradient. The evaporation duct height (EDH) is the height at which the gradient of M becomes zero as it increases with height from negative near surface values to positive values.

Based on the definition of evaporative duct height and the dM/dz formulation in Equation 4.9, one can solve for the evaporative duct height. This will be the focus in this section.

a. Neutral and Stable Surface Layer

Rewriting Equation 4.9 here for convenience, we have:

$$\frac{dM}{dz} = A\frac{dp}{dz} + B\frac{d\theta}{dz} + C\frac{dq}{dz} + 0.157$$

where,

$$A = \left[\frac{400}{\theta p^{.286}} + \frac{1.34 \times 10^7 q}{\theta^2 p^{.572}}\right]$$

$$B = \left[-\frac{560 p^{.714}}{\theta^2} - \frac{6.28 \times 10^7 p^{.428} q}{\theta^3}\right]$$

$$C = \left[\frac{3.14 \times 10^7 p^{.428}}{\theta^2}\right]$$

To derive the formulation for evaporative duct, we start from the dM/dz formulation in Equation (4.9) and set dM/dz to zero. Substituting Equation (2.8) for θ and q and using the non-dimensional gradient relationship in Equation (2.10) for stable and neutral conditions and the hydrostatic equation $\frac{dp}{dz} = \frac{-\rho g}{100}$ (for mb m^{-1}), we get

$$0 = -A\frac{\rho g}{100} + B\frac{\theta_*}{\kappa z}\left(.74 + 4.7\frac{z}{L}\right) + C\frac{q_*}{\kappa z}(.74 + 4.7\frac{z}{L}) + 0.157$$

Substituting the Monin-Obukhov length (Equation 2.7) into the above equation and solving for z, we arrive at:

$$z = \frac{.74(B\theta_* + Cq_*)}{\kappa g\left(\frac{A\rho}{100} - \frac{4.7\theta_*(B\theta_* + Cq_*)}{\overline{\theta_v}u_*^2} - \frac{.157}{g}\right)} \tag{4.11}$$

Equation 4.11 is hence the formulation for the evaporative duct height in stable and neutral conditions. It shows that the EDH is determined by the state variables as well as surface fluxes scaling parameters (u_*, θ_*, and q_*, respectively). Since the coefficients A, B, and C are functions of height, Equation (4.11) must be solved iteratively.

b.   Unstable Surface Layer

The same derivation procedure was done for the unstable conditions here, except that the nondimensional gradient term is for the unstable surface layer only. Setting *dM/dz* to zero gives

$$0 = A\frac{\rho g}{100} + B\frac{\theta_*\phi_h}{\kappa z} + C\frac{q_*\phi_h}{\kappa z} + 0.157 \tag{4.12}$$

where for unstable cases, as shown in Equation (2.10)

$$\varphi_h = .74\left(1 - 9\frac{z}{L}\right)^{-1/2}$$

Solving for *z* gives

$$z = -\frac{\varphi_h(B\theta_* + Cq_*)}{\kappa\left(\frac{A\rho g}{100} + 0.157\right)} \tag{4.13}$$

As with the stable case, solutions for z need to be obtained using an iterative method.

Once the EDH is obtained, the M-deficit can be calculated based on the θ and q values at EDH level, which can be obtained from Equations (2.12) and (2.13), respectively.

5.   Surface Layer Model to Describe Evaporative Duct

The calculation of the EDH described in the previous section, although functional, does not provide a complete profile in the surface layer that is useful as input to propagation models. An alternative way to arrive at the same answer is to do it numerically through a surface layer diagnostic model based on MOST. This was also

found necessary due to the complex relationship as seen in the subsection above that makes analytical solutions to the EDH impossible. With a given set of measurements of wind, temperature, and specific humidity, and pressure and the sea surface temperature, the mean wind and state variable (θ and q) profiles can be obtained from the model, which can be used to generate an M-unit profiles. The EDH can then be diagnosed from the M-profile numerically.

We used a surface layer model based on COARE surface flux algorithm (Fairall et al. 1996) modified to output vertical profiles of mean wind, θ, and q. This COARE based surface layer model was previously developed into MATLAB code by John Kalogiros (University of Athens) in MATLAB and does not follow the equations exactly as discussed in Chapter II and as just analyzed in the previous section. The basic inputs to the COARE algorithm are SST, surface pressure, and temperature, humidity, and wind speed from one level in the surface layer. Solutions for the mean profiles, from 0 to nominally 50 m above the sea surface, are obtained within the COARE algorithm by iteration. In this thesis, the modified COARE algorithm will be referred to as marine atmospheric surface layer (MASL) model. This model is essentially the evaporative duct model used in this thesis.

The profiles of pressure, temperature, and specific humidity are used to calculate the M profile. It is common that the EDH will be the local minimum of M-units within the surface layer. However, there are conditions where there may not be a local minimum or the local minimum is at the surface. In the special cases where the local minimum is not resolved in the first 50 m, then the local minimum must either occur above 50 m or not occur at all. The cases where the EDH is above 50 m are rare but do occur. Cases without a minimum at all are not realistic. In the special cases where the minimum is at the surface, it is possible that conditions are stable and with small or positive moisture gradient. An evaporative duct does not exist in these rare cases. These special cases will be illustrated and discussed in the next section.

B.   VARIABILITY OF THE EVAPORATION DUCT USING BUOY MEASUREMENTS

In order to assess the surface layer variability, observations from NOAA buoys in various coastal U.S. locations were analyzed based on the theoretical framework presented in Section A. Figure 20 and Table 3 give the information about the buoys selected for this analysis (http://www.ndbc.noaa.gov/). These buoy locations were selected according to several guiding requirements. First, coastal locations of the U.S. were chosen so that on and offshore flow regimes would offer the variable atmospheric air masses to be advected over the stationary coastal buoys. These include continental polar, maritime polar, continental tropical and maritime tropical air masses. Second, locations were chosen in different water temperature regions so that the advected air masses would offer sampling of both stable and unstable conditions. Finally, buoys were selected where a consecutive year's worth of observations for all the pertinent variables of air temperature, water temperature, relative humidity, wind speed, and pressure were available with as much continuity as possible. This was a factor in decision making because of frequent outages in any one of the particular instruments for many buoys. For this reason, the specific years of the dataset samples used are not consistent for all buoys, but this should not invalidate this analysis since the relative continuity of each particular buoy dataset represents the continuous regime conditions as well as the transition conditions so that no particular transient regime is inadvertently oversampled independent of the normal mode of variability.

Location	New Jersey	Bermuda	Gulf East	Santa Monica	Oregon	Santa Barbara	Santa Maria	Monterey
Buoy #	1	2	3	4	5	6	7	8
NOAA ID #	44066	41048	42003	46025	46029	46054	46011	46042
Valid Year	2009	2013	2013	2013	2012	1997	1991	2000
# Good Obs	3443	6923	8751	8668	4328	1285	5844	8413
# Total Obs	47,655							

Table 3.   Information about the NOAA buoys used for evaporative duct analysis

All the buoys were 3-meter discus buoys that made measurements of temperature and humidity at a height of 4 meters, wind at 5 meters, pressure at the waterline inside the

buoy, and SST at 0.6 meters below the waterline. Buoys 1 through 5 were used in initial analyses; however we added three more buoys from the California coast to increase the chances of having more stable cases.
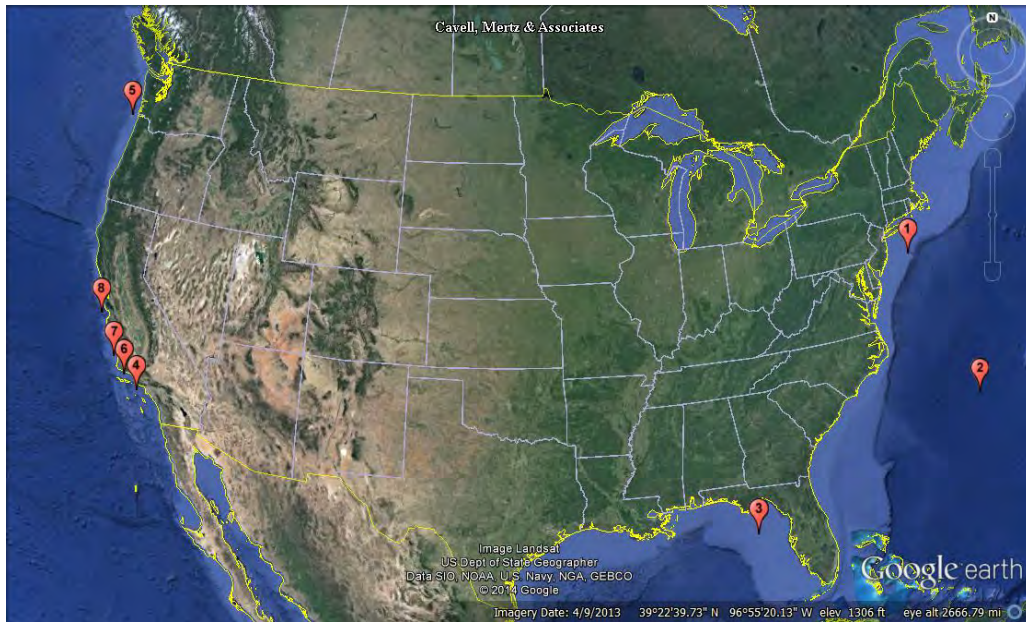
Figure 20.   Locations of the surface buoys providing data for this analysis.
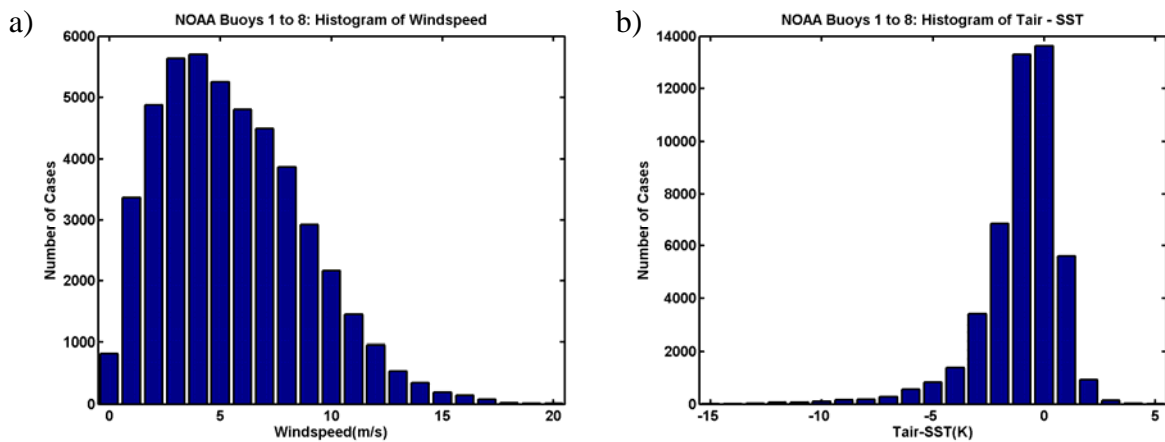
Figure 21.   Probability distribution of a) wind speed, b) air-sea temperature difference. Total number of buoy observations is 47,655 from all 8 buoys.

This combined NOAA buoy dataset consisted of 47,655 usable observations that have been analyzed to describe the variability of the atmospheric conditions observed. Further analyses of the EDH properties in the framework in Section A use these buoy data as input instead of a hypothetical range for each input variable. This practice ensures that the input variables are internally coherent among themselves and hence avoiding results from non-realistic inputs to the ED analyses.

Figure 21 shows the distribution of the wind speed and air-sea temperature difference (ASTD), respectively, to denote the range of dynamical and thermal forcing of the surface layers to be analyzed. This dataset predominantly contains weak to moderate wind less than 12 m s^{-1} and ASTD is typically between -5 to +2 K. While these figures provide a quick look at the conditions of the dataset, a further analysis is needed to assess the typical conditions observed, particularly on the near-surface humidity. Figure 22 shows a joint probability distribution function (JPDF) for all usable buoy observations under all wind conditions. It reveals the preferred state of the atmosphere with respect to stability and relative humidity: ASTD between -3 and +1 K and relative humidity at greater than 60%. The peak point of JPDF is at ~87% relative humidity with ~-0.3 ASTD (slightly unstable). Additionally, noting that there is a general tilt in the peak JPDF values from lower left to upper right, Figure 22 shows that lower RH conditions are more prevalent with lower stability and higher RH conditions with higher stability. This may be due to the unstable conditions being more likely to mix dry air into the surface layer. These findings help identify the common variability found in nature and can be used in several manners. First, we clearly bound the conditions in which a surface layer model must perform well. Second, when modeling the surface layer in an ensemble manner, this variability will aid in bounding the range of perturbations.

The MASL model as described in the preceding section was applied to the buoy observations. Figure 23 shows a typical profile that was produced from a buoy observation for an unstable environment with an air-sea temperature difference of -0.5 K, wind speed of 5 m/s, and relative humidity of 85%. The temperature and humidity profiles appear reasonable. The EDH is obtained at the level of zero M-vertical gradient at 8.7 m and has an EDS (or M-deficit) of 6.6 M-units.
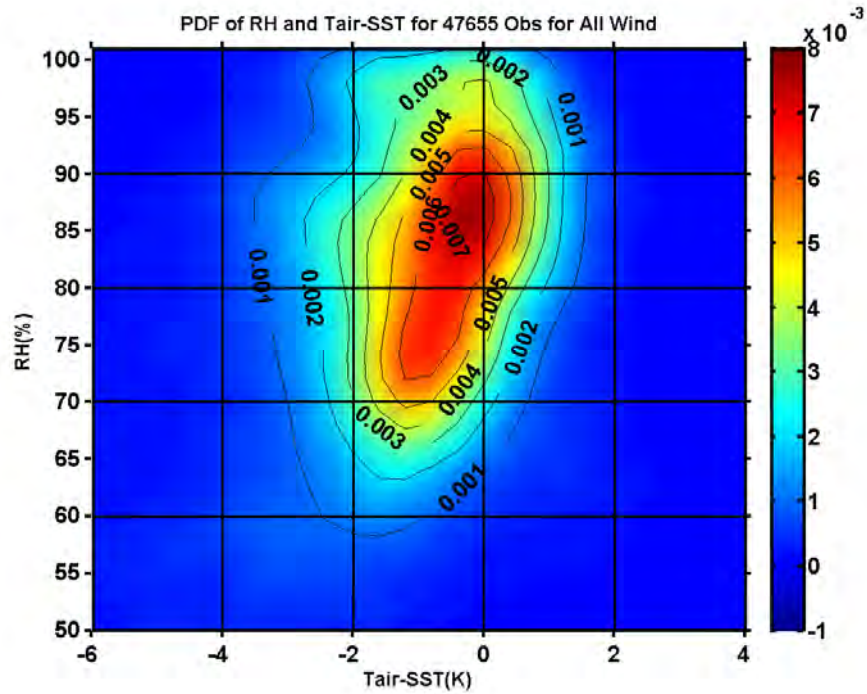
Figure 22.   Joint probability distribution of relative humidity (RH%) and ASTD
(T_{air}-SST) from observations of all 8 buoys selected for this study.
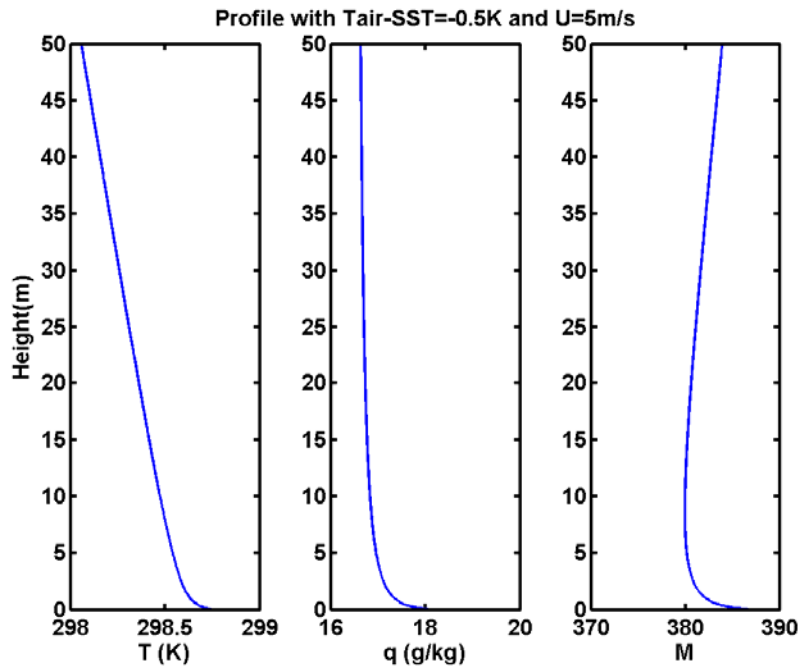
Figure 23.   Profile generated by the surface layer duct model introduced in the
previous section for temperature (K), specific humidity (g kg^{-1}), and
modified refractivity (M-units).

74

The MASL model was applied to the 47,655 buoy observations and the EDH and EDS were calculated from the resulting M profiles. Figure 24a shows the empirical probability distribution of the EDH. We found that the EDH is typically less than 20 meters and peaks between 3 to 5 m for the buoy measurements discussed here. The anomalous large bin at 50 meters is because that bin includes all the cases where the EDH was 50 meters or greater as well as bogus profiles with continually decreasing M profiles. As mentioned, these cases will be illustrated. Figure 24b shows the PDF of EDS. The EDS is typically less than 20 M-units and is predominantly less than 7 M-units. As in Figure 24a, the last bin at 50 M-units also includes all the cases with EDS greater than 50 M-units and these cases will be examined later in this section.

To assess the sensitivity of EDH to naturally occurring conditions, the EDH values were plotted against variations of turbulence stability and humidity. Turbulence stability will be represented using bulk Richardson number, while humidity is represented by specific humidity difference between the buoy measurement level and at the surface (estimated from SST assuming 98% relative humidity), which will be referred to as humidity depression. The Richardson number was calculated using the following formula:

$$Ri_b = \frac{g \Delta \theta_v / \theta_v}{\Delta u^2 / \Delta z} \tag{4.14}$$

where g is gravity, $\Delta \theta_v$ is the difference between virtual potential temperature at the measurement height (assumed 4.5 m) and the surface, Δu is the difference between wind at the measurement height and surface (assumed to be zero), and Δz is 4.5 m which was the approximate difference between the measurement height and z_0. The 4.5 m measurement height was used as a compromise between the wind measurement at 5 m and the temperature and humidity measurements at 4 m.

The results, shown in Figure 25, indicate different behaviors of the EDH in different ranges of the bulk Richardson number. The very stable regime is clearly different from others and so is the very unstable regime. When Richardson number is between -0.03 and 0.01, the EDH displays significant dependence on both stability and moisture depression. These three regimes of atmospheric conditions will be discussed

75

below and will be referred to as very stable, moderate stability, and very unstable conditions.

The observed cases in the very unstable condition compose about 20% of the total cases. In this region, EDH varies with moisture depression only indicates no sensitivity to thermal stratification. Furthermore, it appears that the gradient with moisture depression is constant for all bulk Richardson values less than -0.03. There is apparently negligible sensitivity to the instability when the bulk Richardson number is less than -0.03. However, EDH is sensitive to specific humidity depression in that larger depressions yield higher EDH values.

The very stable region in Figure 25 is considered where the bulk Richardson number is more than about 0.01 which is about 4.5% of the total cases. In this region, the sensitivity of EDH to humidity is extreme in that the EDH increases from nearly zero to greater than 20 meters with a change in specific humidity depression of less than a gram per kilogram. Similarly to the unstable region, the sensitivity to stability is small to negligible in comparison to the sensitivity to humidity.

The moderate stability conditions shown in Figure 25, where the bulk Richardson number is between -0.03 and 0.01, consists of 75.5% of the total cases. In this region the EDH is very sensitive to both humidity and stability, although the sensitivity loosens when the specific humidity depression is small.

The stable conditions are special in several ways. First, we find positive specific humidity depressions exist only in this stability regime, the magnitude of which rarely exceed 4 g kg^{-1} and almost never exceed 6 g kg^{-1} (not shown). These are the cases where there are higher specific humidities in the air than at the ocean surface. Most of these cases are in the moderate stable region seen as a positive spike at small positive Richardson numbers in Figure 25. A good example of these types of conditions is a fog layer in stable stratification. Similar cases also occur in the strong stable regime. EDH is defined as 0 m in these cases.
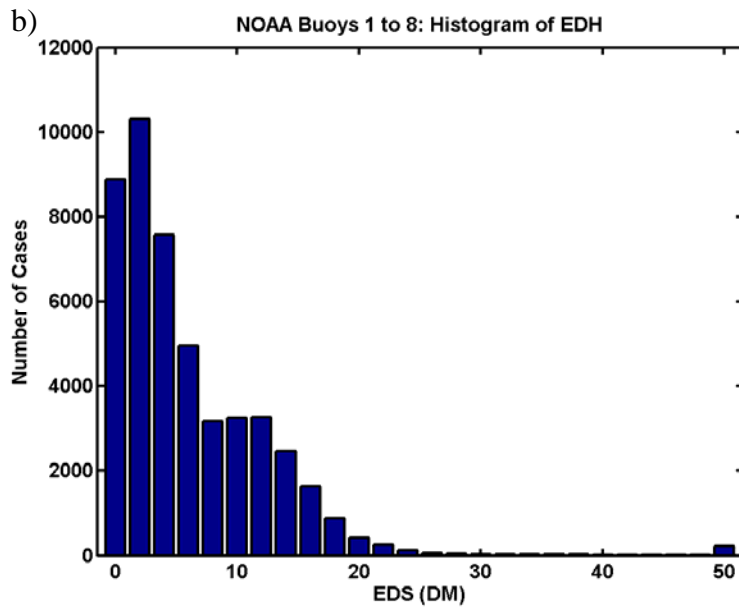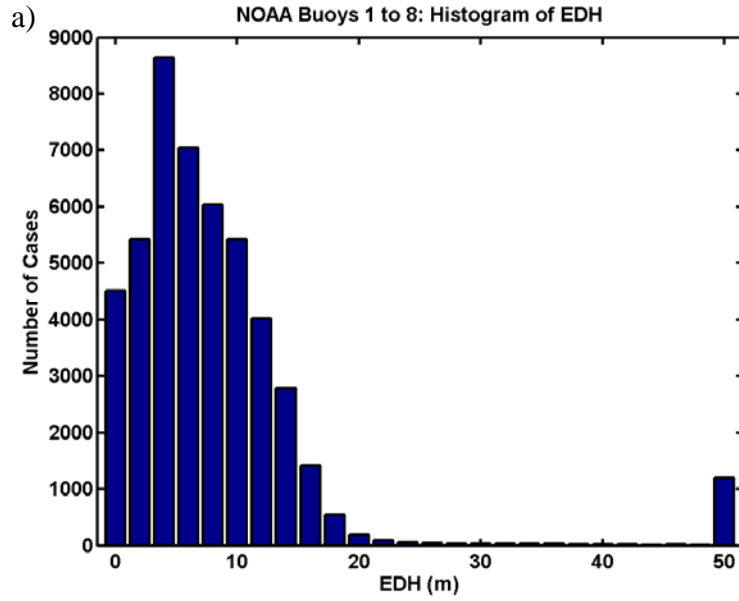
Figure 24.   (a) Evaporative duct height (EDH) and (b) evaporative duct strength
(EDS) derived from the COARE surface layer model based on
inputs from the buoy measurements.
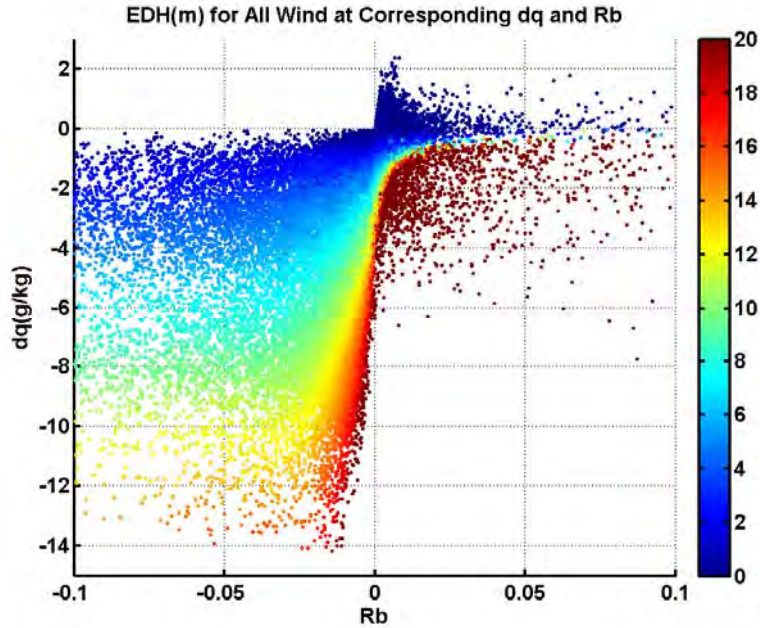
Figure 25.   Evaporation duct height in meters (colorbar) as a function of
specific humidity depression (g kg^{-1}) and bulk Richardson number
for all wind speed conditions.

Wind speed, or its vertical gradient, is a key parameter determining the dynamic mixing in the surface layer. The sensitivity of EDH on wind speed also needs assessment. Figures 26a-f show EDH plotted against specific humidity depression and bulk Richardson number at different ranges of wind speed. Figure 26a shows that the low-wind conditions may occur in any stability regime. This figure resembles the all wind plot (Figure 25) at a glance. Closer inspection reveals that the plot is missing EDH values greater than about 12 meters on the unstable side of the moderate stability region. This suggests that a surface layer predominantly driven by buoyancy (weak wind shear) does not produce the deeper evaporative ducts. On the stable regime side, however, all the diagnosed high EDH cases are in this category of wind speed. The uncertainty in these low-wind but high EDH cases will be discussed in further detail later in this section. Close inspection of all subplots of Figure 26 suggests that the cases of positive humidity depression in the strong stable cases mostly had weak winds (Figure 26a), while those occurred in the moderate stability regime (a positive spike in small magnitude of Richardson numbers) are mostly associated with wind speed between 4 and 20 ms^{-1}(Figs.

78

26 b-f). This may suggest that advection is a key parameter for positive moisture gradient.
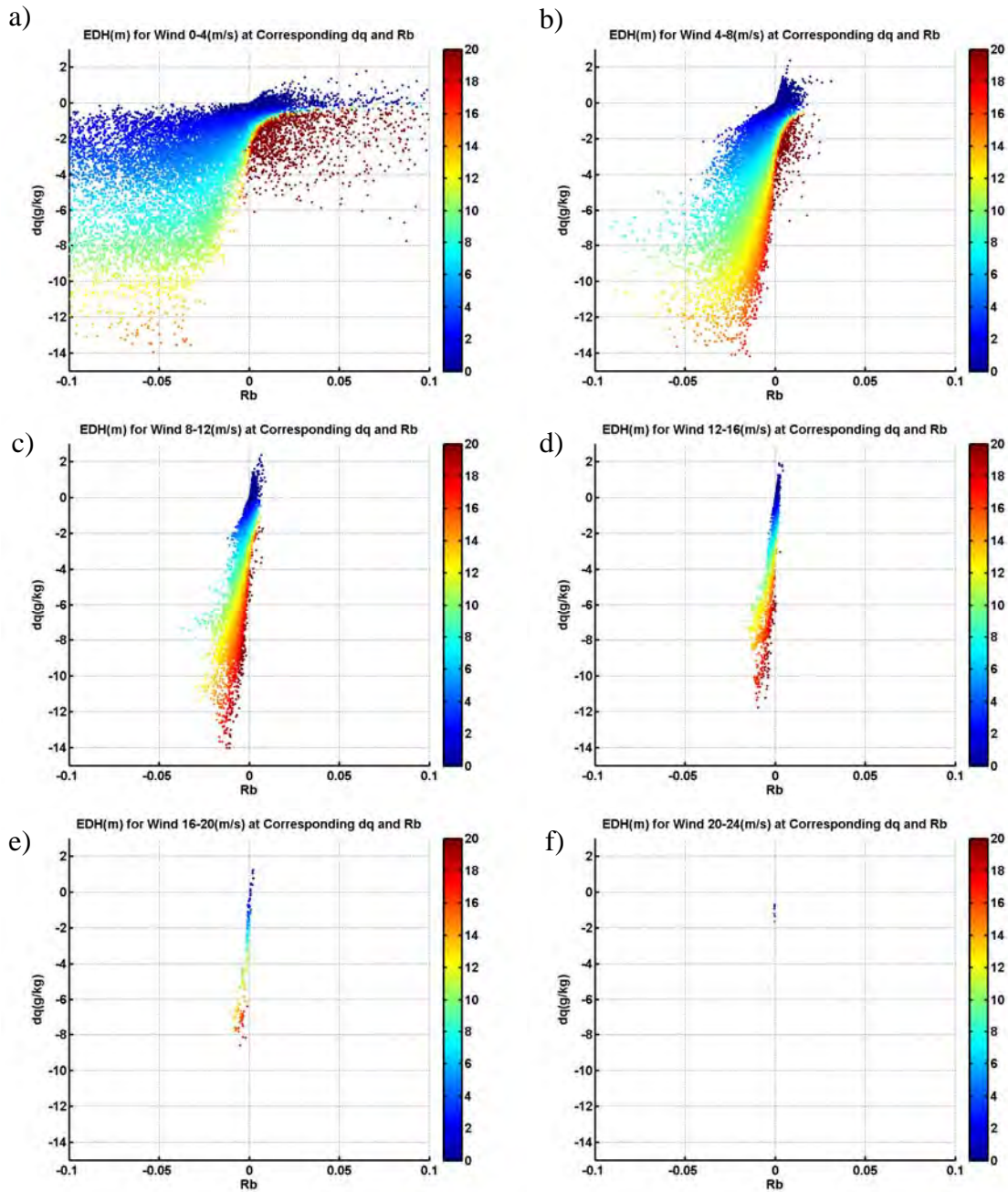
Figure 26. Same as Figure 25 except for wind speeds between a) 0 to 4 m s^{-1}, b) 4 to 8 m s^{-1}, c) 8 to 12 m s^{-1}, d) 12 to 16 m s^{-1}, e)16 to 20 m s^{-1}, and f) 20–24 m s^{-1}.

Figures 26b-f clearly shows that increasing wind speed brings the stability parameter into the moderate stability regime because wind speed occurs in the denominator of the bulk Richardson number. We found that wind speed greater than 8 m s^{-1} producing exclusively cases in the moderate stability regime and most of the cases in the 4–8 m s^{-1} wind speed range also fall into the moderate stability regime. Additionally, as wind speed increases, more observed cases are found on the unstable side. It is clear that in these cases (Figs. 26 b-e, moderate stability regime and moderate to high winds) EDH increases significantly with increasing magnitude of the humidity depression. We can also see that the dependence on stability is different in stable and unstable regimes in these categories. On the unstable side, at a given specific humidity depression, EDH increases significantly as stability moves towards neutral. On the stable side, however, EDH decreases as the stability goes towards neutral, although most of the stable cases under moderate stability regime are in the wind speed range of 4–8 m s^{-1}. Finally, there is a clear pattern that becomes more apparent with higher wind speeds that stable conditions only exist with small specific humidity depression and have low EDH values whereas the unstable environment is more likely to be associated with greater specific humidity depression and produces deeper EDH with greater instability. This was also confirmed while examining plots that filter only deep EDH cases and sort by wind speed (not shown). The deep EDH values existed almost exclusively in low wind speeds for stable conditions whereas at high wind speeds the deep EDH values existed almost exclusively in unstable conditions. As to be discussed later in this section, the deep EDH cases in the stable regime are not physical.

The EDS was also plotted against specific humidity depression and bulk Richardson number and the results are depicted in Figure 27. Overall, EDS shows strong sensitivity to Richardson number around the neutral and slightly stable conditions, and away from neutral the EDS shows the greatest sensitivity to humidity depression and it is weakly sensitive to the Richardson number. This is similar to the behavior of EDH. Specifically, with very unstable conditions, the EDS is fairly sensitive to humidity depression with some weak sensitivity to stability. In all unstable cases, the strong ducting strength cases are all cases with large magnitude of moisture depression. For very

stable conditions the sensitivity is again dominated by humidity and only slightly sensitive to stability. In general, dependence on stability and on humidity depression is not the same. The significant gradient spans the specific humidity depression range from -0.5 to -1.5 g kg^{-1} for the EDS plot, whereas the gradient is sharper and spans the range from about -0.25 to -0.75 for the EDH plot. Lastly, the moderate-stability regime for the EDS spans over a narrower range of the Richardson number. The sensitivity to stability is small in unstable conditions from a bulk Richardson number of about -0.005 and below for the EDS, whereas EDH sensitivity to stability was small from about -0.03 and below.
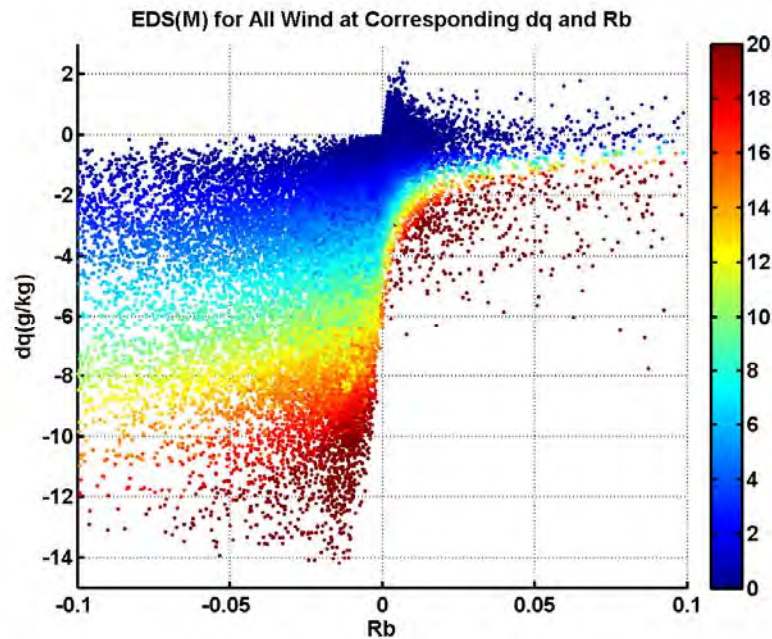
Figure 27.   Evaporation Duct Strength (EDS) in M-units (colorbar) plotted with corresponding humidity (specific humidity depression in g/kg) and stability (Bulk Richardson number) for all wind speeds.

Some special profiles resulting in no evaporative duct or very large EDH are worth of further discussion. Figure 29 shows a typical profile for cases with no evaporative ducts where the minimum M value in the derived profile is at the surface. Here, the specific humidity increases with height in stable thermal stratification. As a result, M profile increases monotonically with height. Most cases like this one are with wind speed greater than 2 m s^{-1} at buoy level. The surface layer turbulence was thus

maintained by the wind shear. The moderate wind in these cases may suggest advection of moist air into the region. The cloud/fog free surface layer is possible because of the surface-based temperature inversion, keeping the near-surface air below saturation.
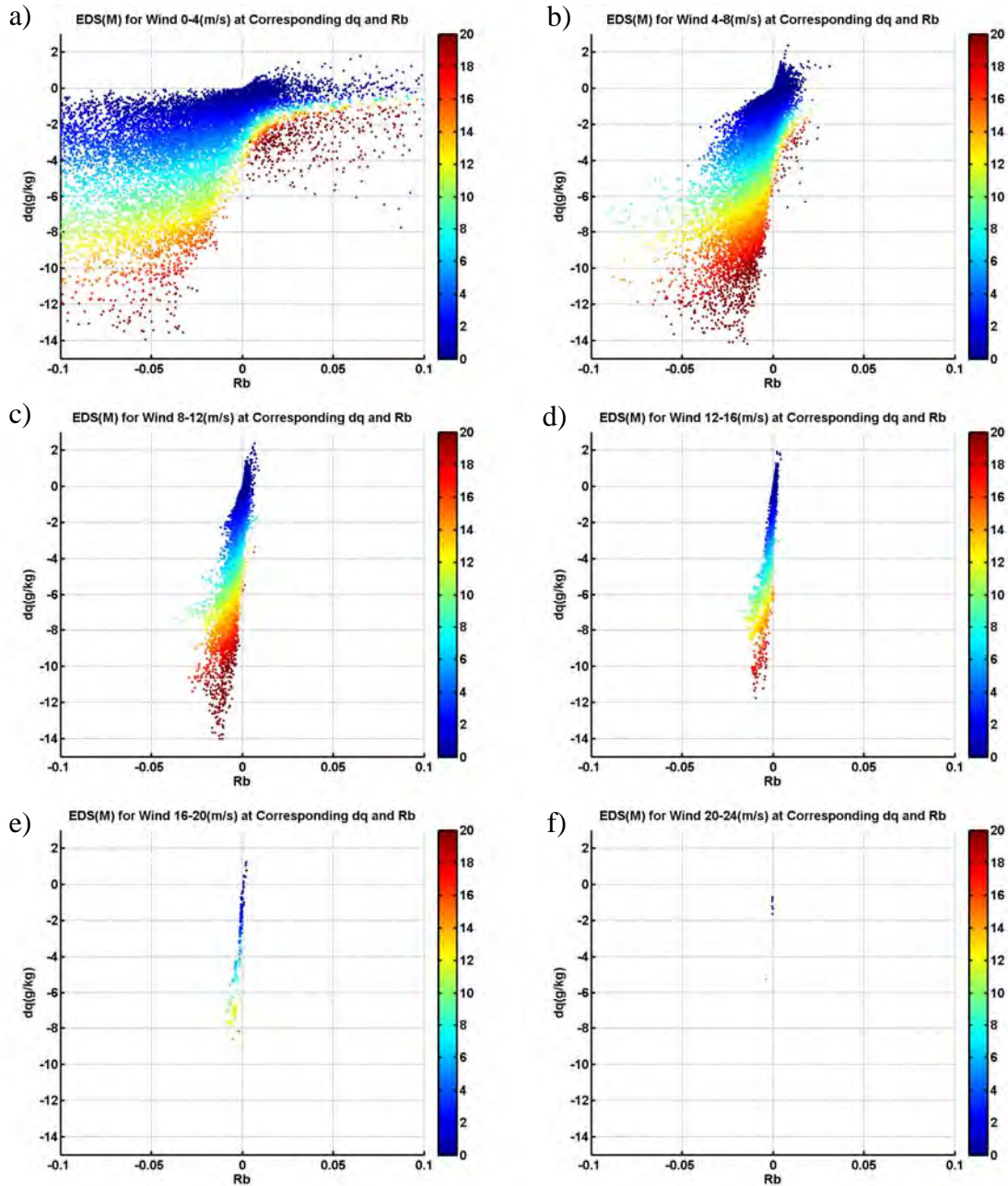
Figure 28.   Same as Figure 26 except for EDS
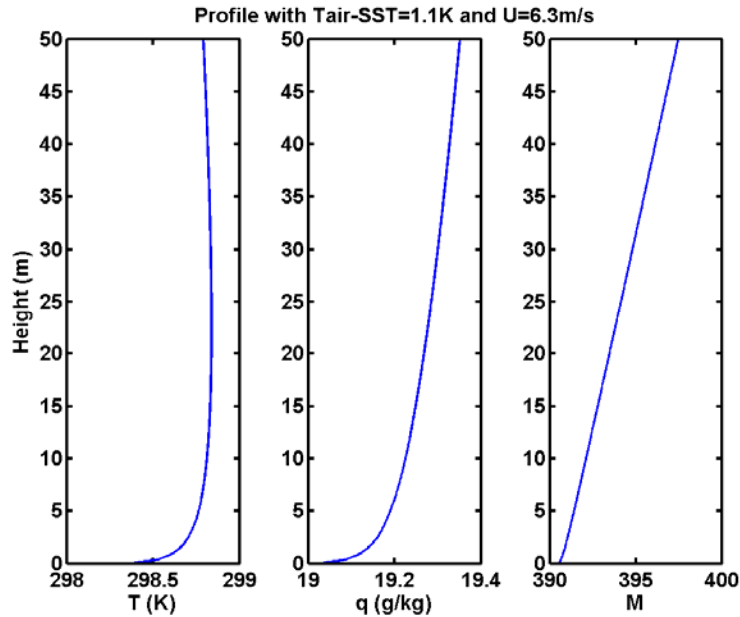
Figure 29.   Same as Figure 23 except for a profile where EDH is defined at the surface.

Figure 30 shows a stable case with low wind speed. The significant increase of specific humidity (i.e., 10 g/kg) in the lowest 50 m above the surface does not appear to be realistic. A stable stratification with such weak wind implies extremely weak turbulence in the surface layer, if any. The application of MOST to this case is questionable as the knowledge on extremely weak and intermittent turbulence field is very limited (Mahrt et al. 2014). These cases may be associated with some of the zero EDH values in Figure 24a. This is not to say that conditions leading to a subrefractive profile in the surface layer doesn't exist, rather that some of these calculated profiles may be unrealistic and contribute to the total cases of zero EDH in the bin as described.

The stability and specific humidity depression conditions that yielded an EDH of zero are shown in Figure 31. Although some cases were in the unstable region, most were stable with either an increase in specific humidity with height, or a very small decrease. Most of the unstable cases have small but negative humidity depression, but clearly all cases are with very weak wind. Most of the cases, including the cases with wind speed greater than 2 m s^{-1}, had a small but positive bulk Richardson number and a positive specific humidity depression.
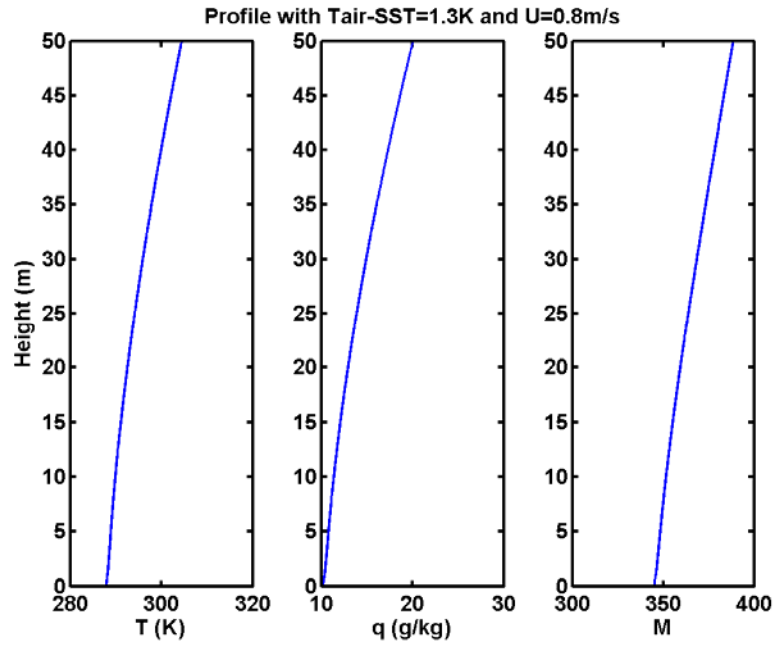
Figure 30.   Same as Figure 29 except for a case with low wind speed.
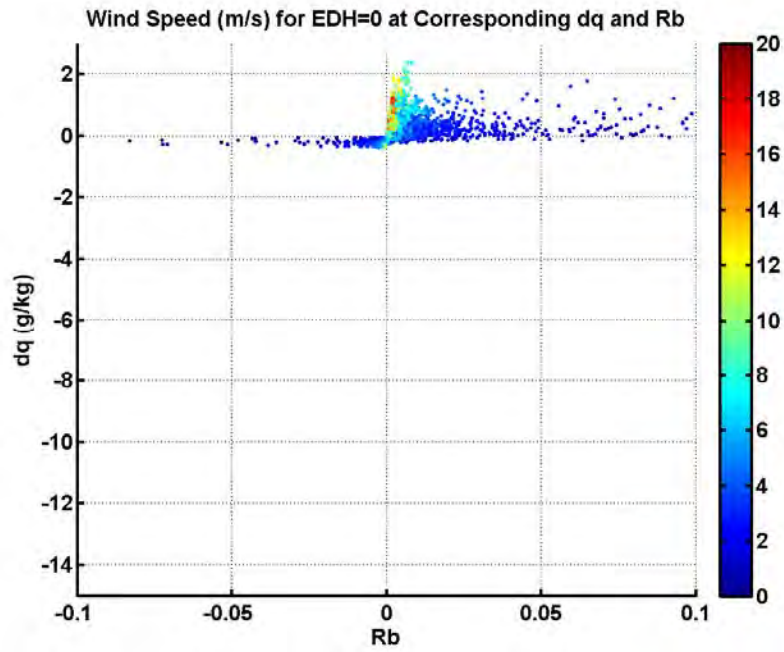
Figure 31.   Observed wind speed as a function of specific humidity depression
and bulk Richardson number where EDH was calculated to be zero.
The colorbar indicates wind speed.

Also as mentioned, some profiles yielded EDH heights greater than the maximum height (i.e., 50 m) of the MASL. Out of the 47,655 cases, 1191 cases indicated a 50 m or more EDH which is about 2.5% of the cases. Figure 32 shows an example profile where M decreases continuously to 50 m. Examination of the T and q profiles also shows significant temperature increase and specific humidity decrease (4 K increase and 20 g kg^{-1} decrease, respectively) in 50 m depth, which are totally unreasonable. This is one of the cases in which the EDH was determined to be at 50 meters or greater. The cases are almost exclusively stable and all have low or light wind conditions. These cases appear to confirm that the MOST breaks down in stable and low wind conditions. About 50% of the cases with EDH of 50 m or higher are similar to the example in Figure 31, indicating the breaking down of MOST. The other 50% of the cases (not shown) show reasonable temperature and specific humidity profiles and appeared to be approaching a zero vertical gradient of M above the model's vertical range. These cases had the higher wind speed values typically greater than 1.5 m s^{-1}. These profiles, which are more realistic, indicate that EDH values higher than 50 m likely do exist and are possibly being resolved by the surface model.
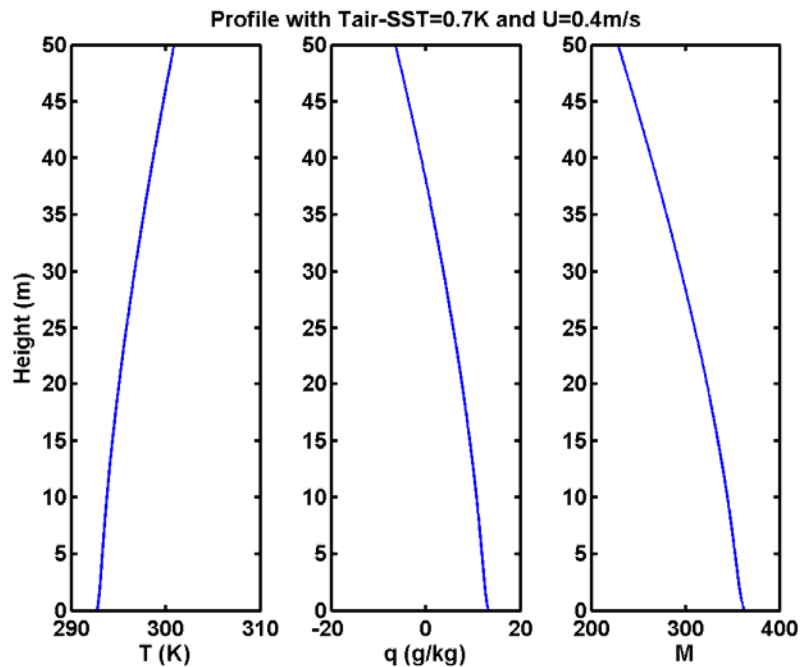
Figure 32.   Same as Figure 29 except this profile indicates EDH to be greater than 50 m.

Ultimately, we need to understand how the variability in the environmental variables affects propagation loss (PL). To investigate this relationship, we use the M profiles derived in the previous analysis to run AREPS and analyze the propagation loss results. Specifically, the surface layer M-profile that was produced using the COARE algorithm was limited to the lowest 50 m. For the purposes of this particular sensitivity analysis, we are not interested in upper air features such as elevated ducts or surface or surface-based ducts that have the depth of the boundary layer. Therefore, we simply append a standard atmosphere M profile for the remainder of the atmosphere above 50 m to the surface layer M profile produced. This method has cases where the resulting profile is far from physically consistent such as for the M profile shown in Figure 32. However, for the number of cases run, the outliers will be insignificant. The AREPS run was set up with a C-Band radar operating at 5.5 GHz and transmitting from a height of 10 m.
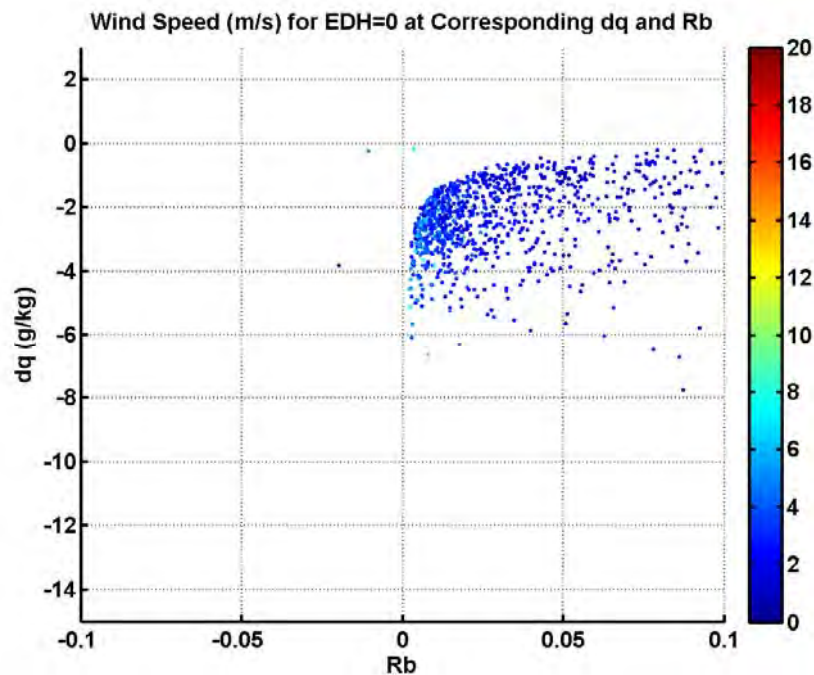
Figure 33.   Same as in Figure 30, except for cases where EDH was calculated to be greater than 50 m (typo in title, should read EDH>=50).

We further need to understand how the variability in the environmental variables affects propagation loss (PL). To investigate this relationship, we use the M profiles

derived in the previous analysis as input to AREPS and analyze the results of propagation loss. Specifically, the surface layer M-profile that was produced using the COARE algorithm was limited to the lowest 50 m. For the purposes of this particular sensitivity analysis, we are not interested in upper air features such as elevated ducts or surface or surface-based ducts that have the depth of the boundary layer. Therefore, we simply append a standard atmosphere M profile for the remainder of the atmosphere above 50 m to the surface layer M profile produced. For most of the profiles, this is reasonable since this particular portion of the study we are looking at the effects of the surface layer gradient and a standard atmosphere M profile (i.e., positive M profile) appended to the top will not add nor subtract energy into the layer below 50 m. This is because energy that propagates up to 50 m will continue to propagate away from the surface.

Some of the surface layer profiles, such as the one shown in Figure 32, were not realistic (i.e., negative specific humidity with a decreasing trend with height) and would therefore give erroneous AREPS results. The total number of cases that were collected in the bin for EDH greater than or equal to 50 m was 1191, or 2.5% of the total cases, and all but one of the cases indicated a stable air-sea temperature difference. After examining some of these profiles for reasonableness (i.e., reasonable temperature, specific humidity, and relative humidity values and gradients), a pattern showed that inflection in the M profile was a good test as an indicator for whether a profile was reasonable or not. In other words, the profiles derived using this COARE algorithm should not show an inflection in M; it should always be increasing trend (i.e., concave to the right). It was found that when the profile was concave to the left and the minimum M value was at 50 m, then the variable values and gradients were unreasonable. Also, when the profile did not show an inflection, then the M profile was approaching a vertical slope at the 50 m height and temperature and humidity values and gradients were within reason. These profiles appear to have been approaching the EDH that may have occurred at or above 50 m and the surface layer model may have shown it had it not stopped the profile derivation at 50 m height. The number of reasonable cases was 671 of 1191, or 56% of the cases in this bin and 1.4% of the total cases. The number of unreasonable cases was then 1.1% of the total cases. Regardless, even these realistic profile cases are usable for the AREPS

87

portion of this analysis because the process of appending a standard atmosphere profile to the top would truncate the evaporation duct profile. However, for the number of cases run, these 2.5% of the cases will not impact the analysis results discussed later in this section.

The AREPS run was set up with an X-Band radar operating at 10 GHz and transmitting at a height of 20 m. The surface roughness (due to wind speed) was kept at zero. Albeit this effect is very important for PL considerations, it would add another variable and complicate this particular analysis. EM energy leakage out of the ED does still occur even without the additional leakage that would exist from the surface roughness scattering.

Figure 34a shows PL as a function of EDH for a target at 15 m height at a range of 75 km for 26,085 different profiles. The pattern of the red data set shows essentially two regimes. The first is for EDH between 0 m and 10 m. The flat part of the curve of grouped data between zero and 4 m EDH is a result of the high loss levels reaching the dynamic range of the internal APM calculations and numerical precision in AREPS (Amalia Barrios, personal communication). Propagation loss greater than 200 dB can fairly well be ignored in this analysis. Otherwise, the pattern of this dataset shows that for EDH less than 10 m there is a persistent reduction in PL with increasing EDH. The grouping of the dataset appears rather condensed with just a few outliers. The slope of this portion of the dataset indicates a strong sensitivity of PL to EDH with a reduction in PL of about 50 dB over a change in EDH of just 5 m (i.e., between 5 m and 10 m EDH). As was described in Chapter II and will be further supported in the next set of figures, the sensitivity in this range of EDH values is due to the sensitivity of PL to the frequency of the EM energy. Assuming an EDH of 5 m and an EDS of 5 M-units, Equation 2.3 yields a wavelength of 2.8 cm or a frequency of 10.7 GHz. As EDH increases (D in Equation 2.3), the cutoff frequency decreases. Also, as EDS increases (dM in Equation 2.3), the cutoff frequency decreases but at a slower rate because cutoff frequency varies as the square root of EDS varies. As mentioned, the cutoff is not sharp so it is around this EDH and EDS combination that we would expect large sensitivity in the effectiveness of the duct to trap the energy.

In Figure 34a for cases where the EDH is higher than 10 m, the PL shows a more complex relationship to EDH. There is a large group of data points that indicate an increase in PL for EDH between about 10 m and 13 m and then a decrease again between about 13 m and 18 m. Also, the grouping of the dataset disperses significantly compared to data where EDH is less than 10 m. Although there is a larger dispersion, there is a predominant grouping of data that indicates the peak in propagation loss when the EDH is about 13 m. This is a result of multi-modal interference pattern as discussed in Chapter II. This was determined after examining coverage diagrams in this range of the dataset. The dispersion of data indicates that more parameters than just EDH are important when considering how PL varies such as the shape of the M profile.

The shape of the ED profile is attempted to be described in part by the EDS as discussed previously and Figure 34b is the same data set as Figure 34a except that the EDS is color coded. Several patterns become apparent. The narrow dispersion of PL data points with EDH less than 10 m indicates that the higher EDS values are producing a lower PL result. This is congruent with Equation 2.3 and the discussion above. For EDH values greater than 10 m the pattern is complex again. The plot appears to have a narrow ribbon of higher EDS values that increase in PL to the peak at 13 m EDH and then decrease and increase again. The plot also appears to have a much broader ribbon of lower EDS values that increase in PL to a second peak at about 16 m EDH and then decrease again. A closer look at the first ribbon shows that a great portion of the larger EDS values indicate the highest PL values between 10 and 14 m and lower EDS values in the same EDH bins have less PL. For EDH values above 14 m, this ribbon appears to invert. This may be showing that the multimodal interference null will exhibit a range shift depending on the EDS and therefore the effectiveness in which the ED traps energy. This is discussed in context of ranges within the horizon in Anderson (1995), but not for ranges over the horizon as shown here. Additionally, the large width of the ribbon in which there are similarly high EDS values in the middle and at the bottom indicates that the EDH and EDS do not completely describe the shape of the evaporation duct. Lastly, also observed is that the second ribbon peak at about 16 m EDH is composed of only smaller values of EDS.

Figure 34. a) AREPS calculated propagation loss (dB) vs EDH (m) of an X-band radar transmitting at 20 m height and PL is estimated at a target height of 15 m at a range of 75 km. b) same as a) except the EDS (M-units) is color coded.

Figure 35 is the same as Figure 34a except that many ranges between transmitter and target are plotted on the same graphic. This shows that for the longer ranges (i.e.,

more than 75 km and therefore well over the horizon) the propagation loss is also very sensitive to change in EDH below a value of 10 m. Closer inspection reveals that the PL to EDH slope gets steeper as range is increased indicating higher sensitivity with range. At ranges beyond 125 km, the relationship is essentially binary in that over an EDH change of just a meter or two results in a PL difference of 40 dB or more. The grouping for 50 km range (green markers) also resembles the longer range sensitivity except the relative minimum is at slightly the slightly lower EDH value of about 9 m.

The short range grouping for the 25 km range (blue markers) shows a distinctly different pattern. The lack of apparent sensitivity to EDH is due to the target essentially being within direct line of sight (i.e., within the horizon). The peak in the 25 km range propagation loss at 10 m EDH is due to multimodal interference. There is another such multimodal interference null at about 20 km for this short range. These multimodal interference peaks and nulls are also very sensitive to target height.
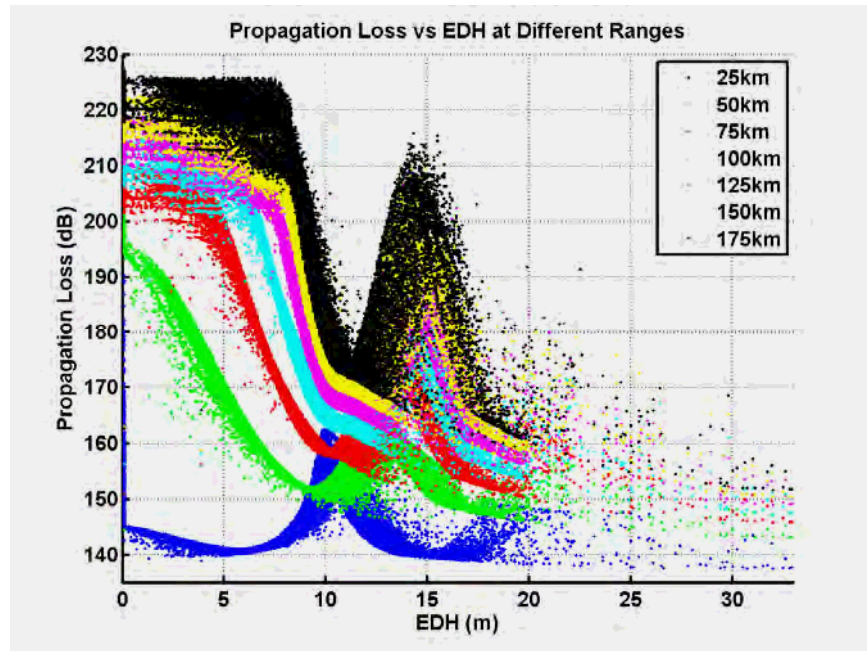
Figure 35.   Same as Figure 34a (X-band) except for ranges of 25, 50, 75, 100, 125, 150, and 175 km.

For longer wavelengths (i.e., lower frequencies) a deeper EDH is needed to effectively trap the EM energy. Figure 36 shows similar plots to Figure 35 except for C-band and S-band radars operating at the same height detecting the same target at the same height. For the C-band (Figure 36a) the initial slope of sensitivity is up to an EDH value of about 15 m due to the longer wavelength. Above 15 m, the direct sensitivity still exists, however, which is different than the transition to the interference pattern shown for the X-band radar. For the S-Band (Figure 36b) this slope continues up to between 17 m EDH (at 50 km range) and about 25 to 30 m EDH for the 175 km range. For higher EDH values, again there is still a direct sensitivity. These plots show the need for deeper EDs to better duct the energy.

Figure 36 shows the same type of plot as Figure 34b above for the 75 km range except PL is plotted against EDS and EDH is in color. The visualization of a ribbon is very clear in this image. For the majority of the data points, the EDH values get larger as you visually progress along the ribbon from left to right. However, the image is slightly difficult to interpret. The fold in the ribbon where it appears to climb up in PL again is the indication of the multimodal interference null as shown at 13 m EDH in Figure 34. The green data region (EDH from 13 to 15 m) shows a rather large dispersion in both EDS values (from around 4 to about 23 M-units) and in PL (from about 153 to 180 dB). little difficulty for interpretation. This is the same ranges and dispersion of the data from Figure 34b, showing the consistency in the data. It does show that PL is sensitive to EDS to some degree by decreasing PL while increasing EDS along the ribbon from left to right. However, since the ribbon folds and since the ribbon appears to steadily change color from left to right, it is difficult to discern how much the sensitivity is to EDS or to the EDH as shown before.

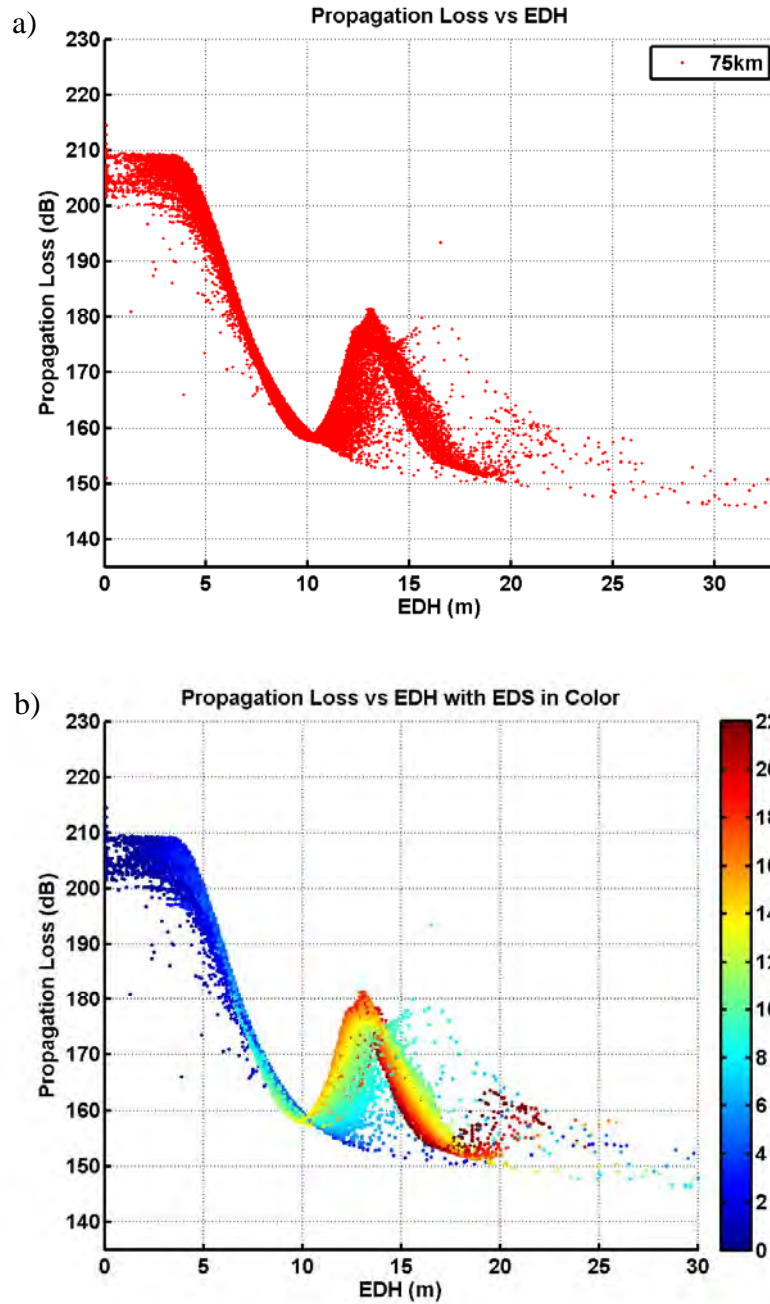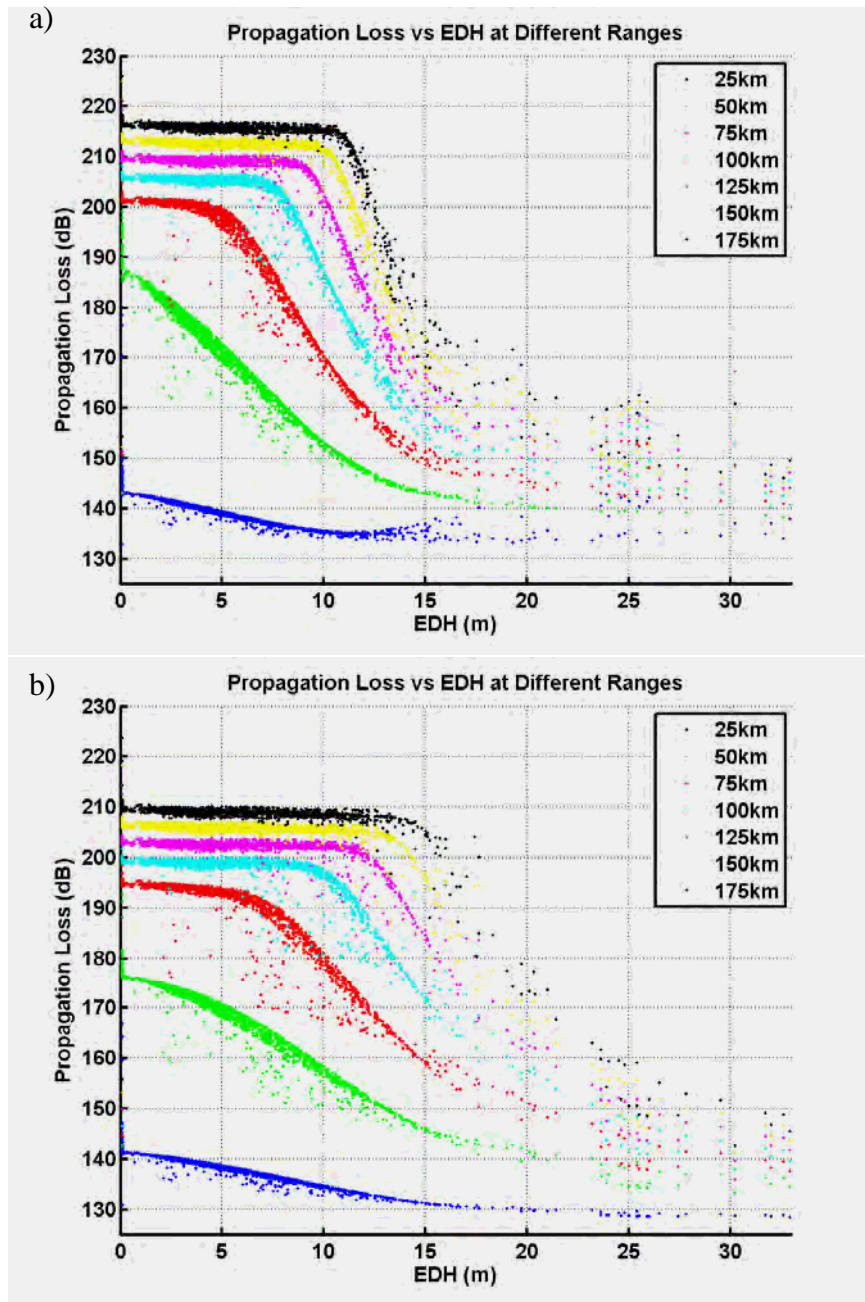Figure 36. Same as Figure 35 except for a) C-band and b) S-band.
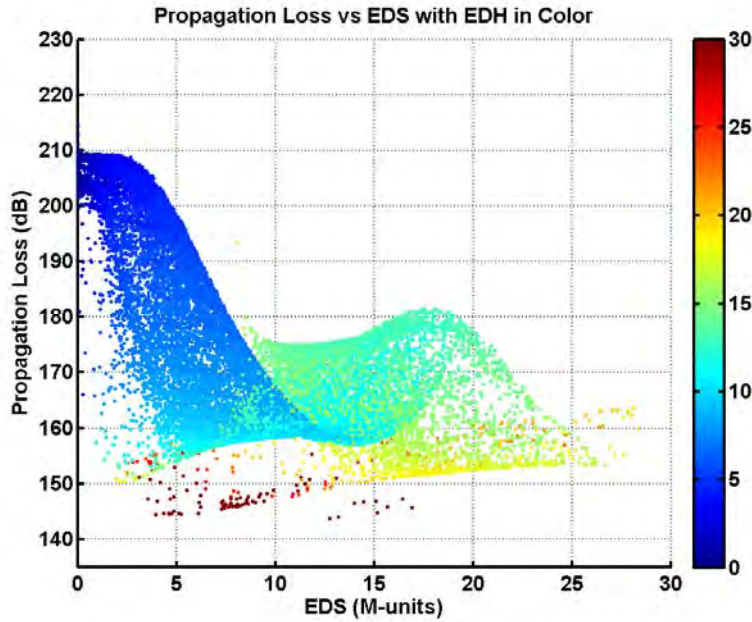
Figure 37.   AREPS calculated propagation loss (dB) vs EDS (M-units) of an X-band radar transmitting at 20 m height and PL is estimated at a target height of 15 m at a range of 75 km. EDH (m) is color coded.

To investigate if a coherent dependency of PL on both parameters exists coincidently, we plot the PL as a function of both parameters in Figures 38. Figure 38a indicates the PL for the same X-band radar described above at a 75 km range, and Figure 38b is the same except for a range of 200 km. A clear pattern is revealed in these figures. The PL color contours are mostly horizontal for EDH values less than 10 m indicating the dominant dependence on EDH in that region of the plot. However, there is a slight angle to the contours indicating some dependency on EDS. Also, the band of higher PL values when EDH is greater than 10 m and EDS is greater than 9 M-units is evident and is the multimodal interference null. This band is clearly dependent on the combination of both EDH and EDS. Another feature of these plots is the very sharp edge of the color region indicating larger EDS values require a minimum EDH. An edge this sharp is seldom seen in nature and is likely some limiting factor in the surface layer model that was used based on the MO similarity theory. Figure 39 shows the same data points plotted with the color code representing the bulk Richardson number. It clearly indicates that this sharp edge is lined with the most unstable conditions. The red circles indicate the bulk Richardson

number values between approximately -0.04 and -0.03. The figure only shows a small range of the bulk Richardson number to highlight the stability effect in determining the EDS and EDH relationship. Clearly, the stable condition tends to give high EDH and small EDS ducting conditions, while unstable surface layers tend to have rather large EDS for the same EDH.
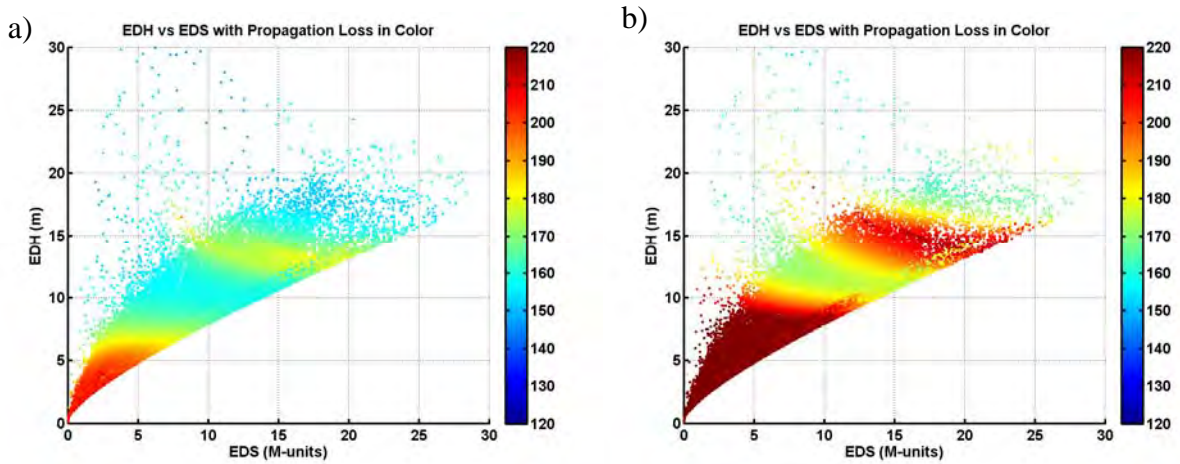
Figure 38.   AREPS calculated Propagation Loss (dB) (color coded) is plotted against EDH (m) and EDS (M-units) for an X-band radar transmitting at 20 m and PL is estimated at a target height of 15 m at a range of a) 75 km and b) 200 km.
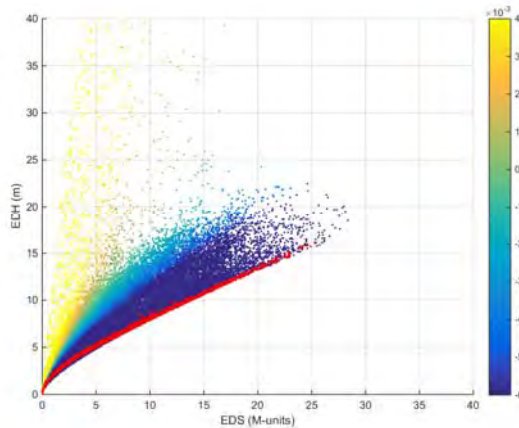
Figure 39.   Same as Figure 38 except that the color code is the bulk Richardson number.

95

THIS PAGE INTENTIONALLY LEFT BLANK

V.   HYBRID MODEL RESULTS

This chapter will evaluate the approach of using a hybrid COAMPS/SCM for environmental characterization of EM propagation. The hypotheses are:

Hypothesis 1: Higher vertical resolution SCM model can better capture ducting layers in and above the surface layer due to its ability to better resolve vertical gradients in the predicted variables that are significant over a vertical extent less than what can be resolved by COAMPS with coarser vertical resolution.

Hypothesis 2: SCM with higher vertical resolution is capable of capturing surface duct characteristics based on MOST and providing a smooth transition to the rest of the boundary layer with consistent model physics throughout the boundary layer.

The process for this evaluation is as follows. First the SCM will be run using idealized forcing in a case of stratocumulus topped boundary layer sampled from a previous field project. This part of the work will evaluate the hybrid approach for cases of strong elevated ducting layers that result in a stratocumulus regime due to the strong inversion and sharp humidity gradient found at the cloud top. The rest of the evaluation will be based on cases observed during TW13 because of the available measurements. In this part, we will first examine the performance of 3-D COAMPS during the TW13 campaign using soundings. The forcing terms (as defined in Chapter III. and include large scale vertical motion, horizontal pressure gradient force, sea surface temperature, and horizontal advection of temperature, moisture, and momentum) derived from COAMPS 3D model during TW13 via the FAM will be analyzed next. Although there were no data to evaluate the forcing terms, their spatial and temporal variability are indicative of whether the results are valid at least qualitatively. The majority of this chapter will concern testing the SCM approach. SCMs with different settings will be first run using idealized forcing conditions to understand the evolution and behavior of the SCM simulations in relatively simple forcing conditions. Finally, the SCM simulations will be made using the full forcing derived from the 3D COAMPS results. The advantage and limitations of such approach will be highlighted using multiple case analyses. Lastly,

we will evaluate a new approach involving SCM to effectively blend the surface evaporative duct with the rest of the boundary layer and troposphere. Results from this new approach will be contrasted with a no-blending approach.

A.   INITIAL TESTING OF SCM FOR STCU REGIME

1.   Aircraft Observations for UPPEF RF01

The Unified Physical Parameterization for Extended Forecast (UPPEF 2012) field campaign was conducted along the central California coastal waters in August and September 2012. Part of the measurement plan included a Twin Otter research aircraft operated by the Center for Interdisciplinary Remote-Piloted Aircraft Studies (CIRPAS). The aircraft was instrumented with a 5-hole Radome gust probe that measured wind and turbulence in addition to fast-response Rosemont total temperature sensors, and sensors for static and dynamic pressure, dew point, water vapor, and absolute humidity. The aircraft was also fitted with downward looking pyranometers measuring SST in addition to other instrumentation not relevant to this work.

Research flight 1 (RF01) was performed on August 31, 2012. The synoptic pattern featured a quasi-stationary 500-mb trough oriented north to south along the coast and the East Pacific High was centered west of the California and Oregon border. This pattern provided large scale subsidence over the cool coastal waters normal for this time of year along the California coast. As the atmosphere stabilized, an extensive regime of marine stratocumulus clouds developed along the coast south of Cape Mendocino and east of 125W (Figure 40). Boundary layer winds were generally northwest and the nearby Fort Ord profiler showed a deep marine layer with the inversion base at about 762 m.
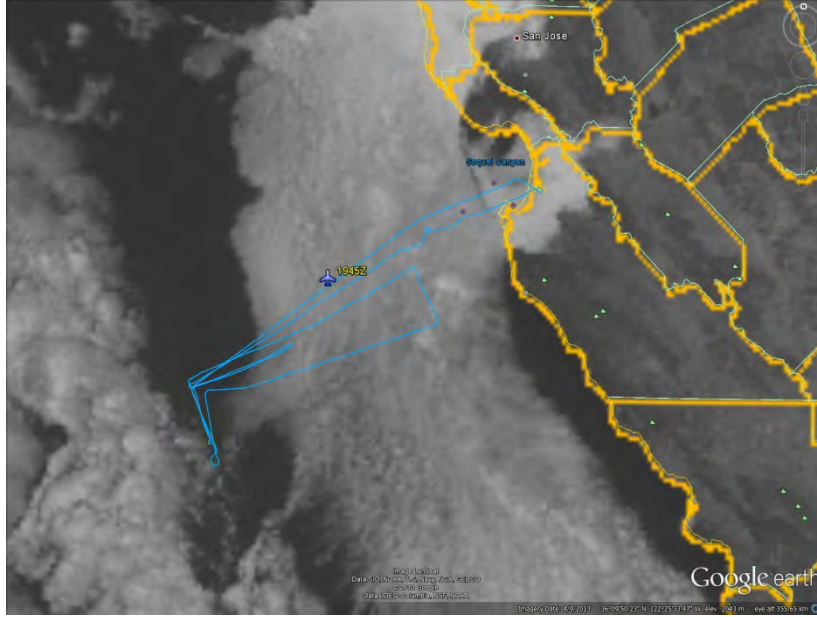
Figure 40.   Visual satellite image and track for RF01 on 31 August, 2012
(from Qing Wang, personal communication, 2013)

The aircraft performed five full soundings (FS) during RF01, two of which (FS2 and FS5) penetrated the cloud top. These measurement profiles are shown in Figure 41 and are similar to each other in many aspects. Closer inspection of the FS2 potential temperature and total specific humidity show a well-mixed layer from about 670 m to the cloud top at about 900 m. Inspection of the FS05 shows a similar well-mixed layer from about 600 m to the cloud top at about 820 m. These well-mixed layers that extend below the cloud layer are evidence of the turbulent mixing caused by the cloud top cooling. Below these well-mixed layers is a decoupling layer. In FS2 there is a stable gradient in potential temperature, negative gradient in specific humidity, and wind shear that extends from about 360 m to about 670 m. Additionally, there is a decrease in measured turbulence in this height range as indicated by relative decrease in vertical velocity variance in the vertical velocity plot. In the FS5 profile there is also a slightly stable gradient, slightly negative humidity gradient, slight wind shear, and a slight decrease in the turbulence from about 380 m to 600 m. They are similar, but the FS2 characteristics are more profound. These portions of the profiles indicate the decoupling of the cloud induced mixed-layer from the surface. Below these transition layers, the profiles are different. In FS2, below the decoupling layer from about 50 m to about 360 m is a more

99

neutral profile of potential temperature, a continuing negative gradient of specific humidity, wind shear, and an increase in turbulence. Below about 50 m the profile indicates an unstable surface layer with a negative potential temperature gradient and indiscernible moisture gradient accompanied by shear and turbulence. This indicates the mixing driven by shear and buoyancy. In FS5, below the decoupling layer from the near surface to about 380 m is a stable temperature profile, a stronger negative humidity gradient, and larger shear with less turbulence. This indicates that the mixing is weaker due to the stability and is largely shear driven. In both cases, the decoupling is evident in the structure. This is common in cloud topped boundary layers, especially so in deep boundary layers, and demonstrates a common complex structure. This is caused by the separation between the two turbulence generation layers (i.e., the cloud layer due to cloud top cooling and cloud bottom warming) and the surface layer due to shear and buoyancy as a result of surface flux.
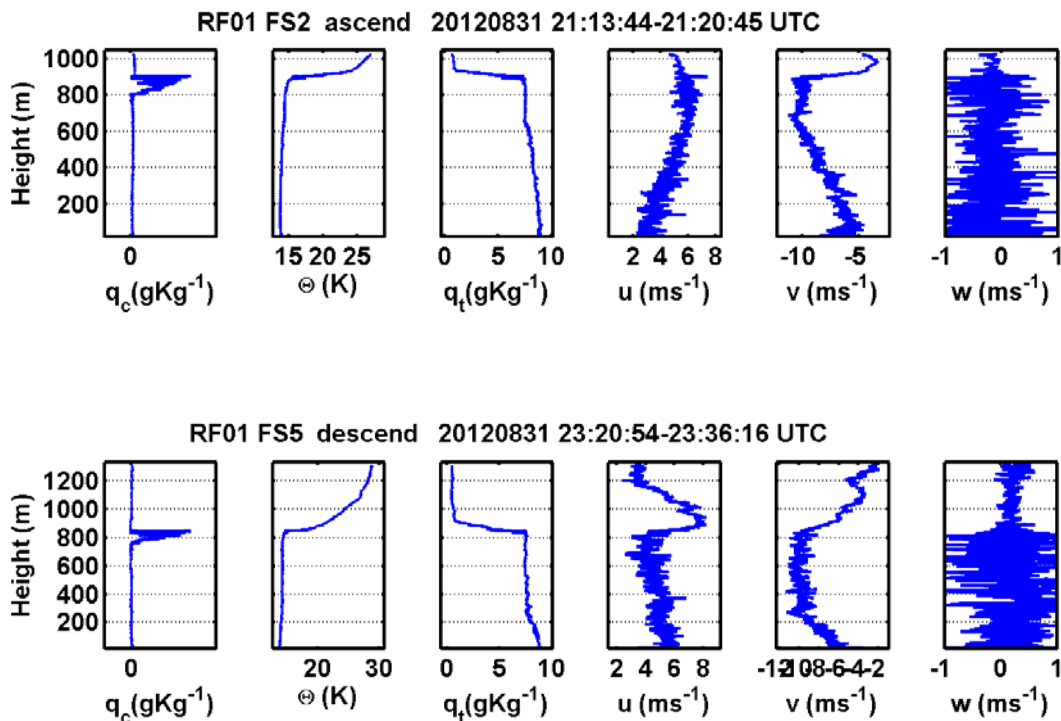
Figure 41.   Vertical profiles from two aircraft soundings. From left to right, the panels are cloud mixing ratio, potential temperature, total water, u and v wind components, and vertical velocity. The soundings were made by CIRPAS Twin Otter RF01 of UPPEF on August 31, 2012. (Wang, personal communication, 2013)

2. Idealized SCM Simulation for UPPEF RF01

The SCM is initialized using simplified profiles based upon the combined mean of the full sounding profiles collected during RF01 and is depicted in Figure 42. The profiles indicate the cloud top at 900 m with a constant potential temperature and a slightly stratified moisture profile in the boundary layer. The idealized vertical motion, also shown in Figure 42, indicates a linear increase in subsidence in the boundary layer with constant subsidence for about 1 km above the inversion. The SST was set at a constant 285 K based on average measurements under the stratocumulus cloud deck. Horizontal advection of both temperature and humidity was set to zero to assume a horizontally homogeneous regime. Latent heat flux and wind stress were prescribed with reasonable values as measured by the aircraft. The sensible heat flux and short wave radiation were set to zero to help prevent the cloud from dissipating. This setup was intended to allow the simulation to balance the processes of subsidence, turbulent mixing, longwave radiation, and surface flux (except sensible heat) while allowing the cloud to persist as long as possible.

The simulation was run using four different vertical grid coordinate systems summarized in Table 4 below. The SCM in this work, as mentioned previously, is intended to be used only over the ocean. Hence the sigma levels are equivalent to height.
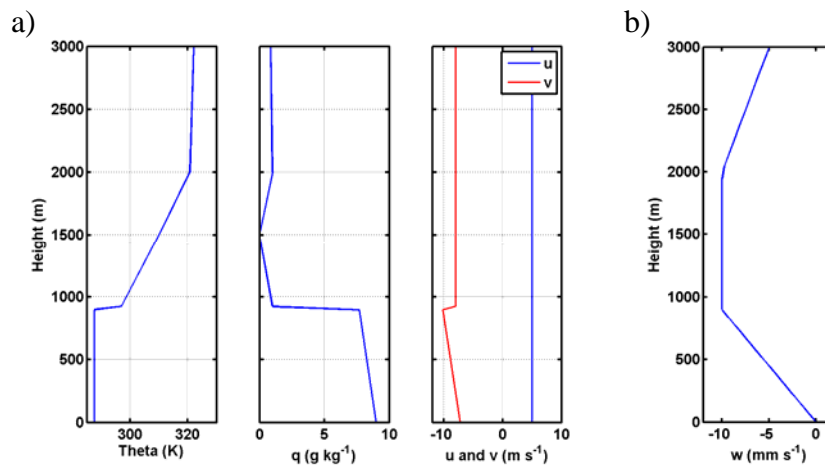
Figure 42.   UPPEF idealized a) initial conditions of potential temperature, specific humidity, and wind and b) idealized large scale subsidence forcing.

101

SCM name	SCM 60	SCM 96	SCM 180	SCM 200
# levels	60	96	180	200
First level height (m)	10	2.5	0.25	0.1
# levels in first 10 m	1	3	20	11
Avg Δz 100-1000m	60	36	10	10
Notes:	Same as 3D COAMPS	Medium High Resolution. About Twice Resolution of COAMPS in boundary layer	0.5 m levels in first 10 m and 10 m levels through 1 km	Logarithmic spacing in first 10 m, 2.5 m levels through 100 m, 10 m levels through 1 km

Table 4.   Summary of vertical grid level setups of the SCM simulations.

The simulations were run for 24 hours but the initial major adjustments were essentially pseudo-steady state after 3 hours of simulation. Comparisons at forecast hour 5 of the runs using different SCM vertical schemes in Table 4 are shown in Figure 43. The potential temperature and specific humidity profiles that the different model resolutions represent in the inversion are significantly different. At the 800 m inversion level, the SCM 60 has 86 m resolution, the SCM 96 has 80 m resolution, and both the SCM 180 and SCM 200 have 10 m resolution. The gradients represented by the lower resolution models are significantly weaker than the higher resolution runs. The cloud mixing ratio plot shows that all the models are indicating cloud at the top of the boundary layer. A closer look reveals that the cloud from the SCM 60 is in the shape of a triangle which indicates that the non-zero cloud water is only at one vertical level at 636 m. Inspection of the SCM 180 and SCM 200 runs reveal that the shape of the profile is more of a saw tooth where the gradient at the top of the cloud is represented over a vertical length scale of just 10 m and the cloud is represented over a span of 12 grid points (or 120 m). The SCM with higher resolution has superior performance in representing the cloud structure as observed in Figure 41. The radiation heating rate also has a significantly more detailed structure where it indicates the cloud top cooling rate at about -85 K day^{-1} coupled with a positive heating rate just above the cloud top. This significant

cloud top cooling destabilizes the cloud and generates thermally driven turbulence. The SCM 60 shows the cooling rate dispersed over a larger thickness (volume) which is also at an elevation 100 m lower than the SCM 200. The TKE profile also shows a very sharp increase at cloud top level with a peak in the cloud for the high resolution SCMs. The relative minimum at about 500 m corresponds to the decoupled signature mentioned previously and observed in Figure 41. The high resolution SCMs also show another relative maximum at about 100 m. Alternatively, the SCM 60 shows an almost linearly decreasing TKE profile above the surface layer. Finally, the impact on refractivity shows a clearly sharper gradient representation with the higher resolution SCMs. The negative M gradient is much larger, the duct depth is shallower and the M deficit is larger with the high resolution SCMs.

One side note about turbulence is that the second vertical level in COAMPS has a spurious large TKE value (Shouping Wang, personal communication) which is previously known but the exact cause is yet to be identified. In this set of simulations, the spike is much larger with the lower resolution SCM runs.

In summary, the SCM 180 and SCM 200 models are the relatively the same at the inversion level with altitude and strength of the gradient layers for all the parameters discussed and clearly indicate sharper gradients than the lower resolution SCMs. We conclude that the SCM cloud thermodynamic structure is sensitive to vertical resolution and that these high resolution simulations resolve these structures in a way that is significantly closer to what is observed (e.g., compare with Figure 41). Finally, this resolved structure at the inversion has a particularly large impact on the M profile.

These results suggest that the SCM approach has potential merit for cloud topped boundary layer cases. A full 3D COAMPS model was not available for comparison at the time of this study and EM propagation measurements were not collected during the UPPEF campaign. Trident Warrior 2013 was a campaign which was designed to provide exactly these pieces for comparison and validation, which will be the focus of analyses in the rest of this chapter.
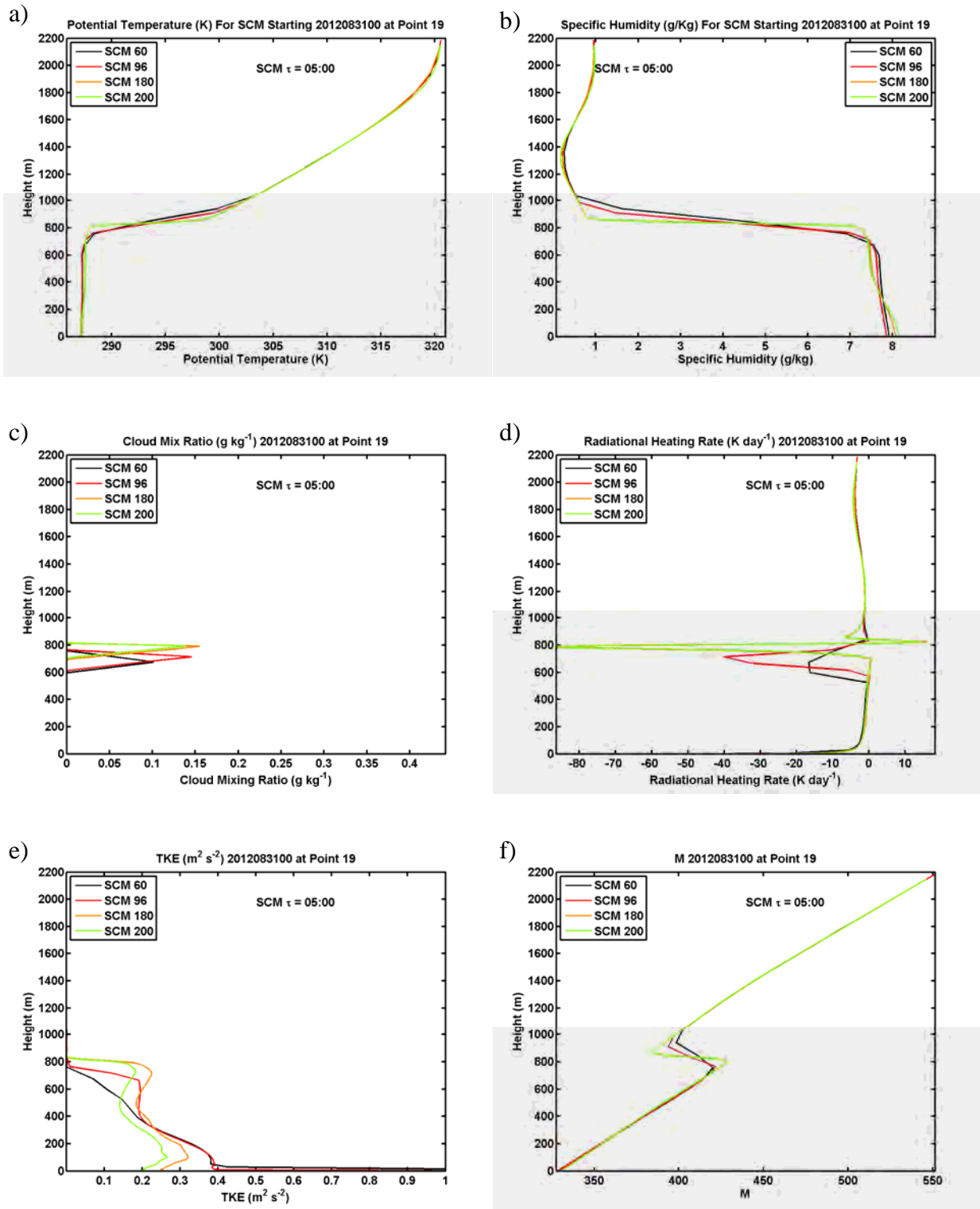
Figure 43.   Comparison of different SCM vertical resolution runs for the
UPPEF idealized case after 5 hours of simulation for a) potential
temperature, b) specific humidity, c) cloud mixing ratio, d) radiation
heating rate, e) TKE, and f) modified refractivity.

104

B. HYBRID APPROACH FOR TW13 CASES

1. COAMPS Simulations versus TW13 Observations

Building on the results of the idealized case for cloud topped boundary layers in the previous section, we move forward with testing SCM simulations in a cloud free environment with forcing provided by the full 3D COAMPS in order to assess the potential benefit of this hybrid modeling system.

In this section, we first assess the performance of the 3D COAMPS model during the TW13 by comparing the 50 atmospheric soundings collected during the campaign with coincident profiles derived from the COAMPS simulations. We use COAMPS forecast output between 6 and 12 hours after initialization for our validation assessment since atmospheric models normally demonstrate an initial adjustment period. Figure 44 shows the comparison between COAMPS and the soundings on a one-to-one scatterplot for the mean variables and modified refractivity. We noticed that the discrepancies between the SCM and COAMPS results are generally smaller above 2 km. Hence, the comparisons are separated for altitudes below and above 2 km. In general, the scatterplots show a good comparison overall with all data points scattered around the 1:1 line. It is clear that more scattering is seen in the results below 2 km compared to those above. The statistical results of the inter-comparison are given in Table 5. COAMPS generally has a cold bias by a half degree, which is a known bias of COAMPS. The specific humidity indicates no real bias below 2 km but is too moist aloft. The mean errors for wind speed components are also smaller than 1 ms-1 at all levels. The overall performance of COAMPS as a weather forecast model is rather impressive for this coastal area. It is also noted that forecasts for the East coast have advantage of abundant upstream data that can be used to assimilate into the forecast.
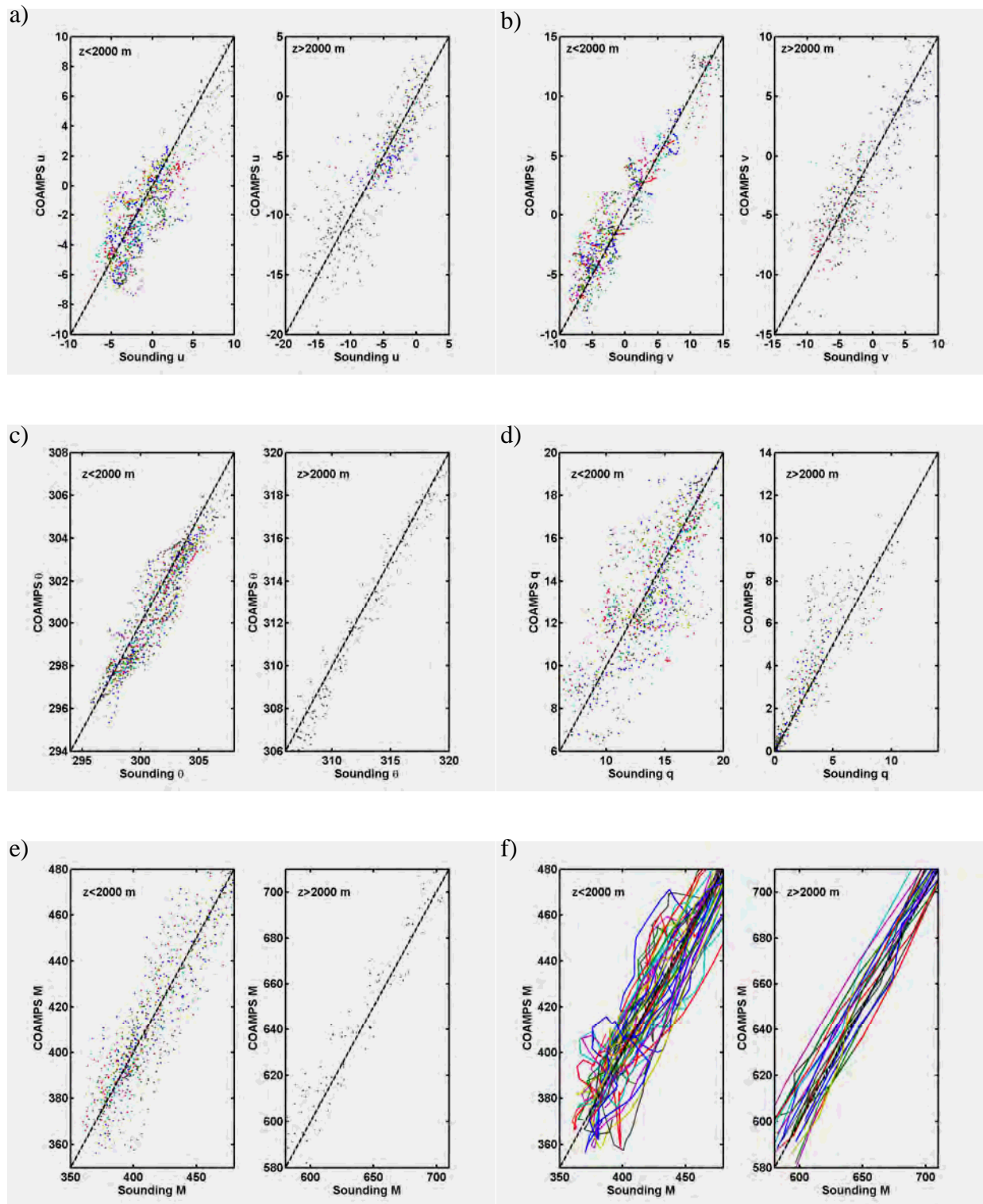
Figure 44.   Comparison of TW13 soundings and coincident COAMPS forecast
profiles above and below 2 km for a) u wind, b) v wind, c) potential
temperature, d) specific humidity, e) modified refractivity and f)
same as in e) except using line plots

106

Variables	theta (K)		q (g kg^{-1})		M (M unit)		U (m s^{-1})		V (m s^{-1})	
	<2 km	2 - 5 km	<2 km	2 - 5 km	<2 km	2 - 5 km	<2 km	2 - 5 km	<2 km	2 - 5 km
Mean	-0.52	-0.44	-0.06	0.84	0.24	4.6	-0.78	-0.56	0.8	0.25
Std	0.9	0.8	2.1	1.7	13.4	9.6	1.97	1.61	1.9	1.98
Abolute Error	0.85	0.74	1.62	1.49	10.4	8.2	1.68	1.4	1.6	1.68

Table 5.   Error statistics on the comparisons between COAMPS forecast profiles and soundings as shown in Figure 44. The mean shows the results of $\phi_{COAMPS} - \phi_{soundings}$, where ϕ is the variable of concern.

The goal of comparing how COAMPS is representing refractive features in the atmosphere requires us to consider the gradient of M. As described in Chapter II, the negative gradient of M forms a propagation duct. Figure 44f is the same as in Figure 44e, except that the adjacent data points are connected by a straight line. In addition to the larger scattering for comparisons below 2 km compared to higher levels, we found, from Figure 44f, that the errors above 2 km is introduced as a bias (lines are parallel with the 1:1 line) while significant discrepancies should be expected in the layer below 2 km, especially in the gradient of M-profile. Figure 45a shows a sounding derived M profile from July 14 at 17:50Z with significant ducting layers indicated by the horizontal lines (ducts resulting from small scale variability have been filtered out). The result is a profile with three significant elevated ducts as measured by sounding. Figure 45b shows the same sounding (plotted only above 50 m) compared to the coincident COAMPS 6 hour forecast profile. COAMPS represents a surface-based duct that is not present in the sounding (note the lowest 50 m of the sounding profile was removed to avoid ship contamination). COAMPS also shows a single elevated duct which is weaker and at a higher altitude than the sounding. This figure shows that the magnitude of error in the ducting layers derived from the forecast profiles can be quite significant for each time/location in spite of the generally good error statistics.
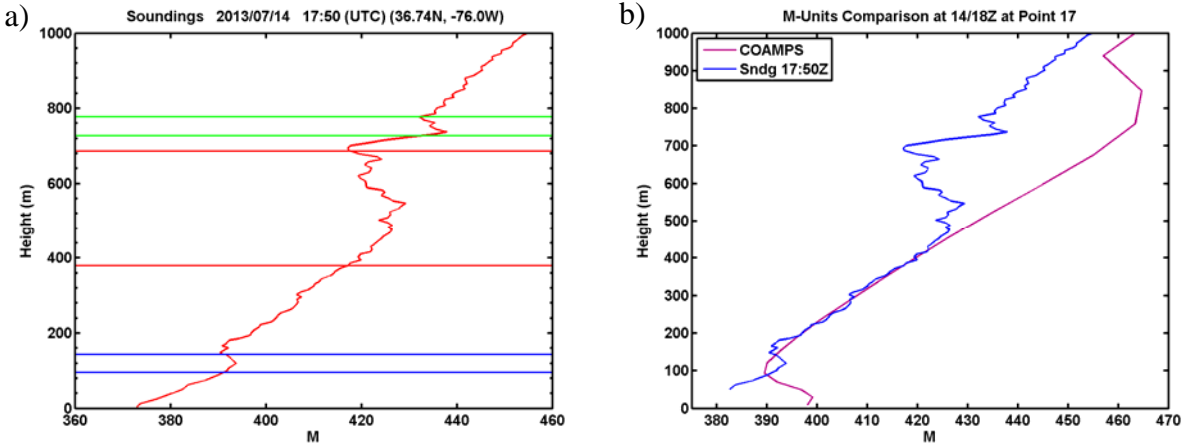
Figure 45.   a) Modified refractivity profile derived from July 14 sounding at 17:50Z. The horizontal lines indicate the top and bottom of propagation ducts. b) Comparison of coincident COAMPS six- hour forecast.

We apply this same analysis technique to all the soundings and corresponding COAMPS profiles of M and compare the results in Figure 46a. The sounding ducting layers are indicated using the blue error bars and are ordered chronologically from left to right. The ducting layers from COAMPS profiles are indicated using the red error bars. The asterisks indicate the height of the local maximum of M or the trapping layer base. The plus marks near the y-axis mark the COAMPS model vertical grid levels for a reference since the ducts indicated by COAMPS must start and end at a grid point. Ducting features indicated by sounding above 1500 m were omitted because they were rarely represented by COAMPS and they also become less tactically relevant, except for satellite occultation retrievals (OA 2006).

Figure 46a shows that nearly every sounding has a fairly complex profile containing multiple elevated ducts. Conversely, COAMPS typically only indicates a single elevated duct in any given profile although COAMPS does occasionally indicate an elevated duct in conjunction with a surface or surface based duct. To a very rough approximation, it appears that on July 14 and 15, COAMPS indicates mostly elevated ducts between about 300 and 1000 m and surface, surface based, or low level elevated ducts for the remainder of the period. This appears be the pattern for the soundings as well although it is difficult to compare because of the resolution mismatch.

108

A more useful comparison between the sounding and COAMPS may be accomplished by interpolating the sounding to have the same resolution as the model. The sounding refractivity values were interpolated onto the COAMPS 60 vertical level grid and the duct feature comparison figure was redrawn in Figure 46b. This method has simplified the sounding duct layer structure tremendously. For several soundings, however, this approach has completely removed the presence of any ducts due to the COAMPS grid levels not existing near the same height as the local maximum or minimum M values. This was especially true at the elevated duct levels where COAMPS grid level spacing was on the order of 80 m. This reinforces that the 60 level COAMPS grid is inadequate to preserve or represent many of ducting features in the atmosphere.

The comparison in Figure 46b provides another view at the COAMPS performance in capturing the ducting features although there is no change to the conclusion. Overall, during July 14 and 15 both model and sounding indicate elevated ducting features. During the 16 and 17 surface and surface based ducts are represented, however the COAMPS fails to capture the combined elevated and surface based duct profiles prevalent on July 17. We also showed that the vertical resolution can change how the layers are identified. The average duct depth in the sounding was 51.9 m without interpolation on the COAMPS levels, 72 m after interpolation, and the COAMPS model average duct depth was 80 m.

Although ducting features are frequently represented by the COAMPS simulations, the gradient strength, ducting height and ducting depth appears to be very poorly represented with errors of up to 100 to 1000 m difference in ducting layer height. Another contributor of error to consider is the variability of each sounding and its ability to represent the atmosphere. The mismatch in these comparisons is not entirely due to issues with the internal physics of the COAMPS model. The coastal region adds an additional influence of variability which leads to complicated layering structure in the lower atmosphere due to horizontal and differential advections.
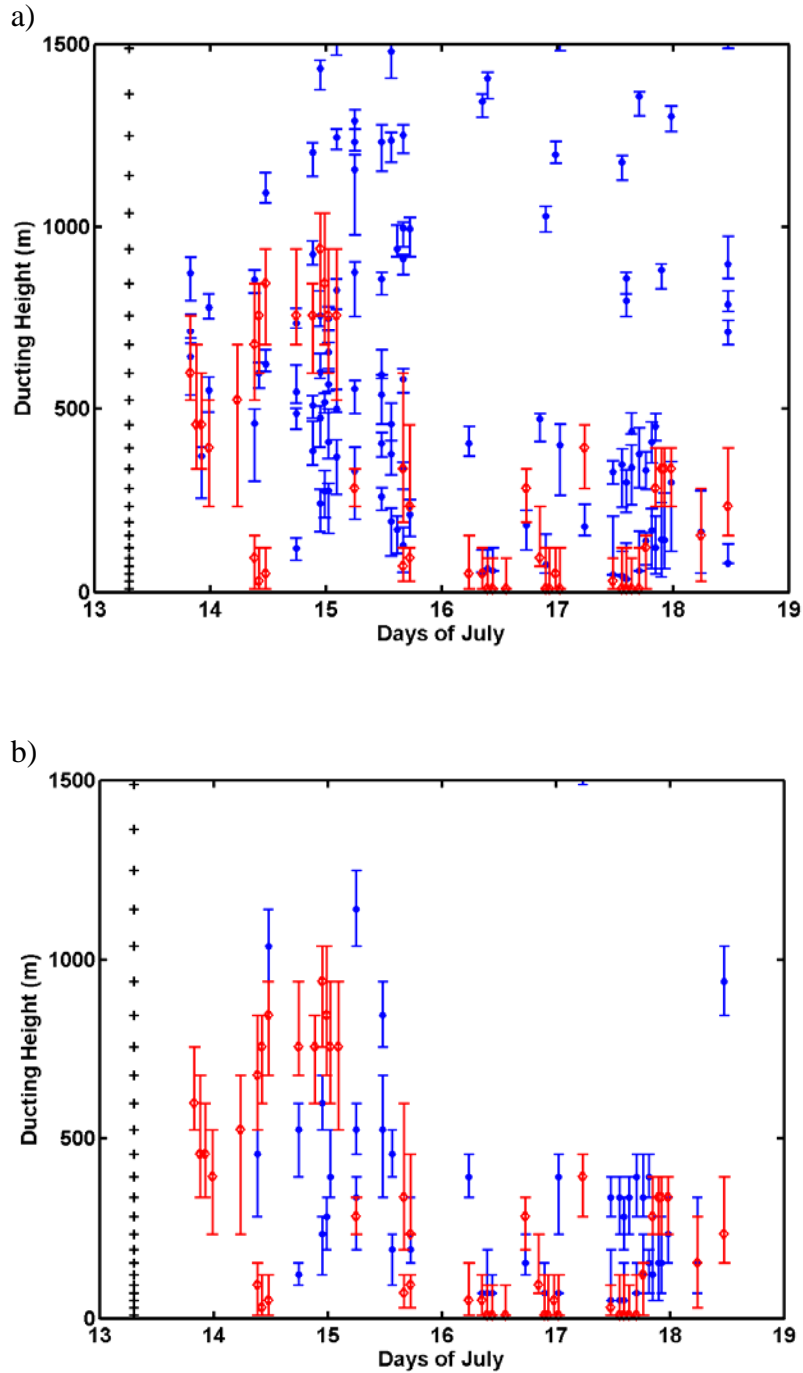
Figure 46.   Comparison of resolved ducts at coincident time and location between sounding (blue) and COAMPS forecast (red) for a) ducting layer identified from original sounding data and b) ducting layers identified from sounding data interpolated onto COAMPS vertical levels. The error bars indicate the duct top and bottom and the asterisks indicate the trapping layer base. The plus marks on the left are COAMPS vertical levels for reference.

110

Sea surface temperature is also compared between COAMPS and ship observation during TW13. Since COAMPS was run in coupled mode with the ocean circulation model, SST updates were available every hour. SST observations were determined to be most reliable using the Scripps Institute of Oceanography bow mounted radiometer since it measured the undisturbed surface in front of the ship and was continuous (Wang, personal communication 2013). The comparison is shown in Figure 47 and the corresponding statistics are given in Table 6. The coastal locations (indicated by a star marker) tended to be cooler and more variable with more error than the offshore locations (indicated by a circle marker). The colors indicate data points on different days; specifically red indicates July 14, green indicates July 17, and blue indicates all the other days. Overall COAMPS tended to have a warm bias in the cooler coastal waters by almost 0.5 K. Also, the absolute error was over 0.8 K in coastal waters and more than 0.4 K in offshore waters. Since the SST is a critical boundary condition for the SCM, these errors may prove to be significantly impacting the stability representation in the boundary layer (especially in consideration of COAMPS having a cold bias in the atmosphere).

2.   COAMPS Derived Forcing and Initial Conditions

Initial and forcing conditions for the SCM were derived from the COAMPS runs that were described in Chapter III. Initial conditions required for the SCM include vertical profiles of potential temperature, specific humidity, pressure, and winds. The forcing conditions, as introduced in Chapter III.E.2, included SST, vertical wind, and horizontal advection (tendency) of temperature, moisture, and momentum. The profiles were calculated at the interpolated location between the grid points that corresponded to the SCM location. In this section we examine the initial and forcing conditions for the July 14 case. The COAMPS run was initialized at 6Z and we use the nest 3 which had 4 km horizontal resolution. The SCM was initialized at 14Z and run for six hours.
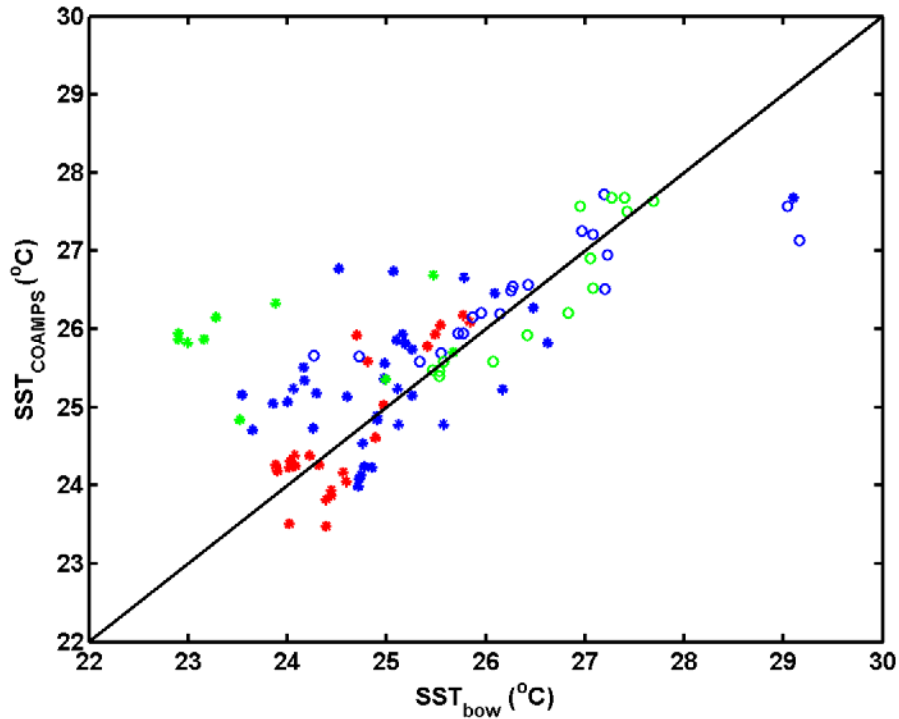
Figure 47. SST comparison of COAMPS and ship observation for TW13. The star markers indicate near-shore and the circle markers indicate off-shore locations. Red is data from July 14, green is July 17, and blue indicates the other days.

Date	All TW13 days		7/14/2013		7/17/2013	
Location	Coastal	Offshore	Coastal	Offshore	Coastal	Offshore
Mean	0.47	-0.01	0.06	-	1.98	-0.08
Std	1.02	0.62	0.5	-	1.15	0.37
Abolute Error	0.82	0.42	0.42	-	1.98	0.28

Table 6. Statistical comparison of SST between COAMPS and ship observation for TW13. The mean is for SST_{COAMPS}-SST_{ship}.

The COAMPS wind speed field is plotted in Figure 48 at 10 and 283 m heights and indicates southeasterly and onshore flow. Near the surface at 10 meters there is clearly two separate regimes indicated with moderate winds over the destabilizing warmer waters to the southeast becoming weaker winds over the cooler waters north and west of the Gulf Stream (see Figure 8 for SST). Localized variability in surface winds is

also noted although generally weak for this case. The apparent correlation with sea surface temperature suggests that stability is important in mixing higher momentum winds to the surface within COAMPS. Aloft winds are greater, generally from the southeast, and vary on a similar scale. Figure 49 shows a vertical profile of the wind speed at 14Z at the coastal location (Point 17 as indicated by the white triangle in Figures 48a through 48f) and indicates gradual increase in wind speed from surface to a low level maximum at 600 m, a local minimum at 950 m, and increasing above. Over the open ocean, surface winds increase by 1 to 2 m s^{-1} during the next 6 hours and winds aloft generally decrease by the same magnitude (not shown).

Potential temperature and specific humidity also show significant horizontal spatial variability. Figure 48 shows the horizontal contour plots of potential temperature at 10 m and 676 m for the July 14 case at 14Z. These figures show a horizontal gradient of up to 1 K per 25 km over water (or about 1 K per 6 grid points). Additionally, Figure 50 shows the potential temperature contour plot at 18Z and the effects of diurnal heating over land has created a very large cross shore gradient. A large temperature difference also exists aloft (not shown) but the gradient is much more diffuse. The horizontal gradient of specific humidity is up to 1 g kg^{-1} per 12 km (or 1 g kg^{-1} per 3 grid points) over water and Figure 50 also indicates a very significant cross shore gradient at the surface. Vertical profiles of potential temperature and specific humidity are shown in Figure 49a at the same near coastal location Point 17. An inversion is evident at about 850 m. Also, the lower boundary layer gradient suggests a stable surface layer as expected over the cooler SST. Figure 51 shows time series of potential temperature, specific humidity, and wind speed profiles. The tendency of the inversion is to decrease gradually throughout the forecast period in addition to the boundary layer undergoing slight warming and drying up to 17Z and then cooling and moistening. The wind speed in the boundary layer reduces 1 to 1.5 m s^{-1} during the 4 hour period before increasing again.

The SST was an evolving parameter through the forecast due to the coupled settings of the model run as described in Chapter III.C. Figure 52 shows the ground temperature (SST for over water) output at two different times during the July 14 case.

Generally, the warmer waters of the Gulf Stream are evident to the southeast and cool coastal counter current waters near shore with a mix of warm and cool eddy features in between. The horizontal variability in these features were on the scale of up to 1 K per 12 km, or about three atmospheric grid points in grid nest 3. This significant variability makes location specification important when extracting the SST for forcing. The time evolution is also evident in Figure 52. Of immediate notice is the significant land surface warming from 14Z (10 a.m. local) to 18Z (2 p.m. local). Additionally, the SST has undergone a diurnal broad scale warming. In this particular July 14 case, the coastal location (Point 17) indicated by the white triangle was situated in the along shore southward coastal counter current which caused a local cold feature and was favorable to provide for a stable surface layer.

Vertical velocity shows horizontal variability on the same scale as the mean variables discussed above. Figure 53a shows the horizontal variability of vertical velocity in the upper boundary layer (676 m) which indicates coupled regions of rising and descending air, some of which appear organized in lines. These over water features produce vertical motion of up to about 40 mm s^{-1} in the upper boundary layer which is equivalent to about 144 m per hour. The contoured vertical profile time series in Figure 53b shows that the transient nature of these features is affecting the hourly profile output in alternating rising and sinking air. It appears, however, that from 14Z to 18Z subsidence is dominating especially below the inversion. The subsidence in the boundary layer ranges from 7 to 35 mm s^{-1} during this period. This subsidence is then followed by rising motion exceeding 20 mm s^{-1} at 19Z.
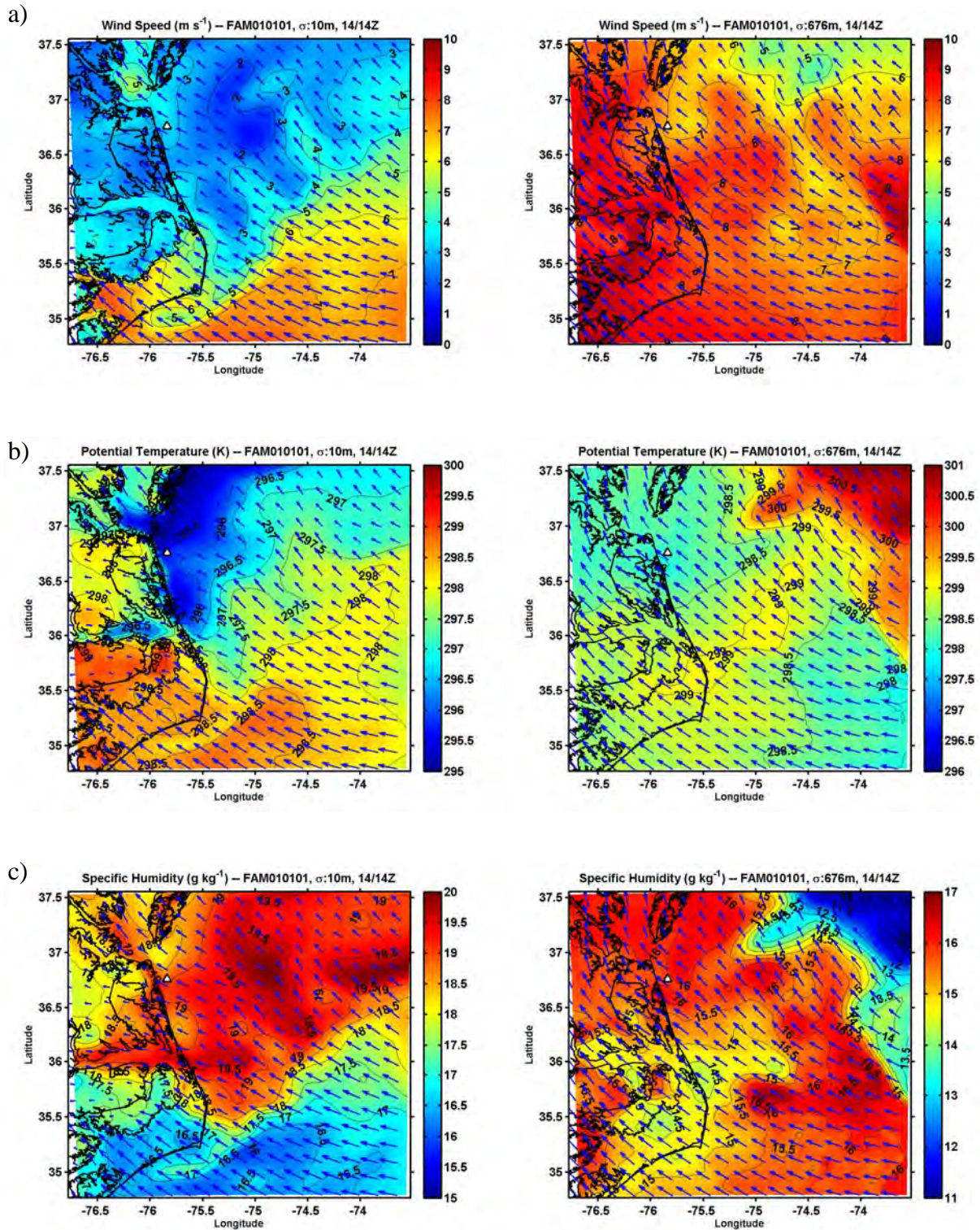
Figure 48.   Horizontal contours of COAMPS nest 3 (4 km resolution) with wind
             vectors for at 10 m (left) and 676 m (right), for a) wind speed, b)
             potential temperature, and c) specific humidity at 14Z (10 a.m.
             local). Point 17 is indicated by the white triangle.

115
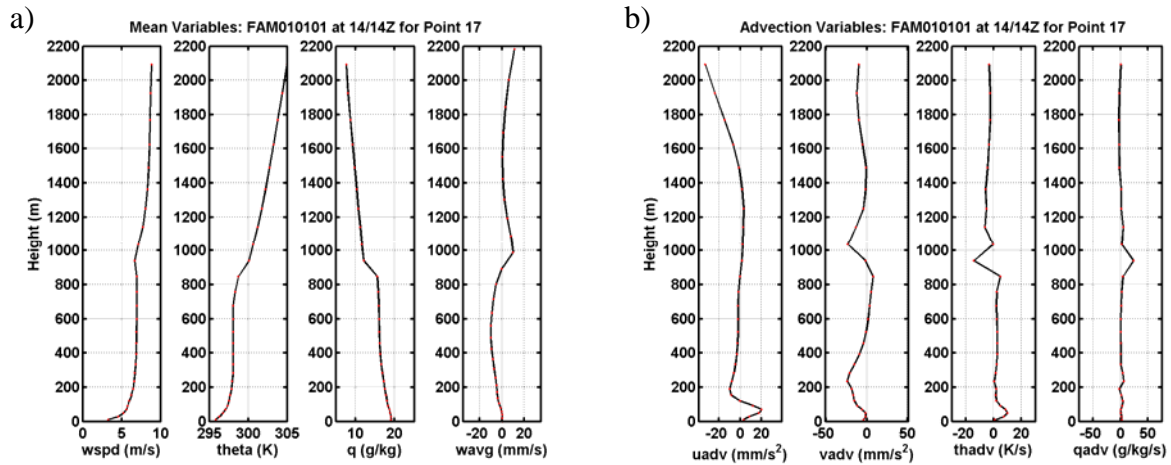
Figure 49. Vertical profiles of COAMPS a) mean variables and b) horizontal advection variables at 14Z for the July 14 case at point 17.
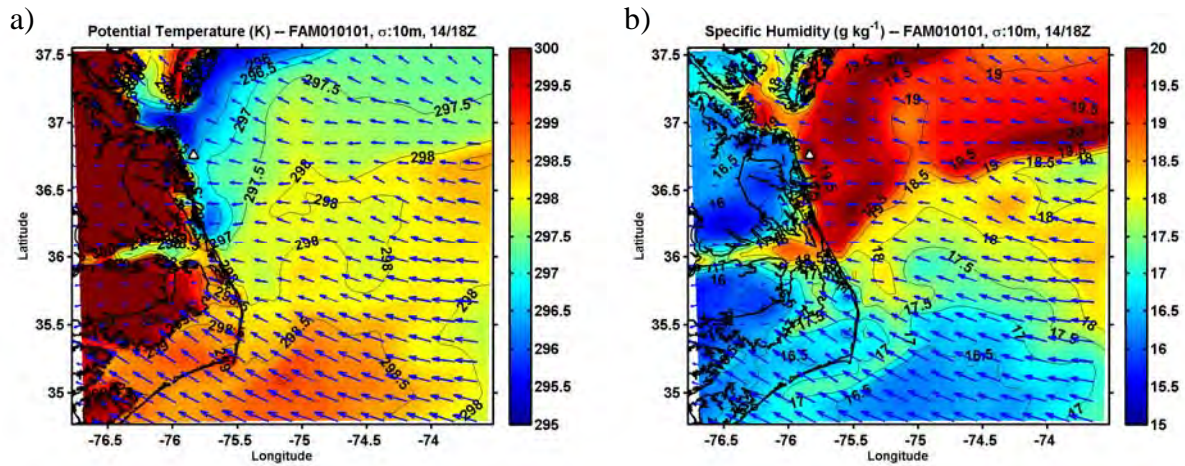
Figure 50. Horizontal contours of COAMPS nest 3 (4 km resolution) with wind vectors at 10 m for a) potential temperature and b) specific humidity at 18Z (2 p.m. local) 4 hours later than Figure 48. Point 17 is indicated by the white triangle.
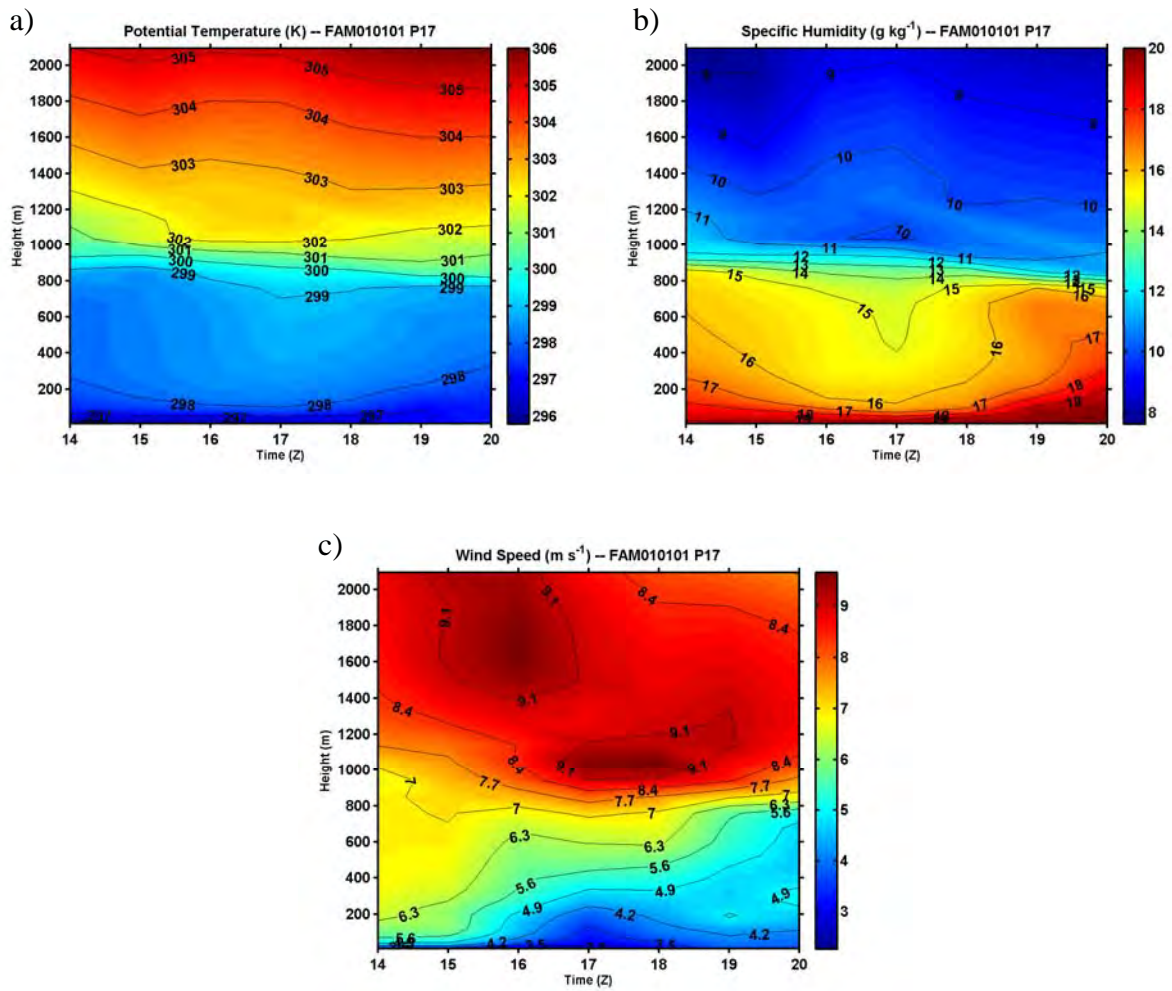
Figure 51.   Contoured time series of the COAMPS derived vertical profiles for
a) potential temperature, b) specific humidity, and c) wind speed.
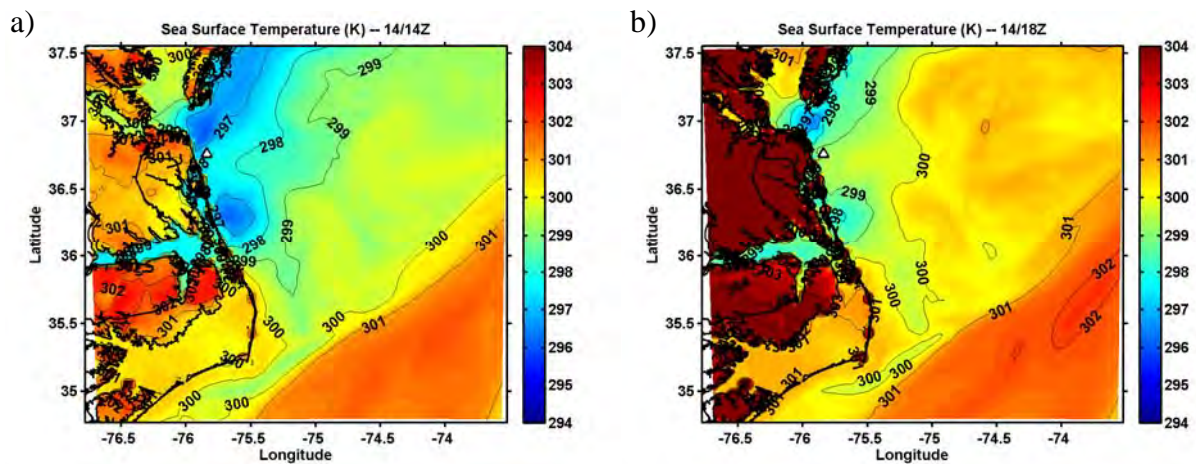
Figure 52.   Contour plots of COAMPS Sea Surface and ground temperature for
the July 14 case at a) 14Z (10 a.m. local) and b) 18Z (1 p.m. local).

117
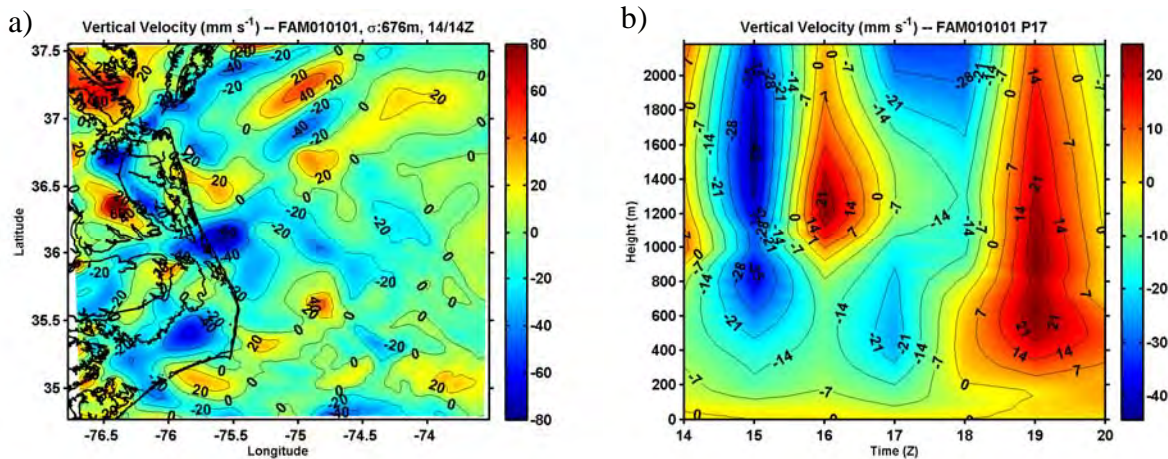
Figure 53.   Vertical velocity a) horizontal contour plot at 14Z and b) contoured time series of vertical velocity profiles. Point 17 is indicated by the white triangle.

Potential temperature advection shows significant horizontal and vertical variability. The horizontal contour plot at the surface in Figure 54a show strong areas of warming and cooling which are sometimes organized in pairs that correspond with the warm and cool features reflected in the potential temperature plot Figure 48b. To clarify, downwind of a relative warm feature is positive potential temperature advection and upwind of the same warm feature is negative potential temperature advection. Over open water, this relationship correlates strongly with the features in the SST field (Figure 52). Most obvious at the surface is the linearly organized warming and cooling pair oriented along and just offshore of the coast corresponding to the cooler SST and surface layer of the coastal counter current. The magnitudes range from -20 to +12 K day^{-1}. Point 17 is incidentally located exactly in the middle of this coastal advection pair. In the upper boundary layer these advection couples are even stronger on average although the very strong near coastal advection pair is not evident.   Aloft the magnitudes range from -30 to +30 k day^{-1}. Contour plots for four hours later (18Z) are shown in Figure 55. At the surface, diurnal heating has expanded the region of significant negative potential temperature advection inland indicative of a sea breeze. Diurnal land heating has warmed the boundary layer and cool air advection is now evident over land aloft as well. A similar variability pattern of advection exists over open water and through a time progression (not shown) these coupled features propagate towards the northwest as

transient advection features. The vertical profile time series in Figure 56a shows significant variations in the vertical for coincident warming and cooling in the same column with up to a 25 K day^{-1} difference near the inversion level. Vertical potential temperature advection (not shown) advected the column vertically as expected so that when there was subsidence, there was significant warming especially at the inversion. Rising air had the opposite effect.

a)

b)
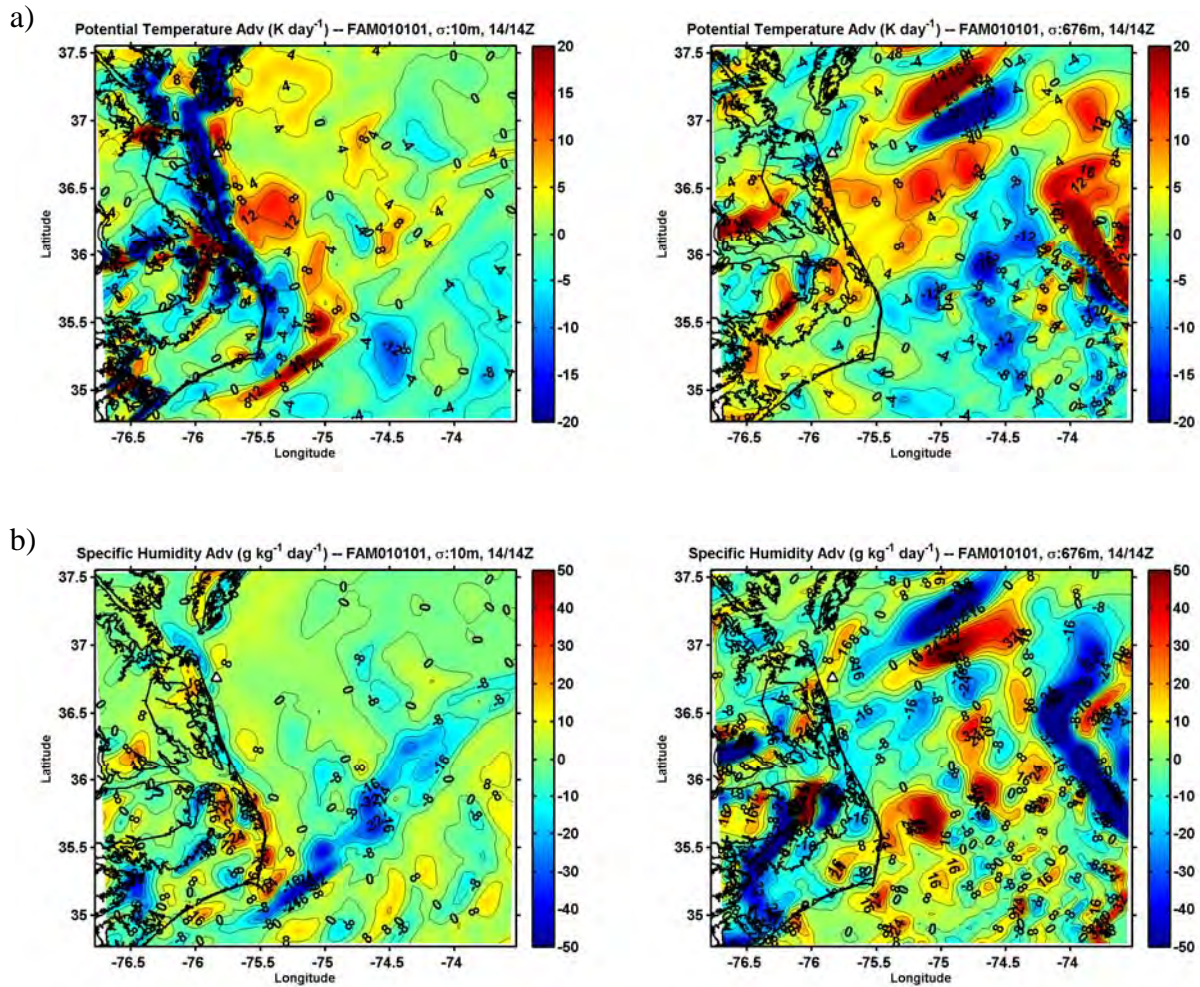
Figure 54.   Horizontal contours at 10 m and 676 m height for a) potential temperature advection and b) specific humidity advection. Point 17 is indicated by the white triangle.

Specific humidity advection also shows significant horizontal and vertical variability. Figure 54b shows the horizontal variability which largely resembles the

119

inverse of the potential temperature advection plots with the exception of the near coastal surface feature in vicinity of point 17. However, four hours later (Figure 55b) the surface moisture advection feature is strong in vicinity of point 17 on the lee side of the cold current and extending inland. The aloft plot shows transient features similar to the potential temperature plot but with opposite sign. Comparison with column cloud water content (not shown) indicates that these cool moist features are the result of convective precipitation which leads to moistening and evaporative cooling under the cloud. The vertical profile time series plot (Figure 56b) also shows significant vertical variability that resembles the inverse of the potential temperature plot. Differential advection at adjacent levels is on the order of 35 g kg^{-1} day^{-1} near the inversion.

Horizontal momentum advection shows similar horizontal (Figure 57) and vertical (Figure 56) variability. Over open water, the advection pattern resembles the scale and speed of the transient features mentioned previously. The difference in magnitude between adjacent advection values exceeds 50 m s^{-1} day^{-1} at the surface and up to 80 m s^{-1} day^{-1} aloft. Additionally, the momentum advection pattern near shore clearly indicates acceleration which substantiates the sea breeze. Additionally, the aloft u momentum plot (not shown) indicates a deceleration in the coastal zone further substantiating the superimposed secondary circulation.
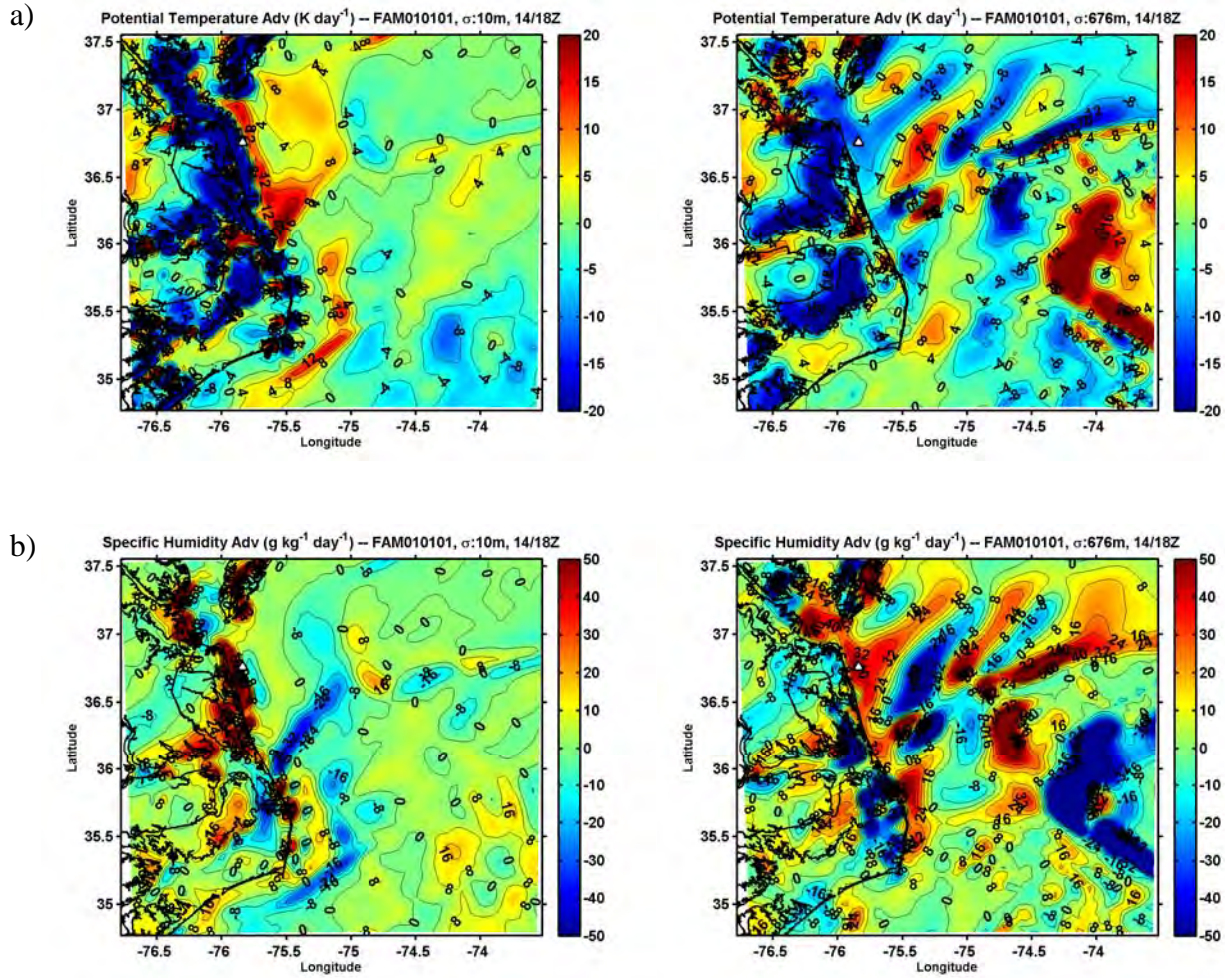
Figure 55.   Same as Figure 54 except 4 hours later at 18Z.
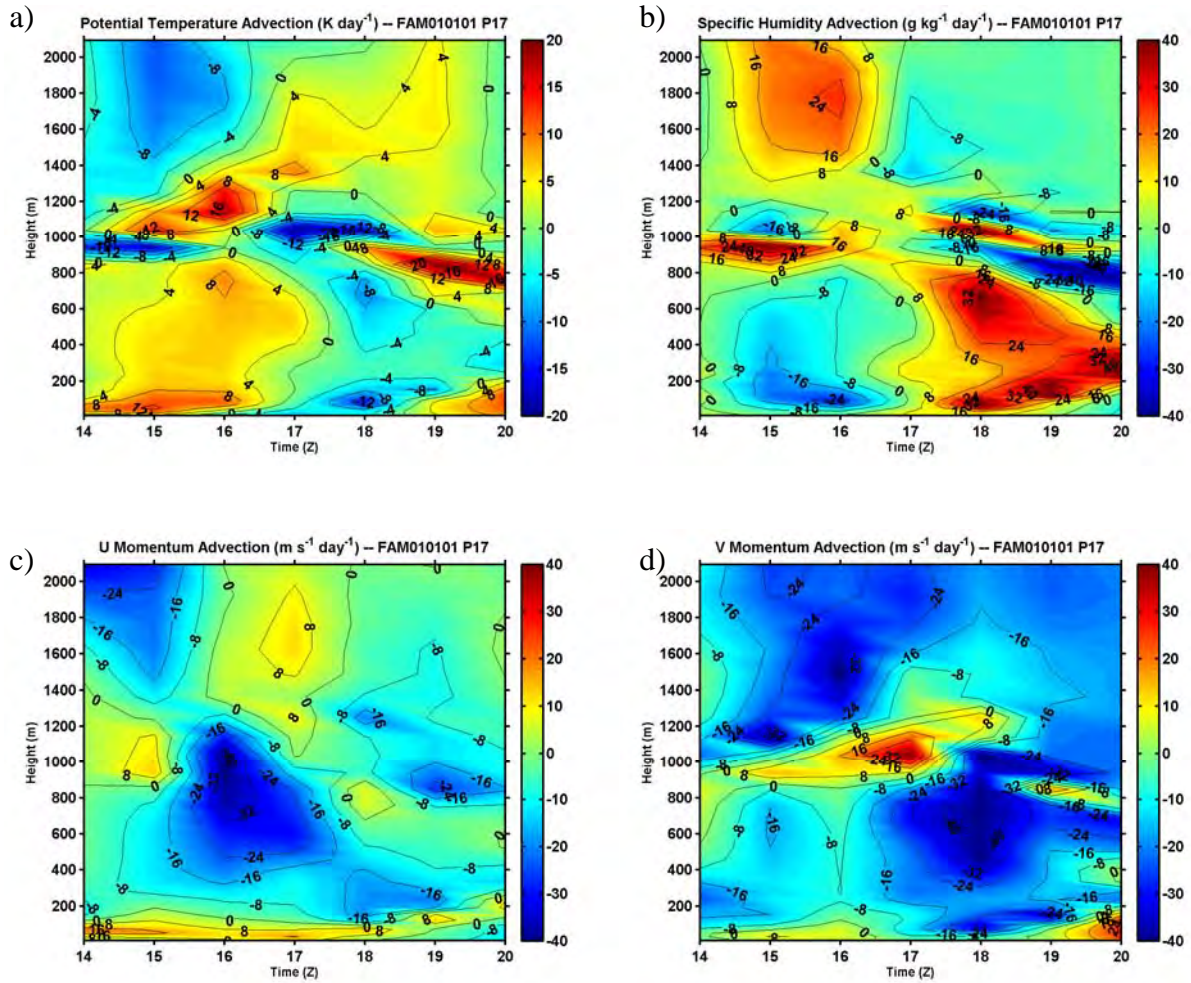
Figure 56. Contoured time series profiles of advection of a) potential temperature, b) specific humidity, c) u and d) v momentum.
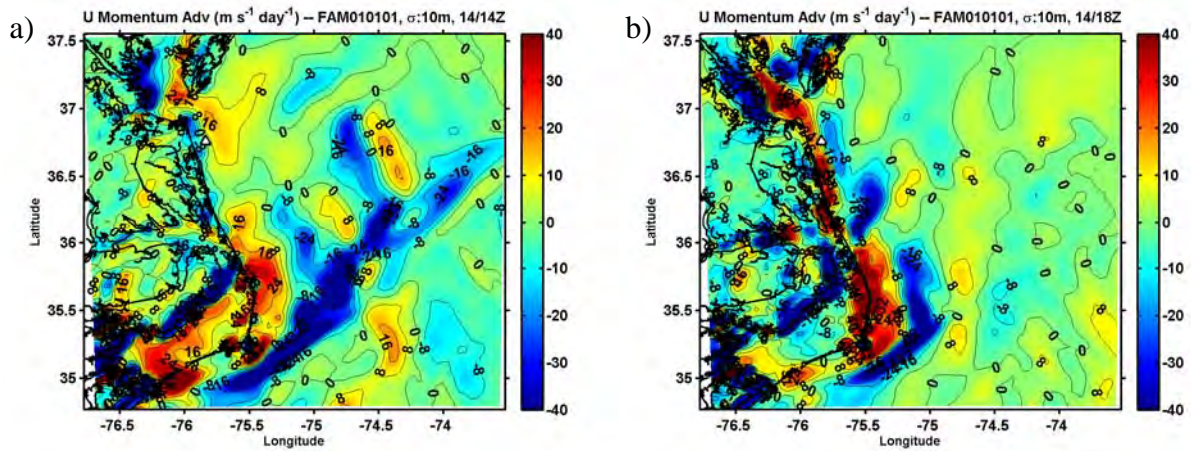
Figure 57. Horizontal contours of u momentum advection at 10 m at a) 14Z and b) 18Z. Point 17 is indicated by the white triangle.

3. SCM Simulation Using Idealized Forcing

The complexity of the forcing as described in the previous section prompts the development of an idealized forcing profile for testing the SCM and establishing a baseline for comparison of results and expectations in these TW13 cases. Idealized forcings are derived from the 3-D COAMPS output, but are highly simplified to remove small vertical variations while retaining the "big" picture. We present two cases of which idealized forcing was applied to the SCM. The time and location of these two cases are determined by the time and location of corresponding measurements from TW13.

a. July 14 Case

The first case is initialized using interpolated output from the COAMPS 14/06Z run at 15Z (tau = 9 hours), which is 11 a.m. local time at a near coastal location (Point 17) described in the preceding section. This point corresponds to the drifting buoy location and the location where a synoptic sounding was launched at 18Z. The general synopsis is a 1028 mb high situated off the coast to the northeast providing benign weather with some cloud bands propagating northwest, some cirrus and light onshore winds from the southeast. The idealized forcing was generated to roughly resemble the COAMPS forcing from 15Z to 18Z with the intent of comparing the 3 hour SCM forecast with the synoptic sounding. The idealized forcing is shown in Figure 58. It essentially represents slight column warming and drying under subsidence with the exception of the near surface which indicates cool and moist advection. COAMPS indicates this near surface advection to start at about 16Z (Figure 56). The subsidence rate was taken as a rough column average of -16 mm s^{-1} which linearly decreases from 600 m to the surface. The SST was fixed at 299 K obtained from buoy measurements at 18Z at Point 17. The SST was varied by ±0.5 K to examine the effect within the measurement and variability error range as described previously.
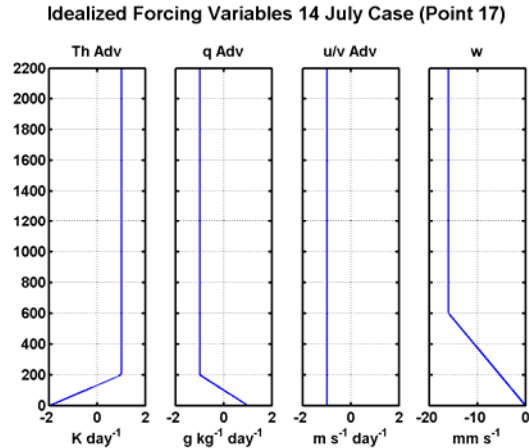
Figure 58.   Profiles of idealized forcing used for SCM July 14 case at point 17.

The initial evaluation of the approach was made using the forecast from the SCM 200 configuration. The initial conditions and three hour forecast is compared to both COAMPS and the nearly coincident 18Z sounding in Figure 59. The blue line represents the sounding recorded at 1750Z on July 14. The pink marker on the horizontal axis of the potential temperature plot is the actual SST (not corrected for pressure) for the COAMPS run (displayed as pink). The SST for the SCM run is set at 299.5K for this particular simulation. At initialization, the SCM and COAMPS profiles overlap each other. A stable surface layer with a residual mixed layer above starting at 200 m is seen in the initial temperature profile. The inversion is at about 820 m and is strong indicating the effects of recent subsidence. Above the inversion, COAMPS extends to a profile above that largely matches the synoptic sounding at 18Z fairly well with the obvious small scale variability and some minor layer discrepancies (not shown). Thus, COAMPS is performing well in representing the large scale synoptic pattern as indicated by observation. The M profile at initialization shows a 170 m thick elevated duct as a result of the strong inversion and a 116 m thick surface duct as a result of the strong temperature and humidity gradient of the near surface layer.

The three hour forecast is compared to the coincident COAMPS solution and the synoptic sounding (Figure 59). The COAMPS model evolved to roughly match the synoptic sounding especially above the inversion level. This again shows that COAMPS is representing the large scale effects well. The subsidence has pushed the inversion down

to about 620 m for the SCM and about 750 m for COAMPS. Neither the SCM nor the COAMPS subsided enough to match the inversion height represented by the sounding and there may be several reasons that contributed to this discrepancy. The COAMPS solution at SCM initialization may have incorrectly resolved the inversion too high as well as the rate of subsidence too low. Also, the sounding may be showing a local variability which is expected especially in the coastal regime. Both the SCM and COAMPS roughly match the sounding inversion gradient of potential temperature, although the depth of the inversion layer is thicker than observed. The specific humidity gradient at the inversion is slightly stronger for COAMPS which appears to match the sounding. The residual layer remains fairly neutral for the SCM but the COAMPS shows some stability. Also, the COAMPS specific humidity shows an increase in moisture just below the inversion that is not present in the SCM result or in the sounding profile. However, there is a spike in moisture at the corresponding sounding level above the inversion, so COAMPS may be capturing a real moist level advection (Figure 56b) but due to the inaccuracy of the represented inversion, it is advecting the moisture below inversion level. Regardless, these inversion and residual layer differences between COAMPS and SCM are due to the absence of different vertical velocity and horizontal advection forcing applied to each model. The M profile indicates an elevated duct as a result of the inversion temperature and humidity gradients.

Nearer to the surface, the 17:50Z sounding shows an inversion at about 120 m and what is likely a shallow mixed layer below. In the model runs, the surface and boundary layer has destabilized in both the COAMPS and SCM. The SCM actually matches the boundary layer top from the sounding in both height and gradient of potential temperature. COAMPS matches the height of the mixed layer depth in the following hour (not shown). This delay in COAMPS is likely due to the COAMPS SST starting at 15 Z at 298 K and warming until 18 Z whereas the SCM SST was set to 295.5 K and persistent throughout the three hour simulation. Or, more appropriately, the acceleration in the SCM to match the representation of the mixed layer is due to persistent warm surface forcing. Another reason that the SCM may have mixed the layer earlier and deeper than the COAMPS is due to the shear generated turbulence at and below the inversion. It will

be shown later in Figure 62 that the wind speed and turbulence for the SCM 200 run indicates there is an increase in wind speed across the inversion. COAMPS shows much weaker gradient in wind speed across this inversion. The sounding actually shows a low level jet at the inversion top and COAMPS resembles that jet in the next hour (not shown). Therefore, the stronger shear in the SCM combined with the persistent warmer surface forcing may have destabilized the lower boundary layer earlier in the SCM than in COAMPS. The remainder of the profile evolves primarily as a result of the forcing (i.e., advection and subsidence). Both models indicate too much moisture in the lower boundary layer which is more apparent in COAMPS. This is likely another result of the stronger turbulence in the SCM mixing down drier air.   The resulting M profile therefore indicates a surface based duct for COAMPS, but an elevated duct for the SCM. The sounding indicates an elevated duct that is weaker than the SCM.

The comparison of the lowest 100 m is shown in Figure 60. The SCM wind profile resembles a logarithmic profile as expected. The potential temperature and specific humidity profiles shows strong gradients in the lowest 10 m above the surface. These surface layer profiles provide confidence that the high resolution surface model is behaving appropriately in resolving the surface layer and yet, importantly, it has a physical connection to the rest of the atmospheric profile. As a result of the resolved surface layer gradient of temperature and humidity, the M profile indicates an evaporative duct. This feature will be examined closer in a later section. The 3-D COAMPS is, of course, limited to its lowest level at 10 m and is incapable of resolving the evaporative duct. Because the sounding was made from the ship, the lowest 50 m of the sounding was removed to avoid misleading representation of the surface layer using the ship-affected sounding profile. Note the differences among the three profiles are highly exaggerated in this figure by using small horizontal axis range in order to highlight the resolved evaporative duct layer in the high resolution SCM simulation.

126

a)
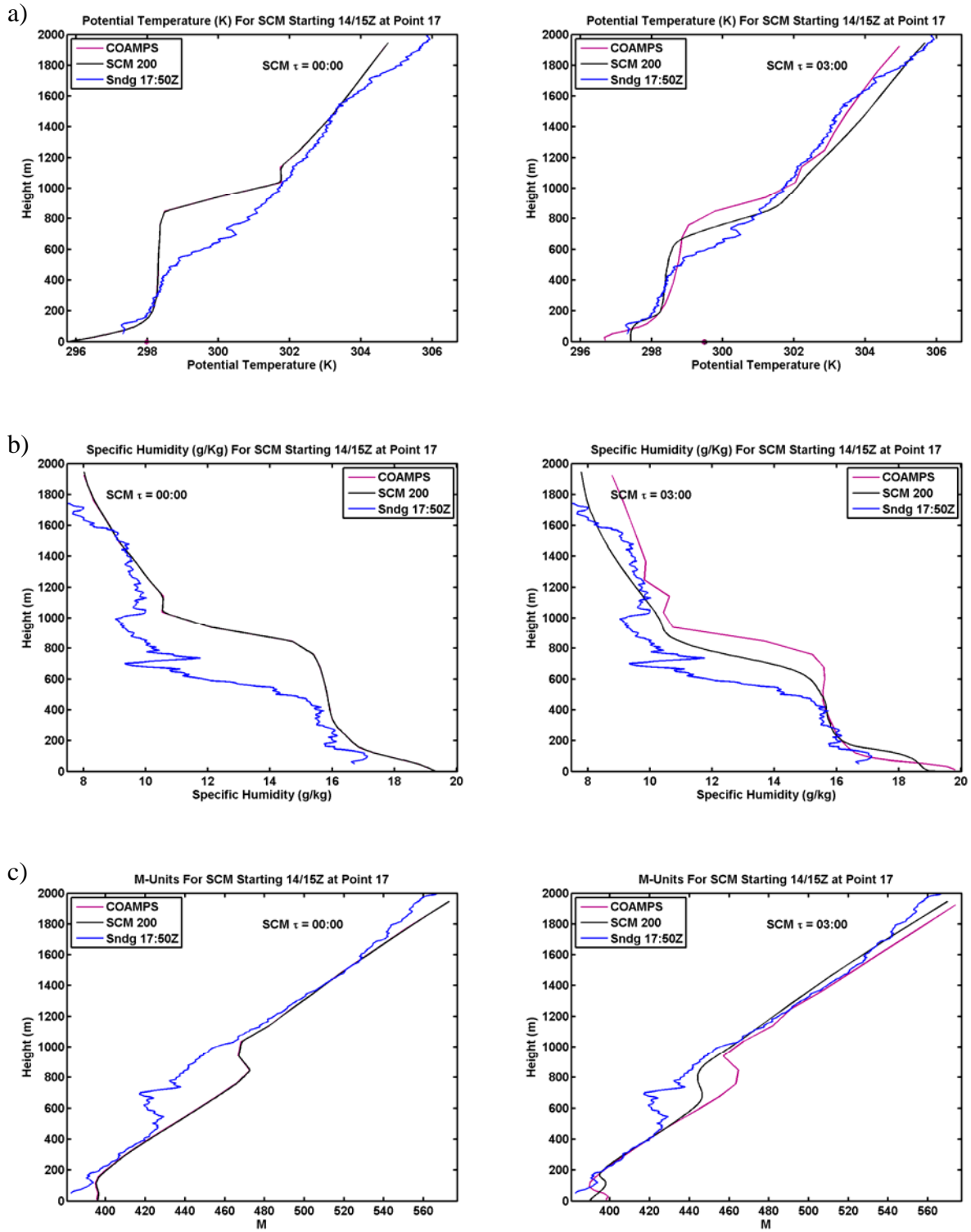
Figure 59.   Comparison of SCM results to COAMPS and rawinsonde sounding
             for idealized forcing at point 17 at SCM initialization (tau=0) and
             SCM 3 hour forecast (tau=3 hours) for a) potential temperature, b)
             specific humidity, and c) modified refractivity.

127
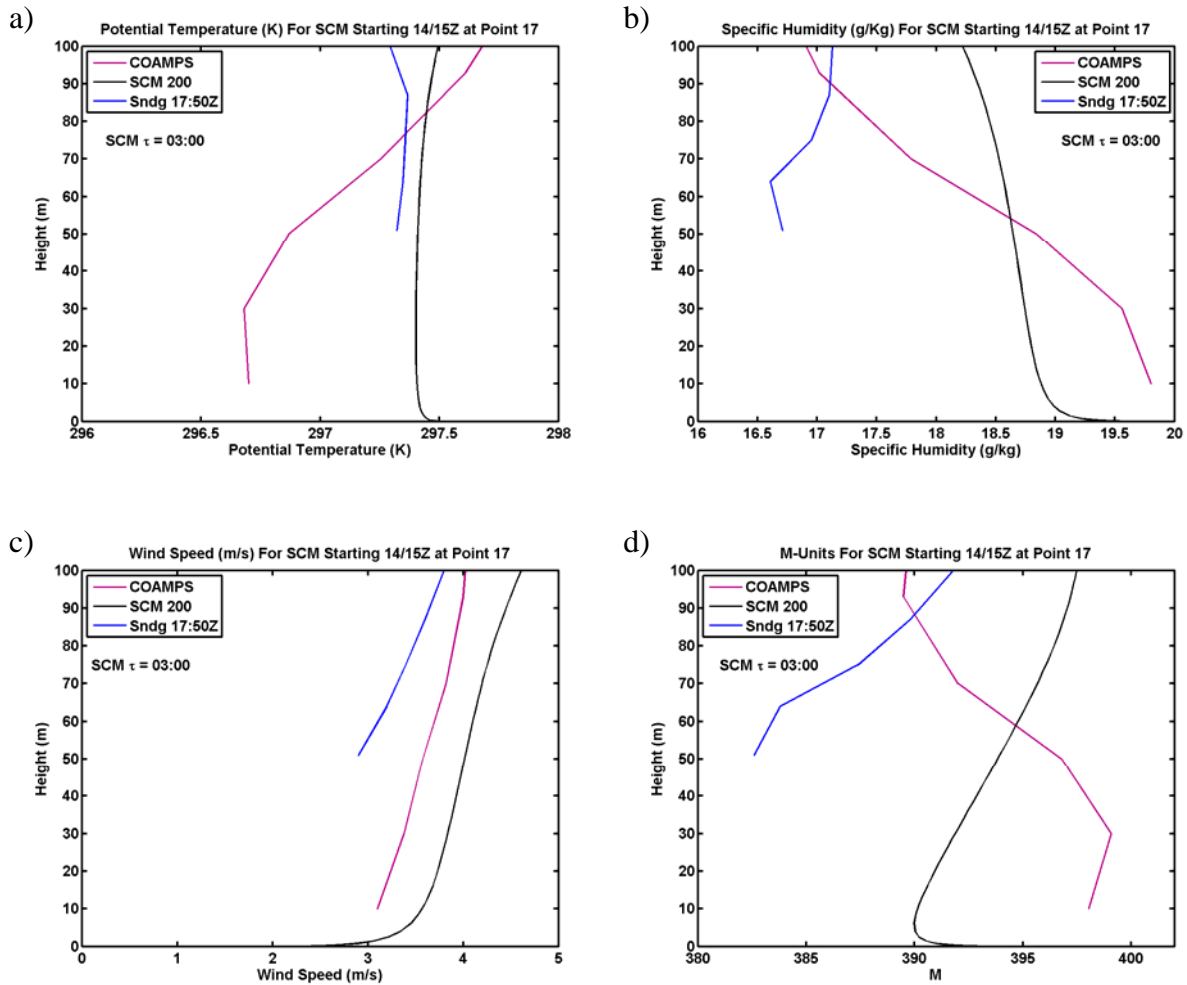
Figure 60.   Comparison of lowest 100 m of SCM 3-hour forecast to COAMPS
and sounding profiles for idealized forcing at point 17 for a)
potential temperature, b) specific humidity, c) wind speed, and d)
modified refractivity. SST was set at 299.5K.

The adjustment period of the SCM from initial conditions to a pseudo-steady state
was very fast. COAMPS needs on the order of 6 hours to make such an adjustment due to
the large domain and time scales of the dynamic processes involved. The SCM adjusts in
the surface layer on the order of 15 minutes due to the model focusing on the small scale
physical processes.

The simulation was made again using the different setting of vertical resolutions
as described in Table 4. Figure 61a shows the initialization for the potential temperature
profiles for all the SCM models. The differences at the inversion levels among

simulations from four resolution schemes are caused by interpolation of the coarser resolution COAMPS results onto the SCM grids. Three hours later, Figure 61b shows that higher resolution models indicate a much stronger gradient between 650 and 800 m compared to the lower resolution models, indicating a clear advantage to higher resolution representation of strong gradient layers. The specific humidity plot (not shown) resembles similar differences in the gradients and the effects on the M-profiles are apparent in Figure 61e. These effects are significant enough that the lower resolution SCM runs do not even indicate an elevated duct on Figure 61e. Some minor dispersion is also noted in the potential temperature gradient just above the boundary layer at 200 m (insert of Figure 61b) where the profiles of the lower resolution SCMs had the gradient smoothed. This is also evident in the specific humidity plot (not shown). The 60 level SCM shows the highest inversion and weakest gradient, followed by the 96 level SCM, and the other two SCMs compare very closely. The zoomed-in specific humidity and wind speed plots (Figures 61c and 61d) in the boundary layer also show some differences between the different resolution SCMs. These differences may be caused in part by the difference in TKE as shown in Figure 62b. Generally speaking, the lower resolution indicates stronger TKE. While these differences appear minor in these plots, when these profiles are used to calculate M, a potentially significant profile difference results as shown in Figure 61e and 61f. The Figure 61e insert shows an elevated duct with about half the M deficit for the SCM 60 compared to the higher resolution SCMs. Additionally, there is dispersion in the surface layer at the 10 m level which, when connected to the M value at the surface assuming saturation at the same SST, significantly changes the evaporative duct strength and potentially the duct height as well (Figure 61f).
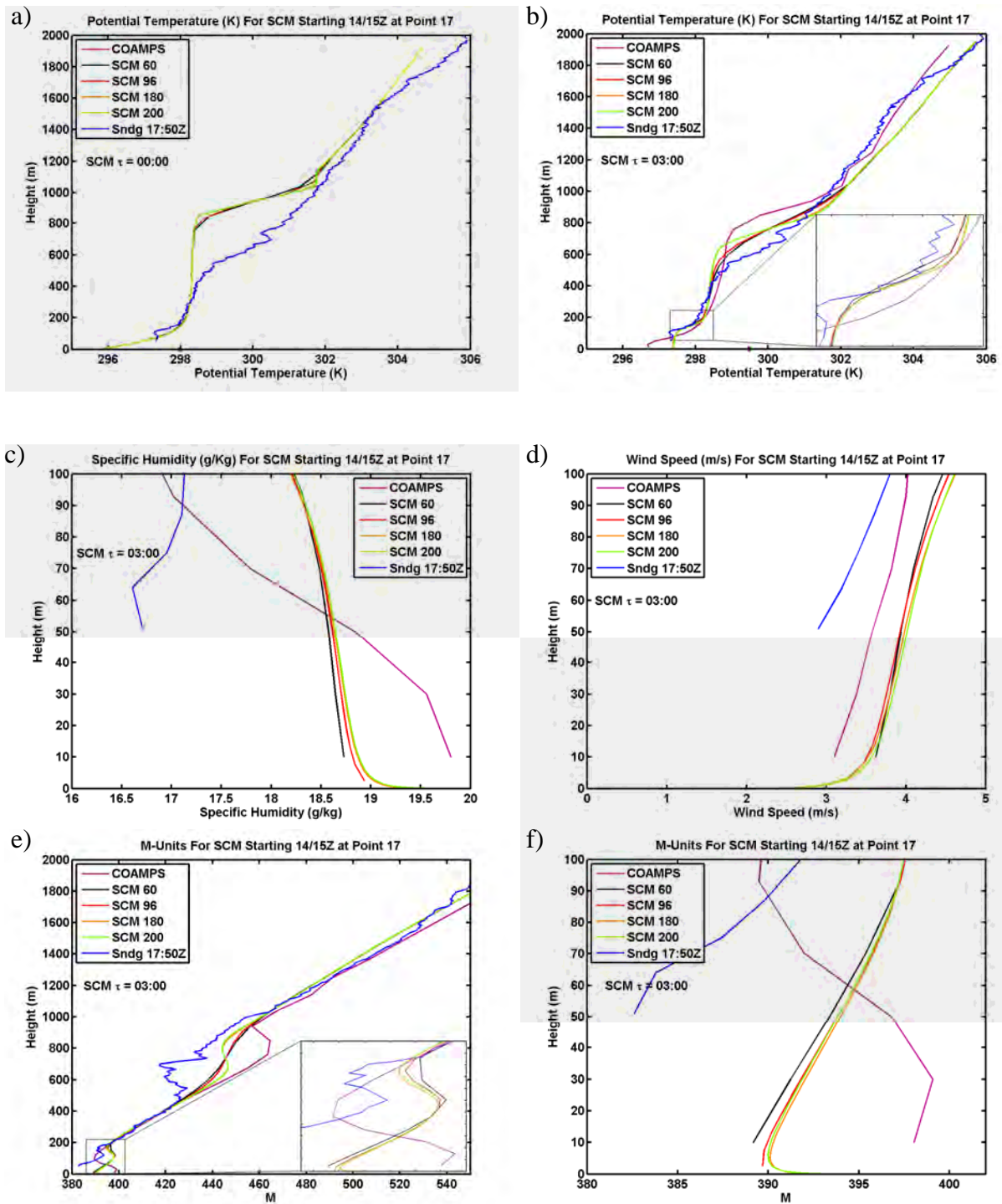
Figure 61.   SCM results for different vertical resolutions using the same idealized forcing. a) initial potential temperature, b) forecast potential temperature, c) forecast specific humidity, d) forecast wind speed, and e) and f) forecast M-units. SST was set at 299.5K. All forecast profiles are from tau=3 hour. Note panels c, d, and f have zoomed-in vertical axes to the lowest 100 m.
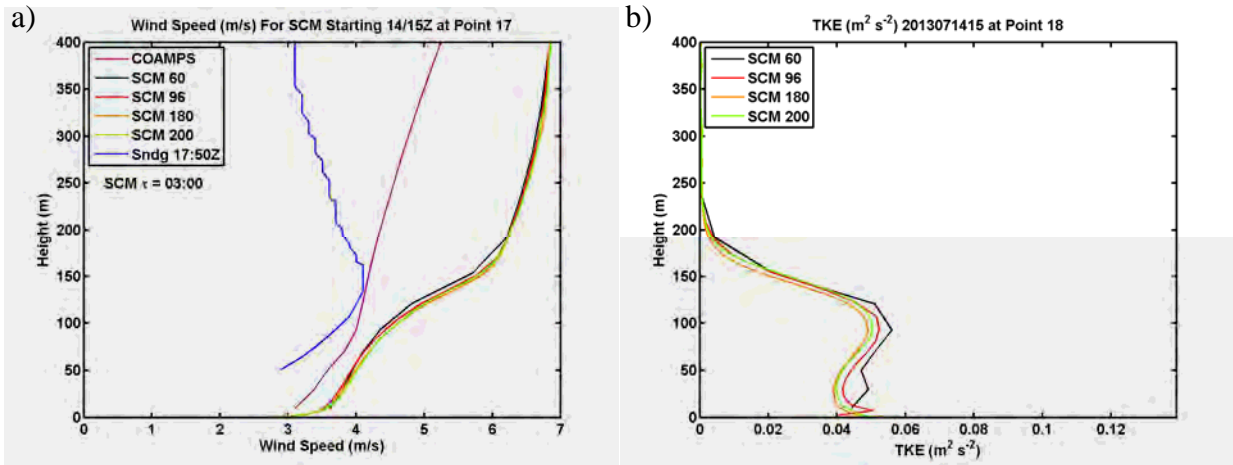
Figure 62.   Same as Figure 61 except for a) wind speed and b) TKE.

The simulation with this idealized forcing was also run with the modified eddy diffusivity (K) scheme as described in Chapter III. A comparison of the SCM 60 and SCM 200 with using the modified ("new K") and the original ("old K") eddy diffusivity is shown in Figure 63. Only results from below 400 m are shown because the difference between simulations with the original and modified K diminishes above 400 m. It is evident in this case that the modified K runs show a slightly warmer and drier boundary layer and weakens the gradient at the inversion and moisture lapse. Additionally, there is slightly stronger wind shear in the lowest 10 m of the surface layer in the SCM 200 simulations. The M profiles indicate that the SCM 200 run with modified eddy diffusivity results in a deeper evaporative duct layer with stronger duct strength.
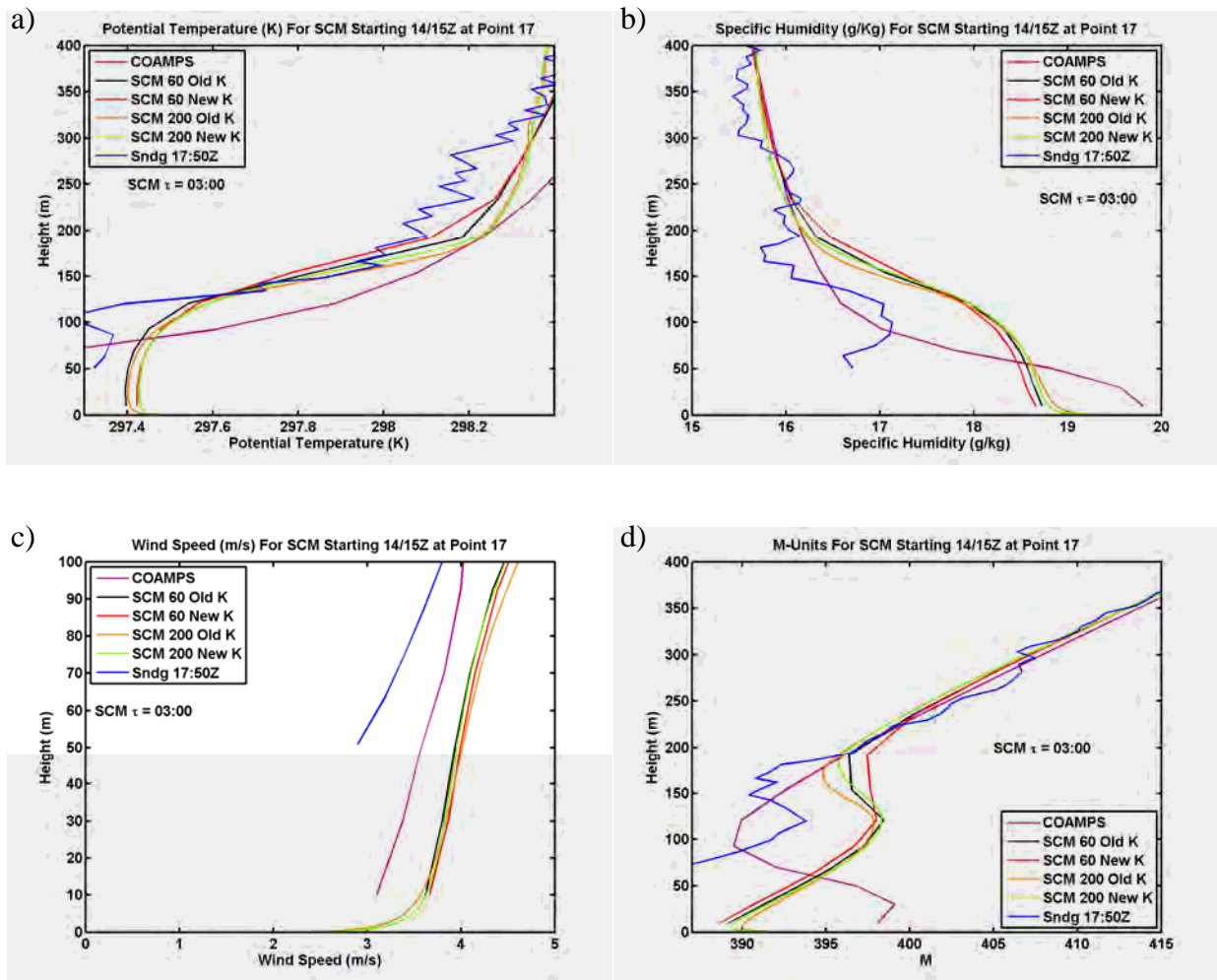
Figure 63.   Comparison of SCM simulations using original ("old K") and modified ("new K") eddy diffusivity. Results for SCM60 and SCM 200 are shown here. a) potential temperature, b) specific humidity, c) wind speed, and d) modified refractivity. All results are from three hour forecast. SST was set at 299.5 K for all simulations.

Given the uncertainties in the measured and forecasted SST, the simulations were made again with same forcing and initial conditions, except for a lower SST of 298.5 K. The three hour forecast results are shown in Figure 64 to illustrate the sensitivity of the simulations to choice of the SST. In this case, the cooler SST has failed to create a mixed layer as the boundary layer remains stable. There are more water vapor and stronger wind at lower levels, possibly due to the reduced entrainment and downward transport of dry air and momentum. Additionally, the inversion gradient is slightly weaker in simulations with the cooler SST. The change in SST resulted in significant variations in the ducting

layer seen in the M profiles. With the cooler SST, the elevated duct (nearly a surface based duct) layer is approximately 50 m lower than the warm SST run. The evaporative ducts in the SCM 200 runs show a weaker and shallower evaporative duct with cooler SST.
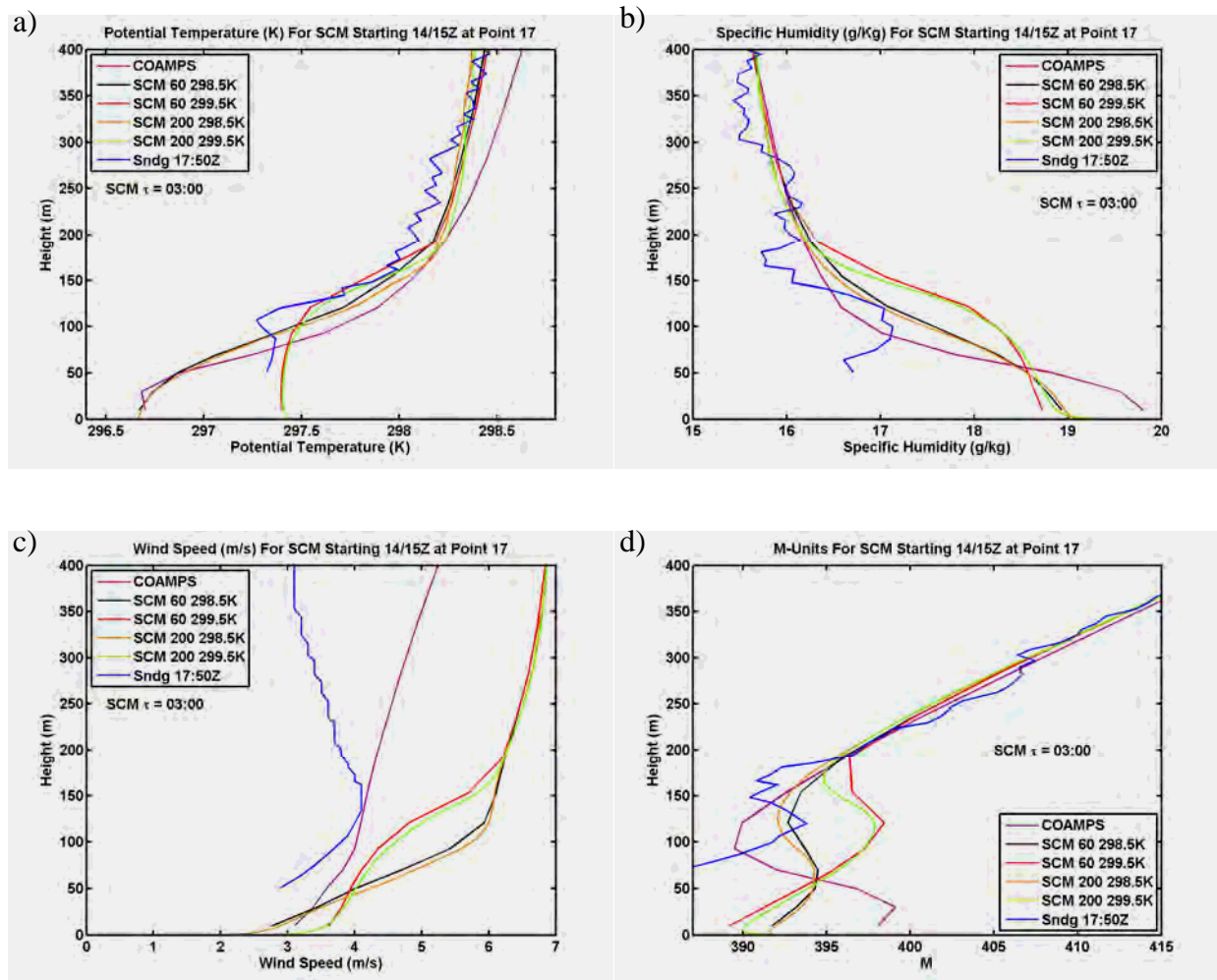
Figure 64.   Comparison of SCM profiles at different SST values. Results from SCM 60 and SCM 200 are shown. a) potential temperature, b) specific humidity, c) wind speed, and d) modified refractivity.

Overall, the results from the high resolution SCM simulations using idealized forcing are encouraging in resolving the elevated ducting layers and evaporative duct. Furthermore, the modified eddy diffusivity to better follow the MOST seems to make a difference in near-surface mixing and hence the evaporative duct properties. The SCM

results is proven to be rather sensitive to small changes in SST, which points out the importance of obtaining accurate SST from measurements or coupled model simulations. Using reasonable profiles of forcing with a reasonable SST, the model evolved similar to full 3-D COAMPS and resulted in a profile similar to what was observed.

b. *July 17 Case*

This second case study is initialized using the COAMPS 17/06Z run at 17Z (tau=11 hours) which is 1 p.m. local time at an open ocean location. This point (point 22) corresponds to the location of the R/V Knorr on July 17 where hourly consecutive balloon soundings were launched. The SST used was the average COAMPS SST during the forecast interval which was 300.5 K. The general synopsis was a 1027 mb high over the Mississippi River Valley and a weak trough south and east of the area of interest. Clear skies prevailed under light northeasterly winds. The idealized forcing was based on the 5 grid point (20 km) averaging of the COAMPS forcing parameters and the result is shown in Figure 65. It essentially represents slight warming and moistening of the boundary layer under weak subsidence with the addition of a cold and moisture advection in the layer between 800 and 1800 1800 m.
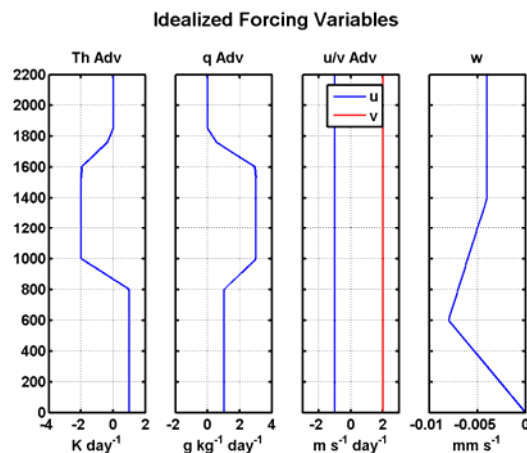
Figure 65.   Profile of idealized forcing used for SCM July 14 case at point 22.

The comparison between COAMPS, the SCM 200 run, and two sounding profiles is shown in Figure 66. The blue and teal lines represent the soundings recorded at 1824Z and 1937Z, respectively. The markers at the surface is the actual SST (not corrected for pressure) which was set at 300.5K for the SCM run (black), and varied for COAMPS (pink). The potential temperature plots shows COAMPS has a weakly stratified shallow mixed layer of about 150 m deep at initialization. This layer becomes well mixed and slightly deeper through the forecast. The soundings show a slightly deeper mixed layer capped by a deep and strong inversion up to about 700 m. A near neutral layer is observed from 700 to 1100 m. This vertical stratification structure is generally resembled by the COAMPS and SCM three hour forecast, however the SCM represents the near neutral layer better while COAMPS maintains some stratification. The TKE plot shows some turbulence between 700 and 1000 m which indicates this layer had destabilized and turbulent. Inspection of the specific humidity profile also indicates a moist layer between 900 and 1400 m. The initial COAMPS profile only weakly represents this feature and shows too much moisture between this moist layer and the boundary layer. During the forecast, the advection of the moist layer and subsidence act to increase the humidity gradients near 900 m and 1400 m for the SCM and 1400 m for COAMPS, but generally these gradients are underrepresented in all plots including the M profiles. Additionally, just above the boundary layer there is another thin but strong moist layer in the sounding profiles which is also completely missed by COAMPS and therefore the SCM. Otherwise, the SCM and COAMPS boundary layer representations are relatively close and the remainder of the atmosphere above 2000 m (not shown) also matches very closely.
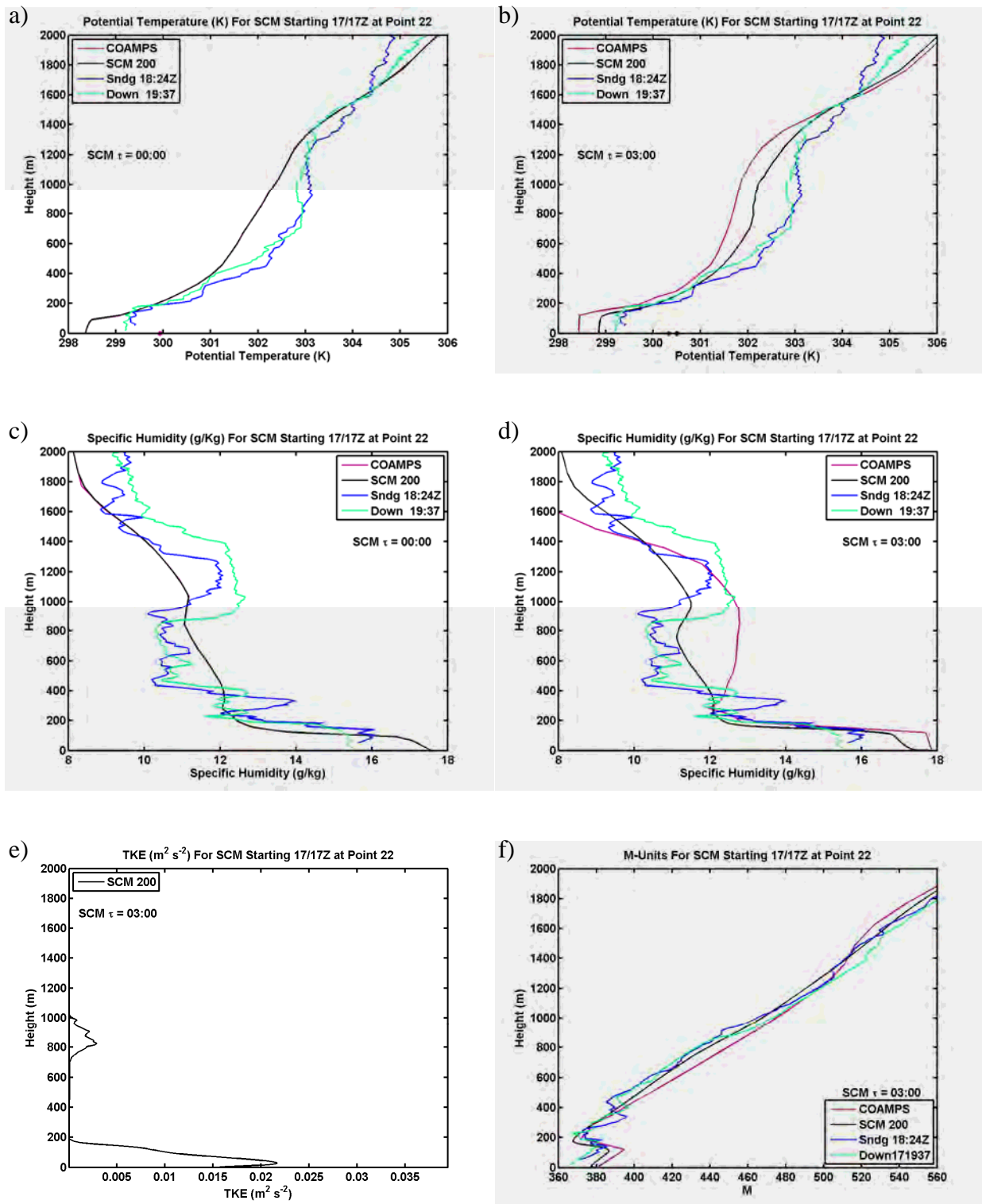
Figure 66. Comparison of SCM 200 idealized forcing results, soundings and COAMPS at point 22. a) and b) are potential temperature at SCM initialization and tau=3 hours, respectively. c) and d) are the same except for specific humidity. e) TKE at tau=3, f) M profile at tau-3.

136

Figure 66 shows that both 3-D COAMPS and the SCM 200 represent the general features of the soundings quite well. Compared to the July 14 case, this July 17 case is different in the following aspects. First, all SCM resolutions had a similar gradient to that of COAMPS. The SCM 60 and SCM 200 runs had comparable moisture content in the boundary layer which was greater than the SCM 96 and SCM 180 whereas in the July 14 case the lower the resolution resulted in lower boundary layer moisture content. All SCM simulations had less moisture in the boundary layer than COAMPS in the July 17 case. Finally, the TKE near the surface does not vary with vertical resolution in the same way as in the July 14 case. Lastly, the M profiles looked very similar at nearly all levels except the surface layer where the higher resolution models provided evaporation duct profiles. This appears to be a case where the SCM approach and higher resolution did not provide significant improvement other than the ability to represent the surface layer and the smooth transitions in gradient change.

4.   SCM Simulations Using Full COAMPS Forcing

The first step to running the SCM with full COAMPS forcing is to provide the forcing conditions. As we saw in Chapter V.B.2, variability is significant in both the horizontal and the vertical directions. Using the FAM as described in Chapter III, we conduct horizontal and vertical averaging over a prescribed area centered at the location of the SCM to smooth the local variations into an averaged forcing over a desired spatial scale. Failure to eliminate large variations in forcing causes extreme variability in the SCM results as the forcing is persistently applied until another update is available. This causes instabilities in the SCM evolution resulting in unrealistic solutions and frequently even model crash.

The averaging scheme is intended to smooth out very small-scale variations and reduce extreme local variations without losing the level of fidelity desired to drive a high resolution SCM. COAMPS output is only available every hour and therefore more frequent updates to the forcing for the SCM is not possible. Operationally, more frequent output is not feasible due to the significant space and time required to write the output files. The direct output from COAMPS represents the modeled results at one instance of

time. Its temporal representativeness is a concern, which may introduce substantial error since the forcing derived from this instantaneous model output field will force the SCM at every SCM time step until another update is available one hour later. The spatial averaging is intended to smooth out the small-scale variations that introduce significant "noise" to the horizontal advection term while retaining advection by significant mesoscale or large scale features.

A consequence of conducting spatial averaging is that strong gradients are reduced. This occurs for two reasons. First, it's obvious that vertical averaging yields a smoother profile. However, horizontal averaging also dilutes vertical gradients in all variables due to the contributions from mesoscale vertical variations of like features. The simplest examples include sloping inversions, gravity waves, fronts, etc. Values from above, in, and below the gradient are contributed to the average by neighboring grid points so that the steeper the slope of the feature, the more vertically diluted the gradient becomes from what was originally represented at a single grid point.

Large amounts of numerical testing were made in this dissertation work to decide on the optimal averaging domain to be used to calculate the initial and forcing conditions. Figure 67 shows a horizontal variation of potential temperature advection calculated without averaging for the July 14 case at 18Z and the July 17 case at 20Z at a height of 336 m. The boxes that are drawn indicate the extent of averaging schemes that use 5, 11, or 25 grid points (20, 44, or 100 km) horizontally centered on the point of interest. The domain needed to be large enough in order to ensure that advecting features in the boundary layer did not pass completely through an averaging domain in between hourly updates. The coastal locations (measurement location on July 14) limits the extent of averaging to less than 5 grid points without contamination of over land values entering the average whereas the offshore locations (measurement location on July 17) allows large averaging domain. Figure 68 shows the vertical profiles of potential temperature advection calculated from COAMPS using no averaging, 5 grid point averaging (20 km), and 11 grid point averaging (44 km). The smoothing effect on the profile is apparent with a direct relationship between number of grid points included in the averaging to the reduction in variability and extreme values through the profile while still maintaining the

significant advection features. However, a closer look reveals that the larger averaging region does reduce the vertical gradient of the forcing as well. Figure 68b shows a close up of the lowest 500 m and the reduction in gradient even at the inversion is clear. Note forcing of a single column model with weak gradients nullifies the advantage that is being sought with the use of the high resolution SCM.
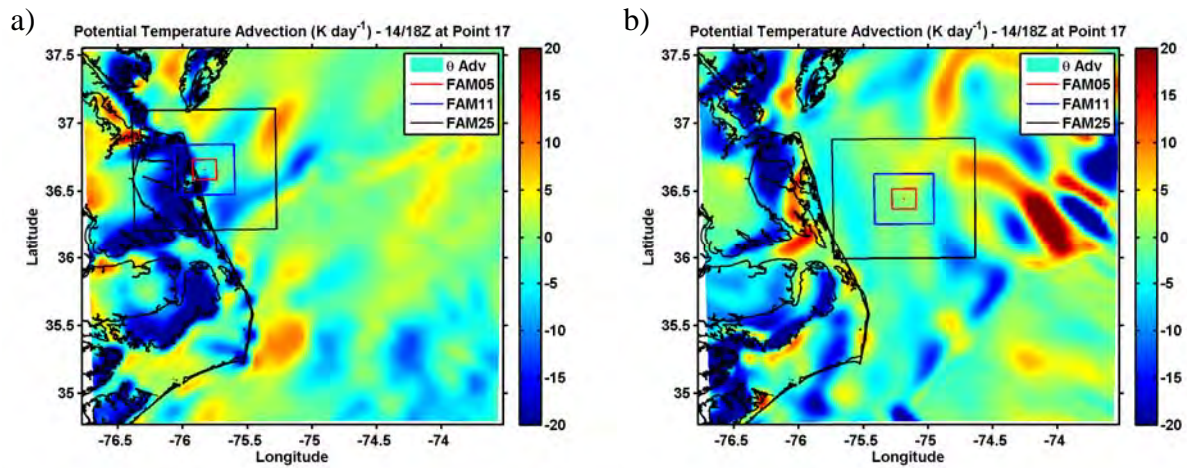
Figure 67.   Potential temperature advection derived from COAMPS at 336 m for a) July 14 at 18Z and b) July 17 at 18Z. The boxes indicate the coverage area using 5, 11, and 25 grid point average, respectively. Note: panel b) has a typo and should be 17/18Z at Point 22.
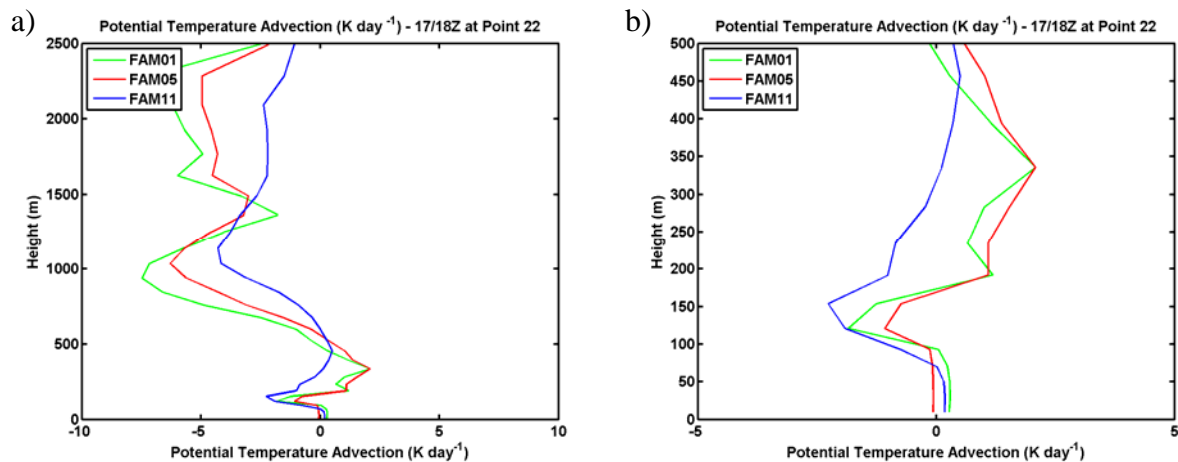
Figure 68.   a) Profiles of potential temperature advection derived from COAMPS output with no spatial averaging (FAM01), and 5 (FAM05) or 11 (FAM11) grid point averaging, respectively. b) Same as (a) except zoomed to the lowest 500 m.

139

The coastal location presented a further complication to the choice of averaging scheme. Figure 69 shows the vertical profiles of potential temperature and specific humidity advection at Point 17. The figure shows the impact of the large coastal gradient leading to large advection values and over land contamination especially near the surface. Averaging at this location to achieve smooth representativeness did not turn out to be feasible to force the lower boundary layer. A more sophisticated method to provide forcing from COAMPS output would be required.
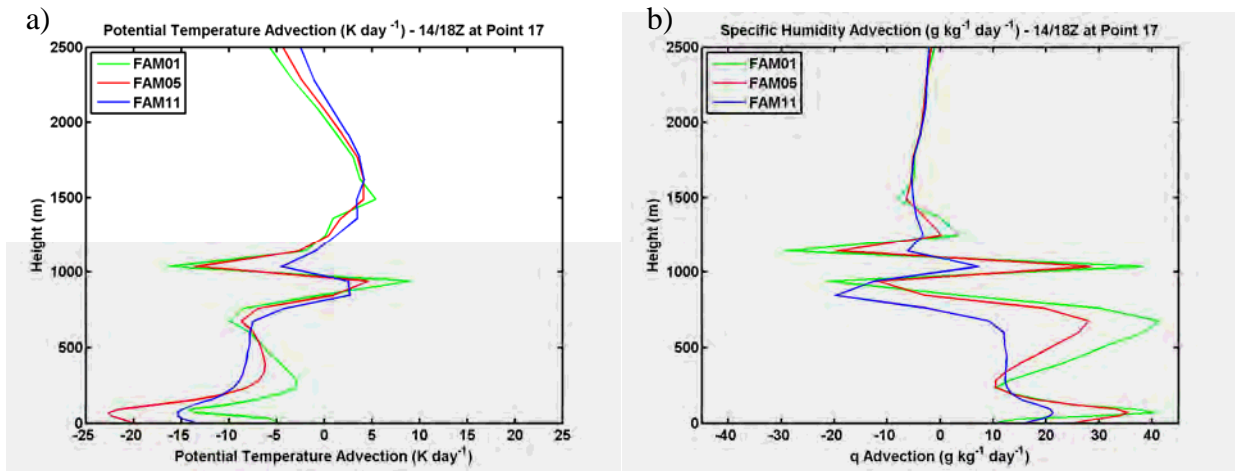
Figure 69. Same as Figure 68a except for the coastal July 14 case at point 17 for a) potential temperature advection and b) specific humidity advection.

The vertical velocity is a critical parameter in SCM forcing. The significant horizontal spatial and temporal variability was shown previously in Figure 53. Large scale averaging was required to create a smooth large scale subsidence forcing term. The comparison between the 25 grid point averaging and no averaging for the open ocean location (point 22) on July 17 is shown in Figure 70 for two consecutive hourly updates. The profile without averaging (black) oscillated between rising air (17Z) and subsidence (18Z) with large differences in vertical velocity. Magnitudes of the vertical velocities were on the order of 5 cm s^{-1} which is also unreasonably large. The 100 km averaging scheme (red) mostly eliminated extreme vertical velocity values, produced a consistent environment of mostly subsidence and the individual layers of convergence was kept to a

minimum. This persistent forcing better resembles the forcing similar to that used in the successful idealized cases described earlier.
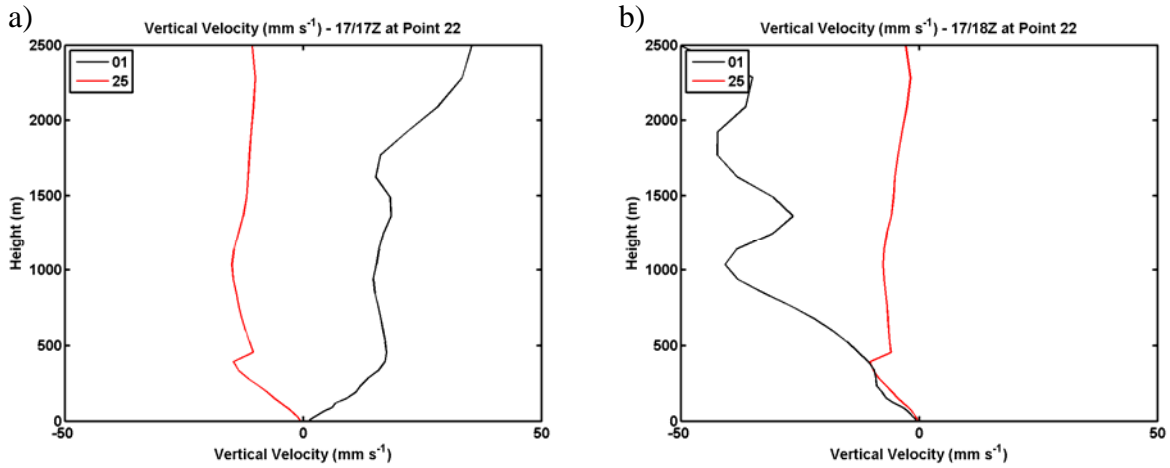
Figure 70.   Profiles of vertical velocity derived from COAMPS using no averaging (red) and 25 grid point averaging (black) for two consecutive hours at a) 17Z and b) 18Z on July 17, 2013.

For the reasons stated in the previous three paragraphs, it was determined and tested that the following averaging scheme provided the best results. The initial conditions and horizontal advection were averaged using 5 grid point with no vertical averaging. The large scale subsidence is provided using 25 grid point averaging and no vertical averaging. Coastal regimes proved extremely difficult to model with much success due to the large layered variability and coastal and overland contamination. These conditions are expected in this coastal regime. Finally, a linear interpolation in time to all forcing parameters was implemented to reduce the significant shock to the SCM at each intermittent hourly update.

a.   July 14 Case

The SCM was run for the July 14 case using the COAMPS initial and forcing conditions averaged as described in the preceding paragraphs. Additionally, the forcing was linearly interpolated for each time step between hourly updates. The potential temperature and specific humidity advection and its evolution with time is shown in Figure 71 along with the SCM forecast results at 2 and 3 hours for the SCM 60 and SCM

200, respectively. The SCM 96 and SCM 180 profiles lie between the plotted profiles and were omitted to simplify the figures. At 2 hours the SCM generally produced the same structure as seen in the sounding with a shallow mixed layer capped by an inversion, a slightly stable residual layer, and a weaker inversion.
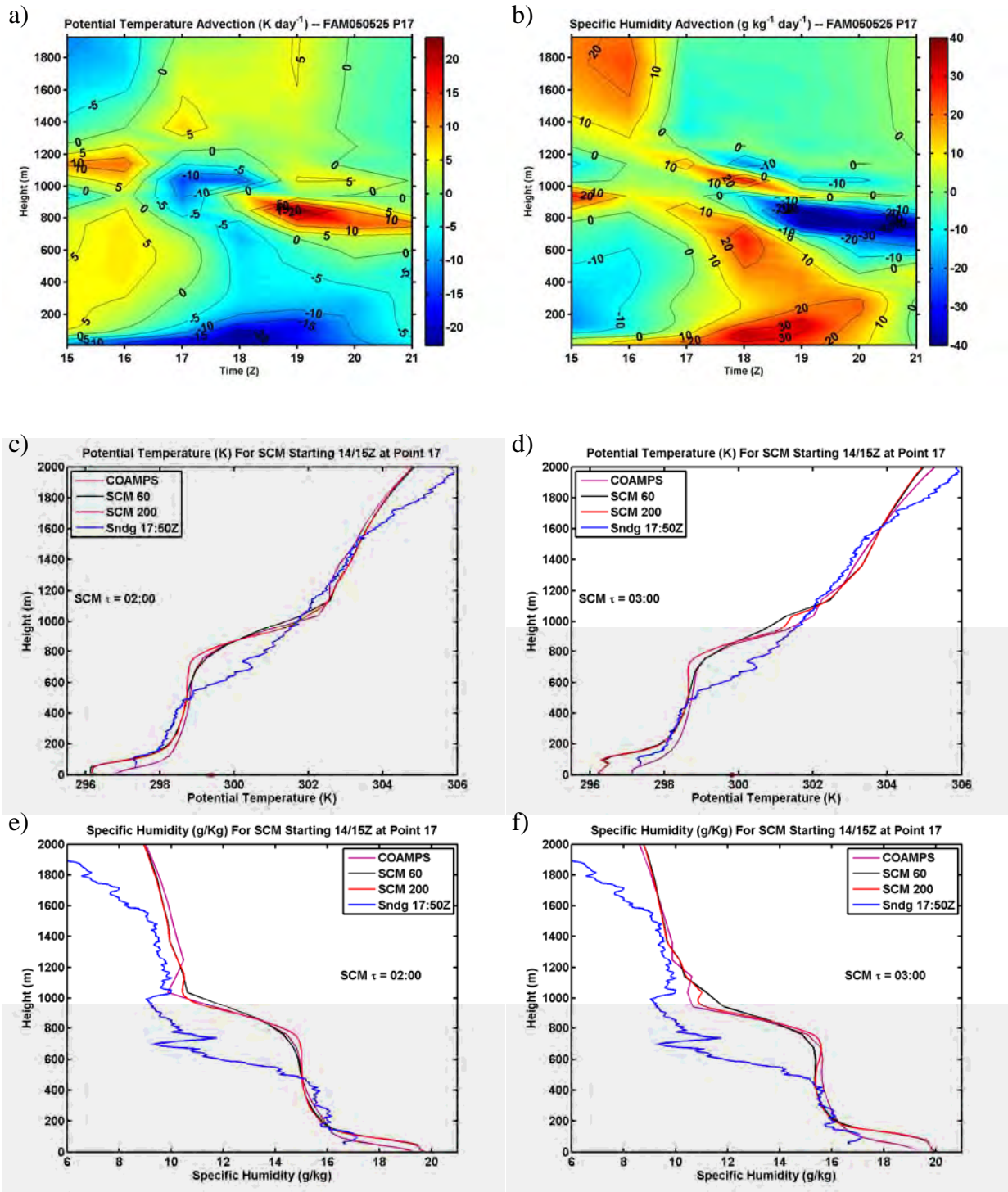
Figure 71.   a) Time evolution of the potential temperature advection on July 14,
b) same as in a) except for specific humidity advection, c) and d)
SCM forecast results of potential temperature at 2 and 3 hour
forecast times, respectively, and e) and f) same as in c) and d),
except for specific humidity.

Figures 71c-71d shows that the SCM mixed layer is much more defined than the COAMPS results and matches the mixed boundary layer suggested by the bottom of the sounding although SCM results in a much cooler mixed layer. The colder SCM mixed layer is likely due to the persistent cold advection near the surface. As discussed before, the instantaneous and 3D nature of the COAMPS output may not have such persistent cold air advection as represented by the once hourly update. With a weaker cold air advection cooler SST, COAMPS is likely to remain stable stratification throughout the boundary layer while the SCM becomes unstable and well-mixed. The persistent advection of cool and moist air eventually forms a cloud just after the second forecast hour. This changes the boundary layer dynamics which further leads to deviation from the cloud-free COAMP result. At forecast hour 3, the potential temperature shows an unstable profile at the top of the mixed layer (Figure 71d) that is the result of the cloud (Figure 72). The radiation heating rate in Figure 72c shows large magnitude cloud top cooling which is causing the thermal instability in Figure 71d. The depth of the mixed layer, the strength of the inversion, the cloud mixing ratio height and magnitude, the level of turbulence, and the timing of the formation of the cloud are all roughly comparable between the lower resolution and higher resolution SCM runs. At the level of the cloud layer, a subtle difference exists between the results from SCM 60 and SCM 200 although their grid resolutions are about 26 and 10 m, respectively. The benefit of the higher resolution in this shallow feature case is not readily obvious. However, aloft at the weaker inversion around 800 m, SCM 200 does represent a sharper gradient at initialization and it persists through the first 5 forecast hours, whereas SCM 60 shows comparable inversion to it 3-D COAMPS forcing as SCM 60 uses the same vertical grid setup as in COAMPS. This high-resolution advantage was discussed previously in the idealized case. The top of the weaker inversion aloft is 200 m higher than that seen in the sounding and is likely due to the inaccurate representation of this feature by COAMPS at initialization of the SCM.
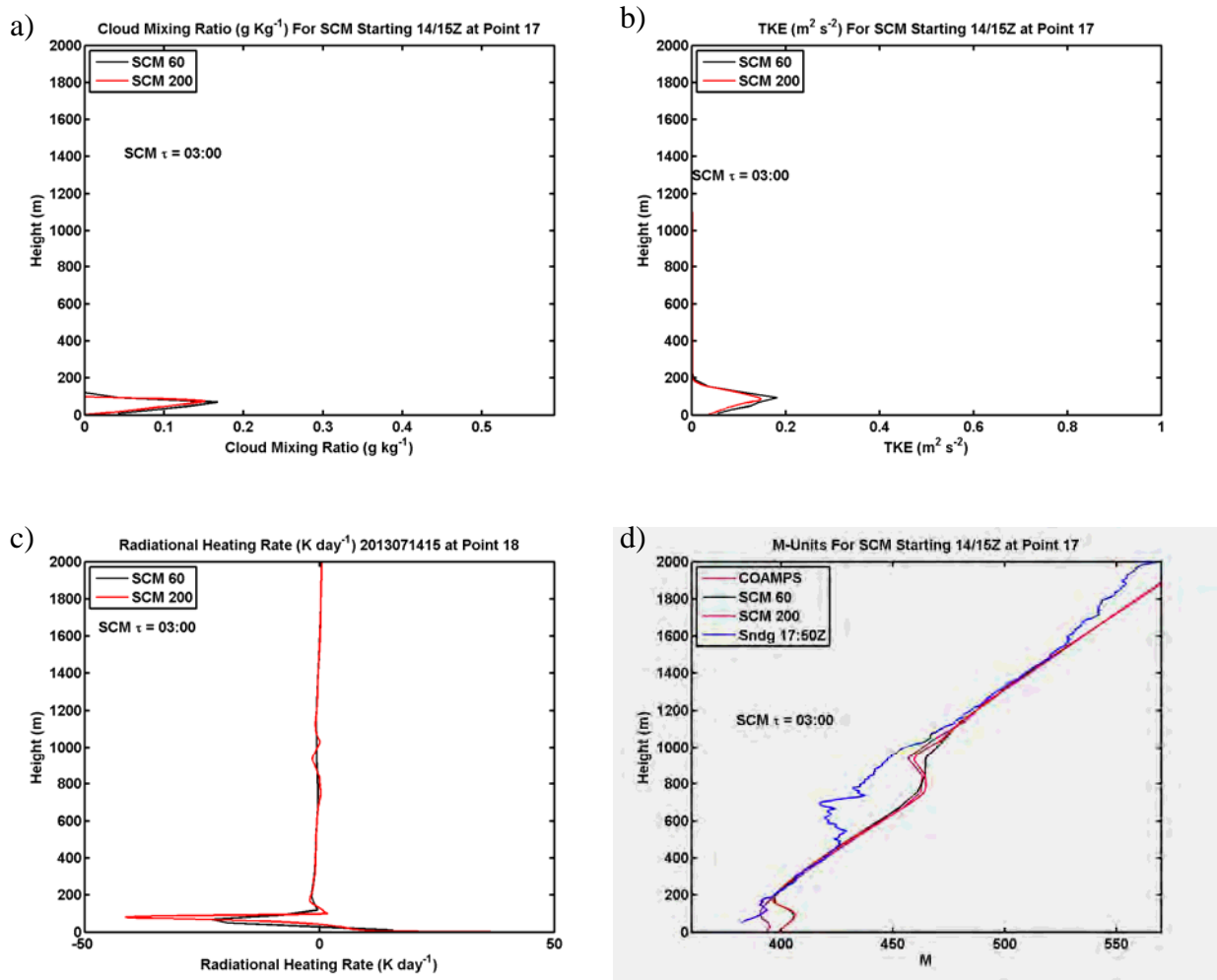
Figure 72.   Comparison between COAMPS, high and low resolution SCM, and
a synoptic sounding for parameters of a) cloud mixing ratio, b)
turbulent kinetic energy, c) radiation heating rate, and d) modified
refractivity. All results shown are for July 14 at 15Z

This test case indicates that overall the SCM behaves as expected according to the complex forcing that was provided and is able to reproduce similar features as shown in the sounding. However, the ultimate effect on propagation is determined by the M gradient. Even if the magnitude of the temperature and humidity features are off, the M gradient features may still be well represented. As shown in Figure 72d, the M profile from the SCM does indicate the trapping layer top at 200 m that is consistent with the sounding. However, the M excess appears too large. Also, the trapping layer aloft is represented too high but both COAMPS and the SCM 200 do resemble the thickness and

strength close to that of the sounding. The lower resolution SCM fails to produce the same trapping layer aloft.

The other additional feature that the SCM 200 was able to resolve is the surface layer gradient and the evaporative duct. Figure 73 shows a closer view of the surface structure of temperature, humidity, and modified refractivity. The SCM surface gradients represent an unstable surface layer with rapidly decreasing humidity which produces the evaporation duct.
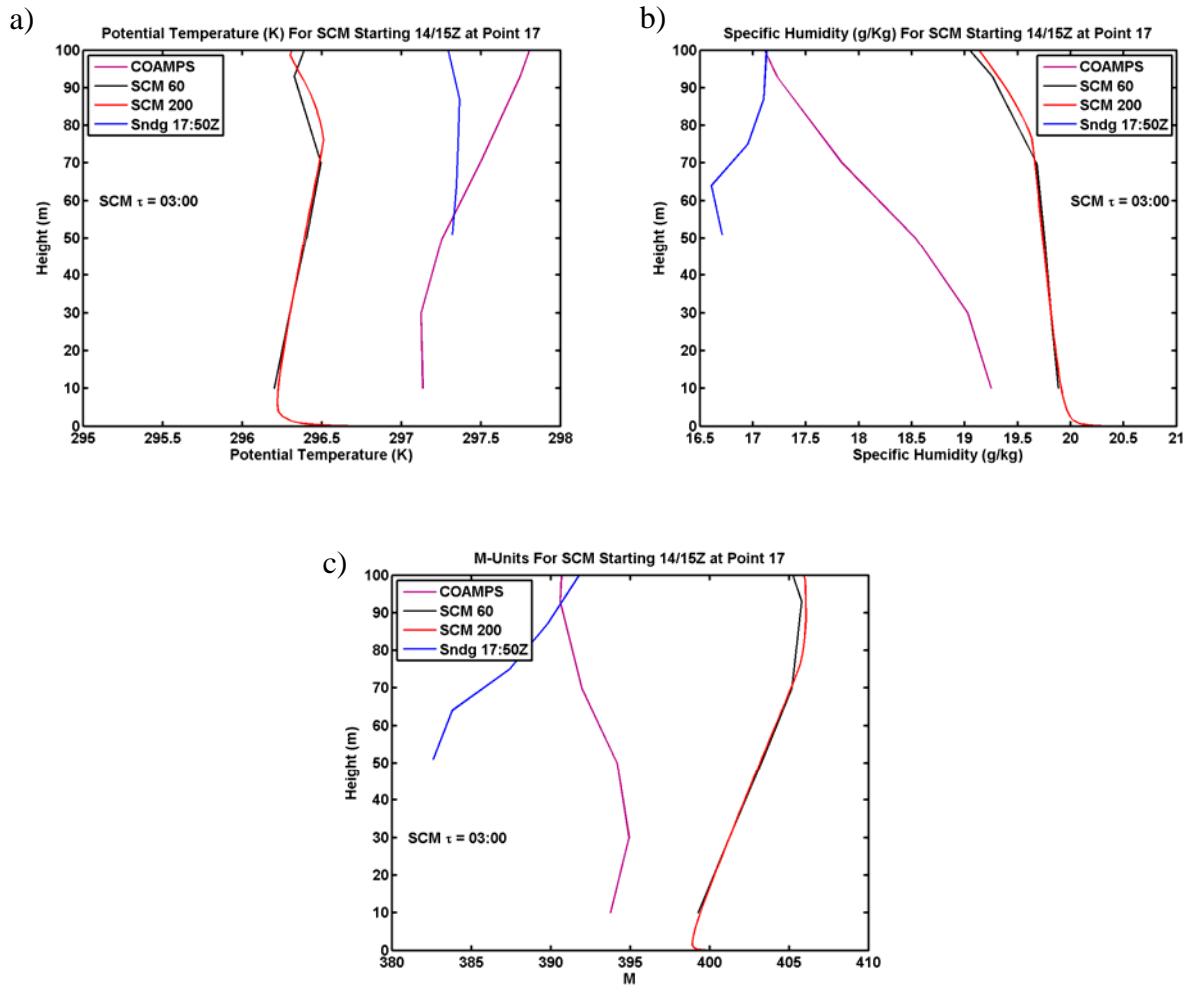
Figure 73.   a) potential temperature, b) specific humidity, and c) modified refractivity surface layer profiles from sounding, SCM simulations, and 3D COAMPS for the July 14 test case.

b. July 17 Case

The SCM run for the July 17 case used the same initial and forcing condition and vertical velocity averaging scheme as the July 14 case above. Figure 74 shows the contoured advection time series and the SCM forecast comparisons with COAMPS and observation at forecast hours two and three. The forcing shows some initial dry and warm advection aloft but quickly transitions to advecting a cool and moist layer that is rising in magnitude and height throughout the forecast. Another cool and moist advection layer begins at about 200 to 400 m height starting at forecast hour two.

The SCM temperature and moisture structure generally follows the COAMPS evolution closely for most of the column regardless of SCM resolution. The SCM runs are a little warmer which is closer to the soundings in the boundary layer and above, but this is a result of the complex and persistent external forcing and probably not an advantage of the SCM. The COAMPS and SCM at forecast hour two fail to indicate a relatively dry layer between 400 and 800 m. Since this feature is not resolved by COAMPS, there is no possibility that the SCM would resolve it either. Cool and moist advection is apparent between 600 to 1200 m and destabilizes the profile. This effect does match the nearly neutral profile that was observed albeit a degree cooler. The specific humidity plots also show a bulging in the profile at around 1000 m but, again, do not indicate the dry layer. Both sounding profiles indicate two sharp negative moisture gradients at 200 and 400 m. This top moisture lapse layer near at 400 m is completely missed by COAMPS and the COAMPS derived forcing and therefore the SCM runs also do not indicate the feature. This case illustrates that the high resolution SCM can be limited by the lower resolution forcing derived from the 3D model.
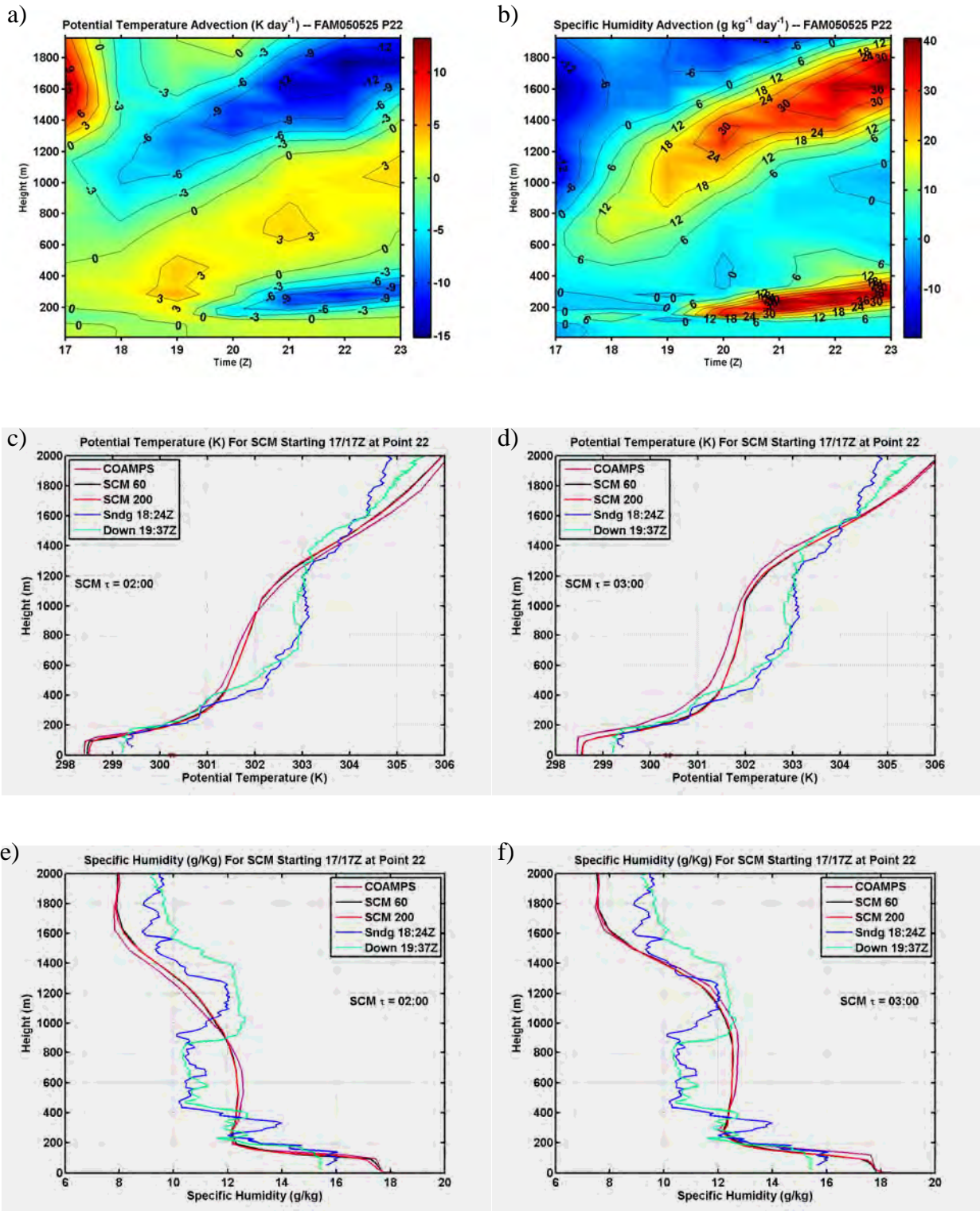
Figure 74.   Same as Figure 71 except for July 17 case.

The profile of moisture in the boundary layer is different between the higher and lower resolution SCM in this case. A closer look at the turbulence profile between the SCM runs in Figure 75 shows that the SCM 200 result has stronger turbulence near 100 m than that from SCM 60. The SCM 200 wind profile shows a weak low level jet at 140 m which is also indicated by COAMPS. The SCM 60 indicates that the jet has mixed out, which may have contributed to the difference in turbulence structure. The stronger turbulence in the SCM 200 results in larger eddy diffusivity and hence likely stronger entrainment mixing which produces the boundary layer gradient in moisture in the lowest 100 m (Figure 74e). By forecast hour three, this jet and the turbulence and moisture gradient for both SCM runs converge to be more similar. However, COAMPS retains its mixed layer and inversion gradient structure even with the same vertical resolution as the SCM 60.
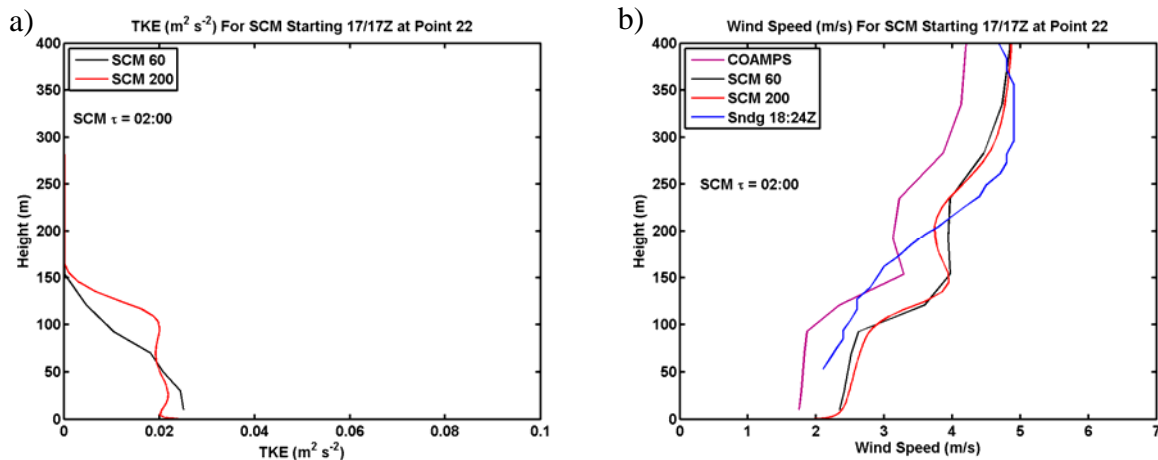
Figure 75. Comparison plots for July 17 case for a) TKE and b) wind speed.

The evolution of this SCM follows the COAMPS closer than the July 14 case did and shows potential for the SCM to have a reasonable profile evolution for open water cases given the smoother forcing while also yielding a surface layer. Figure 76a shows the M profile which is largely in agreement above the boundary layer with some slight difference in the gradient of M in the boundary layer. The biggest notable difference is that the SCM profile extends to the surface with continuous and consistent physics to resolve an evaporation duct as shown in Figure 76b.   In addition to the cloud topped

boundary layer case discussed in the UPPEF case, a clear advantage of the high resolution SCM may be in resolving the near surface vertical structures in thermodynamics and wind where turbulence is the dominant driving force. The potential of the SCM to represent the evaporation duct will be specifically discussed in the next section.
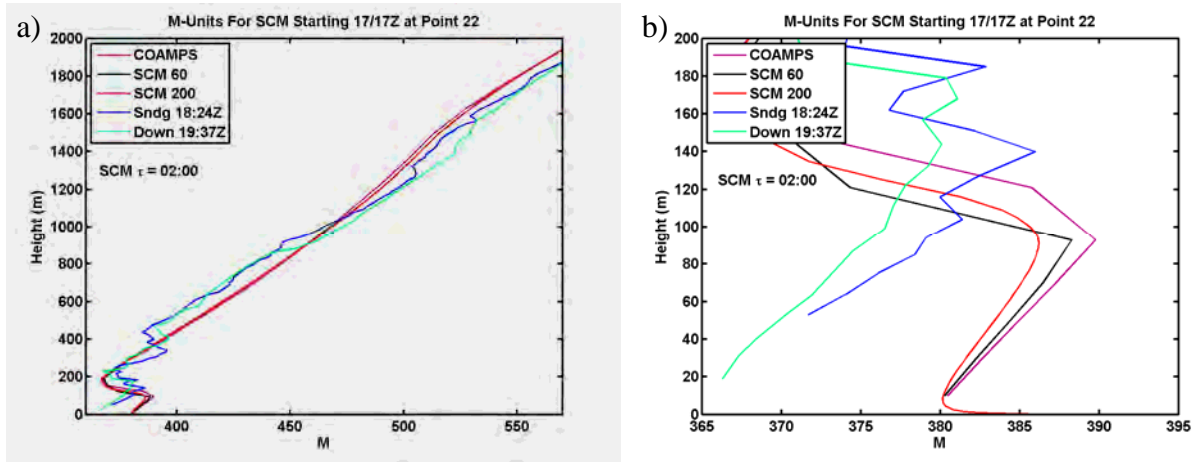
Figure 76.   Comparison of COAMPS, SCM, and soundings for modified refractivity for the July 17 case study.

C.   A NEW APPROACH FOR REPRESENTING EVAPORATION DUCT IN COAMPS

Up to this point, the SCM has shown that it behaves as hypothesized and performs reasonably well for at least the short term before the forecast diverges significantly with using external forcing that resembles the full 3D model. The advantage of the high resolution SCM approach is notable in resolving the inversion of the cloud topped boundary layer and resolving the surface layer with continuous and consistent physics throughout the boundary layer. The complications of this hybrid approach are its sensitivity to complex forcing that is vulnerable to error due to multiple factors including infrequent updates limited by the 3-D model output interval and the lack of 3D feedback. It is worth noting that the forcing is derived from the low vertical resolution 3D model, although the SCM can be setup at much higher resolution.

As introduced in Chapter III, current methods in modeling to represent the evaporation duct have some shortcomings. The full 3D COAMPS model does not explicitly represent the surface layer especially in the lowest 10 m or so where the evaporative duct occurs. Instead it is the general practice to use a diagnostics evaporative duct model, such as NAVSLaM, to produce an independent evaporation duct representation based on the 3D model's results in its lowest level(s). The resultant M-profile is then appended or blended to the bottom of the 3D forecast model M-profile as introduced in Chapter II.B.4. The two models are not necessarily consistent in their representation of the near surface properties such as surface flux parameterization or even formulations in calculating the M-profile. This blending approach works well in some cases, but may experience difficulties in producing a reasonably smooth transition at the intercepting altitudes, which sometimes produces a kink in the profile. Also, the diagnostic evaporation duct model itself has limitations in its basic assumptions associated with MOST, for example, and the choice of empirical stability dependent functions particularly in the stable and light wind conditions.

An alternative to the traditional "blending" technique in order to avoid discontinuity at the transition levels is to use a high resolution SCM that covers the entire atmospheric column to produce the M-profile of the column. However, as seen in previous sections, the SCM results can deviate from the "mother" model quite quickly because of the uncertainties in deriving external forcing from the 3-D model to drive the SCM. In order to leverage both the strength of the SCM's advantage of high resolution to resolve the surface layer and the strength of the 3D COAMPS model to forecast the large scale evolution, we attempt to run the SCM using a nudging technique which nudges the SCM to follow 3D model for the atmosphere above the surface layer. Since the atmospheric layers above the surface layer are forced to be consistent with the 3D COAMPS model result, there is no need to consider the effects of the external forcing for these layers. In this manner the boundary layer and the surface layer will be evolving forward in time as a result of turbulent mixing and surface fluxes.

For comparison purposes, an evaporative duct model will be used here for each COAMPS M-profile that initializes the SCM simulation. The evaporative duct model we

use is an extension of the COARE surface flux algorithm with the added capability of producing temperature and specific humidity profiles in the surface layer following MOST and with inputs from the lowest COAMPS (10 m) level and SST. These model results will be referred to as COARE profiles in the comparisons in this section. We also collaborated with Frederickson who ran the same scenarios through the NAVSLaM model and performed the blending algorithm on the results so that we could compare the final M-profiles with the SCM. Comparison between the COARE and the NAVSLaM results showed similar M-profile results for most cases.

The new blending approach through SCM is tested using the July 14 case with the SCM 200 setup. No averaging for initial conditions are made for this simulation and all external forcing conditions are turned off. The SST is provided from COAMPS initially and remains the same throughout the simulation. The added nudging term is described in Chapter III. A few technical issues need to be resolved in this approach.

First, the heights and timescales where nudging to the 3-D model results needed to be determined. After multiple test runs, we decided to apply a gradual nudging scheme from 30 to 50 m where there is no nudging at 30 m (very large nudging time scale), very short nudging timescale of 2 minutes at 50 m and above, and a linear interpolation of nudging timescales in between. This timescale of 2 minutes at the upper blending height allowed several time steps for mixing to smoothly transition the profiles at and above 50 m so as to not create unintended instabilities. The start of the nudging at 30 m is necessary to avoid SCM model deviating substantially from the 3-D COAMPS results since no external forcing is applied to this SCM simulation. Attempts were made at using the PBL height to drive the nudging height interval, but the cases in TW13 had highly variable and often very low PBL heights as calculated internally within COAMPS (i.e., sometimes 100 m) which did not allow a consistent method of driving the nudging height interval. A new scheme for determining the nudging height interval dependent on the situation may be recommended for future work. However, because the evaporative duct height is normally less than 30 m, this choice of the lowest nudging level should minimally affect the formation of most the evaporative ducts for our cases.

Secondly, there was the need to decide on appropriate eddy diffusivity (K). The modified eddy diffusivity (the new K) will be used mainly because it theoretically represents better the altitude dependence of K on thermal stability. The comparison between new and old K will be discussed in the following examples in detail.

Finally, we decided to run the SCM for one hour. This run duration allows turbulent mixing to be in effect while it is short enough to allow minimum drift from the COAMPS results due to the lack of external forcing in the blending SCM runs.

The SCM simulations with nudging were run for July 17 cases at 12Z for a line of 20 km spaced off-shore locations whose positions are indicated as black triangles in Figure 77d. These six points are numbered 32 to 37 from west to east and the group is referred to as "Row 3." SCM results for Row 3 are shown in Figure 77a-77c and the six profiles from left to right correlate with the positions from west to east. The scales are not shown in order to display the many profiles on the same plot and for this figure it is the shape that is of significance for this discussion. The plot compares the profiles of the SCM, COARE and the COAMPS model output. Five of the six cases are thermally unstable with well-mixed boundary layers whereas the Western most point is stable in the surface layer and the shallow boundary layer. The wind speed at 10 m is roughly between 4 to 5 m s^{-1} (not shown) for all the cases. The potential temperature profile shapes of the SCM runs are similar to the COARE profiles for all the cases, and almost exact for the most unstable cases (point 36 and 37). The humidity gradient is also negative for all the cases in the surface layer and the SCM profiles are nearly indistinguishable from the COARE profile. Under these conditions (e.g., moderate wind and either unstable or the one just slightly stable case), we expect MO theory to work well and the COARE profiles well represent the surface layer structure. Since the SCM profiles are very similar to the COARE profiles in shape and value, confidence is gained that the model is behaving as expected and producing reasonable results in these conditions. As a result of temperature and humidity behaving consistently as expected, the M profiles also indicate consistency with the COARE derive M profile. The stable case (point 32) shows the largest difference in shape, but is still very similar. The third point from the left (point 34) also shows that the SCM profile is somewhat offset from the COARE profile.
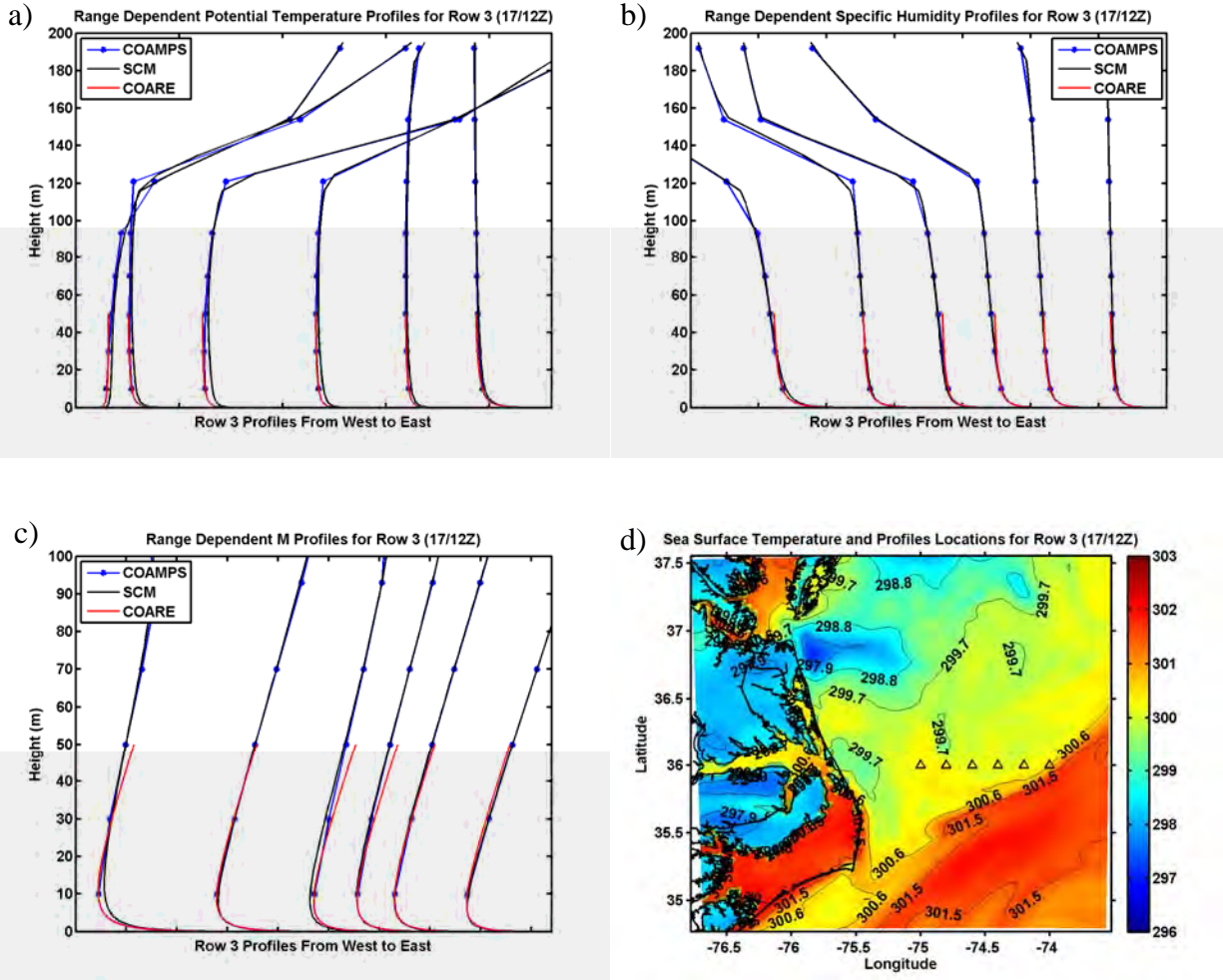
Figure 77. SCM, COARE, and COAMPS profiles at locations as shown by black triangles ("Row 3") from West to East in panel (d). a) Potential temperature, b) specific humidity, and c) modified refractivity.

We desire to make a comparison of the SCM results and the profiles that result from NAVSLaM and the blending. The NAVSLaM profiles and blended profiles were generated and provided by Paul Frederickson (NPS) using an updated version of the blending algorithm which is not the same as currently employed in AREPS. The comparisons for the cases in Row 3 are shown in Figure 78. As expected from the results in Figure 77, the profiles are mostly similar for points 33 and 35 through 37. Point 32, the stable case, appears to have a similar profile but the SCM EDH is about 3 m higher. The profile with the largest comparison difference is point 34 in which the SCM resolved an EDH about 1 m higher and the slope above and below the EDH was slightly less steep.
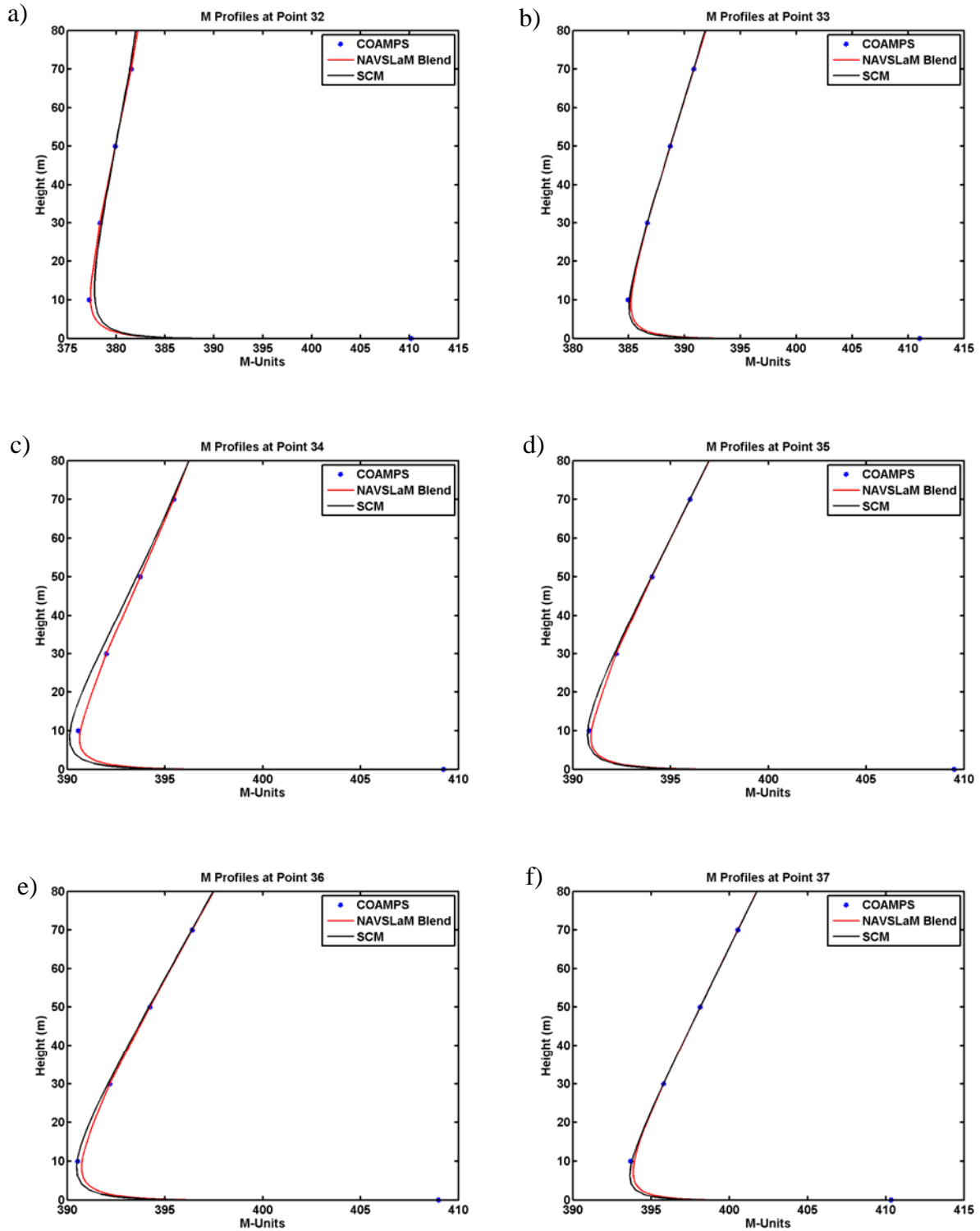
Figure 78.   Comparisons of SCM and the corresponding blended NAVSLaM
profile for points 32 through 37 (a-e) in Row 3 for cases on 17 July
at12Z (same points shown in Figure 77).

155

Another profile comparison is examined in Figure 79a in which the conditions are stable with a moderate 5 m s^{-1} wind at point 38. The black line shows the SCM results as a smooth profile with an EDH of about 9 m. The blend profile (red) indicates an irregularly shaped profile that has an EDH at 6.5 m, a relatively sharp increases to near the COAMPS grid point at 10 m, and then a kink in the profile at about 14 m altitude. This is possibly the result of the blending interval being too high for this case. The green line shows the NAVSLaM profile specifically and it is apparent where the slope of the M profile from NAVSLaM transitions to the course grid slope of the COAMPS which causes the kink. Additionally, regardless of the blending interval used, there would be a discrepancy between the SCM solution and the blended solution because the blend solution follows the COAMPS grid values and the SCM solution deviates between 10 and 50 m. This example demonstrates a case where the blend technique may introduce a kink to the profile and the high resolution SCM results in a smooth profile based on consistent physics in the model throughout the surface and boundary layer.

Another profile comparison is examined in Figure 79b in which the conditions are light wind and unstable at point 24. This example shows almost overlapping surface layer and evaporation duct profiles between the SCM and the blend solutions. Again this gives confidence in both solutions. The biggest difference in this profile is actually above the evaporation duct at the base of the surface duct. The NAVSLaM Blend is bound to the COAMPS values at the low resolution vertical grid whereas the SCM is able to evolve based on the physics at these levels in combination with the nudging. The result is that the SCM yields a smoother profile and demonstrates another potential advantage to the SCM approach.
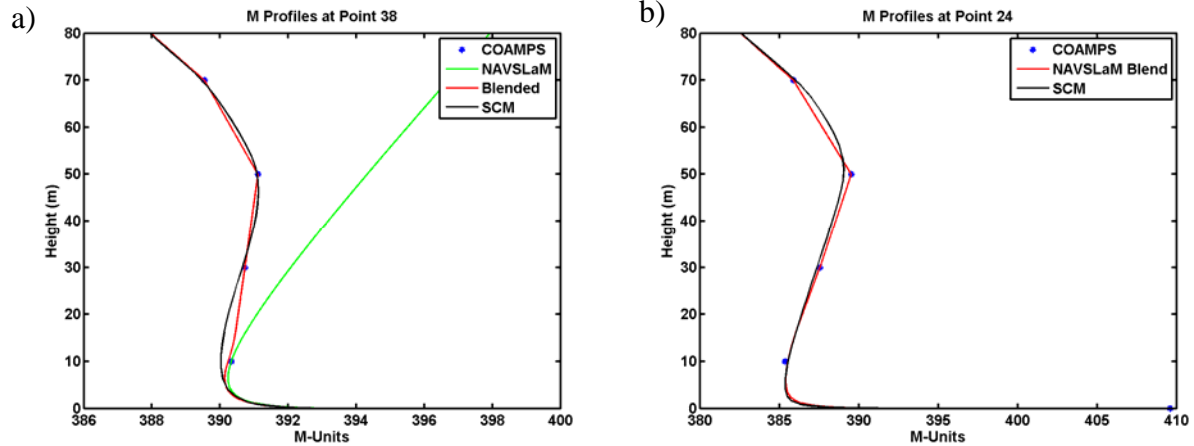
Figure 79.   Same as Figure 78 except for point a) point 38 and b) point 24.
Figure (a) shows the NAVSLaM results also.

The next examples illustrate cases where the SCM approach resulted in the appearance of reasonable profiles and the blending approach resulted in irregularly shaped profiles. Figure 80a shows the M-profile comparison for point 28 and Figure 80b is for point 56. Both cases are stable cases with a wind speed of 3 m s^{-1}. The blend profiles both show a curve in the profile that appears irregular with the 10 m value seeming to weight the profile heavily which results in a steeper M gradient below the 10 m and a relaxed M gradient between 10 and 30 m. This is likely a result of the blending algorithm assigning the blending interval for this stable case at a low altitude with a small height range. The M-profile slope from the NAVSLaM surface model at low levels merges with the COAMPS M-profile which dominates between 10 and 30 m and forces the profile to follow the COAMPS profile. Whereas the SCM nudging interval was at higher altitude which allowed the turbulent processes below the lower nudging height to evolve the variable profiles freely based on the physics of the model. This does not necessarily mean that the blended profile is incorrect and the SCM is correct. These locations were under stable conditions with a light southeasterly flow advecting low level warm moist air from the Gulf Stream over the coastal cool counter-current. The advection may be playing a role in producing such a profile. However, with only one grid data point (10 m) and the SST used as input to the NAVSLaM and the blending algorithm, it is uncertain if such advection is correctly accounted for. The SCM is not accounting for

157

advection, but is using the physics and turbulence to evolve the profile. These stable advecting cases require more research.

a)

b)
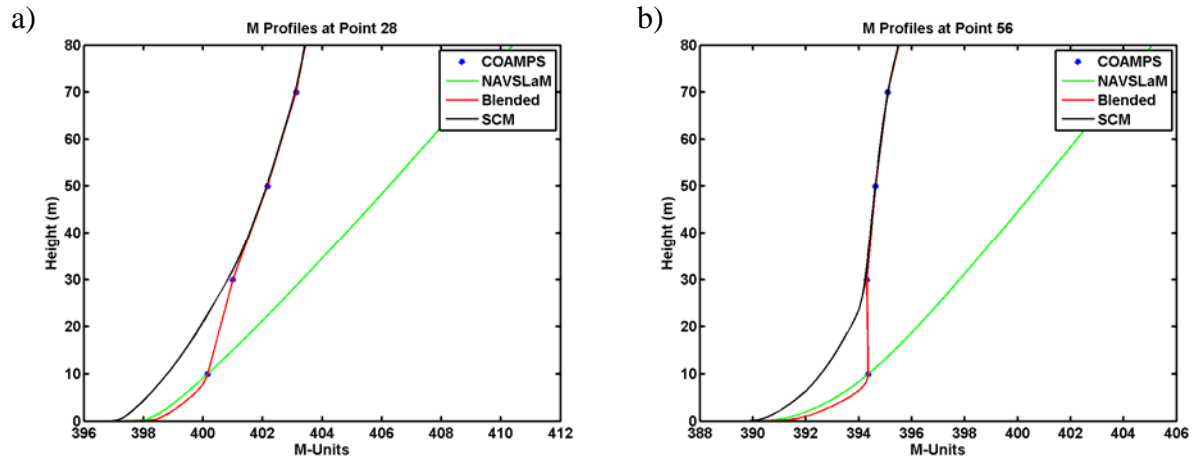
Figure 80.   Same as Figure 79a except for a) point 24 and b) point 56.

The next set of comparisons shows where the SCM can result in an irregular kink in the profile. Figure 81a and b show two stable condition comparisons with moderate wind. The blended profiles show smooth transition between the NAVSLaM and the COAMPS and the results appear reasonable. Point 58 (Figure 81b) shows how the blending algorithm offsets the NAVSLaM profile in order to smoothly merge with the COAMPS profile in that the resulting surface layer profile is about two M-units greater than the original NAVSLaM profile. However, as mentioned, the important aspect of the profile is the slope of M and not the M value itself. The SCM profiles, however, show a kink resulting from the nudging between 30 and 50 m. It is apparent in Figure 81a at about 39 m and in Figure 81b at about 33 m. This shows that some improvement in the determination of the nudging interval may be necessary.

158
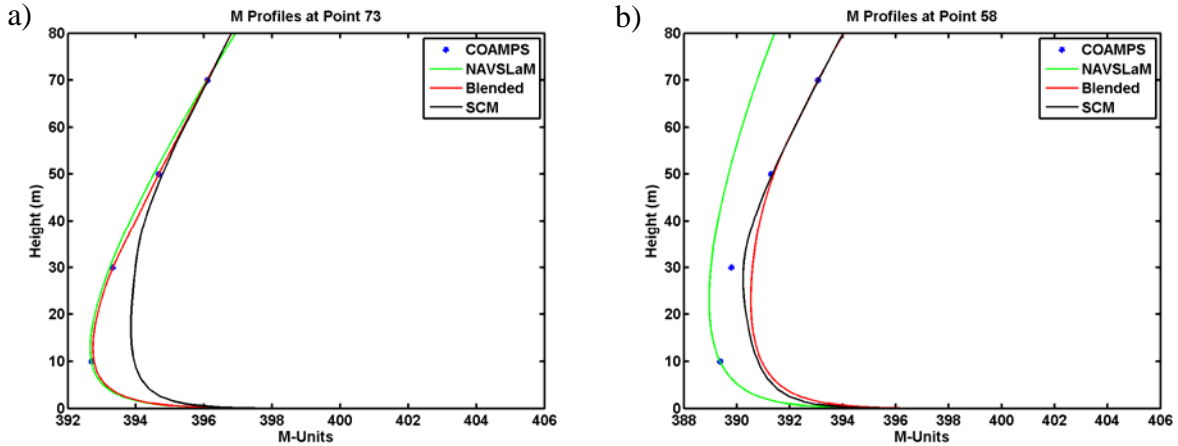
Figure 81.   Same as Figure 79a except for a) point 73 and b) point 58.

A total of sixty-five SCM and NAVSLaM blending runs similar to those discussed above were conducted and Table 7 shows the qualitative performance comparison in different stability conditions. For the qualitative analysis, a profile was considered "good" if it did not have any of the apparent kinks or appeared unrealistic due to the proximity of the nudging or blending interval. These types of profiles were discussed in Figures 73 through 75 above. For the SCM, if a noticeable kink is apparent at or around the 30 m bottom nudging interval height, then that case was not considered to run good.

The results in Table 7 show that the SCM method qualitatively performed well in 88% of the cases (57 of 65). The NAVSLaM blending method performed without irregular kinks in 65% of the cases (42 of 65). The results show that in the unstable cases, both the SCM and NAVSLaM blending method performed good in 78% of the cases. Also in unstable cases, the SCM profile had no irregularities for 6 cases in which the NAVSLaM Blend did have an irregularity. For stable cases, both methods performed well for 42% of the cases. Also for stable cases, the SCM had no irregularities for 12 cases when the blending method did have irregularities, and the blending method had no irregularities for 3 cases when the SCM did have irregularities. Both the SCM and NAVSLaM Blend had comparably smooth profiles in 60% of the cases and two-thirds of those cases were unstable. Finally, there were 5 cases where both the SCM and NAVSLaM Blend produced profiles with irregularities. These were predominantly stable

159

cases, low wind speed cases, or an extremely low boundary layer case. These results were based on cases where about half the cases were stable conditions.

	Good Profile for Unstable Case	Good Profile for Stable Case	Total
Both	25 (78%)	14 (42%)	39 (60%)
NAVSLaM Blend Only	0 (0%)	3 (9%)	3 (5%)
SCM Only	6 (19%)	12 (36%)	18 (28%)
Neither	1 (3%)	4 (12%)	5 (8%)
Total	32	33	65

Table 7.   Qualitative lower boundary layer profile performance comparison between the SCM blending model and the NAVSLaM Blending Algorithm. A profile was not considered good if it appeared to have a kink or appeared unrealistic due to the blending interval influencing the profile significantly.

A quantitative comparison between the two methods is performed by comparing the evaporation duct height. The comparisons are shown as scatter plots (Figure 82) and color coded by surface layer stability. There were 39 cases where both the SCM and the NAVSLaM produced good profiles and those cases are indicated by circle markers. The "x" markers indicate cases where one of the methods produced an irregular profile. The duct height from SCM is limited to the SCM vertical resolution, which is apparent. The SCM produces lower EDHs when EDH is lower than 7 m and these tend to be unstable cases. The two methods are comparable when EDH is around 10 m. The SCM produces higher EDHs when EDH is higher than 15 m and these tend to be the stable cases. Overall, the two methods show a reasonable correlation with a correlation coefficient of 0.863.
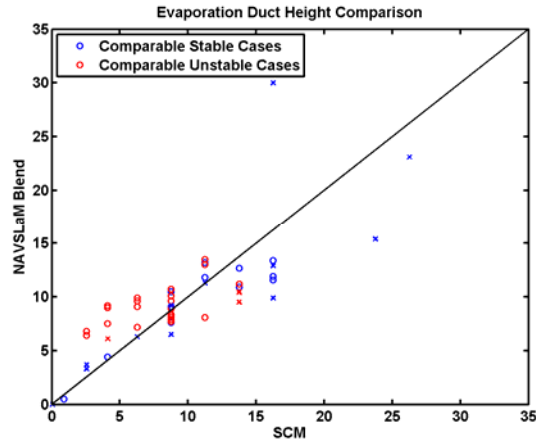
Figure 82. Comparison of EDH between the SCM and NAVSLaM Blending
profiles.

As mentioned above, the examples shown thus far in this section compare SCM results that have used the modified eddy diffusivity as discussed in Chapter III and in this chapter. The inclusion of this height dependence relationship modifies the non-linear system that relates the K value, TKE, mixing length scale, and stability. Ultimately, this changes the structure of the modeled surface layer and thus the evaporation duct. The difference introduced by the modified eddy coefficients is discussed in detail here. Figure 83 shows the comparison of the potential temperature, specific humidity, TKE, and M profiles calculated using the SCM 200 with nudging (as above) with both the "old" and "new" Ks at point 33 (this case previously shown in Figure 77b and 78b). The figures also show the COAMPS 3D and COARE derived results as references. For the temperature, humidity, and refractivity profiles, the results with the new K show adjustment towards the COARE derived profile compared to those with the old K. They also show the adjustment towards the lowest points in the COAMPS profile as well. Overall the new K results show an improvement in the smooth transition and resemble the expected results that behave more like Monin-Obukhov relationship in the surface layer.

At the core of the formulation for the eddy diffusivity is the choice of the mixing length scale. The mixing length scale used in COAMPS is a combination of several mixing length scales described in Chapter II. The profiles of these mixing length scales at

one instance of the model are shown in Figure 84a. The black line, labeled as "$1/(zk+zkk)$," is the original geometric average of the surface layer length scale and the boundary layer turbulence length scale following the Blackadar scheme as described in Chapter II. This is the length scale that is modified for this study as discussed in Chapter III and is represented by the cyan line and labeled as "alm." The blue line in Figure 84a, labeled as "al3," is the mixing length scale derived from stability and the Brunt-Vaisala frequency. The green line in Figure 84a, labeled as "al1," is the dissipation length scale following Burk and Thompson's work in COAMPS (no date) which is established upon model initialization essentially setting l_∞ to 5 in Equation 2.21 and sets the minimum length scale used in the model.

The final length scale used to calculate eddy diffusivity at each model grid level is the result of logical selection of these length scales. The first selection is the minimum between the geometric averaged length scales (the black or the cyan lines) and the length scale derived from stability (the blue line). The next selection is the maximum between the first selection and minimum length scale (the green line). The overall result for original setting in COAMPS is highlighted in yellow in Figure 84a. In this case the modified length scale used in the modified K would essentially select the cyan in place of the black line up to about the same height, and then be the same at higher heights.

The effective difference in the eddy diffusivity calculated using the original and modified length scales described above is shown in Figure 84b. The "new K" in this case results in larger eddy momentum diffusivity at all levels in the boundary layer. This enhanced diffusivity should initially increase turbulent mixing and cause a series of non-linear feedbacks to the SCM results and hence the differences seen in the M-profiles using the original and modified index of refraction.

a)

b)

c)

d)
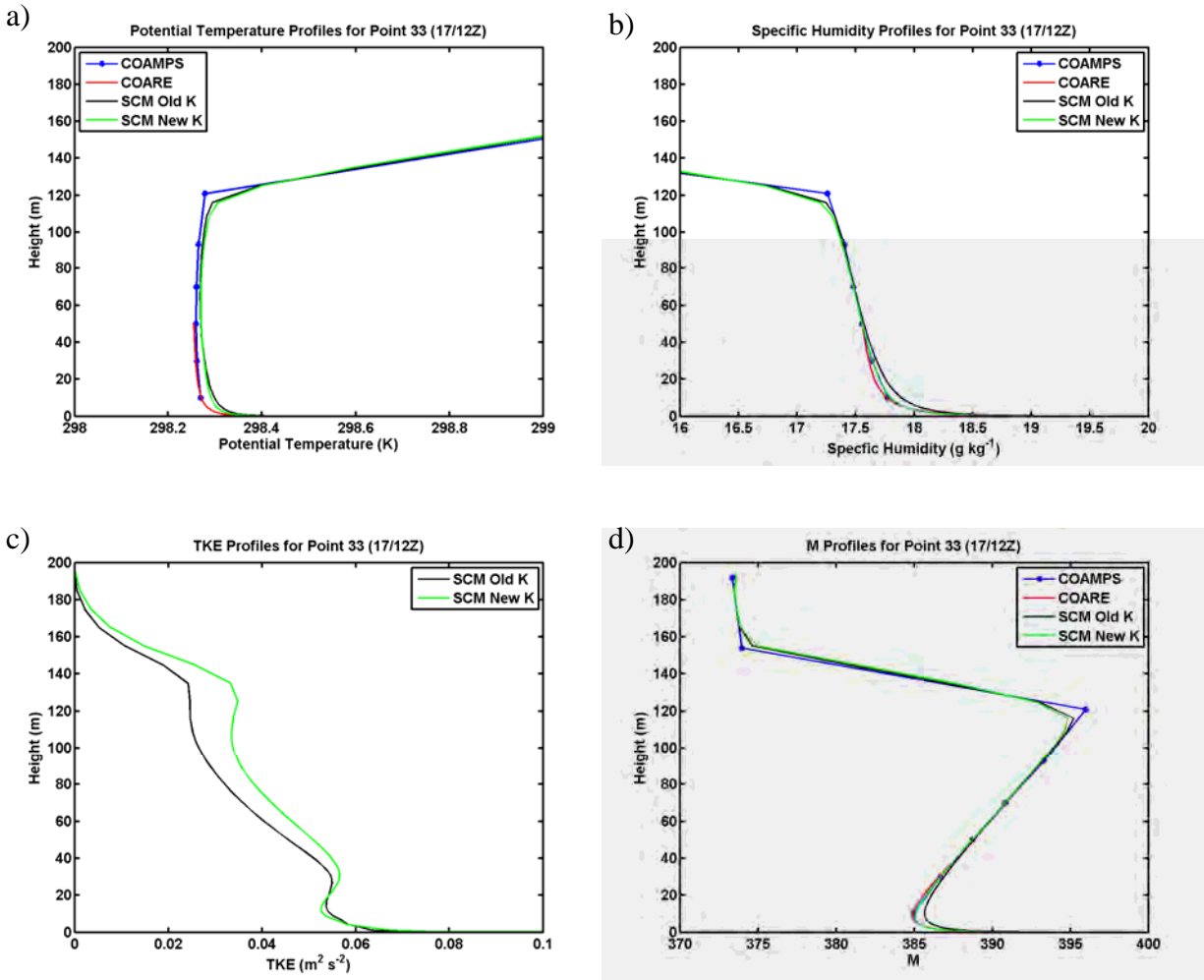
Figure 83.   Comparison plots of SCM run at point 33 using COAMPS original
and modified eddy diffusivity (Old K and New K) for a) potential
temperature, b) specific humidity, c) TKE, and d) modified
refractivity.

163
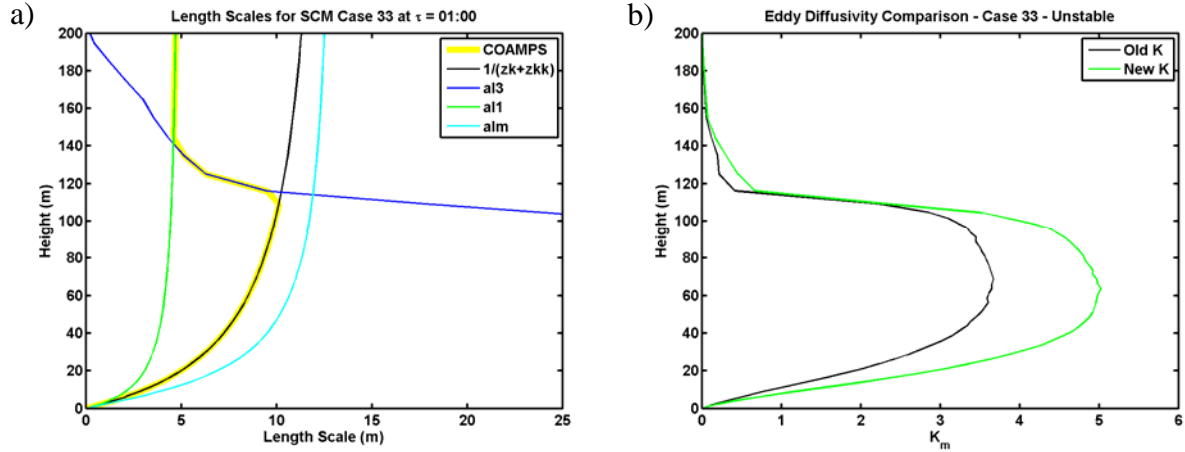
Figure 84.   An example of components in the original and modified eddy
diffusivity at point 33. a) Mixing length scales for both original and
modified K, and b) original and modified K.

The impact of the modified eddy diffusivity varies in different cases. The various length scales in a stable surface layer case (point 56 on July 14 at 06Z) is shown in Figure 85a. In this case the new mixing length (cyan) is less than original mixing length (black). Following the same logic to select length scale as described earlier, the original mixing length profile is again highlighted in yellow for COAMPS. The new mixing length profile, conversely, follows the green line throughout the entire profile. The result is that there is no longer a low-level local maximum in the mixing length of the boundary layer in this case. The impact on the profile of eddy diffusivity is shown in Figure 85b where the new K does not have an outstanding local maximum in the middle boundary layer as in the simulation with the original K.

a) Length Scales for SCM Case 56 at τ = 01:00

COAMPS
1/(zk+zkk)
al3
al1
alm

b) Eddy Diffusivity Comparison - Case 56 - Stable

Old K
New K
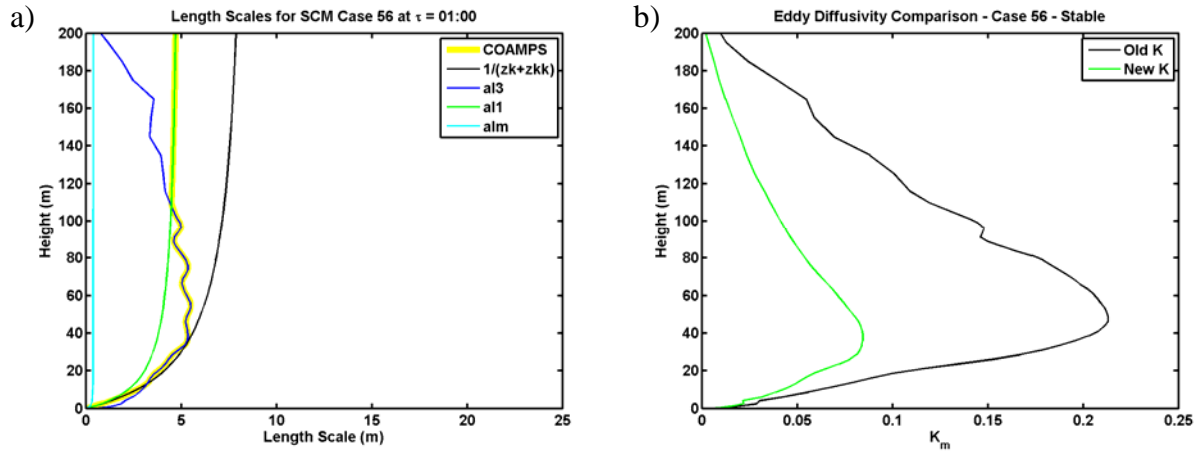
Figure 85.   Same as Figure 84 except for Point 56.

The impact of the new K on the profile of temperature, q, and M in case 29 is shown in Figure 86. The potential temperature profile shows a slightly weaker gradient in the first 20 m and overall lies between the old K run and the COARE profile. The specific humidity is slightly increased. There is less TKE overall. The refractivity profile shows a slight increase in positive gradient in the first 30 m and a slightly smoother transition at the bottom of the nudging interval.
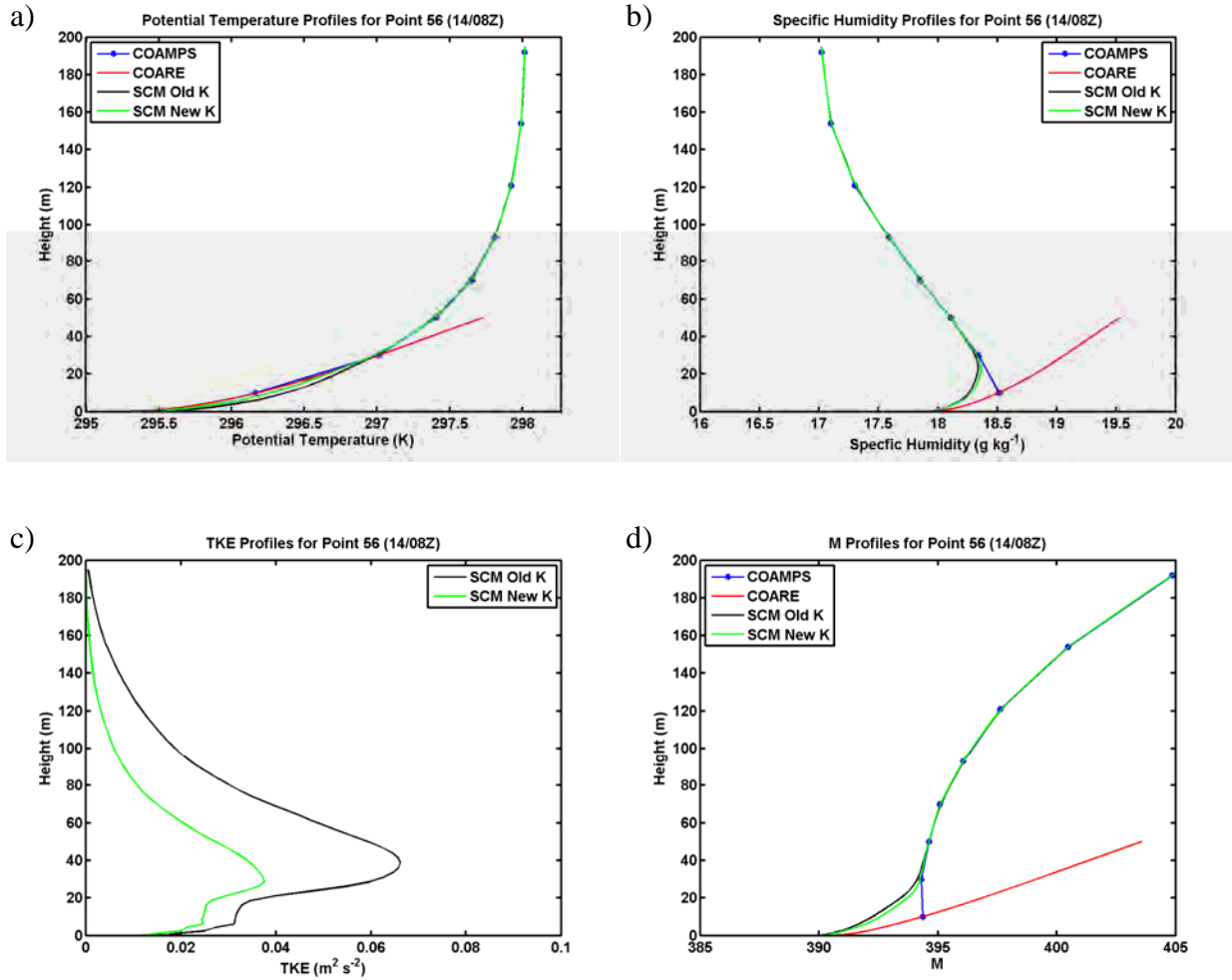
Figure 86.   Same as Figure 83 except for point 56.

VI. SUMMARY, CONCLUSIONS, AND RECOMMENDATIONS

A. SUMMARY OF ISSUE AND METHODS

The ability to predict the propagation of electromagnetic energy through the atmosphere has numerous tactical implications to the Navy and DOD. The atmospheric property that determines propagation behavior is refractivity which is dependent on temperature, humidity, and pressure. Electromagnetic wave propagation is particularly sensitive to the vertical gradient in refractivity, which results in anomalous propagation behavior that significantly impacts the performance of sensors and communication systems. Thus, adequately quantifying the gradient layers in the lower atmosphere is the key to accurate EM propagation prediction, which should be the focus of improvements of environmental forecast models for purpose of EM propagation prediction.

Mesoscale atmospheric models have been used in the past to provide environmental data input to propagation models. Because of its capability to generate a valuable data set to be used for EM propagation prediction in any operational area deemed necessary, mesoscale models will continue to be the major tool for future EM propagation prediction. In addition to imperfect physical parameterizations, the atmospheric mesoscale models are limited in their vertical resolution to produce realistic vertical gradients of forecasted thermodynamic variables, especially near the inversion level and over the surface. However, it is computationally impractical to increase the vertical resolution to the extent that vertical gradients can be adequately resolved for simulations to cover a domain of several hundred kilometers on the sides. An innovative approach is thus needed to fill this gap, which is the focus of this thesis work.

This thesis work contains three major components. The first part involves a thorough theoretical analysis on the dependence of the refractive index on various predicted variables, which was supplemented with empirical sensitivity analyses using buoy data and an evaporative duct model. The second part of the thesis work involves testing two hypotheses regarding the potential of a hybrid SCM and 3D mesoscale model approach for environmental forecast to improve EM propagation prediction. A special

167

application of the SCM with nudging technique result in a new approach that smoothly extend the mesoscale model results to the atmospheric surface layer so that the evaporative duct and refractive layers above the surface layer can be both represented without creating gradient inconsistency in the boundary layer.

Theoretical analyses were performed to examine the sensitivity of the refractivity gradient to the atmospheric variables. Given the complexity of the resultant formulation, the results were obtained numerically by giving a reasonable range of surface layer temperature, water vapor, and pressure, which allows an investigation of the relative contributions of these variables leading to anomalous refractivity gradients. The theoretical analysis continued by solving for the evaporation duct height and strength which are key properties of the surface layer ducting environment. A surface layer model based on the COARE surface flux algorithm (MASL) was then used to produce many surface layer profiles by using buoy observations as input in order to examine the range of variability of evaporative ducts occurring in the marine surface layers. Finally, propagation estimates were obtained using AREPS with MASL produced M profiles to examine the sensitivity of propagation loss to evaporation duct characteristics.

The second part of this study centered on evaluating the two hypotheses given at the beginning of Chapter V on a hybrid approach for generating a full refractivity profiles for EM propagation application. The Navy's operational mesoscale model, COAMPS, was used in single column model (SCM) mode with the intent of addressing the vertical resolution issue of full 3D atmospheric model as input to EM propagation models. First the SCM was run using idealized initialization and forcing for a stratocumulus topped marine environment sampled during the UPPEF experiment in 2012. Similar simulations were made for cases observed during the TW13 campaign with idealized forcing. Finally, external forcing derived from COAMPS 3D simulations for the TW13 was used to drive the SCM simulations. In all case analyses, the SCM results are compared with COAMPS 3D results and rawinsonde soundings to evaluate the advantages and limitations of the hybrid modeling approach. Simulations with the idealized forcing allowed for controlled testing to evaluate the effects of different vertical grid resolution and different surface layer parameterization settings without complex forcing.

The new blending technique proposed and tested here also involves the SCM with significant nudging to the 3-D model profile down to ~30 m above the surface. Unlike the traditional blending technique of smoothing M gradients between two different models, the blending technique here employs a prognostic approach to allow boundary layer mixing and surface fluxes to adjust the mean profiles at very high vertical resolution in the lowest levels. This dynamic blending technique with SCM intends to blend the evaporative duct layer with the M-profile above with internal consistency of the physics and to avoid discontinuity in the gradient of the M-profiles. This thesis work also examined the impact of a modified eddy viscosity in the SCM in an attempt to be more consistent with MOST in the surface layer.

B.   CONCLUSIONS

1.   Sensitivity Analyses for Factors Affecting Evaporative Ducts

Scale analysis of the modified refractivity quantified the contributions of moisture, temperature, and pressure to the refractivity gradient as depicted in Equation 4.9. Table 2 shows the range of variation for each term in the M-gradient equation. All terms show some overlap in range, suggesting that all of the terms have the potential to dominate the equation depending on the values of the input variables and their gradients. However, based on typical values of the variables, the moisture gradient term is typically the dominant term affecting refractivity gradient and, therefore, propagation. This conclusion is consistent with previous studies (e.g., Babin et al. 1997), although more thorough derivations and analyses were done in this thesis work. Due to conditions near the marine surface, evaporation ducts occurs frequently as suggested by the analyzed evaporative duct properties derived from buoy measurements. The sensitivity analyses here identified the variables critical to represent correctly in order to accurately determine the refractivity environment.

The EDH formulations derived from this study involve complex non-linear relationship among the state variables and surface flux scaling parameters that makes an explicit solution difficult to obtain. An alternate method for finding the EDH is to solve for the entire surface layer profile of the state variables using a surface layer model

169

(MASL) based on the COARE surface flux algorithm in order to calculate *M* and obtain the corresponding EDH and EDS. The MASL is equivalent to an evaporative duct model such as NAVSLaM. To further investigate the effects of the various surface layer conditions on propagation, the surface layer profile is blended to the standard atmosphere M profile above the surface layer to provide a complete refractivity profile throughout the atmosphere as input to propagation models such as AREPS.

An extensive dataset based on measurements from eight NOAA NDBC buoys on the east coast and the west coast of U.S. was used as input to MASL to produce EDH and EDS in real atmospheric environment. A large amount of observational data, a total of more than 49,000 data points from eight buoy locations, is used to in order to analyze the dependence of ED properties on atmospheric variables using reasonable combination of low-level temperature, humidity, wind, and SST. The peak of a probability distribution of the surface layer at the buoy observation height was around 87% relative humidity and slightly unstable at -0.3 air-sea temperature difference seen from all buoy data. The range of conditions noted in this analysis bound the conditions in which a surface layer model must perform well, at least for the coastal U.S. where these observations were used. Also, this variability analysis will aid in bounding a range of perturbations for ensemble studies in the future. Results from this study in these locations suggest that EDH is typically less than 20 m. Its probability distribution peaks between 3 to 5 m for this dataset. The M-deficit, or EDS as described in this paper, is predominantly less than 20 M-units and usually less than 7 M-units. We tested on different set of variables to characterize the dependence of EDH/EDS on state variables and stability indicators and found that Richardson number and specific humidity depression forms an advantageous combination compared to ASTD and relative humidity. The use of surface layer bulk Richardson number and specific humidity depression offered considerable insights into the sensitivities of EDH and EDS. The range of turbulence stability was divided into three categories referred to as very stable, moderate stability, and very unstable conditions with Richardson number ranges of greater than 0.01, between -0.03 and 0.01, and less than -0.03, respectively. The frequency of occurrence for these three stability regions is 4.5%, 75.5%, and 20%, respectively. In the very stable region, EDH was found

to be extremely sensitive to specific humidity depression and not sensitive to Richardson number. In the moderate stability region the EDH showed large sensitivity to both stability and humidity depression with less sensitivity at smaller magnitudes of specific humidity depression. In the very unstable region, the EDH was again sensitive to humidity depression but showed essentially no sensitivity to stability represented by bulk Richardson number.

Analysis of EDH sensitivity to wind speed revealed that a surface layer predominantly driven by buoyancy did not produce deeper evaporative ducts. Very stable and very unstable conditions mostly only exist with light winds of less than 4 m s^{-1}. Deep EDH in stable conditions existed almost exclusively in low wind speeds. Deep EDH values for unstable conditions existed almost exclusively in high wind speeds.

About 1.4% of the cases indicated EDH was greater than 50 m and about 1.1% of the cases were undefined. Many of the undefined cases were in stable and low wind where MOST, and therefore the MASL model, does not perform well. About 11% of the cases indicated EDH less than 1 m. These cases included profiles with weak or positive moisture gradients in stable stratification or moist air advection where the MASL model did not perform well.

The EDS sensitivity analysis showed very similar results compared to the EDH although the stability value range of the categories is slightly different (smaller range for moderate stability category). Also, the EDS did show some additional small sensitivity to stability in the very stable and very unstable cases.

The sensitivity of propagation loss to EDH and EDS was investigated and there was an apparently strong sensitivity to EDH and a lesser but still notable sensitivity to EDS. Propagation Loss was most sensitive to EDH when the EDH varied in the range of the cutoff frequency for the particular radar in consideration. The X-band radar was the most sensitive in that range (e.g., less than 10 m EDH) and also displayed a significant sensitivity in deeper evaporative ducts where multimodal interference became significant in creating interference lulls and peaks. The C-band and S-band radars were also sensitive in the interval range of EDHs that had cutoff frequencies around the frequency of the

radar, however the sensitivity was weaker. Also, multimodal interference was not as significant as with the X-band. The EDS shows similar behavior as the EDH, except the shows less sensitivity to EDS compared to EDH.

2.   Hybrid SCM/COAMPS Approach for Environmental Characterization

The ability of the full 3-D COAMPS for EM propagation prediction was evaluated first by comparing profiles extracted from the 3D model field with coincident sounding launched during the TW13 exercise. COAMPS in general performed well statistically with weak or no systematic bias compared to the soundings. However, at much coarser vertical resolution, large deviations are seen in the gradients of M, especially in the lower 2 km of the atmosphere. In that sense, COAMPS was unable to represent complex profiles with multiple layers yielding multiple elevated ducts. Although the general ducting features were somewhat represented by COAMPS simulations, the gradient strength, ducting height and ducting depth appeared to be very poorly represented with errors varying from 100 to 1000 m difference in ducting layer height. The complex near coastal regime may have been a key factor in the performance problems with COAMPS in these cases.

Two hypotheses were postulated in this thesis regarding a hybrid SCM/COAMPS approach for environmental short-term forecast. Hypothesis 1 states that high vertical resolution SCM would better resolve significant gradient layers in mean variables especially when the gradients are results of subgrade-scale processes. This was confirmed for cases where the vertical gradient is sharp such as with the cloud topped boundary layer and the surface layer. The case of a cloud topped boundary layer was selected with concurrent measurements from UPPEF 2012. The results indeed show that the higher resolution SCM runs provided significantly sharper gradients at the cloud top as well as provided detailed boundary layer structure not present in the lower resolution SCM. This initial testing provided confidence in the SCM approach.

The concept behind the hybrid modeling approach was to utilize the full 3D model to provide initial and forcing conditions to the SCM. The FAM was developed to

extract and process information from the raw 3D output to produce initial and forcing conditions. The analysis of this process and results provided a solid understanding of the horizontal, vertical, and temporal variability within the TW13 regime during TW13 and optimized the spatial averaging technique used to produce initial and boundary conditions.

The SCM runs were made first using idealized boundary conditions nominally derived from FAM generated forcing terms. These idealized simulations allowed us to evaluate the roles of vertical resolution and other choices of model configurations for the conditions in TW13 experiment. It was found that higher vertical resolution allowed for sharper vertical gradient representation both at initialization and throughout the forecast. Systematic analysis of turning on and off specific configurations of the model allowed us to identify whether the evolution of the SCM was consistent with the forcing. When reasonable forcing conditions were used, the SCM evolved similarly to the full 3D COAMPS and also resulted in a profile similar to what was observed. There were also cases where no clear difference or advantage to the higher resolution SCM was apparent. Testing using modified eddy diffusivity was considered necessary and designed to be more consistent with Monin-Obukhov Similarity Theory due to the many vertical grid levels in the surface layer. The modified eddy diffusivity showed a distinct impact on the resulting forecast structure of the boundary layer. Finally, this testing and evaluation also revealed the large sensitivity of the boundary layer evolution to the sea surface temperature from COAMPS 3-D simulations.

The SCM was then run using full COAMPS 3D model derived forcing. The Forecast Analyses Model (FAM) was developed to retrieve the 3-D COAMPS results for a particular location and also to perform the spatial and temporal averaging to obtain the average initial and forcing conditions. This was necessary to avoid extreme initialization and unrealistically persistent forcing. Model run without a smoothing or averaging of the forcing conditions created instabilities in the results and often the model may even crash before completion. After many initial testing, the averaging scheme when using the COAMPS 4 km grid (nest 3) was set to be 20 km horizontal averaging for initial conditions and horizontal advection, and 100 km horizontal averaging to represent large

scale subsidence. Vertical averaging was found to significantly dilute vertical gradients beyond benefit and was thus not implemented. Lastly, linear interpolation of the forcing terms between hourly updates was used. These measures were necessary because the near coastal regime was difficult to model due to the layered and complex variability and coastal and overland contamination.

The SCM runs using the full 3D COAMPS derived forcing evolved as expected and the model functioned appropriately for short term forecast. In some cases, the modeled features represented similar features in the validating sounding although the properties of the features such as height, thickness, and strength were different. Higher vertical resolution in the SCM did make a difference as to how well the modeled feature gradient matched the verifying sounding. We also showed a case where the SCM failed to produce some specific features as indicated in the verifying sounding. This case illustrated the significant limitation of the hybrid modeling system. Specifically, in complex layered profile regimes, if the layering forcing is not resolved by the parent model output, the SCM has no possibility in representing the complex structure. Simply put, the high resolution SCM is still limited by the lower resolution forcing derived from the 3D model. However, the SCM simulation over the open ocean followed the evolution of the COAMPS reasonably well and showed good potential for the SCM to have a reasonable profile evolution while also resolving higher resolution gradients at the inversion and in the surface layer. The benefit of the higher resolution cloud free inversion representation is yet to be evaluated extensively.

3.   A New Blending Technique Using SCM

One of the major contributions of this thesis work is the development of a new blending technique to append M-profile of the evaporative duct with that from the mesoscale model for the rest of the atmosphere. The use of SCM enables high vertical resolution to allow explicit representation of the evaporative duct in the surface layer, while the gradual nudging scheme allows smooth transition from the surface layer to the COAMPS M-profile. This concept is thoroughly tested using a total of 65 time/locations in comparison with the AREPS blending scheme that blends NAVSLaM and COAMPS.

The 65 testing cases include both stable and unstable boundary layers under low to moderate wind. The results indicate that the dynamic blending approach proposed here is comparable to the existing blending scheme in AREPS when the existing scheme works well. The new approach provides better results in cases when the existing approach does not work well, which is the advantage of the new approach. Further testing results also suggest that the modified eddy diffusivity works better compared to the original K formulation because it results in a profile that better represents the MOST profile while yields smoother transition to the COAMPS profile aloft.

C.   RECOMMENDATIONS FOR FUTURE WORK

The single column model proved to be very sensitive to the forcing conditions. The FAM was created to extract profiles from the 3D model and process them for initial and forcing conditions. As such, spatial averaging schemes were used by the FAM to smooth potentially extreme or unstable profiles. One drawback of this approach was the dilution of the vertical gradient. One possibility to address this inadvertent vertical smoothing would be to perform a smarter averaging technique to first recognize a feature and do a spatial average of that features height while preserving the feature's other properties such as gradient and thickness. In this manner, large spatial averaging could be employed without diluting the feature's properties which are the very properties that this work was intent on representing at higher resolution with greater accuracy. A similar feature preservation interpolation scheme is used by AREPS to interpolate modified refractivity profiles between grid points when preparing environmental files for the APM.

The SCM requires further adjustment, testing and evaluation on overall vertical grid scheme. There remain many possibilities in readjusting the vertical grid level distribution possibly to focus on a particular feature in certain conditions or regimes, but certainly to fine tune for best performance both in the surface layer and boundary layer. In this new approach for modeling evaporation duct and surface layer, the nudging used was of such strength above the surface layer that most of the free atmosphere may be neglected or minimally represented allowing for more focused high resolution in the surface layer. In this manner a higher resolution in the surface layer may be attained

allowing for more bins of possibility for EDH. Additionally, testing remains to derive a method of more actively determining the nudging interval based on the conditions.

In addition to physical model level adjustments, improved parameterization of physical process can be tested and evaluated. Processes that can be considered include surface flux and profiles to include waves and sea sprays and in conditions when the basic assumptions of MOST are violated (e.g., in heterogeneous conditions). Because of the availability of coupled ocean-wave-atmospheric modeling, surface fluxes and surface layer profiles using sea-state dependent parameterizations are worth investigating. As the evaporative duct property is extremely sensitive to choice of the SST, better ways to obtain more accurate SST would be crucial to future research similar to this work.

Another investigation of a 1D model system employed to improve very short term (1-2 hours) forecast skills of fog, cloud, and visibility by Bergot et al. (2005). They also demonstrated that the use of a 1D model to forecast fog and low clouds could only be beneficial if it is associated with local measurements and a local assimilation scheme. This approach can be tested in future research to include assimilations of soundings or near-surface measurements in hope to improve the local forecast skill.

Finally, future work can benefit from more extensive concurrent EM propagation measurements. This research will be continued in this direction as part of a new research initiative, Couple Air-Sea Processes and EM ducting Research (CASPER). In addition, direct measurements of temperature and humidity profiles in the lowest levels of the atmosphere to resolve evaporative duct height and strength will be extremely valuable to further evaluate the hybrid model approach and the SCM approach for blending the M-profile in the surface layer with that from the mesoscale model.

LIST OF REFERENCES

Almond, T., and J. Clarke, 1983: Consideration of the usefulness of microwave propagation prediction methods on air-to-ground paths. *Proc. IEEE, Part F,* **130**, 649–656.

Anderson, K. D., 1995: Radar detection of low-altitude targets in a maritime environment. *IEEE Trans. Antennas Propag.*, **43(6)**, 609–611.

Arakawa, A., and V.R. Lamb, 1977: Computational design of the basic dynamical processes of the UCLA general circulation model. *Methods Comput. Phys.,* **17,** 173–265.

Atkinson, B. W., and M. Zhu, 2006: Coastal effects on radar propagation in atmospheric ducting conditions. *Meteorol. Appl.*, **13(1)**, 53–62. doi:10.1017/S1350482705001970

Atkinson, B. W., J. G. Li, and R. S. Plant, 2001: Numerical modeling of the propagation environment in the atmospheric boundary layer over the Persian Gulf. *J. Appl. Meteorol*. **40**, 586–603

Ayotte, K. W., P. P. Sullivan, A. Andren, S. C. Doney, A. A. M. Holtslag, W. G. Large, and J. C. Wyngaard, 1996:. An evaluation of neutral and convective planetary boundary-layer parameterizations relative to large eddy simulations. *Bound.-Layer Meteor.*, **79(1-2)**, 131–175.

Babin, S. M., G. S. Young, and J. A. Carton, 1997: A new model of the oceanic evaporation duct. *J. Appl. Meteor*., **36**, 193–204.

Barrios, A.E., 1992: Parabolic equation modeling in horizontally inhomogeneous environments, *IEEE Trans. Antennas Propag.*, **40**, 791–797.

Barrios, A. E. and W. L. Patterson, 2002: Advanced propagation model (APM) ver. 1.3.1 computer software configuration item (CSCI) documents, *SSC SD TD 3145*, 254 pp.

Bean, B. B., and E. J. Dutton, 1968: Radio Meteorology. *Dover Publications*, 435 pp.

Bergman, J. W., and P. D. Sardeshmukh, 2003: Usefulness of single column model diagnosis through short-term predictions. *J. Climate,* **16**, 3802–3818.

Bergot, T., D. Carrer, J. Noilhan and P. Bougeault, 2005: Improved site-specific numerical prediction of fog and low clouds: A feasibility study. *Wea. Forecasting,* **20(4)***,* pp. 627–646. doi:10.1175/WAF873.1.

Blackadar, A.K., 1962: The vertical distribution of wind and turbulent exchange in a neutral atmosphere. *J. Geophys. Res.*, **67**, 3095–3102.

Bretherton, C. S., J. R. McCaa, and H. Grenier, 2004:. A new parameterization for shallow cumulus convection and its application to marine subtropical cloud-topped boundary layers. part I: Description and 1D results. *Mon. Wea. Rev.*, **132(4)**, 864–882. doi:10.1175/1520-0493(2004)132(0864:ANPFSC)2.0.CO;2

Brooks, I. M., A. K. Goroch, and D. P. Rogers, 1999: Observations of strong surface radar ducts over the Persian Gulf. *J. Appl. Meteor.*, **38**, 1293–1310.

Bunker, A.F., 1956: Measurements of counter-gradient heat flows in the atmosphere. *Australian J. Phys.*, **9**, 133–143.

Burk S. D., and T. Haack, 2003: Coastal Atmospheric Boundary Layer Impacts on Refractivity and EM Propagation. *6th Conference on Coastal Atmospheric and Oceanic Processes and Prediction*, San Diego, CA. Amer. Meteor. Soc., 8–14 January 2005.

Burk, S. D. and W. T. Thompson, 1982: Operational evaluation of a turbulence closure model forecast system. *Mon. Weather Rev.,* **110***,* pp. 1535–1543.

Burk, S. D., and W. T. Thompson, 1997: Mesoscale modeling of summertime refractive conditions in the Southern California Bight. *J. Appl. Meteor.*, **36**, 22–31.

Businger, J. A., J. C. Wyngaard , and Y. Izumi, 1971: Flux profile relationships in the atmospheric surface layer. *J. Atmos. Sci.,* **28**, 181–189.

Charnock, H., 1955: Wind stress on a water surface. *Quart. J. Roy. Meter. Soc.*, **81**, 639.

Cook, J., & Burk, S. (1992): Potential refractivity as a similarity variable. *Bound.-Layer Meteor*, **58(1-2)**, 151–159.

Director of Naval Oceanography and Meteorology, 1984: The Effects of the Environment on Radio and Radar Wave Propagation. *Naval Oceanography and Meteorology Memorandum No. 1/84*. London Hydrographic Dept, Ministry of Defence

Djolov, G. D., 1973: Modeling of interdependent diurnal variation of meteorological elements in the boundary layer. Ph.D. thesis, University of Waterloo, 219 pp.

Doyle, J., T. Holt, J. Cook, C. Amerault, D. Flagg, D. Geiszler, T. Haack, T. Holland, J. Hao, J. Nachamkin, P. Pauley, D. Tyndall, 2013: Overview of synoptic conditions and COAMPS modeling during TW13. Conference Briefing at NRL Monterey, Sept 2013. ppt, 15 slides.

Edson, J. B., C. J. Zappa, J. A. Ware, W. R. McGillis, and J. E. Hare, 2004: Scalar flux profile relationships over the open ocean, *J. Geophys. Res.*, **109**, C08S09, doi:10.1029/2003JC001960.

Edson, J., T. Crawford, J. Crescenti, T. Farrar, et al., 2007: The coupled boundary layers and air-sea transfer experiment in low winds. *Bull. Amer. Meteor. Soc.,* **88.3**, pp. 341–356.

Fairall, C. W., J. D. Kepert, and G. J. Holland, 1994: The effect of sea spray on surface energy transports over the ocean. *Global Atmos.Ocean Syst.*, **2(2-3)**, 121–142.

Fairall, C. W., E. F. Bradley, D. P. Rogers, J. B. Edson and G. S. Young, 1996: Bulk parameterization of air-sea fluxes for tropical ocean-global atmosphere coupled-ocean atmosphere response experiment. *J. Geophys. Res.,* **101***, pp. 3747–3764.

Frederickson, P. A., K. L. Davidson, and A. K. Goroch, 2000: Operational bulk evaporation duct model for MORIAH,. Naval Postgraduate School, Draft Version 1.2, May 2000, 70 pp.

Frederickson, P., K. Davidson, J. Stapleton, D. Shanklin, R. Wiss, T. Nguyen, E. Burgess III, C. Weeks, W. Thornton, and T. Brown, 2012: Validation of AREPS propagation assessments using different evaporation duct models. Naval Postgraduate School, Draft, 23 pp

Frederickson, P., 2014: An Evaluation of Evaporation Duct Models and Methods Used for SPY-1 Radar Performance Predictions, *Brief for Naval Air and Missile Defense Command via teleconference.*

Frederickson, P. A., 2015a: Software Design Description for the Navy Atmospheric Vertical Surface Layer Model (NAVSLaM), Version 1.1. Prepared for the Naval Oceanographic Office, Systems Integration Division, 16 January 2015, 52 pp.

Frederickson, P. A., 2015b: Software Requirements Specification for the Navy Atmospheric Vertical Surface Layer Model (NAVSLaM), Version 1.1. Prepared for the Naval Oceanographic Office, Systems Integration Division, 16 January 2015, 58 pp.

Frederickson, P. A., 2015c: Validation Test Report for the Navy Atmospheric Vertical Surface Layer Model (NAVSLaM), Version 1.1. Prepared for the Naval Oceanographic Office, Systems Integration Division, 16 January 2015, 32 pp.

Ghan, S. J., L. R. Leung, and J. McCaa, 1999: A comparison of three different modeling strategies for evaluating cloud and radiation parameterizations. *Mon. Wea. Rev.,* **127**, 1967–1984.

Godfrey, J. S., and A. C. M. Beljaars, 1991: On the turbulent fluxes of buoyancy, heat and moisture at the air-sea interface at low wind speeds. *J. Geophys. Res.*, **96**, 22 043–22 048

Gregory, D., Estimation of entrainment rate in simple models of convective clouds, 2001: *Quart. J. Roy. Meteor. Soc.,* **127(571)**, pp. 53–72.

Guichard, F., J. C. Petch, J. L. Redelsperger, P. Bechtold, J. P. Chaboureau, S. Cheinet, M. Tomasini, 2004: Modelling the diurnal cycle of deep precipitating convection over land with cloud-resolving models and single-column models. *Quart. J. Roy. Meteor. Soc.*, **130(604)**, 3139–3172. doi:10.1256/qj.03.145

Haack, T. and S. D. Burk, 2001: Summertime marine refractivity conditions along coastal California. *J. Appl. Meteor.*, **40**, 673- 687.

Haack, T., C. Wang, S. Garrett, A. Glazer, J. Mailhot, and R. Marshall, 2010: Mesoscale Modeling of Boundary Layer Refractivity and Atmospheric Ducting. *J. Appl Meteor and Climatol*, **49**, 2437–2457.

Hitney, H. V., and R. Vieth, 1990: Statistical Assessment of Evaporation Duct Propagation. *IEEE Trans. Antennas Propag*., **38**, 794–799

Hodur, R M., 1997: The Naval Research Laboratory's Coupled Ocean/Atmosphere Mesoscale Prediction System (COAMPS). *Mon. Wea. Rev*., **125**, 1414–1430.

Hogstrom, U., 1988: Non-dimensional wind nd temperature profiles in the atmospheric surface layer: A re-evaluation. *Bound.-Layer Meteor.*, **42**, pp 55–78

Jeske, H., 1973: State and limits of prediction methods of radar wave propagation conditions over the sea. Modern Topics in Microwave Propagation and Air–Sea Interaction, A. Zancla, Ed., D. Reidel Publishing, 130–148.

Kerr, D. E., 1951: Propagation of short radio waves. New York, McGraw-Hill Book Co.

Lee, W.-H., S. F. Iacobellis, and R. C. J. Somerville, 1997: Cloud radiation forcings and feedbacks: General circulation model tests and observational validation. *J. Climate,* **10**, 2479–2496.

Lin, X. and R. H. Johnson, 1996: Kinematic and thermodynamic characteristics of the flow over western Pacific warm pool during TOGA COARE, *J. Atmos. Sci.*, **53**, 695–715.

Liu, W. T., and T. V. Blanc, 1984: Liu, Katsaros, and Businger (1979) bulk atmospheric flux computational iteration program in FORTRAN and BASIC. United States Naval Research Lab., Wash., D.C., NRL Memorandum Report 5291, May 8, 1984, 20.

Liu, W. T., K. B. Katsaros, and J. A. Businger, 1979: Bulk parameterization of the air–sea exchange of heat and water vapor including the molecular constraints at the interface. J. *Atmos. Sci.*, **36**, 1722–1735.

Lohmann, U., N. McFarlane, L. Levkov, K. Abdella, and F. Albers, 1999: Comparing different cloud schemes of a single column model by using mesoscale forcing and nudging technique. *J.Climate,* **12**, 438–461.

Louis, J., 1979: Parametric model of vertical eddy fluxes in the atmosphere. *Bound-Layer Meteor.,* **17(2)***,* pp. 187–202.

Mahrt, L., D. Vicker, and E. L. Andreas 2014: Low-level wind maxima and structure of the stably stratified boundary layer in the coastal zone. *J. Appl. Meteorol. Clim.,* **53**, 363–376.

Manabe, S., and R. T. Wetherald, 1967: Thermal equilibrium of the atmosphere with a given distribution of relative humidity. *J. Atmos. Sci.,* **24**, 241–259.

Mass, C. F., 2012: How High Do Weather Balloons Fly. Personal blog, http://cliffmass.blogspot.com/2012/10/how-high-do-weather-balloons-rise.html

Mellor, G.L. and T. Yamada, 1974: A Hierarchy of Turbulence Closure Models for Planetary Boundary Layers. *J. Atmos. Sci.*, **31**, 1791–1806.

Monin, A. S., and A. M. Obukhov, 1954: Basic laws of turbulent mixing in the surface layer of the atmosphere. Trudy Geofiz. Inst. Aca. Nauk SSSR, **24**, 163–187.

Neggers,. R. A. J., M. Köhler and A. C. M. Beljaars, 2009: A dual mass flux framework for boundary layer convection. part I: Transport. *J. Atmos. Sci.* **66(6)***,* pp. 1465–1487.

Paulus, R. A., 1984: Practical application of the IREPS evaporation duct model. *NOSC Tech. Rep*. **966**, 68 pp. [Available from National Technical Information Service, U.S. Department of Commerce, Technology Administration, 5285 Port Royal Road, Springfield, VA 22161.]

Paulus, R. A., 1985: Practical application of an evaporation duct model. *Radio Sci.,* **20,** 887–896.

Paulus, R. A., 1989: Specification for Environmental Measurements to Assess Radar Sensors. NOSC Tech Document 1685, 43 pp. [Available from National Technical Information Service, U.S. Department of Commerce, Technology Administration, 5285 Port Royal Road, Springfield, VA 22161.]

Paulus, R. A., 1990: Evaporation Duct Effects on Sea Clutter, *IEEE Trans. Antennas Propag*., **38**, 1765–1771

Randall, D. A., and D. G. Cripe, 1999: Alternative methods for specification of observed forcing in single-column models and cloud system models. *J. Geophys. Res.,* **104**, 24,527–24,545.

Randall, D. A., Q. Hu, K. Xu and S. K. Krueger, 1994: Radiative-convective disequilibrium. *Atmospheric Research, Amsterdam, the Netherlands 31(4),* pp. 315–327.

Reilly, J. P., and G. D. Dockery, 1990: Influence of Evaporation Ducts on Radar Sea Return. *Proc. IEE, Part F*, **137**, 80–88

Rogers, L. T. 1996: Effects of the variability of atmospheric refractivity on propagation estimates, *IEEE Trans. Antennas Propag.*, **44(4)**,460-465.

Somerville, R., and S. F. Iacobellis, 1999: Single-column models, ARM observations, and GCM cloud-radiation schemes. *Physics and Chemistry of the Earth.B: Hydrology, Oceans and Atmosphere, Amsterdam, the Netherlands*, **24(6)**, 733–740.

Stull, R. B., 1988: An introduction to boundary layer meteorology. Dordrecht, Holland, Kluwer Academic Publishers, 1988. 666 pp.

Sverdrup, H.U., M.W. Johnson and R.H. Fleming, 1942: The Oceans, Their Physics, Chemistry, and General Biology. Prentice Hall, New York, 1087 pp.

Terradellas, E. and D. Cano, 2007: Implementation of a single-column model for fog and low cloud forecasting at Central-Spanish airports. *Pure & Applied Geophysics 164(6-7),* pp. 1327–1345. doi:10.1007/s00024-007-0221-8.

Therry, G., and P. Lacarrere, 1983: Improving the eddy kinetic energy model for planetary boundary layer description. *Bound.-Layer Meteor.*, **25(1)**, 63–88.

Tompkins, A. M., K. Gierens and G. Raedel, 2007: Ice supersaturation in the ECMWF integrated forecast system. *Quart. J. Roy. Meteor. Soc.,* **133(622)**, pp. 53–63. doi:10.1002/qj.14.

Troen, I., and L. Mahrt, 1986: A Simple Model of the Atmospheric Boundary Layer; Sensitivity to Surface Evaporation. *Bound.-Layer Meteor.,* **37**, 129–148.

Trigo, I. F., and P. Viterbo, 2003: Clear-sky window channel radiances - A comparison between observations and the ECMWF model. *J. Appl. Meteorol*. **42(10)**, pp. 1463–1479. doi:10.1175/1520-0450(2003)042(1463:CWCRAC)2.0.CO;2.

Wieringa, J. (1980). Revaluation of the Kansas mast influence on measurements of stress and cup anemometer overspeeding. *Bound.-Layer Meteor.*, **18(4)**, 411–430.

Wyngaard, John C., 1985: Structure of the Planetary Boundary Layer and Implications for its Modeling. *J. Appl. Meteor.*, **24**, 1131–1142.

Wyngaard, John C., and Richard A. Brost, 1984: Top-Down and Bottom-Up Diffusion of a Scalar in the Convective Boundary Layer. *J. Atmos. Sci*. **41**, 102–112.

Yu, T., 1977: Comparative study on parameterization of vertical turbulent exchange processes. *Mon. Wea. Rev.*, Boston, **105(1)**, 57–66.

Zuniga, C. A., 2013: A small flux buoy for characterizing marine surface layers, MS thesis, Naval Postgraduate School, Monterey, CA, June 2013.

THIS PAGE INTENTIONALLY LEFT BLANK

INITIAL DISTRIBUTION LIST

1.   Defense Technical Information Center
        Ft. Belvoir, Virginia

2.   Dudley Knox Library
        Naval Postgraduate School
        Monterey, California